UNIVERSITÉ DE STRASBOURG

L'Ecole Doctorale de Physique et Chimie-Physique – ED 182

Observatoire Astronomique de Strasbourg

THÈSE

présentée par:

Anu KUNDU

soutenue le : **17 Septembre 2018**

pour obtenir le grade de : **Docteur de l'université de Strasbourg**

Discipline/ Spécialité : Astrophysique

Contribution of multipolar electromagnetic fields to the radio and high energy emission of pulsars

(Contribution des champs électromagnétiques multipolaires à l'émission radio ethaute énergie des pulsars)

THÈSE dirigée par :
[Mr PETRI Jérôme] Maître de conférences HDR, Université de Strasbourg

RAPPORTEURS :
[Mme WEBB Natalie] Astronomer HDR, L'Institut de Recherche en Astrophysique et Planétologie, Toulouse
[Mr GALLANT Yves] Chargé de recherche HDR, Laboratoire Univers et Particule, Montpellier

---

AUTRES MEMBRES DU JURY :
[Mr KIRK John] Professeur, Max-Planck-Institut für Kernphysik, Heidelberg, Allemagne
[Mr SMITH David] Directeur de recherche HDR, Centre d'Études Nucléaires de Bordeaux Gradignan
[Mr HAMEURY Jean-Marie] Directeur de recherche HDR, Université de Strasbourg

Acknowledgements

My first and foremost thanks goes to my supervisor *Jérôme Pétri* for his invaluable guidance throughout these three years. I appreciate you being available for discussions even if they were not scheduled in advance at times. Your patience and acceptance towards my work style (be it working from home when needed or late in the afternoons) made my journey easier. I thank you for your valuable moral support on guiding me how research can be slow and time consuming when I was being hard on myself for being stuck with something which seemed trivial at first. Most importantly, thank you for keeping a good balance between giving me the freedom I needed and to be there when I needed guidance.

I would like to extend my gratitude to my ex-colleague *Iwona Mochol* who offered her kindness in my initial time in a foreign country, for starters. Updating you every day at afternoon coffee about my activities and listening to yours had been incredibly motivating. And thank you for being my rock climbing partner - those sessions are missed!

My fellow PhD friends, *Patricia Andrea Rojas Lobas* and *Djordje Savic*, all those fun jokes on PhD woes and stress made things simpler; especially with a touch of the chocolates and ice creams we shared.

Mari Kolehmainen, my workplace guide to the real professional world; *Yelena Stein*, one of the most wonderfully supportive person I have come across; *Frédéric Marin*, one of those rare people who can be admired for their work-life balance and *Ada Nebot*, serving as someone to look forward to for suggestions - your mere presence in the Observatory made me relieved that there are people I can go to when I need a colleagues expertise. I thank all of you for being extremely supportive and motivating.

Beyond the workplace support, the moral support I received from my family and friends should be mentioned as they are the people who in one way or another, helped me in this intense journey of PhD.

Mum and *papa*, thank you for trusting me with every decision I made in making my way to this point and thank you for being amazingly understanding at times

when I needed to prioritize my work over other things. And, *Sunny Kundu*, the coolest brother ever; I know that if I thank you formally, you will probably faint out of shock, so I am making it a note to bring you a big chocolate box and I promise that I won't ask you to share any of it with me. Hope you realize how much your support has meant to me. Also, my dear *cousins*, a huge thank you for sending me videos and pictures of my sweet little nephew and niece, watching them had been one of my favourite stress busters!

Richard Crew, my best friend, without your perfectly timed reminders to divide any complex journey in small simple steps whenever I stumbled, it would have been tough, really tough. Thank you for putting up with my crazy meltdowns, for believing in me and for everything else.

Alina Tomescu-Baciu, co-founder of our 'PhD Justice League', our long PhD story texts started just right in time this year. It is pleasantly surprising to achieve a deep support network with you in such a short span of time; thank you for being a lovely listener.

My *friends* back in India, and here, every little act and message and call making me realize I have got so many friends who care, thank you for being there. Also, my friends who have been amazing listeners whenever I needed them to be - *Dino, Alisha, Michael, John, Vinay, Sarah and Roy* - you guys are the best!

A special mention of my three most favourite things in this world - sketching Batman, watching Star Trek and listening to Pink Floyd - which gave me the peace of mind I needed during this roller coaster ride.

Contents

List of Figures

List of Tables

Chapter 1

Introduction

1.1 Brief history of discovery

Predicting astrophysical phenomena based solely on theories and coming across an observational evidence for them later, is one of the most impressive things about science. And so are the discoveries which are made unexpectedly, or serendipitously. One of the most fascinating facts related to pulsars is that it involves both the above scenarios.

It was Baade & Zwicky (1934) who mentioned neutron stars for the first time while describing supernovae. They suggested that supernova explosions represent the transition of an ordinary star into stars that consist of extremely closely packed neutrons. It was correctly proposed that this star would possess a very small radius and extremely high density.

Hewish & Okoye (1965) discovered the presence of an object of small angular diameter in the Crab nebula which was observed to be more pronounced at radio frequencies. It was declared an unusual object at the time since there was no entirely satisfactory explanation found to describe the emission as strong as 20% of the total emission from the nebula from such a small source.

Until 1967 neutron stars were thought to be too faint in luminosity to be detectable and only a small, albeit significant, amount of work focused on these objects. For instance, Zwicky (1938a,b) summarized conclusions of a series of theoretical in-

vestigations concerning the properties of neutron stars; Hoyle et al. (1964) suggested the possibility of degeneracy pressure acting in a dying star resulting in a stable remnant as white dwarf or neutron star; Cameron (1965, 1966) explored the possible magnetospheric phenomenon and properties associated with neutron stars.

Pacini (1967) pointed out that the spinning neutron stars having large magnetic fields will emit low frequency electromagnetic waves with a strong amplitude. It was also insisted that this could explain the emission from the unusual source in the Crab nebula which must have resulted in the formation of a neutron star as an end product from the great supernova of 1054. It was justified since the energy from the pulsar spindown luminosity, which is 5×10^{31} W, is efficiently converted into the synchrotron emission from the Crab Nebula, which is $\sim 1.3 \times 10^{31}$ W (Woltjer, 1971; Hester, 2008).

Hewish et al. (1968) using the radio telescope at the Mullard Radio Astronomy Observatory, reported the observation of periodic signals having a repetition cycle of 1.337 lasting for about 0.3 seconds each. The absence of parallax highlighted that the source was far outside the solar system. They tentatively proposed that the observed periodic signals could originate from white dwarfs or neutron stars.

The final confirmation that the discovered unusual source is, indeed, a pulsar was established by Gold (1968) claiming that the periodic behaviour of the signal is generated by the rotation of a neutron star. They[1] based their claim on the explanation that the strong magnetic fields and high rotation speeds would give rise to relativistic velocities of the particles in the surrounding magnetosphere and hence, generated the electromagnetic radiation. This radiation is observed periodically which reflects the rotation of the star and the time interval between the different radiation peaks is utilized to derive the rotation period of the star.

Almost all the follow up works, for instance by Hoyle & Narlikar (1968), Ryle & Bailey (1968), Saslaw (1968), to name a few, converged on this explanation. Finally, the iconic signal establishing discovery of pulsars earned Antony Hewish and Martin Ryle, the 1974 Nobel Prize in Physics. In 2018, Jocelyn Bell Burnell was awarded

[1]Throughout the thesis, gender neutral pronouns are used; that is, single authors are referred to as 'they'.

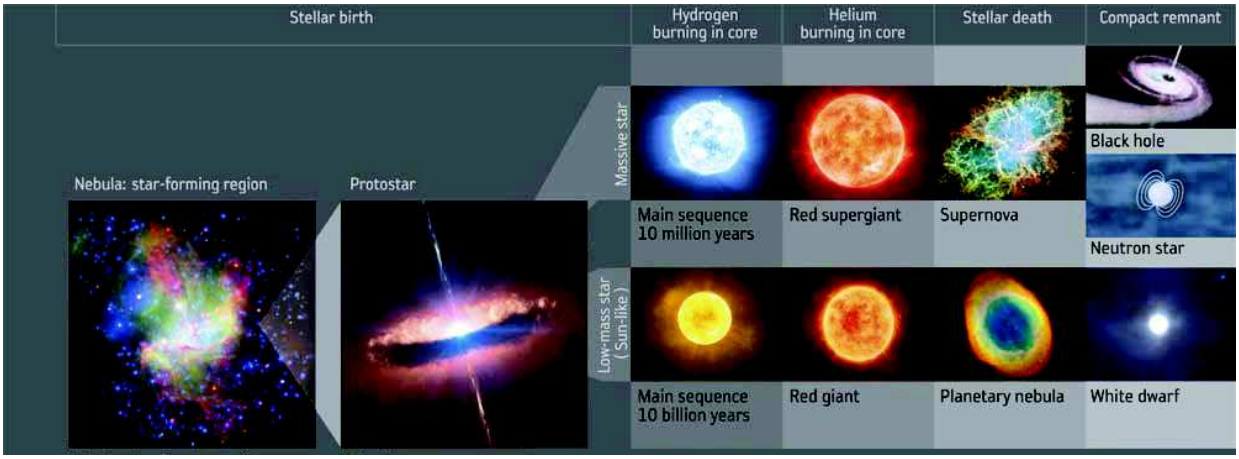

Figure 1-1: Different stages of stellar evolution - the diagram depicts the various stages in the life cycle of stars depending on their mass ESA-AOESMedialab (2012)

the Special Breakthrough Prize in Fundamental Physics for her contribution in discovering the first pulsar as a postgraduate student in 1967 under the supervision of Hewish.

1.2 The birth of a neutron star

The life cycle of a star varies depending on its mass. The process by which a star changes over the course of time constituting different phases of its life is termed as stellar evolution. The different stages of stellar evolution are summarized in Fig. 1-1 and the entire process is explained (Lamers & Levesque, 2017) in three major steps, as follows :

1. **Birth of a protostar, brown dwarf :** The interstellar medium is filled with trace amounts of elements which have been ejected from the dying stars. Some regions have high density of these elements forming dense molecular clouds called nebulae which are also called stellar nurseries as they are the regions leading to birth of stars. These dense molecular clouds, comprising mostly of hydrogen, remain in hydrostatic equilibrium meaning the outwards pressure of the gas is balanced out by the potential energy of the inward acting gravitational force. Now, if the cloud is so massive that the gas pressure is not enough to

withstand the gravitational force, the cloud collapses. Also, another scenario is triggered star formation when the equilibrium is disrupted by some external agency like two clouds colliding or a nearby supernovae affecting the cloud by ejection of gases. Once the equilibrium is disturbed, the collapse gives rise to small fragments which serve as star embryos.

The term used for these very young stars, which are still gaining mass from the parent gas cloud, is protostar. This phase ends when protostar starts rejecting the infalling gas from its parent, thus becoming an optically visible pre-main-sequence star. At this stage, if the star is not hot enough to sustain nuclear fusion and release energy, it ends up becoming a brown dwarf or sometimes, if not massive enough, a planet. However, if the temperature in its centre becomes so large that hydrogen begins to fuse into helium, a main sequence star is formed.

2. **Main sequence :** The main sequence is the phase in which star stays in hydrostatic equilibrium for millions or billions of years depending on its mass. The fusion reaction converting hydrogen into helium is responsible for releasing the energy which results in an outward pressure from the core of the star. Acting against this outward pressure is the inward acting gravitational energy trying to collapse the star. The outward acting thermal pressure and inward acting gravitational force balance each other creating a long lasting equilibrium phase where the star shines by itself.

3. **Stellar remnants :** Once the hydrogen fuel at the core of a main sequence star is consumed, the fusion reaction stops. What happens next, depends on the mass of the star it had during its main sequence lifetime. These stellar remnants can take one of the three forms described below.

    - *For low mass stars :* The stars with masses less than 8.0 $M_{\odot}$ (Koester & Reimers, 1996), after their main sequence ends, expand to become a red giant during which phase it fuses helium to carbon and oxygen in its

core which is called the triple alpha process. The initial mass leading to this red giant does not provide it enough mass to generate large enough temperatures to fuse carbon and oxygen further. Hence, what is left in the core is an inert mass of unfusable carbon and oxygen. The outer layer of the red giant is shed in form of a planetary nebula and the left over core, is the remnant white dwarf. As there is no fusion inside the white dwarf, the star has no source of fusion energy to support itself against the gravitational collapse. However, it is supported by energy generated by the electron degeneracy pressure which leads to extreme density of a white dwarf. The degeneracy pressure limits the maximum mass a white dwarf can withstand against collapse, which is known as the Chandrasekhar limit and is calculated to be approximately 1.44 $M_{\odot}$ (Chandrasekhar, 1931). If the mass of a white dwarf is higher than this limit, it collapses under its own gravity as the degeneracy pressure is not enough to work against it. So, for low mass stars, white dwarfs are thought to be the final evolutionary state.

- *For intermediate mass stars :* For the stars with masses above 8.0 $M_{\odot}$, the nuclear fusion continues until the core is rich in iron, leading to evolution of a red giant into a red supergiant. Since, the mass is above the Chandrasekhar limit at this stage to withhold the star against gravitational force by electron degeneracy pressure, the core collapses. This collapse leads to temperatures where electrons and protons come together to form neutrons by electron capture giving rise to large numbers of neutrinos. The creation of neutrons makes the core extremely compact and when the density approaches the neutron degeneracy pressure limits, the contraction stops. However, the infalling matter is heated by the outward flow of neutrinos igniting it and resulting into a supernovae explosion. The remnant left at the core of the explosion is the neutron star. The maximum mass against which neutron degeneracy pressure can withstand the gravitational collapse, based on earlier theoretical work, is 3.0 $M_{\odot}$ (the

Tolman–Oppenheimer–Volkoff limit) (Oppenheimer & Volkoff, 1939; Bombaci, 1996) beyond which the star will collapse under its own mass forming a black hole as discussed next. However, many works have condemned it to be uncertain; for instance the recent detection event GW170817 of gravitational waves and their electromagnetic counterpart from the merger of a binary neutron star published by Abbott et al. (2017) led to a follow up tide of papers constraining the maximum mass to be varying between $2.15-2.28\ M_{\odot}$ (Margalit & Metzger, 2017; Shibata et al., 2017; Ruiz et al., 2018; Rezzolla et al., 2018).

- *For high mass stars :* If the mass of the remnant exceeds the Tolman – Oppenheimer – Volkoff limit, meaning even neutron degeneracy pressure is not enough to withstand against gravitational force, the star collapses. This usually happens when the mass of the main sequence star is greater than about $20.0\ M_{\odot}$ (Maeder, 1992; Kobulnicky & Skillman, 1997). This collapsed entity is called a black hole, marking the end of the life cycle of an extremely massive star. These are usually referred to as stellar mass black holes. If the black hole lies at the centre of the galaxy, it can continue to grow by accretion from other stars or merging with other black holes to form supermassive black holes. Although, it remains an open field of research.

1.3 Why study neutron stars?

The current understanding of the electromagnetic activity of neutron stars, and especially pulsars is still quite limited to us, even though plenty of models and observations make attempts to fulfil the purpose. Apart from the reason to solve the puzzle of their own features, their study contributes to better comprehend many other varying areas of fundamental and high energy physics, for instance neutron stars help to constrain galactic electron density, magnetic fields, test gravity and nuclear matter in string field and high densities. Some of them are summarized below.

An understanding of the magnetic field geometry and radiation processes inside the magnetosphere and the wind outside gives an insight about how electromagnetic radiation is produced and how it interacts with charged particles. These topics are of interest for *fundamental physics* studies and their basic understanding is well established nowadays but considering the extreme environment of neutron stars, it helps us better constrain the physical equation of state of matter at extreme densities, giving a relation between the mass and size (or density and pressure) of the star within stable limits.

Also, for fields like, *nuclear and particle physics*, the extreme nature of pulsars is an insightful subject to understand the behaviour of matter in ultra-high density environments, which can't be produced in laboratories. The density of neutron star is similar to that of an atomic nucleus, and can even exceed it. Several equations of state for a neutron star have been proposed (e.g. Haensel et al. (2007); Ozel & Freire (2016)) based on different types of matter, such as quarks, nucleonic matter or more exotic particles, in different potentials. However, the equation of state describing neutron stars is still unconstrained. Also, unlike an atomic nucleus, neutron stars are predicted to consist of multiple layers with varying compositions and densities. The composition of the core of the neutron star, along with its equation of state, are the biggest puzzles related to neutron stars. Various models and observational features have put forward the idea that the innermost core consist of exotic matter.

Observing signals from pulsars and considering their propagation effects through the *interstellar medium* could contribute, at least a little, towards measurements of the structure of our galaxy (Gordon, 1987; Dwarkadas et al., 2000; Science, 2003). Pulsars are also proving useful for the field of *strong gravity* by working as one of the finest tools to test the theory of general relativity (Esposito-Farese, 1996; Kramer et al., 2004; Wex et al., 2012). Also, events related to pulsars, like their merger, are an excellent contribution to *multi messenger astronomy* because they provide the opportunity to observe gravitational and electromagnetic signals simultaneously. Projects like *Pulsar Timing Array (PTA)* have been actively observing the relations between arrival timings of pulsars to check for any signatures of gravitational waves

which will disrupt the arrival time of pulses from a pulsar. For future deep space explorations and associated *space navigation*, we need GPS like we have on Earth. NASA's project NICER-SEXTANT (Gendreau et al., 2012; Mitchell, 2015) is an ongoing mission to observe X-ray pulsars to use them as reference points to design a space navigation system. The importance of studying pulsars is still unfolding and there is so much more to discover and understand about them. With these objectives in mind, there are big projects like the *Square Kilometre Array (SKA)* which are currently in progress to contribute to solving puzzles of pulsars among many others (SKA Science Website, 2011; Stairs et al., 2011).

1.4 Properties of neutron stars

Neutron stars are complex objects containing exotic matter and showing different properties as compared to normal main sequence stars. A discussion of the characteristics like size, mass, radius and magnetic field strength of neutron stars for the sake of completeness is useful. Therefore, we list below a number of properties of these objects giving the observational and/or theoretical values known for them, wherever possible.

Mass and radius : The main sequence stars are composed of non degenerate matter which means particles are in different energy states and hence, gives rise to energy gradient and gaseous pressure from thermal motion. However, neutron stars are in degenerate state (lowest possible energy called zero point energy) and hence, the temperature gradient does not exist. This implies that to study their composition, temperature does not play an important role (Oppenheimer & Volkoff, 1939). The important information is the relation between density and pressure which is called equation of state (EOS). Given the EOS, for instance by Lattimer & Prakash (2001), the relation between mass and radius is easily calculated and then, using observational parameters it is theoretically possible to constrain the EOS.

Observations of neutron stars in binary systems have allowed the mass to be determined fairly accurately with an average of 1.35 $M_{\odot}$ (Thorsett & Chakrabarty,

1999). Theoretically, based on different models for EOS, neutron stars have both minimum and maximum mass limits as discussed by Lattimer & Prakash (2004). They argued that the maximum mass is of purely general relativistic origin and is unknown but lies in the range of 1.44 to 3 $M_\odot$. The upper bound was suggested to be because of causality (Rhoades & Ruffini, 1974) which means that the speed of sound in dense matter is less than the speed of light, whereas the lower bound was taken to be the largest accurately measured pulsar mass at that time, 1.4408 ± 0.0003 $M_\odot$ in the binary pulsar PSR 1913+16 (Weisberg & Taylor, 2003). However, a number of measurements of mass of neutron stars like - PSR J1614-2230 (1.97 ± 0.04 $M_\odot$) by Demorest et al. (2010), PSR J0348+0432 (2.01 ± 0.04 $M_\odot$) by Antoniadis et al. (2013) and PSR J2215+5135 ($2.27^{+0.17}_{-0.15}$ $M_\odot$) by Linares et al. (2018) have challenged the earlier lower bound of 1.44 $M_\odot$. Based on the EOS given by Baym et al. (1971a), the minimum stable mass was calculated to be 0.0925 $M_\odot$ by Baym et al. (1971b). Although, it highly varies based on the EOS; for instance, Haensel et al. (2002) found the minimum mass to be 0.61 $M_\odot$ for the SLy EOS (Douchin & Haensel, 2001) and 0.54 $M_\odot$ for the FPS EOS (Pandharipande & Ravenhall, 1989).

To limit the radius of the neutron star - balancing the centrifugal force and gravitational force for the mass on the neutron star surface of mass M, radius R, rotating with angular velocity Ω,

$$\Omega^2 R = \frac{GM}{R^2} \tag{1.1}$$

For period $P = 2\pi/\Omega$, the radius is

$$R = 1.5 \times 10^3 \left(\frac{M}{M_\odot}\right)^{1/3} P^{2/3} km \tag{1.2}$$

This is the upper limit to the radius (Lyne & Graham-Smith, 1990). Any rapid uniformly rotating star may generate viscous instabilities which are essentially a vehicle for the centrifugal force to dominate the gravitational attraction. These instabilities were analyzed by Morsink et al. (1999) explaining that the viscous effects will result in radiation of gravitational waves and hence, angular momentum losses leading to the slowing down of the rotation. They also determined that the rotation speed

limit is affirmed by Equation 1.1. Based on the EOS relation, Lattimer & Prakash (2004) constrained radius between 10.5 to 11.2 km. However, Li & Steiner (2006) used terrestrial laboratory measurements of nuclear matter to constrain the radius for a 1.4 $M_{\odot}$ neutron star between 11.5 and 13.6 km using the EOS derived from the potential given by Das et al. (2003), Li et al. (2004a) and Li et al. (2004b).

Hessels et al. (2006) discovered PSR J1748-2446ad which has a frequency of 716-Hz, the fastest spinning pulsar known. Considering a mass of 1.4 $M_{\odot}$, an upper limit of 14.4 km radius is calculated using an equation independent of the true EOS derived by Lattimer & Prakash (2004).

Period : As discussed above the fastest rotating pulsar PSR J1748-2446ad has a frequency of 716-Hz, which gives the fastest period observed to be 1.4 ms. The slowest-spinning radio pulsar PSR J0250+5854 with a period of 23.5 s was discovered by Tan et al. (2018). However, 1E 161348-5055, the source at the center of the supernova remnant RCW 103, is an isolated magnetar with a period of 6.67 hr making it the slowest neutron star ever detected (Rea et al., 2016; Borghese et al., 2018).

Density and composition : For commonly assumed parameters, radius 10 km and mass 1.4 $M_{\odot}$, the density of a neutron star is $6.7 \times 10^{14}\ kg\ m^{-3}$. The density of an atomic nucleus is $\rho_0 = 2.7 \times 10^{14}\ kg\ m^{-3}$ which is almost half of that of the neutron star, making a neutron star seem like a gigantic nucleus in terms of density. But that is not the case, while a nucleus is held together by strong interaction, the neutron star is held by gravity. Also, a nucleus is uniform in composition and density while neutron stars are predicted to consist of a complicated internal composition arranged in multiple layers as explained below.

The surface of a neutron star is a rigid crystalline solid composed of ordinary atomic nuclei crushed into a solid lattice with a sea of electrons flowing through the gaps between them (Arponen, 1972). Below the surface, the neutron star is divided into a number of layers, see Fig. 1-2, based on density. The outer crust is a sea of ions and electrons with no neutrons. Underneath it is the inner crust spanning about 1-2 kms, which has neutrons as well. As we go deeper towards the core, at higher densities, it becomes energetically favourable for relativistic electrons to penetrate the

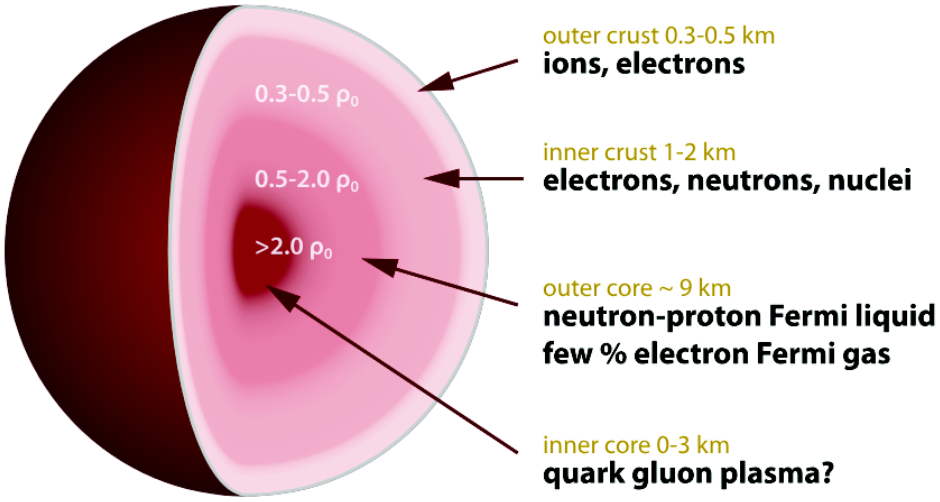

Figure 1-2: Cross-section of neutron star. Densities are in terms of ρ_0 which is the nuclear matter density saturation, where nucleons begin to touch (Schulze, 2010).

nuclei, combine with protons and form nuclei with unusually high numbers of neutrons which are unknown in laboratory. Such nuclei, with large number of neutrons, such as ^{118}Kr - a remarkable nucleus with 82 neutrons and 36 protons (Baym et al., 1971a) - decay rapidly on Earth but the large pressure inside neutron stars keeps them stable and electrons have no space or energy states left to fill. The outer core spans the most of the inner volume of the neutron star and is considered to be a neutron-proton superfluid region with no viscosity. The electrons interact weakly and have little part in structure and behaviour of neutron star. At the heart of the neutron star is the innermost core which is proposed to consist of exotic matter; at central densities about as high as six times the nuclear density saturation, neutrons may be squeezed to form degenerate stranger matter containing quarks, kaons etc (Lattimer & Prakash, 2007; Demorest et al., 2010; Kurkela & Vuorinen, 2016).

Magnetic field : The magnetic field strength on the surface of neutron stars ranges from 10^4 to 10^{11} T (Olausen & Kaspi, 2014). While the magnetars have strong magnetic fields of order of 10^{11} T, for older, millisecond pulsars, the value can go as low as 10^3 T. Despite the intense magnetic field, it has very little effect on the structure of the neutron star. However, outside the star, in the magnetosphere and

even beyond, the magnetic field dominates all the physical processes outweighing the effects of the gravitational field by a very large factor. This factor can be calculated using the ratio of the gravitational field and electrostatic forces on a particle near the surface given by,

$$\frac{GMm}{R^2} \Big/ \frac{e\Omega RB}{c} \tag{1.3}$$

where M, R and Ω is mass, radius and the rotational angular velocity of the neutron star with magnetic field B; and m and e is the mass and the electric charge of the charged particle near the surface. For instance, for the Crab pulsar, it gives 10^{-12} which shows how much weaker the gravitational field is, compared to electrostatic forces and consequently, influences the particle only slightly near the surface of Crab pulsar as compared to the dominance of the electromagnetic force (Lyne & Graham-Smith, 1990).

1.5 Significant observational characteristics

Observations have led to the discovery of more than 2000 pulsars in total with most of them being the normal pulsars while about 10% being the millisecond pulsars (Lorimer, 2012). The surveys like Parkes multibeam pulsar survey and targeted searches of Fermi gamma ray sources has led to a significant increase in the number of detection of pulsars. We show a couple of plots which are derived from observations and are used widely in pulsar studies.

To explain the rotational behaviour of pulsars, two quantities rotation period P and spindown rate $\dot{P}$ are usually mentioned. $\dot{P}$ is measured as a change in rotation period of pulsar over time and is dP/dt, which is considered to be result of magnetic dipole braking. All isolated pulsars are spinning down owing to the magnetic dipole radiation losses and this spindown measure helps in determining the characteristic age of pulsars, given as $\tau_C = P/2\dot{P}$ which cannot be used as true age of a pulsar. For instance, Jiang et al. (2013) and Dodson & Golap (2002) gave evidence that the PSR B1706-44 has a characteristic age about 17500 while its associated supernova is only about 5000 years old. A number of other cases showing the difference in the ages

are being discussed by Nicastro et al. (1996) and the references therein. In Fig. 1-3 (taken from The Second Fermi Large Area Telescope Catalogue of Gamma-ray Pulsars (Abdo et al., 2013)) the relation between this spindown rate and the period of observed pulsars has been shown.

In the figure, the characteristic age, calculated assuming the magnetic dipole braking as the energy loss mechanism to be $\tau_C = P/2\dot{P}$, is shown as constant blue dashed lines. Similar to this, the rate at which the rotational energy is decreasing and the surface magnetic field could be calculated from the timing information, since they are also a function of period and period derivative. The formulae could be derived as follows:

- The rotational kinetic energy E_{rot} is,

$$E_{rot} = \frac{1}{2} I \Omega^2 \tag{1.4}$$

  where I is the moment of inertia, and is considered to be $2MR^2/5$ as for a uniform rotating body of mass M and radius R. Also, Ω is the angular velocity, and is $\Omega = 2\pi/P$.

  Now, the rate of loss of E_{rot}, using above quantities, is,

$$\frac{dE_{rot}}{dt} = \frac{-4\pi^2 I \dot{P}}{P^3} \tag{1.5}$$

  The rotational kinetic energy loss, $\dot{E} = dE_{rot}/dt$ is shown in constant red dashed lines in the Fig. 1-3.

- Using the Larmor formula, the power of the magnetic dipole radiation from a magnetic dipole is,

$$P_{rad} = \frac{2}{3} \frac{(\ddot{m_\perp})^2}{c^3} \tag{1.6}$$

where $m_\perp$ is the perpendicular component of the magnetic dipole moment. Considering the magnetic dipole rotates with angular velocities Ω, m can be expressed in exponential form as $m = m_o e^{-i\Omega t}$, which gives ($\ddot{m} = \Omega^2 m$, and also, the magnetic dipole moment for a uniform sphere of radius R and surface magnetic field strength B_S, is $m = BR^3$ (Jackson, 1962). Using this information and $\dot{E}$ from Eqn. 1.5 as an estimate for P_{rad}, we get,

$$B_S = \frac{1.5Ic^3P\dot{P}}{2\pi R^3} \tag{1.7}$$

The surface magnetic field strength, B_S, is shown in constant green dashed lines in the Fig. 1-3.

The Fig. 1-3 also shows different types of pulsars. The red triangles, showing the millisecond pulsars, have much smaller spindown rate than that of the radio pulsars (shown in blue squares, green circles and black dots). The radio quiet pulsars, shown as blue squares are also much younger than the older millisecond pulsars, as indicated by the constant blue dashed lines for the τ_C and higher surface magnetic field strength B_S, indicated by the constant green dashed lines. Also, the red triangles and green circles show objects that have also been detected in gamma-rays. A more detailed classification, from a theoretical point of view, is discussed in Section 1.6.

Next, we show the pulsar population distribution in Galactic coordinates. This gives us an insight into the age and nature of pulsars. In Fig. 1-4, the location of radio and millisecond pulsars are shown. As seen in the figure, the radio pulsars lie close to the galactic equatorial disc (0°) while the millisecond pulsars are scattered almost all over the sky. This difference in distribution justifies that most of the millisecond pulsars are indeed, older than the radio young pulsars and hence, they have had enough time to move away from the galactic disc and spread throughout.

A rotating neutron star slows down over time which is usually attributed to the electromagnetic radiation losses of the rotating dipolar field of the star. For a pulsar rotating with frequency ν whose derivative is $\dot{\nu}$, the relation between the two is given

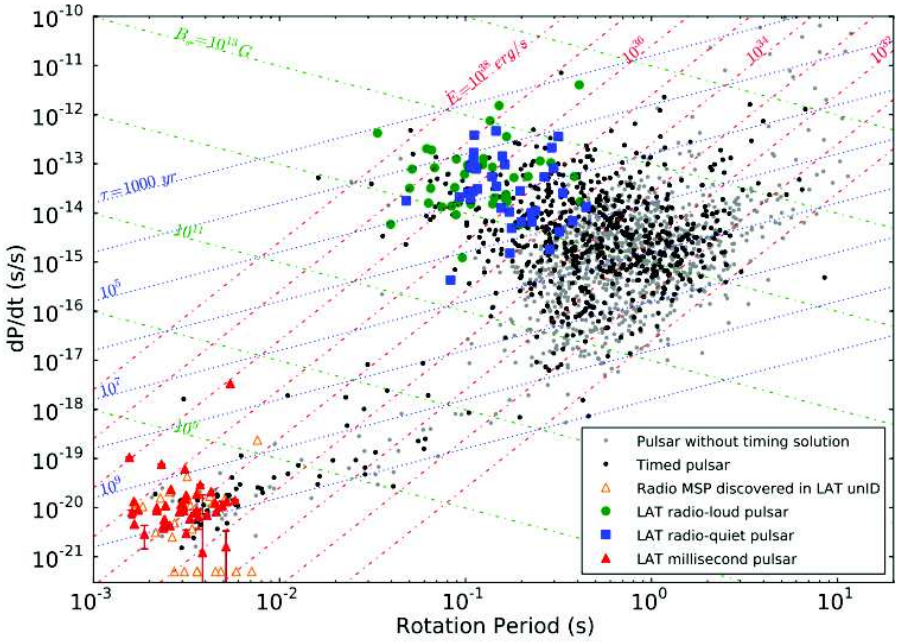

Figure 1-3: Pulsar spindown rate $\dot{P}$ versus the rotation period P. The magnetic field at the neutron star surface B_S and characteristic age of pulsars $\tau_C = P/2\dot{P}$ are also shown. The former is considered to be 5×10^{-22} when its value is not available (Abdo et al., 2013).

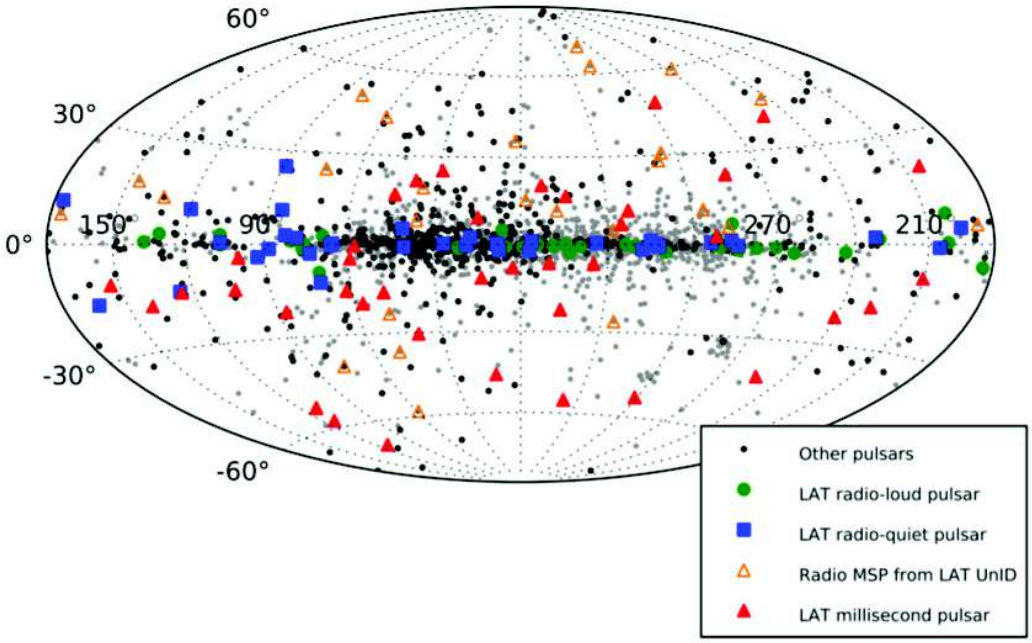

Figure 1-4: Pulsar sky map in Galactic coordinates (Abdo et al., 2013).

(Manchester et al., 1985) as ,

$$\dot{\nu} = -K\nu^n \tag{1.8}$$

where K is a constant of proportionality depending on pulsar's moment of inertia and magnetic field. The quantity n is the braking index, which relates the measure of rotation of pulsar and its spin down rate. The simple dipole field model, regardless of whether it is associated with vacuum electromagnetic radiation, a force-free magnetosphere or a relativistic magnetohydrodynamic wind, predicts it to have a value of 3 (Manchester & Taylor, 1977) while some other realistic models predict a range of $1.8 - 3$ (Melatos, 1997). Differentiating Eqn. 1.8 with respect to time, we are left with,

$$n = \frac{\nu\ddot{\nu}}{\dot{\nu}^2} \tag{1.9}$$

which gives a direct relation between the braking index and observable quantities ($\ddot{\nu}$ being the second derivative of spin frequency ν). For old pulsars $\ddot{\nu}$ is too small to be measured, and hence, only eight pulsars of all the observed ones have well measured braking indices, whose range lies from 0.9 ± 0.2 to 2.839 ± 0.001 (Lyne et al., 2015). Recent measurement by Archibald et al. (2016) for PSR J1640-4631 showed a braking index of 3.15 ± 0.03 raising questions (if proved to be stable over time) on the theoretical upper limit which is being predicted to be three. Although, gravitational radiation of a quadrupolar nature could yield a braking index between 3 and 5 (Blandford & Romani, 1988; Petri, 2015).

1.6 Types of neutron stars

The neutron star population is quite diverse and difficult to categorize. The attempts usually involve dividing them on the basis of their observational properties, classifying strictly in the $P\dot{P}$ diagram, as in Fig. 1-3. However, since the observed emission spans across a wide range of the electromagnetic spectrum and with some pulsars

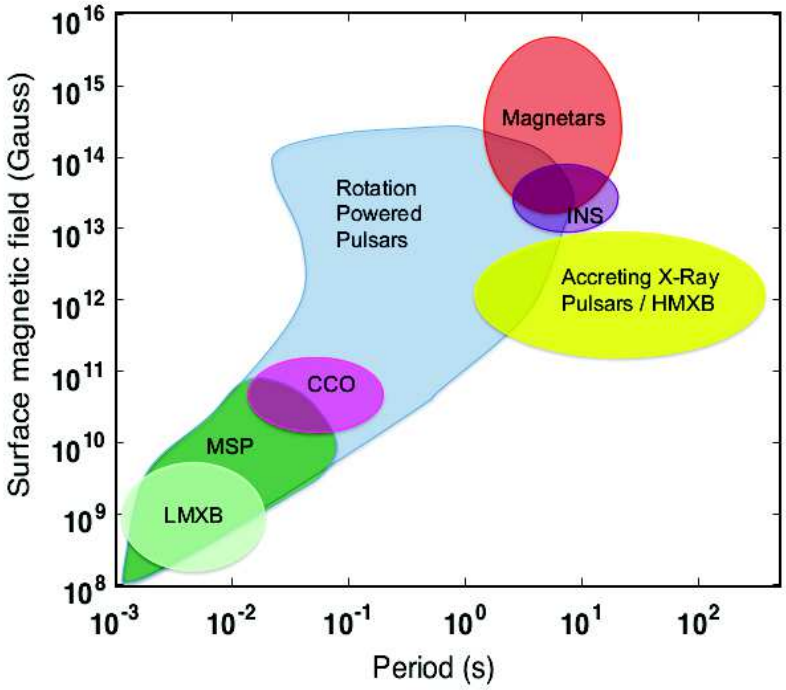

Figure 1-5: Schematic diagram of neutron star populations with respect to their periods and derived surface magnetic field strengths (Harding, 2013).

featuring multiple characteristics falling into several populations, it is difficult to rank them separately. On theoretical grounds, the categorization on the basis of their features rather than the emission properties itself is preferable currently, for instance that given by Harding (2013), and shown in Fig. 1-5. As seen from the plot, the different classes overlap. This implies that the division solely on basis of period and its derivative, probably does not justify the complicated classification behaviour of the pulsars. We use Fig. 1-5 as a reference and also classification suggested by Petri (2017a), attempting to divide pulsars according to their major source of emission. This basically gives five separate categories for neutron stars :

- *Rotation powered pulsars :* The neutron stars which derive their emission from their rotation magnetic braking which affects the strong electromagnetic field surrounding them and hence, giving rise to emission of pulses of radiation directed towards us at regular intervals in a broadband spectrum, if the line of sight is directed towards the observer.

- *Accretion powered pulsars :* The pulsar in a binary system in which it derives energy by accreting matter from the companion star and emits strongly in the X-rays regime.

- *Magnetars :* The neutron stars with critically strong magnetic field values are magnetars. Their energy reservoir resides in their brutal magnetic field topology readjustments which releases significant amount of magnetic energy resulting mostly in X-ray emission.

- *Isolated neutron stars :* These stars are in thermal equilibrium and the emitted radiation is nearly that of a black body. While the interior of the star is cooling down, the heat energy is emitted visible in X-rays.

- *Nuclear energy :* During accretion, nuclear reactions can occur on the surface of the neutron star releasing heat energy which is mostly visible in X-rays.

Since the plethora of denominations shows the complexity of neutron star activity. It is difficult to get a coherent view of all classes. Below we attempt to create a detailed review of different pulsar categories (Kramer et al. (2006), Petri (2017a)) which are more commonly used throughout the literature.

1. **Normal and millisecond pulsars :** The normal and millisecond pulsars falls under the rotation powered pulsars category mentioned above and span periods ranging from 1 ms to 23.5 s (Tan et al., 2018).

   The rotation periods of normal pulsars span the range of 20 ms through 23.5 s and their magnetic field is of the order of 10^8 T being estimated from magnetodipole losses. They are quite young with their age being less than 100 million years only. The emission from these pulsars falls primarily in the radio domain. Even though a radio pulsar emits steadily, their observation gives an impression that it is blinking on and off. This happens because typically their magnetic axis, along which the radio beam is emitted, is at a certain angle to their rotation axis; and because a pulsar spins, we see the beam only when the magnetic

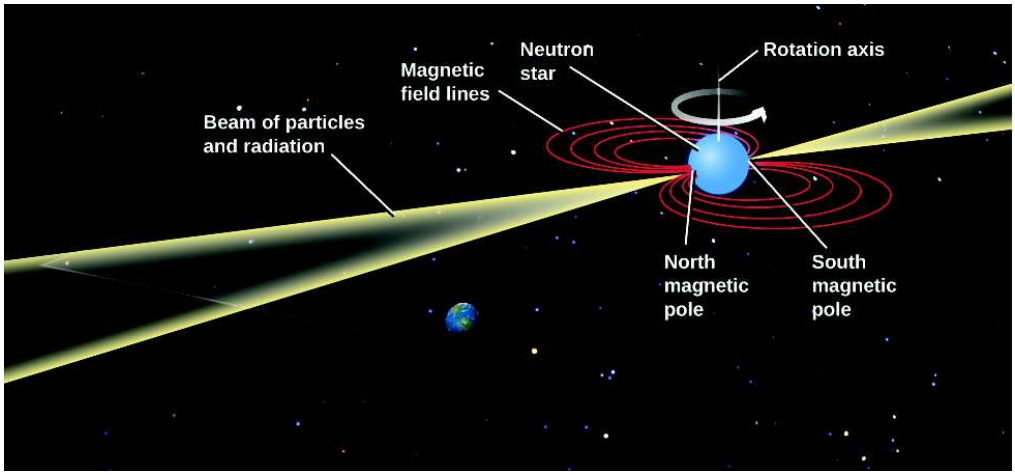

Figure 1-6: An illustration showing how beams of radiation at the magnetic poles of a neutron star can give rise to pulses of emission as the star rotates. As each beam sweeps over Earth, like a lighthouse beam sweeping over a distant ship, we see a short pulse of radiation. This model requires that the magnetic poles be located in different places from the rotation poles. Here the poles of the magnetic field are perpendicular to the poles of rotation, but they could be at any other angle (Astronomy, 2018).

axis is pointing towards us. The effect is often compared to that of a lighthouse which appears going on and off to a ship in the ocean. For this reason, radio pulsars are often referred to as lighthouses in space. This lighthouse model is shown in Fig. 1-6.

The pulsars having period below 20 ms are referred to as millisecond pulsars. Their magnetic field is weaker than the normal pulsars; of the order of 10^3 T to 10^5 T (Olausen & Kaspi, 2014) and they are older with age being more than 100 million years. The general consensus on their formation could be summarized like this : When the normal pulsar in a binary system gradually slows down its rotation and at one point, is unable to derive energy from rotation, it stops emitting like a pulsar. However, its companion in the system, when exceeds Roche lobe limit (the distance at which the tidal forces break an object held together only by gravity), will start transferring mass, and thus, angular momentum to the neutron star. The neutron star re-accelerates by accretion from the companion and starts spinning faster, with periods of a few milliseconds. Since it gains back its rotation, deriving energy from this new rotation the entire electromagnetic activity is regained. This millisecond pulsar is, in a way, reborn from the *dead* pulsar and hence, referred to as a recycled pulsar

(Bhattacharya & van den Heuvel, 1991).

2. **Intermittent pulsars :** On the time scales of their age, the radio pulsars were considered to be emitting steadily. However, Kramer et al. (2006) discovered a pulsar PSR B1931+24 which showed the stable pulsar properties only for a period of time. This pulsar has been observed to behave as an ordinary isolated radio pulsar during its active phases that are 5 to 10 days long and to be undetectable for the next 25 to 35 days, after which it is detected again. This pattern repeats quasi-periodically and only a handful of pulsars are known till date which display such extreme intermittent behaviour. The intermittent pulsars offers a unique opportunity to study the relationship between the spindown and the emission of radio pulsars in an attempt to understand the origin of such behaviour.

3. **Rotating radio transients :** Constant periodic electromagnetic emission was thought to be hallmark of these extremely stable compact objects but in 2006 rotating radio transients (RRATs) were discovered which shows transient behaviour. RRATs are similar to radio pulsars but they don't produce the typical pattern of those; instead, they emit short radio bursts occurring at sporadic time intervals which can range from seconds to hours, unlike typical radio pulsars which have regular and shorter time intervals. Typically, RRATs have been observed to emit very intense short pulses of $1 - 2$ ms up to 30 ms. Their discovery has been significant because it made us acquainted with a population of neutron stars which was earlier missed by radio surveys because they looked only for pulses with a periodic behaviour.

4. **X-ray pulsars :** X-ray pulsars are a class of neutron stars emitting periodically in X-ray domain. The origin of the emission of X-ray from these pulsars can be one of the following :

    - Typically for the first 10^5 years after a core-collapse supernova, neutron stars can evacuate internal heat from the star, referred to as thermal cool-

ing, which results in thermal emission in X-ray wavelength. Another reason could be the local surface reheating by return currents from the magnetosphere, which is common for millisecond pulsars close to the polar caps, for instance. Observations of such emission has potential uses to constrain equation of state of a neutron star.

- As the neutron star spins, plasma in the magnetosphere interacts with the magnetic field and gives rise to electromagnetic emission, inclining more towards X-ray wavelength than the radio emission.
- The plasma from the magnetosphere travels along the magnetic field lines to the polar caps and produces intense radiation as it hits the surface of the neutron star.
- The dissipation of the strong surface magnetic fields could also result in the emission of radiation.

The neutron star classification has been quite ambiguous and poor, especially with new observations which have revealed overlap between two behaviours that ultimately makes the boundaries blurred and uncertain. We need better understanding of these compact objects to divide different types with fine lines between them. For now, the general categories for the neutron stars emitting in X-ray spectrum, commonly used throughout the literature, are as follows :

- *Isolated neutron stars (INS) :* The neutron stars which, as the name indicates, are not accompanied by a companion as those in binary system. They fall under RPPs and are observed to emit across a wide spectrum of wavelength including radio and X-ray with strong magnetic fields.
- *Central compact objects in a supernova remnant (CCO) :* CCOs are usually a type of INS with the difference that they are surrounded by supernova remnants. They are young, recently formed after a supernova collapse, and are usually radio-quiet non-pulsating X-ray sources. However, outliers exist; for instance, RCW 103 (Rea et al., 2016) is a CCO, but a magnetar

and also shows pulsations.

- *Anomalous X-ray pulsars (AXP) :* AXPs are also INS and are widely considered to be magnetars (discussed below) because of their strong magnetic field. They are termed so because their X-ray luminosity is much higher than available rotational energy, which also implies that the energy source must come from the magnetic field.

- *Soft gamma-ray repeaters (SGR) :* SGRs, conjectured to be magnetars, are the neutron stars which emits large bursts of gamma rays and X-rays at irregular intervals. They are unlike normal Gamma Ray Bursts in which the explosion emits extremely energetic photons and do not repeat in time.

5. **Gamma ray pulsars :** Gamma ray pulsars, as apparent from their name, are rotating neutron stars that emit gamma ray photons. Since the launch of the Large Area Telescope (LAT) on the Fermi satellite in 2008, it has dramatically increased our understandings of gamma ray pulsars. It covers the energy range from about 20 MeV to more than 300 GeV (Atwood et al., 2009) and has discovered over 200 pulsars (Ray, 2018). Some of the pulsars emit at both, radio and gamma wavelengths; for instance, Smith et al. (2017) recently presented 10 new radio pulsars for which the gamma ray pulsations were also detected (they can also show X ray pulsations). However, not all gamma ray pulsars show radio emission. It is considered to be most likely a result of their orientation towards the observer meaning that the pulsar beams are not directed towards the observer owing to the different location of source of the two wavelengths (mentioned in Section 1.8).

6. **Magnetars :** Magnetars are types of neutron stars having extremely powerful magnetic field lying in range of $10^8 - 10^{11}$ T. This strong magnetic field produces characteristic bursts of X-rays and gamma rays. They are different from other neutron stars especially because of their extremely high magnetic field and also, their rotation periods are usually longer than normal pulsars. Their period

varies between $2-12$ seconds and their characteristic age is about 10^3-10^4 years (Olausen & Kaspi, 2014) which is very young if compared to pulsars.

1.7 Magnetospheric structure and emission mechanism

Rotation powered pulsars are isolated neutron stars which are rapidly rotating (fastest known pulsar having a period of 1.4 ms (Hessels et al., 2006)) and highly magnetized (of order of 10^8 T (Olausen & Kaspi, 2014)), spinning down by electromagnetic braking due to low frequency electromagnetic waves and particle outflows. The presence of $e^{\pm}$ pair plasma, influenced by the intense magnetic field, their interaction, resulting in generation of radiation and the following emission, are the factors to be considered while modelling a magnetospheric structure surrounding a pulsar. Because of the complicated interaction between different factors, each of these phenomenon needs to be understood in order to model the magnetospheres as precisely to a real case scenario as possible. A simple overview of the processes occurring in the magnetosphere is as follows - The magnetic field rotates with the star and emits electromagnetic wave radiation on its interaction with the surrounding plasma for each rotation period. The emission results in the loss of energy and angular momentum which slows down the rotation. The rotation is also responsible for generation of electric field which extracts a copious supply of charged particles from the surface of the star. The behaviour of these particles is dominated by the magnetic field and hence, all the associated physical processes like particle acceleration, radiation processes and emission mechanism. As the magnetic field influences all the physical processes outside the neutron star, we need to study the magnetosphere composed of magnetic field and plasma co rotating with the star. There exists extensive literature modelling the magnetospheric structure each with its own perks and perils. Below will be discussed the most significant models used throughout in pulsar studies. The summary for the magnetospheric models reviewed by Venter (2017) is utilized for this section. Here we

divide them in three categories, based on the plasma density in the magnetosphere.

Ideal vacuum magnetosphere :

Deutsch (1955) calculated the solutions for the magnetic field for a rigid rotating perfectly conducting star in vacuum for a dipole magnetic field inclined with respect to the rotational axis. The vacuum magnetosphere works under the assumption that the atomic binding energy on the stellar surface is too high for particles to be extracted from the star. This external field near the star possesses an electric component along the magnetic vector. This could have resulted in acceleration of plasma to high energies but in this magnetosphere, there is no ambient charges or currents, as it is considered to be vacuum for this model, also referred to as rotating vacuum dipole (RVD) solution. The RVD solution has been used in several pulsar light curve models like Dyks et al. (2004), Venter et al. (2009), Bai & Spitkovsky (2010). Other models also considered the vacuum static dipole solution (Du et al., 2010; Harding et al., 1978) or a general relativistic corrected static dipole (Muslimov & Harding, 1997) magnetic field solution as the basic magnetospheric structure.

Ideal force free (FF) magnetosphere :

An attempt to study magnetospheric structure was made by Gold (1968) who suggested the presence of a magnetosphere surrounding a neutron star which co rotates with the star. They also proposed that the magnetic field influences only up to a certain distance, giving this limit to be around the region where co rotation is close to the speed of light. It was suggested that this limit gives the boundary of the region within which the magnetosphere co rotates with the star.

Goldreich & Julian (1969) used this idea to further describe the properties of magnetosphere for stars whose magnetic fields are symmetric about their rotation axes. We call this an aligned rotator. They showed that the magnetosphere has to be filled with dense plasma otherwise the surface charge layer could not be in dynamical equilibrium because of the discontinuity in the value of $\mathbf{E} \cdot \mathbf{B}$ within the layer. The characteristics elucidated by them for such a simple aligned case are still used as a standard reference point for studies and therefore, it is necessary to discuss it before proceeding further.

The Goldreich-Julian (GJ) magnetosphere : Consider a neutron star with a dipolar magnetic field which remains continuous at the surface if the star is not rotating. The magnetic dipole axis is assumed to be aligned with the rotation axis. The angular velocity of star's rotation is Ω and period is $P = 2\pi/\Omega$. The interior stellar matter is highly conducting. Also, since the magnetosphere must be filled with highly conductive plasma for equilibrium, it is dense enough to screen out the accelerating component of the electric field parallel to the local magnetic field, such that total electromagnetic force on plasma vanishes. So, for a particle with charge q, moving with velocity $\mathbf{v} = \mathbf{\Omega} \times \mathbf{r}$, under influence of magnetic field $\mathbf{B}$, satisfies,

$$\mathbf{E} + \frac{(\Omega \times \mathbf{r})}{c} \times \mathbf{B} = 0 \tag{1.10}$$

For such a magnetosphere, $\mathbf{E} \cdot \mathbf{B} = 0$ everywhere, also called *force free (FF) magnetosphere*, the so-called GJ charge density is given by

$$\rho_{GJ} = \frac{\bigtriangledown \cdot \mathbf{E}}{4\pi} \approx \frac{\mathbf{\Omega} \cdot \mathbf{B}}{2\pi c} \tag{1.11}$$

The radius where the co rotation velocity is equal to speed of light ($\Omega \cdot \mathbf{r} = \mathrm{c}$) is called *light cylinder radius* given by,

$$R_{LC} = \frac{c}{\Omega \sin\theta}. \tag{1.12}$$

This R_{LC} sets the limit of the magnetosphere, beyond which the magnetic field and plasma does not exactly co rotate with the star. The field lines tangential to this light cylinder are the last closed field lines. The GJ magnetosphere is illustrated in Fig. 1-7 where the right and left vertical lines represent the light cylinder boundary enclosing co rotating magnetosphere inside it. In the equatorial and polar regions, as shown, opposite signs of net charge are found divided by a neutral surface or null charge surface with $\Omega \cdot B = 0$ which are shown as dashed lines and geometrically lie at $\sec\theta = \sqrt{3}$.

Also, the regions on the surface of the star from which the open field lines emanate

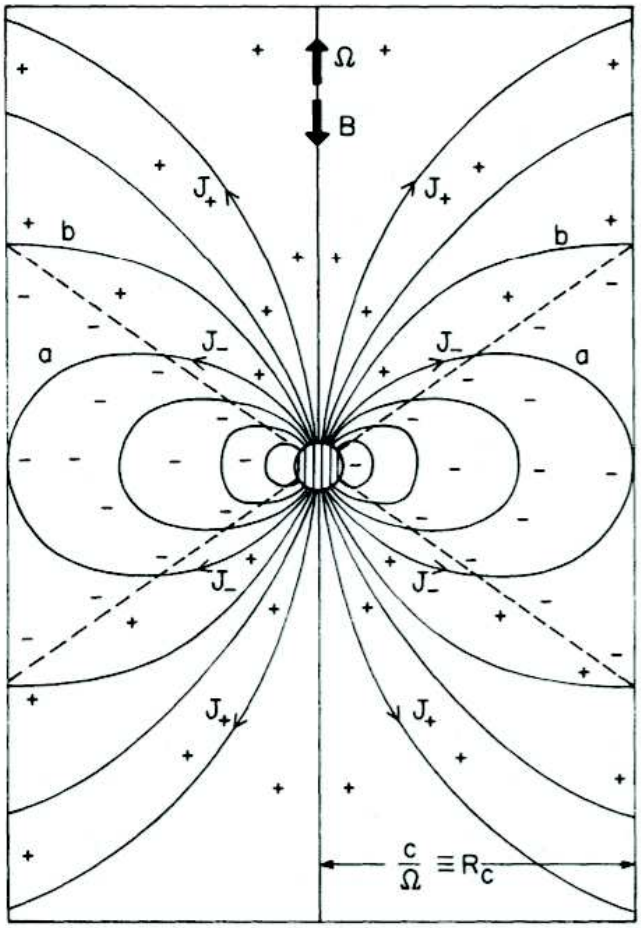

Figure 1-7: The Goldreich and Julian magnetosphere in which rotation (Ω) and magnetic axis (B) are shown to be anti parallel. The dashed line at $\sec\theta = \sqrt{3}$ is the neutral surface and divided the magnetosphere in regions of positive and negative charge density. The magnetic field lines between line a (last closed field line) and line b are open and pass through negative density region to penetrate the light cylinder further; negative current J_- flow along these lines from the pulsar. The open magnetic field lines between line b and the rotation axis or pole, pass through region of positive density and positive current J_+ flow through them (Ruderman & Sutherland, 1975).

are known as *polar caps*, the rim of which lies at a polar angle (for aligned case),

$$\Theta_{PC} = \sin^{-1}\left(\frac{\Omega R}{c}\right)^{1/2} \approx \left(\frac{\Omega R}{c}\right)^{1/2} \tag{1.13}$$

where R is the stellar radius. For more on the basic theoretical framework, see the review Venter et al. (2018). The pulsar equation for the FF conditions has been solved for the aligned (Contopoulos et al., 1999) and oblique (Spitkovsky, 2006) cases, also using full magnetohydrodynamics (Komissarov, 2007; Tchekhovskoy et al., 2013).

Realistic case :

In reality, the conditions in a pulsar magnetosphere must be between the two extremes (vacuum and FF) mentioned above. In the FF case, the plasma is leaving the magnetosphere at relativistic speeds, and if not replenished continuously, it creates gaps in the magnetosphere where $\mathbf{E} \cdot \mathbf{B} \neq 0$. Processes like pair production hold the key to replenish the gaps but despite that, screening can not be fully effective and observations of emission require sites like gaps which are responsible for particle acceleration.

The most commonly used pulsar magnetospheric models in terms of the gaps in the magnetosphere are polar cap model, slot gap model and outer gap model. We will be using the former two in the thesis. However, various other models will be briefly discussed for the sake of a complete study of the magnetospheric structure and gaps.

1.7.1 Polar Cap Model

(Sturrock, 1971) developed a model of the pulsars to explain the pulsar emission. They argued that the magnetic field lines extending out from the light cylinder must be open; if they were closed, the particles moving along those lines would move faster than the speed of light. These open field lines are limited to what is shown in Fig. 1-8 as the emission cone. It was suggested that the current flow associated with the magnetic field could be estimated by inspecting field line configuration at the light cylinder. This is the foundation of the polar cap model which is summarized as follows:

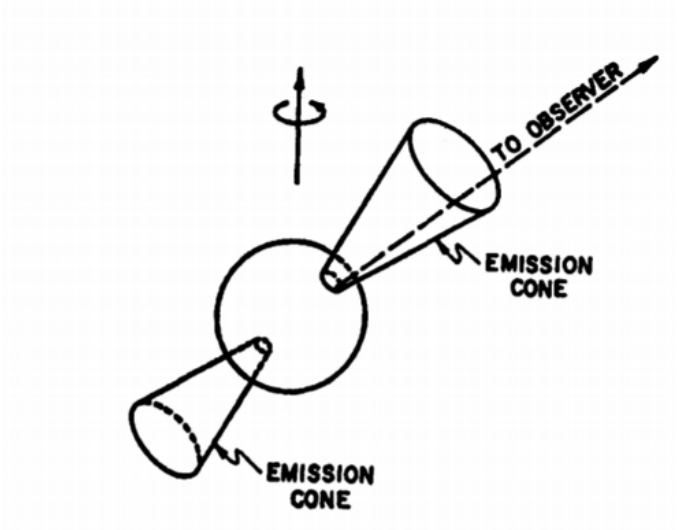

Figure 1-8: Configuration of emitting regions (Sturrock, 1971)

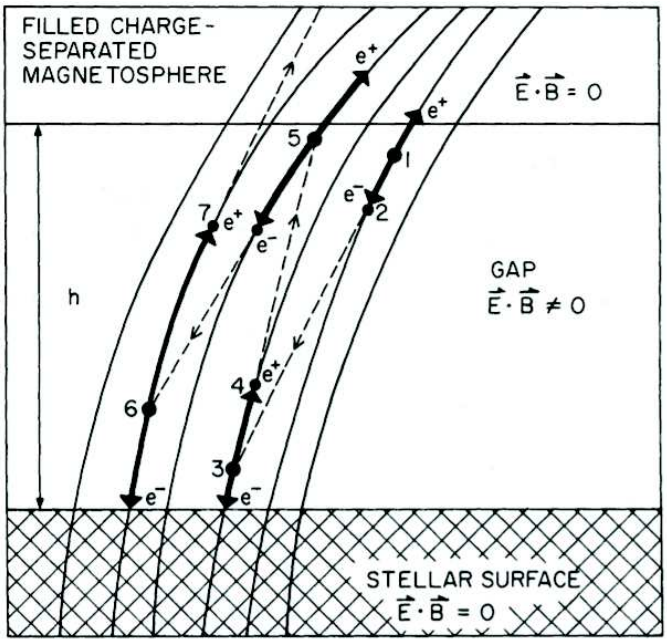

Figure 1-9: Breakdown of the polar gap : The shaded bottom part is the stellar surface, above which, up to a height h is the vacuum gap and beyond h is the plasma filled magnetosphere. The solid curved lines show the magnetic field lines emanating from the polar cap on surface. At 1, a photon creates a pair of electron and positron. While the latter is accelerated out from the gap by the electric field inside the gap, the former moves towards the surface. This electron moves along the curved field line and radiates a gamma ray photon at 2 by curvature radiation process. This photon produced at 2 goes on to create an electron-positron pair at 3 once it has a sufficient component of its momentum perpendicular to the magnetic field. This cascade process of pair creation - acceleration of electrons and positrons along curved field lines - emission of photon by curvature radiation - pair creation continues until the potential limit of vacuum breakdown. (Ruderman & Sutherland, 1975)

The closed magnetosphere region has no current flow and its charged density is given by Eqn. 1.11 but charged particles flow out along the open field lines. This results in a vacuum gap at the polar cap from which the open field lines are emanating. This polar magnetospheric gap spans the open field lines from the stellar surface up to an altitude of about 10^4 cm (Ruderman & Sutherland, 1975). This gap is replenished by the extraction of particles from the surface of the polar cap because of the 10^{12} V potential difference between the base and top of the gap. Also, a cascade process of pair creation takes place within the gap and generates high energy particles (detailed framework given by Daugherty & Harding (1983)). In this process the electric field in the polar gap accelerates a single particle (electron or positron) to high energy. This particle moves with relativistic speed along the magnetic field line and emits photons in gamma-ray wavelength by curvature radiation (discussed in Section 2.1.3, 4.3). The photons produced create electron and positron pairs by the process termed as pair creation. These newly generated electrons and positrons again accelerate to high energy and emit gamma-ray photons. This results in a cascade process forming electron-positron pairs on a time scale of a few microseconds replenishing the gap continuously. The gap would continue to grow until the entire potential drop develops along a field line traversing the gap, but it is limited by breakdown of the vacuum. Before the gap grows to this extent, it breaks down, which means, it becomes unstable against the avalanche growth of the pairs. This breakdown limit is a potential difference of order of 10^{12} V (Ruderman & Sutherland, 1975) across the gap. The positrons from the gap move out along the open field lines and electrons flow towards the stellar surface, forming a closed pulsar circuit, preventing the breakdown of the gap. The cascade process and the breakdown of the polar gap are illustrated in Fig. 1-9.

This polar cap model has been taken forward by Ruderman & Sutherland (1975) who showed that the above process can lead to injection of the ultra-relativistic positrons and pairs into the near magnetosphere leading to coherent radiation explaining the radio emission in pulsars. It has been also further investigated by many authors, for instance, Harding (1981), Daugherty & Harding (1982), Arons (1983).

1.7.2 Outer gap model

Cheng et al. (1986a) presented the origin and structure of particle acceleration process in the outer magnetosphere of pulsars to explain high energy gamma radiation. The dipole field geometry in their outer gap model is similar to that in the polar cap model with the major difference between the two being the emission region. The brief summary of their model is as follows : Assuming global current flow patterns throughout the outer magnetosphere can result in charge depleted regions within the magnetosphere. These regions would develop electric fields along the field lines unless there is a mechanism which continuously sustains the charge production in this region. Various mechanisms act to limit this $\mathbf{E} \cdot \mathbf{B}$ being formed in charge depleted regions completely but there is a volume in the magnetosphere, referred to as outer gap, for which the $\mathbf{E} \cdot \mathbf{B}$ does not vanish. This outer gap (with potential drop of about 10^{15} V for the Crab and Vela pulsars) is the region responsible for the acceleration of particles and is restricted to a region enclosed between the null surface line ($\Omega \cdot B = 0$) and the light cylinder, as shown in Fig. 1-11 as cyan colour region.

The steady charge replenishment of the outer gap includes the continual creation of the particles within it which makes sure that the gap does not grow any further and also that the charge supply from this region is enough to ensure $\mathbf{E} \cdot \mathbf{B} \approx 0$ in the rest of the outer magnetosphere. The value of $\mathbf{E} \cdot \mathbf{B}$ and potential drop is sufficiently large in the outer gap to support the production of gamma rays and the following pair production resulting in a cascade process. To replenish charges, the outer gap has two possible ways to create pairs from gamma rays (γ).

1. Conversions by collisions with X-rays (γ_x) : $\gamma + \gamma_x \rightarrow e^- + e^+$ for high GeV gamma rays

2. Conversion by collisions with soft (optical or IR) photons (γ_ν) : $\gamma + \gamma_\nu \rightarrow e^- + e^+$ for 10^{12} eV gamma rays

For both of these mechanisms, soft photons and X ray flux are needed which can be supplied by the synchrotron radiation of $e^\pm$ pairs created in the weaker magnetic

field of the outer magnetosphere. The necessary gamma ray can be radiated (often by the e^- / e^+ particles they themselves create) by three mechanisms (details in Section 2.1) :

1. Curvature radiation from accelerated e^- or e^+ constrained to move along curved magnetic field lines.

2. Inverse Compton scattering of extreme relativistic e^- or e^+ particles

3. Synchrotron radiation from extreme relativistic electrons spiralling along magnetic field lines.

There are qualitative features of the propagation behaviour of electrons and positrons which are independent of mechanism. The particles moving along the curved magnetic field lines are considered to be responsible for the generation of high energy gamma rays by curvature radiation. The emitted gamma rays, then propagate into the region above the curved B (on its convex side) which is the outer gap region, but generally not into regions below (on the concave side). Therefore copious $e^{\pm}$ pair production in charge depletion regions of the outer magnetosphere can prevent charge depletion at (almost) all other depleted regions depending on their location. This situation is better described by an illustration (Cheng et al., 1986a) shown in Fig. 1-10. Three hypothetical outer magnetosphere charge depletion regions are shown in the figure. The magnetic field line below region (A) is the last closed field line (also marks first open field line above it). Under this, as shown, all the field lines are closed. The energetic high energy gamma rays from regions (B) and (C) do not penetrate this area. Gaps (A) and (C) do not end within the magnetosphere light cylinder. The pair production from gamma rays originating in an outer gap in region (B) could supply the plasma needed to prevent charge depletion in region (C) (or vice versa) but could not perform that same function for region (A). However, pairs from gamma rays from depletion region (A) could not only in principle supply the $e^{\pm}$ pairs needed to prevent that region from growing larger but could also to quench charge depletion in (B) and (C) and thus prevent the formation of outer gaps in those regions. With

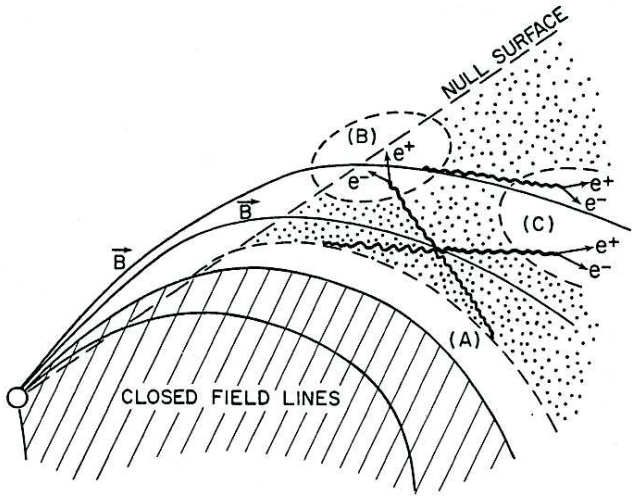

Figure 1-10: Three hypothetical outer magnetosphere charge depletion regions. The magnetic field line below region (A) is the last closed field line (also marks first open field line above it). Under this, as shown, all the field lines are closed. The energetic high energy gamma rays from regions (B) and (C) do not penetrate this area. Gaps (A) and (C) do not end within the magnetosphere light cylinder (Cheng et al., 1986a).

sufficiently copious $e^{\pm}$ production in the outer magnetosphere, strong charge depletion and the large $\mathbf{E}\cdot\mathbf{B}$ that would accompany it may be quenched in the null surface region. However, a curved slab-shaped gap whose lower surface is the open field line boundary which bulges convexly into the charge deficit region cannot be reached by the energetic gamma rays which create pairs elsewhere. But this outer gap, can in principle produce the gamma rays and pairs that limit both its own growth and the formation of charge deficit gaps elsewhere.

Since the development of the outer gap model, there has been many studies revising and using it. A few significant ones are mentioned as follows. Chiang & Romani (1994) used this model to show that the variation in magnetic field through the radiation zone may lead to the spectral index γ_s (measure of the dependence of radiative flux density on frequency ν, as power law spectra $\nu^{-\gamma_s}$) changes during the pulse like those observed for the Vela pulsar (Kanbach et al., 1994). However, they also showed that this model failed to produce self consistent photon fields required to support closure of the gap and hence concluded that the study of radiation processes in the outer magnetosphere needed to be revisited. Romani & Yadigaroglu (1995) developed a model based on above scheme for the beaming of high energy gamma ray emission which reproduced the observed properties of individual gamma ray pulsars including

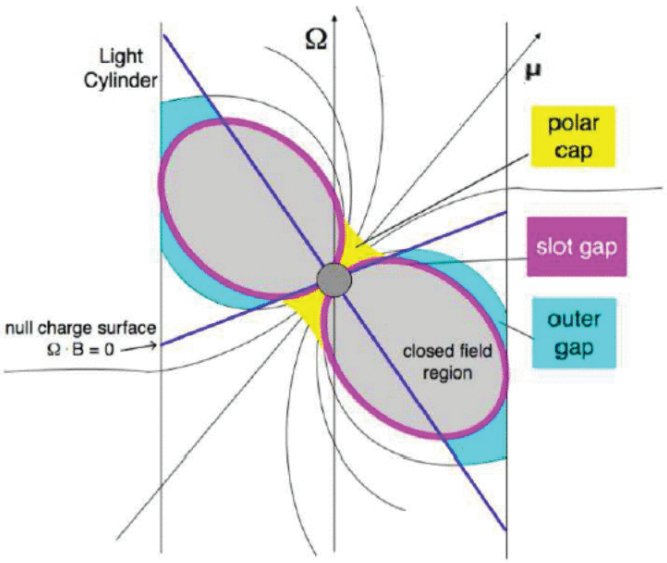

Figure 1-11: A schematic representation of the different geometric pulsar models (Harding (2005))

high energy pulse profiles. Yadigaroglu & Romani (1995) showed that the statistics of gamma ray pulsars were in good agreement with predictions of pulsar properties using this model. Romani (1996) described a revised picture for radiation physics in outer magnetosphere.

1.7.3 Slot gap model

The slot gap model considers the region along the last open field lines all the way from the surface of the star going up to the light cylinder. To differentiate between the various gap models discussed, the regions for different pulsar models are shown in Fig. 1-11.

Arons & Scharlemann (1979) presented their electrodynamic model of pulsar polar caps and suggested that the pair formation front, above which the accelerating field is screened, occurs at increasingly higher altitude as the magnetic co-latitude approaches the last open field line where the electric field vanishes. Based on this, Arons (1983) noted the possibility of this high-altitude acceleration region referred to as slot gap near the polar cap rim and described the model in detail. The model was further revised by Muslimov & Harding (2003) by taking into account the effect of the narrow geometry of the gap on the electrodynamics within the gap and also to include the

effect of inertial frame dragging on the particle acceleration. They showed that the accelerating electric field within the gap being boosted by the frame dragging effects, actually decreases because of the narrow geometry of the gap by a factor proportional to the square of the slot gap width. However, because of the consideration of the small angle approximation, they restricted their study of the slot gap regime to altitudes less than four-five times that of the radius of the star. Since the parallel electric field in the slot gap is not screened on field lines close to the open field boundary, acceleration may continue to much higher altitudes. The extension of this model to much higher altitudes was then studied by Muslimov & Harding (2004)

1.7.4 Other models

Dissipative magnetosphere : Both, the vacuum and the FF limit are idealistic cases. Gold (1968) ruled out the possibility of a vacuum magnetosphere and the FF limit results in no dissipation of energy and hence, there can be no particle acceleration and high energy emission in this framework. Li et al. (2012) noticed that neither of these limits can simultaneously account for both the plasma currents and the accelerating electric fields that are needed to explain the morphology and spectra of high energy emission from pulsars and hence, combined these models, to create a more realistic one. These are known as dissipative magnetospheres and are filled with resistive plasma. Kalapotharakos et al. (2012) formulated a family of resistive solutions that smoothly bridges the gap between the vacuum and the FF magnetosphere solutions. In this model, features like the spin-down luminosity, open field line potential drop, and the fraction of open field lines all transition between the vacuum and FF values as the plasma conductivity varies from zero to infinity. Further, Kalapotharakos et al. (2014) computed the patterns of gamma ray emission due to curvature radiation in dissipative pulsar magnetospheres.

Particle in cell (PIC) : Chen & Beloborodov (2014) presented the first self-consistent global simulations of pulsar magnetospheres using a 2.5D PIC code. The star was spun up from $\Omega = 0$ to a high angular velocity, and the coupled evolution of its external electromagnetic field and plasma particles was followed. The particle

extraction from the surface of star resulted in a plasma magnetosphere. The particles are then accelerated by a rotation induced electric field resulting in curvature radiation and pair production. The evolution is followed until it reaches a quasi steady state with the aim of testing previous ideas for the plasma flow and gaps in the pulsar magnetosphere. Philippov & Spitkovsky (2014) implemented the ab initio relativistic 3D PIC simulation for an aligned pulsar magnetosphere allowing particles to escape freely from the surface and populate magnetosphere. They calculate the magnetospheric structure, current distribution, and spin-down power of the neutron star. The idea of pulsar PIC simulations is still in its infancy and there are computational restrictions attached to it. As the technological constraints are slowly lifted, there is lots to uncover from this approach. The main aim is to move towards more realistic simulations of pair production to determine the detailed requirements like particle acceleration, pair production and radiation to reach different magnetospheric configurations.

1.8 Sites of emission

The source of emission of a pulsar is considered to be rotation of this highly magnetized object and the subsequent acceleration of particles in the co rotating magnetosphere resulting in radiation observed as pulsed emission. As the star rotates, the charged particles in its magnetosphere are accelerated to relativistic velocities and emit radiation powered by the rotational energy losses. The physical processes involved in the emission mechanism are discussed in Chapter 2 which are more or less known but the location of the emission sources still involves a number of widely varying models. In general, there are three sites serving as emission sources in pulsars, for thermal emission, radio emission and high energy emission. The first is the simple thermal radiation observable in the X-ray wavelength regime which originates from the surface of the neutron star where the heating of the polar cap results in formation of hot spots leading to photon flux modulation. For the other two : there are varying studies if the radio emission originates in the polar cap near the neutron star surface

or from an altitude of several hundred kms (Ruderman & Sutherland, 1975; Ginzburg & Zhelezniakov, 1975; Kazbegi et al., 1991); and the general consensus for the high energy emission is that it is produced in the outer magnetospheric region, near the light cylinder (Michel, 1978; Arons, 1981; Michel, 1982). For both locations, the large scale geometry of the simple GJ model magnetosphere is sufficient to provide most of the required relations between observed pulse profiles and magnetospheric structure. Relativistic aberration has a major effect on the outer gap radiation but almost no observable effect on polar cap emission. This is because of the frame dragging effect in which the inner region of the rotating magnetosphere is dragged more than the outer region resulting in field lines being swept back in the outer region and hence, more affected by the aberration. The relativistic effect is discussed in Section 2.2.

Polar cap : The radio source at the polar cap originates as a stream of relativistic particles with very high energy which is a resultant of the pair production cascade mechanism as discussed in Section 1.7.1. Various other features related to the location region are discussed below.

Beamwidth : The assumption of a simple dipolar aligned rotator model makes it easier to find the angular radius of the polar cap θ_{PC} by tracing the last closed field lines back to the surface at radius R of star with rotation period P, given as (Lyne & Graham-Smith, 1990),

$$\theta_{PC} = \sqrt{\frac{2\pi R}{cP}} \tag{1.14}$$

For instance, using this relation, for $R = 10$ km and $P = 1$ sec, the radius of the polar cap is 140 m with field lines leaving the polar cap as a bundle of 1.6° across. However, the observed beamwidths will be larger than that at the surface since the radiated particles move along the field lines which makes roughly a cone of emission; so the beamwidth BW for emission at distance r from the surface of the star is given as,

$$BW = \frac{3}{2} \sin^{-1} \sqrt{\frac{r}{R_{LC}}} \tag{1.15}$$

The relation shows that the observed beamwidth is greater than the width of the polar cap (at the surface) by a factor of 3/2. This is because the width of the polar cap (given by Eqn. 1.14) is calculated by considering the opening angle similar to that of a cone with straight boundary surface; however, the magnetic field lines are curved and hence, emission will be from a wider region than the width of the polar cap. Kijak & Gil (1997) used pulse width measurements to propose an empirical relationship for the pulsar radio emission altitudes depending on their rotation periods, given as $r = (41 \pm 2)P^{0.39\pm0.06}$ km. For a star radius of 10 km and period of 1 sec, the emission is at height of 40 times that of the radius of the star, about 1% of the radius of light cylinder. As an exercise, we studied the pulse widths for radio emission considering different heights and rotations periods which is put together in Section 3.5.3.

Radio to frequency mapping (RFM) : RFM explains the systematic increase of profile widths with decreasing frequency. This apparent frequency dependence suggests that the emission at different frequencies is emitted at different heights above the polar cap (Ruderman & Sutherland, 1975). Also, the observed symmetry of integrated pulse profiles naturally led to a classification in which a central component is called the core which is surrounded by a hollow cone of emission (Komesaroff et al., 1970; Backer, 1976) and the geometry of the model was developed by Rankin (1993). The identification of their profiles in different classes is shown in Fig. 1-12. It was also suggested that the core component often dominates at low frequencies whereas the cone emission is more prominent at high frequencies. Mitra & Rankin (2002) assessed an extensive set of well measured conal component pair widths and found that these widths vary little with frequency. Such observations suggested that RFM applies only to the outer components. If we assume that high frequency emission is concentrated around a fixed height above the polar cap, it follows that the centre of the polar cap around this height is responsible for whole of the radio spectrum emission, while the low frequency emission originates at the boundary of the cap around double the minimum height. Or, the expansion at low frequencies is not related to this geometry and might be like an effect of propagation along diverging field lines.

Outer gap : The pair production cascade process in the outer gap is responsible

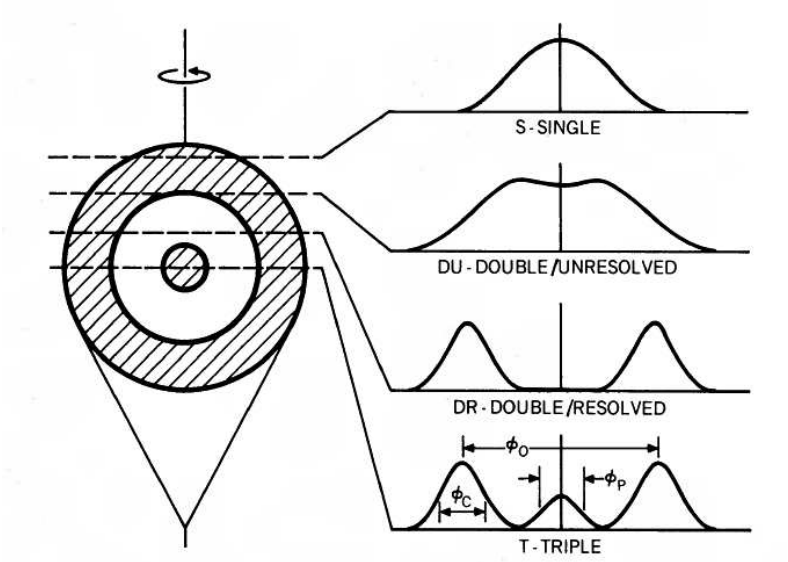

Figure 1-12: Schematic of hollow cone beam geometry (on left) and the average wave forms that would be viewed by four observers with different inclinations from the rotation axis (on right) (Backer, 1976).

for the emission of high energy gamma radiation in outer magnetosphere as discussed in Section 1.7.2. Romani & Yadigaroglu (1995) traced the expected gamma ray pattern (shown for an inclination of the magnetic axis with respect to the rotation axis to be 65° in Fig. 1-13) assuming that all parts of the outer gap surface radiate along the magnetic field lines. Since the radiating region extends through a large part of the magnetosphere, relativistic aberration (discussed in Section 2.2) greatly affects outer gap radiation. The figure shows emission from polar caps in form of contours while the outer gap emission as halftone. The dashed line in the top panel is the reference for cut made across the pattern to produce pulse profile shown in the bottom panel. The leading radio pulse and schematic pulses showing the phase of the hard (magnetospheric) and soft (thermal) X-ray emission is also shown.

Except for a few cases of coincident radio and high energy pulse profiles, the radio emission observed from the gamma ray pulsars is usually from the polar caps. The differently directed emissions from the two gaps could result in no observation of a radio beam from gamma ray pulsars (as in case of Geminga). It is highly probable that the reason for no radio emission from many of the bright gamma ray sources is the orientation of the pulsars, i.e. they are most likely directed away from the

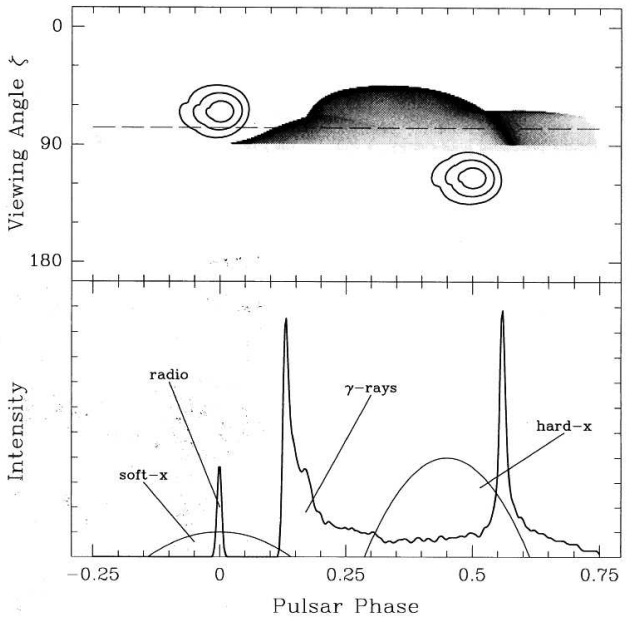

Figure 1-13: Sky map of pulsed beams and pulse profiles for Vela parameters, the angle between the rotation axis and magnetic axis is 65°. *Top :* Pulsar emission as a function of pulsar phase and observed lines of sight cut horizontally across the image at constant ζ. Emission from polar caps is shown as contours while rest is the emission from the observed outer gap. *Bottom :* The dashed line in the top panel is the reference for cut made across the pattern to produce pulse profile here. Leading radio pulse and schematic pulses showing the phase of the hard (magnetospheric) and soft (thermal) X-ray emission is also shown (Romani & Yadigaroglu, 1995).

observer.

1.9 Polarization

Polarization is defined as the property of the transverse waves that specifies the geometrical orientation of its oscillation. The direction of the oscillation is transverse to the direction of propagation of the wave, so the oscillations can have different directions perpendicular to the wave propagation. An electromagnetic wave can have three types of polarization : If the plane of the oscillation does not change as the wave propagates, the wave is said to be *linearly polarized*. If the magnitude of the oscillating components are equal but they have a phase difference of $\pm\pi/2$, the tip of the oscillating vector describes a circle and wave is said to be *circularly polarized*. If the magnitude of the oscillating components are not equal and have a non-zero phase difference, the wave is said to be *elliptically polarized*. Polarization properties are normally described in terms of the Stokes parameters : I (total intensity), Q and

U (linear polarization) and V (circular polarization). The parameter Q implies linear polarization in the direction parallel or perpendicular to the reference plane whereas U is for the directions $\pm\pi/4$ to the reference plane.

The polarization measurements of pulsars offer important indications on the physical processes in pulsar emission by providing insight into the basic geometry of the neutron stars including the information on inclination angle between the magnetic and rotation axis and inclination to the line of sight. Lyne & Smith (1968) showed that the signals from all the known radio sources are linearly polarized. The pulses often seem to be made up of separate components showing a high degree of polarization, mainly linear but also a less pronounced circular polarization. For linear polarization in pulsars, the variation of the position angle ψ across the pulse profile is $\psi = 0.5 \tan^{-1}(U/Q)$.

To explain the observed variations for the angle of polarization of radio pulsars, Radhakrishnan & Cooke (1969) introduced the Rotating Vector Model (RVM). The model was based on the idea that the radiation is polarized in the plane of curvature of field lines emanating from the polar cap in the plane of curvature of the magnetic axis which is a property of the curvature radiation (Komesaroff, 1970). The curvature radiation is discussed in detail in Section 2.1.3, 4.3. In RVM, the angle of polarization ψ for a strict dipole field, measured with respect to the rotation axis, is,

$$\tan\psi = \frac{\sin\chi \sin\varphi}{\sin\zeta\cos\chi - \cos\zeta\sin\chi\cos\varphi} \tag{1.16}$$

where $\varphi = \Omega t$ is the pulse phase with stellar rotation rate as Ω and t being the time of observation. And, χ is the obliquity and ζ is the inclination of the line of sight. RVM does not take into consideration the rotation of star, especially effects like aberration and propagation time delay. However, Blaskiewicz et al. (1991) calculated the impact of these effects on the polarization and further, the deformation of the field lines by the magnetospheric current was included by Hibschman & Arons (2001). Also, recently, Yan et al. (2011) studied polarization profiles for 20 millisecond pulsars and suggested that the observed position angle variations are generally not in accord

with the RVM.

Apart from showing the linear polarization characteristics, pulsars also show a considerable degree of circular polarization. For instance, Wu et al. (1993) presented polarization data, some of them are - PSR B1424-55 showed polarization less than 10%, PSR B1557-50 showed circular polarization approaching 25%, PSR B1737-30 showed polarization approaching 100% which is mostly linear but largely circular on the trailing edge. Indeed, there is no clear pattern in circular polarization and is considered to be diverse in its incidence Han et al. (1998). Studying polarization of pulsars provides information on the geometry of the emission regions, their magnetic field and the height from which these waves originate. Also, the observation of total linear polarization in some pulsars suggests the possibility that the radiation mechanism is inherently completely polarized (Lyne & Graham-Smith, 1990).

1.10 Multipolar magnetic field

The magnetic field topology in the surroundings of the neutron star is a key to the understanding of the physics of the pulsar magnetosphere. Unlike characteristics like rotation period, which are observed directly, magnetic field information involves significant uncertainties because it is not constrained by observations alone. There is no direct method to derive strength and structural information of the magnetic field and it requires a number of assumptions about processes like spindown and hence, it is not accurately known. Since studying the magnetic field is extremely significant to understand the physical processes occurring in the magnetosphere, and without having much knowledge about its configuration, for convenience, the most simple dipolar magnetic field has been considered in the majority of the literature. Many extensive studies simply assume the dipolar field to derive the consequences of the magnetic field on the physics of pulsars. The most widely used solution for the electromagnetic field for a rotating dipole is the first ever solution computed by Deutsch (1955) and the simplest magnetospheric structure used is the one given by Goldreich & Julian (1969).

The assumption of a dipolar field simplifies things greatly; however, it makes much more sense to consider the magnetic field as a general multipolar magnetic field to be sure that there is no loss of information which the higher multipole components might carry. With this intuitive idea, there has been attempts to consider the multipolar magnetic field in various studies. Roberts (1979) developed a formalism for the electromagnetic multipolar fields induced in a neutron star by its rotation considering an arbitrary magnetic multipole at its centre. The higher order multipole components were suggested to help explain the high magnetic field strength and the unusual pulse morphology of millisecond pulsars by Krolik (1991). Arons (1993) showed that the magnetic field structure in the old pulsars must be dipolar based on the spin up of these objects due to accretion and also insisted that the pulsar magnetic fields are basically dipolar, even near the surface of the neutron star. Asseo & Khechinashvili (2002) modelled the total magnetic field as the sum of global dipolar and star centred multipolar fields to study the physical processes close to the surface of the rotation powered pulsars. They studied the effect of such configuration on pair creation process which is the necessary mechanism for generation of radiation from pulsars. A study by Barsukov & Tsygan (2010) suggested that the anomalous braking index values for radio pulsars might be related to the non dipolar fields. Bonazzola et al. (2015) investigated the multipole field in a vacuum and provided an explicit form of the solution. They briefly discussed the consequences of this field suggesting it could explain the stable sub structures of pulses and also offered the solution to the problem of current closure in pulsar magnetosphere. Petri (2015) approached the problem with vector spherical harmonics similar to their scalar fields insisting that their formalism is handier to solve for the electromagnetic field components in vacuum. They also showed the consequences of the topology of the multipolar fields demonstrating that considering only a dipole field can be very misleading.

There is still ongoing work on how the multipolar field leads to differences in our understanding of pulsars but for simplicity, still a vast majority of studies use the dipolar field almost exclusively to describe the magnetosphere of pulsars. This assumption has been fairly sufficient sometimes to explain light curves from radio

and high energy emission but it does not succeed in accounting for the polarization properties of radio pulsars. We really need to focus on taking into account the higher order multipoles because, if not much dominant in regions further away from the star, they can severely affect the regions close to the surface of star and its magnetosphere.

1.11 Off centred magnetic field

As discussed in Section 1.10, considering a dipolar magnetic field is a standard assumption for reasons of simplicity. There is another vastly used assumption when it comes to magnetic field studies. All the major literature considers the assumption that the centre of the magnetic dipole axis coincides with the geometrical centre of the pulsar or say, the centre of the rotation axis of the pulsar. There is no physical reason behind this and it seems highly probable that during the supernova collapse, the induced field was not centred from the beginning. In fact, it has been shown by Stift (1974) and Komesaroff (1976) that a deviation from this centred assumption i.e. an off-centred geometry is possible for stars and planets respectively. Below we mention the minor portion of literature which does consider the off centred scenario to study pulsars.

Harrison & Tademaru (1975) discussed earlier theories on magnetic field of that time and found that they were completely unsatisfactory in confirming the high kick velocity in excess of $100 kms^{-1}$ for observed pulsars. They proposed that all rotating stellar objects have their magnetic field similar to a first order approximation to that of a dipole moment displaced from the centre of the star. Roberts (1979) raised the question 'What is the set of centred multipoles that represents the field of an arbitrary off centred multipole?' and consequently, presented a detailed analysis on computing off centred magnetic multipoles. Good & Ng (1985) studied contributions of quadrupole moments to electromagnetic torques.

One of the fairly recent works is the investigation by Harding & Muslimov (2011) on the effects of offset polar caps on electron acceleration and pair cascades near the neutron star surface. They used a simple model of dipole magnetic fields with

small distortions which gives rise to the shift in the polar caps varying in terms of amounts or directions, hence making them offset. Also, Petri (2016) studied the effect of an offset dipole anchored in the neutron star interior and calculated exact analytic solutions in the form of a series expansion for the electromagnetic field in vacuum outside the star. We will be using these equations to study the consequences of the off-centred approach in the first part of the thesis and also utilizing it in the second part for a complete study of frequency resolved light curves.

Some more recent works have shown positive inclinations towards the multipolar field and the off-centred approach. Archibald et al. (2016) reported the observation of a pulsar with an unexpectedly high braking index. It was proposed that if this is not attributed to a short glitch, one possible case to explain such high value of braking index could be the presence of higher order multipoles and that it could highlight the significance of considering higher components while studying pulsar spin down. Barnard et al. (2016) modelled the pulsar light curves with an offset dipole prescription to fit the observations of Vela pulsar using different emission geometries. It was concluded that for small shifts ($\lesssim 20\%$ of the radius of the pulsar) from the centre and constant emissivity, the offset polar cap dipole magnetic field is a good candidate and also favoured, but only to an extent, for larger shifts considering variable emissivity. Petri (2017b) extended the usual RVM to the off centred configuration giving an exact closed analytic expression for the phase-resolved polarization angle. This model is termed as decentred RVM (DRVM). They showed that contrary to the RVM, for DRVM, the polarization angle also depends on the emission height.

It has been convenient to carry on with the specific dipolar magnetic field but this is not the general case which could improve the study of pulsars and even help in explaining observations which are not yet confirmed by any theory. Also, in the works mentioned above, the importance of considering a more general solution for the magnetic field has been highlighted, and justifies the need to move towards a more general off centred magnetic multipole field solution.

1.12 Aim of the thesis

The magnetic field topology and the magnetosphere of the neutron star are considered to be the most significant subjects when it comes to the understanding of the pulsar physics and hence, should be dealt carefully. Small assumptions in the initial conditions could lead to big differences in the final conclusions of the work being considered. Hence, we need to be particular about the conditions we use to ensure as much accuracy as possible. As mentioned in Section 1.10 and 1.11 the majority of the pulsar literature considers standard dipolar magnetic fields to study the characteristics of pulsars by default. One of our aims is to look beyond these conventional ideas and consider more general situations. The first portion of the thesis is aimed at this area. Instead of dipolar and centred magnetic field, we use the field topology established by Petri (2016) which gives a more general condition for the field. The idea is to study the consequences of this unconventional approach on magnetic field line structure to compare it with the usual standard field topology and look for differences in finer detail. The core of this work is to study the polar cap geometry and the radio and high energy emission. The polar caps are significant when it comes to the pulsar geometry since the field lines from polar caps are considered to be responsible for radio emission and also, they divide the magnetosphere into two regions - open field lines and closed field lines, which is pretty much a basic feature used to study any of the physical processes of pulsars. Our attempt is to show how different approaches result in different geometries, and hence, lead to changes in all the processes associated with it. The light curves for radio and high energy emission are studied and conclusions based on the differences between the standard approach and our off centred approach are made.

The next part of the thesis is to study the evolution of emission features by calculating frequency resolved emission. The observations of pulsars are easily classified in different wavelength regimes. In fact, depending on the instrument used for observation, we know the range of the frequency of the signal which is received. However, when it comes to models and theories, there has been no focus on separating the

emission on the basis of different frequencies. Our aim in this part is to consider both, the centred and the off centred geometry and consider the curvature radiation as the source of the radiation, and analyze the emission for different frequency ranges. For both the radio and the high energy emission, this study is carried out and corresponding light curves are also studied. Unlike most of the literature and work on emission, all photons carry a certain weight which is equal to power radiated by it which makes this study a multi wavelength project to visualize the emission evolving from low to high frequencies. This helps us see which regions in the magnetosphere are dominated by higher frequency photons and which are dominated by lower frequency radiation. This helps in understanding of sites of emission in a finer detail and also to realize how the radiation is distributed in the magnetosphere.

The outline of the chapters in thesis is as follows : This chapter is devoted to the basic understanding of neutron stars and pulsars. Starting from the history of pulsars, there are sections providing a summary of our current understanding of pulsars. In Chapter 2 we describe the radiation processes and the propagation effects on the radiation in a relativistic environment followed by description of the model we used and then, a brief summary of the simulation steps we used in all our calculations. Major portions of the Chapter 3 are a copy paste of our paper (Kundu & Petri, 2017) which studies the consequences of the off centred geometry on the pulsar emission in detail and also compares all the results with those of the standard centred geometry. In Chapter 4 we describe curvature radiation in detail and use this to study the frequency resolved emission for radio and high energy emission in pulsars. Chapter 5 discusses the conclusions of the thesis and further prospects of this work.

Chapter 2

Radiation processes and model

Magnetic fields are present everywhere in astrophysical environments leading to the processes that can be monitored by measuring high energy electromagnetic radiation, giving rise to branch of astrophysics called high energy astrophysics. Since, neutron stars have strong magnetic fields and emit high energy radiation, the dynamics of the charged particles under their influence is an essential subject to understand the physical processes surrounding the neutron stars. The charged particles under the influence of the magnetic field move almost along the magnetic field lines owing to their high strength (of order which can go as high as 10^{11} T), tying them to the magnetic field configuration. However, the smooth streaming motion of the particles along the field lines is limited by plasma instabilities and small-scale irregularities in the magnetic field. This results in relativistic charged particles intersecting the field lines and giving rise to radiation processes responsible for pulsar emission. Also, tracing back these emissions from observations help us identify and constrain the distribution of the high energy particles and magnetic fields.

This chapter focuses on discussing the basic radiation processes responsible for emission in pulsars (Section 2.1). Next, we discuss the significant relativistic effects on photon propagation for a complete study of the processes related to the emission of radiation in Section 2.2. The model used in the thesis, the two pole caustic model is described in Section 2.3. And finally, we describe our numerical approach used in the calculations in Section 2.4.

2.1 Radiation processes

A charged particle moving under the influence of a magnetic field experiences acceleration and emits electromagnetic radiation. The electromagnetic radiation emitted when charged particles are accelerated radially could be different depending on the velocity of the particle. If the particle has non relativistic velocity, i.e. $v \ll c$, the radiation emitted is called cyclotron radiation while for the relativistic particles, it is known as synchrotron radiation (Bordovitsyn, 1999). And if the field strength is quite high to make the particle almost follow the field line, the radiation due to the acceleration of this particle will be termed as curvature radiation. Also, there are essentially two kinds of physical processes leading to the emission; one is the coherent emission whose mechanism is still not known and another one is the incoherent emission which could be synchrotron radiation, inverse compton and/or curvature radiation. The observed radio emission from pulsars is coherent in nature (Ruderman & Sutherland, 1975; Ginzburg & Zhelezniakov, 1975; Kazbegi et al., 1991) while the high energy emission is incoherent (Michel, 1978; Arons, 1981; Michel, 1982). However, in all our calculations, we consider incoherent emission (be it radio or high energy) as a starting point.

Since the pulsar magnetosphere is filled with plasma, the interaction of the plasma particles with the magnetic field is responsible for emission of radiation. Understanding of the basic radiation processes responsible for pulsar emission is necessary to understand the physics of pulsar magnetosphere. The plasma is relativistic in the pulsar magnetosphere, so the emission is considered to be generated by synchrotron and curvature radiation. However, for a complete understanding we explain the most significant basic radiation processes below.

2.1.1 Cyclotron radiation

Consider a charged particle with charge e, mass m, moving in a uniform magnetic field $\mathbf{B}$ with velocity $\mathbf{v}$. The particle will experience Lorentz force $\mathbf{F} = e\mathbf{v} \times \mathbf{B}$ acting on it and hence, will accelerate. If the field is orthogonal to the direction of motion

of the particle, we have $F = evB$; equating it to the centripetal force mv^2/r_L which particle is acted on by because of the circular motion in the field, we get,

$$r_L = \frac{mv}{eB} \tag{2.1}$$

where r_L is called the Larmor radius or gyroradius. Using $v = \omega_L r$ where ω_L is the cyclotron angular frequency, we have,

$$\omega_L = \frac{eB}{m} \tag{2.2}$$

The time period of rotation of the particle, is then,

$$T = \frac{2\pi}{\omega_L} = \frac{2\pi m}{eB} \tag{2.3}$$

Since this charged particle is moving with non relativistic velocity v in vicinity of the magnetic field, it emits radiation which is termed as, cyclotron radiation. This radiation is emitted at a single specific frequency, the Larmor or cyclotron or gyration frequency, and is given by,

$$\nu_L = \frac{1}{T} = \frac{eB}{2\pi m} \tag{2.4}$$

The total power radiated by a particle accelerated to an acceleration a by the field, is given by the Larmor formula, which applies for cyclotron radiation, and is given as,

$$P = \frac{e^2 a^2}{6\pi\epsilon_0 c^3} \tag{2.5}$$

In the case of non-uniform magnetic fields with only slow variation of magnitude of the magnetic field, the motion of the particle is approximately helical. In the plane perpendicular to the field, the motion is circular, as before while in the direction parallel to the field, the motion is uniform. The superposition of these two trajectories results in helical motion.

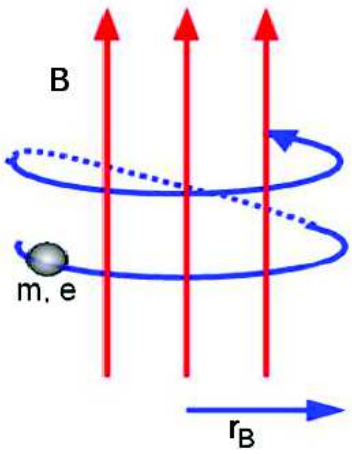

Figure 2-1: A particle gyrates along the magnetic field lines. The particle has mass m and charge e and its trajectory in magnetic field $\mathbf{B}$ is helical with Larmor radius r_B (Figure taken from Ghisellini (2013) and modified slightly)

2.1.2 Synchrotron radiation

Now, consider the particle is relativistic with $v \approx c$, it radiates a spectrum which may extend to higher harmonics of Larmor frequency ν_L. When the relativistic factor γ is large, the harmonics are so densely packed that the spectrum might appear as a continuum. This radiation is called synchrotron radiation. The trajectory of the particle, in general, will have a helical shape of radius r_B , the general Larmor radius (see Fig. 2-1). The angle that the velocity vector makes with the magnetic field line is called pitch angle θ. Below is shown the general formalism of Larmor formula for the relativistic case (Ghisellini, 2013).

The Lorentz force for a relativistic particle under the influence of magnetic field, is,

$$\mathbf{F} = \frac{d}{dt}(\gamma m \mathbf{v}) = e\mathbf{v} \times \mathbf{B} \tag{2.6}$$

Separating out the parallel $\parallel$ and the perpendicular $\perp$ components of force, the acceleration is,

$$
\begin{aligned}
F_{\parallel} &= ev_{\parallel}B = 0 \rightarrow a_{\parallel} = 0 \\
F_{\perp} &= \gamma m \frac{dv_{\perp}}{dt} = ev_{\perp}B \rightarrow a_{\perp} = \frac{evB\sin\theta}{\gamma m}
\end{aligned} \tag{2.7}
$$

where θ is the angle between the direction of velocity of the particle and the magnetic field. Also, using Eqn. 2.7 $a_{\perp} = v_{\perp}^2/r_L$ where r_B is the general Larmor radius,

$$
\begin{aligned}
r_B &= \frac{v_{\perp}^2}{a_{\perp}} = \frac{v_{\perp}\gamma m}{eB} \\
&= \frac{\gamma mc\beta\sin\theta}{eB} = \gamma r_L
\end{aligned} \tag{2.8}
$$

where $\beta = v/c$. The general gyration frequency ν_B (inverse of time) for an orbit of length $2\pi r_L$, then, becomes,

$$
\begin{aligned}
\nu_B &= \frac{v_{\perp}}{2\pi r_L} = \frac{c\beta\sin\theta}{2\pi r_L} \\
&= \frac{eB}{2\pi\gamma mc} = \frac{\nu_L}{\gamma}
\end{aligned} \tag{2.9}
$$

Now, to calculate the total power losses due to synchrotron radiation, we need to move from the instantaneous particle rest frame to the observer frame. To achieve this, we will make use of the fact that the total emitted power is Lorentz invariant. Using Eqn. 2.5, we have,

$$
P_e = P_e' = \frac{e^2}{6\pi\epsilon_0 c^3}a'^2 = \frac{e^2}{6\pi\epsilon_0 c^3}\left[a_{\parallel}'^2 + a_{\perp}'^2\right] \tag{2.10}
$$

where P_e and P_e' are the emitted powers in observers frame and rest frame of particle respectively. Also, a' is the acceleration in the latter frame with $a_{\parallel}'$ and $a_{\perp}'$ being its parallel and perpendicular components. Using the acceleration transformation

equations $a'_{\parallel} = \gamma^3 a_{\parallel}$ and $a'_{\perp} = \gamma^2 a_{\perp}$ (derived by taking time derivatives of Eqn. 2.15),

$$P_e = P'_e = \frac{e^2}{6\pi\epsilon_0 c^3}\left[a'^2_{\parallel} + a'^2_{\perp}\right] = \frac{e^2}{6\pi\epsilon_0 c^3}\gamma^4\left[\gamma^2 a^2_{\parallel} + a^2_{\perp}\right] \tag{2.11}$$

Using Eqn. 2.7 in Eqn. 2.11, we get total power losses due to synchrotron radiation, say P_S, to be,

$$P_S = \frac{e^4}{6\pi\epsilon_0 m^2 c} B^2\gamma^2\beta^2\sin^2\theta \tag{2.12}$$

The relation shows that the power emitted is inversely proportional to the square of the mass of the particle; which means that particles like electrons radiate significant emission. Hence, most models consider only electrons while discussing synchrotron radiation. However, protons are also considered by few.

2.1.3 Curvature radiation

If the magnetic field is very strong as in the case of a pulsar, the relativistic charged particle might be constrained to follow the path of the field line extremely closely, with almost zero pitch angle. For the curved magnetic field lines, the particle will be accelerated transversely and hence, generate radiation. This radiation, which is closely related to the synchrotron radiation, is termed as curvature radiation.

The brightness temperature of the emission from a pulsar could be estimated from the observed quantities like flux, width of pulse and its distance from the observation point. The brightness temperature obtained for radio pulses could go as high as 10^{31} K (for Crab pulsar (Jessner et al., 2004)). The only way such high temperature could be justified is by considering a coherent radiation consisting of a bunch of particles which radiate collectively i.e. coherently rather than as a single particle. However, the pulses observed at higher energies than radio are still consistent within the description of incoherent emission. For instance, the brightness temperature of the X-ray emission is about 10^{11} K which could simply be explained by considering an incoherent radiation of high energy electrons accelerated in pulsar magnetosphere. In both cases, radio and high energy, the acceleration of the charged particles occurs

in the gaps in the magnetosphere as discussed in Section 1.7. These accelerated particles very rapidly lose their velocity component parallel to the magnetic field lines by synchrotron radiation, but as they move along the curved magnetic field lines, they radiate *curvature radiation*. Detailed derivation of formulae associated with curvature radiation is presented in Section 4.3; here, we only mention the equations necessary for our calculation process. The curvature frequency ν_{CF}, where the subscript CF is to specify that it is for co-rotating frame (derived as Eqn. 4.23 in Section 4.3), is given as,

$$\nu_{CF} = \frac{3c}{4\pi\rho}\gamma^3 \tag{2.13}$$

where ρ is the radius of curvature and γ is the Lorentz factor for the relativistic particle under consideration. The value of γ is chosen from literature separately for high energy and radio emission. The curvature (κ) which is the inverse of radius of curvature ρ (Eqn. 4.1) is calculated by numerical method discussed in Section 4.2. Substituting all the values, we get ν_E as (observed) emission frequency. The factor κ ensures that the location of the particle, and hence it's unique frequency/wavelength plays a role in this picture.

Now, when we have the frequency of emission for each particle, we can calculate the power emitted by each of them using the standard expression (Jackson, 1962),

$$P_{crv} = \frac{e^2 c\gamma^4}{6\pi\epsilon_o\rho^2} \tag{2.14}$$

where P_{crv} is the radiated power (in units of Watts, W), $e = 1.6 \times 10^{-19}$ C is the charge of an electron, $c = 3\times10^8 ms^{-1}$ is the speed of light and $\epsilon_o = 8.85\times10^{-12} Fm^{-1}$ is the permittivity of free space.

2.1.4 Synchro-curvature radiation

It has been the general consensus that the relativistic particles in a curved magnetic field either radiate synchrotron radiation or curvature radiation. However, most recently, the formalism for an intermediate form of radiation termed as Synchro-

curvature radiation has been put forward. Kelner et al. (2015) presented the idea and found that the particle trajectory has the form of a helix wound around the the so-called drift trajectory, which describes the particle motion averaged over the fast oscillations. Their explanation for the formalism is as follows. The curvature of the trajectory, hence, is determined by a combined effect of the curvature of the helix and the curvature of the drift trajectory. The curvature of the helix is determined by the strength of the magnetic field and therefore, if it dominates, the radiation is defined by strength of the field which is the case of the synchrotron radiation. On the other hand, the curvature of the magnetic field determines the curvature of the drift. If the particles move along the drift trajectory with a little wobbling around the helix, the majority of the contribution is from the curvature of the drift trajectory which is the case of the curvature radiation. They concluded that the synchrotron and curvature radiation regimes are approximations of synchro-curvature radiation that work only when the helix and the drift trajectory curvature differ significantly and that, if they are comparable, it could result in significantly different features from the individual regime formalism. They also argued that for certain configuration of the electromagnetic field, the gamma ray emission of the pulsar magnetospheres can be dominated by the component radiated in the synchro-curvature regime. Vigano et al. (2015a) presented expressions on the high energy synchro-curvature radiation coming from pulsar magnetospheres and computed particle trajectories associated with this kind of loss. They also produced a number of follow up studies but for the sake of the brevity, we do not discuss them here (refer Vigano et al. (2015b,c); Vigano & Torres (2015) for details).

2.1.5 Inverse Compton

Compton scattering is one of the ways in which light interacts with matter and results in different wavelength of the scattered light from that of the incident radiation. When a high energy photon collides with a low energy charged particle, say an electron, it transfers part of its energy to the electron and hence, the resultant photon scatters with a lower energy, i.e. longer wavelength than before. This is the classical

Compton effect. Inverse Compton scattering occurs when charged particles transfer part of their energy to radiation. It could be regarded as synchrotron radiation from the high energy electrons as they pass through the electromagnetic field. It is a general consensus that some high energy gamma ray emission may be Inverse Compton radiation from high energy particles at high altitudes in the magnetosphere.

2.2 Beaming

Now, after knowing the basic radiation process, we need to consider propagation effects on the emitted particles. Because of the strong magnetic field and relativistic plasma, there are significant relativistic effects on photon propagation which need to be discussed so as to complete the study of the physical process of the radiation. We present here, in a basic fashion, the relativistic effects : Doppler effect and aberration.

Relativistic Doppler Effect :

The special theory of relativity gives us the transformation between two inertial rest frames - a rest frame K and a frame K' moving with uniform velocity v. A factor β is defined which is given as v/c where v is the relative velocity of K' with respect to K and c is the speed of light. This coordinate transformation is known as Lorentz transformation and the basic equations involved are,

$$\begin{aligned} x' &= \gamma(x - vt) \\ y' &= y \\ z' &= z \\ t' &= \gamma\left(t - \beta\frac{x}{c}\right) \end{aligned} \tag{2.15}$$

for a motion along the $x - axis$ with v, (x, y, z) and (x', y', z') are coordinates corresponding to K and K' frame respectively. γ is termed as the Lorentz factor and

is given as,

$$\gamma = \left(1 - \beta^2\right)^{-1/2} \tag{2.16}$$

The two consequences of special relativity, among many others, are :

- *Length Contraction :* It is the phenomenon in which a moving objects length is measured to be shorter than its proper length, which is the length as measured in the objects own rest frame. Also, more formally referred to as Lorentz contraction, it is observed in the direction in which the body is moving. For an object of proper length $\triangle x$ in its rest frame, it is measured as being contracted to $\triangle x'$, via relation, $\triangle x' = \triangle x/\gamma$.

- *Time Dilation :* A clock that is moving relative to an observer will be measured to tick slower than a clock that is at rest in the observer's own frame of reference. The proper time interval $\triangle t$ in observer frame is transformed to $\triangle t'$ in moving frame as, $\triangle t' = \gamma \triangle t$.

The above relations work correctly if lengths are measured by physical rulers and clocks are compared considering a standard reference, such as the decay lifetime of a radioactive element. However, additional effects come into play when there are extended moving objects which carry information about time and position via photons. Since, a photon carries information with finite speed, c, the travel paths of photons for extended objects could significantly vary and have to be considered. Also, their time of emission is important to be taken in account since the photon emitted much later might get observed at the same time as a photon emitted earlier, if the latter has travelled a longer path. Below we mention two of these relativistic effects on photon propagation which are later applied in our calculations for light curves. The review by Ghisellini (2013) has been used as a reference to describe the effects below (for detailed mathematics, refer to the Chapter 2 of the article).

Now, to present the formulation of the relativistic Doppler effect, consider a lamp moving with velocity $v = \beta c$ at an angle θ from the line of sight. Assuming that the

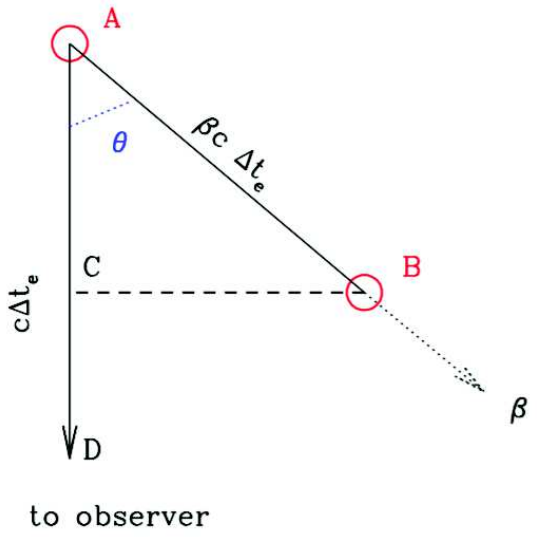

Figure 2-2: Difference between the proper time and the photons arrival time. Consider a lamp moving with a velocity $v = \beta c$ in the direction shown as the dotted line (β). The lamp is turned on at A where it emits the first photon, which travels a distance $AC = c \triangle t_e$ in time $\triangle t_e$ (in observer frame K). The lamp emits the last photon at B where it is then turned off, after covering the distance AB. In the direction towards the observer (at D), the two photons are separated by the distance CD. Considering the lamp remained on for a time interval $\triangle t'_e$ in its frame K', the corresponding time interval measured by the observer at D (at an angle θ) is, $\triangle t_a = \triangle t'_e/\delta$ (Ghisellini, 2013).

lamp is on for a time interval $\triangle t'_e$ in its rest frame i.e. in frame K', using time dilation relation mentioned above as a consequence of special relativity, the corresponding on-time for lamp $\triangle t_e$ is $\triangle t_e = \gamma \triangle t'_e$. Now, using photons as the carrier of information about time, we need to consider the locations of emission of the first photon when the lamp was switched on and the last photon after which lamp is off. Also, their travel paths would be different since the lamp has moved during the time interval, so the last photon did not cover the same travel path as the first photon to reach the observer.

This situation is illustrated in Fig. 2-2. The lamp is turned on at A where the first photon is emitted; the lamp moves with speed βc in time $\triangle t_e$ to reach point B where it is turned off after emission of last photon at B. In the observer frame K, the path AB is,

$$AB = \beta c \triangle t_e = \gamma \beta c \triangle t'_e \tag{2.17}$$

The first photon emitted at A travelled a distance $AC = c \triangle t_e$ and then, reached

the observer at D. The last photon is emitted at B, and in terms of line of sight direction towards the observer, the two photons are separated by distance CD. The time interval corresponding to this distance is the time interval $\triangle t_a$ between the arrival of the first and the last photon, and is given as :

$$\begin{aligned} \triangle t_a &= \frac{CD}{c} = \frac{AD - AC}{c} \\ &= \triangle t_e - \beta \triangle t_e \cos\theta \\ &= \triangle t'_e \gamma (1 - \beta \cos\theta) \\ &= \frac{\triangle t'_e}{\delta} \end{aligned} \tag{2.18}$$

Using $\theta = 90^\circ$ gives the usual time dilation $\triangle t_a = \gamma \triangle t'_e$ because in this case, all photons travel the same distance to reach the observer. Since, frequency is inversely proportional to time, we have the transformation relation for the frequency,

$$\nu = \nu' \delta \tag{2.19}$$

where δ is called the relativistic Doppler factor, defined as,

$$\delta = \frac{1}{\gamma(1 - \beta \cos\theta)} \tag{2.20}$$

The factor $1/\gamma$ is the factor usual in the special relativity and the factor $1/(1 - \beta \cos\theta)$ corresponds to the usual Doppler factor; combining both we get the relativistic Doppler effect.

Aberration :

For a moving source which is carrying information via photons, there is another important effect which needs to be considered while including photon propagation in any calculations. The effect is termed as aberration of light, and, in simple terms, is the change in an object's apparent direction caused by the relative transverse motion of the observer. A well-known example is : If you are standing still in rain, with no wind, the rain drops are falling vertically on the ground. But, if you are in a train

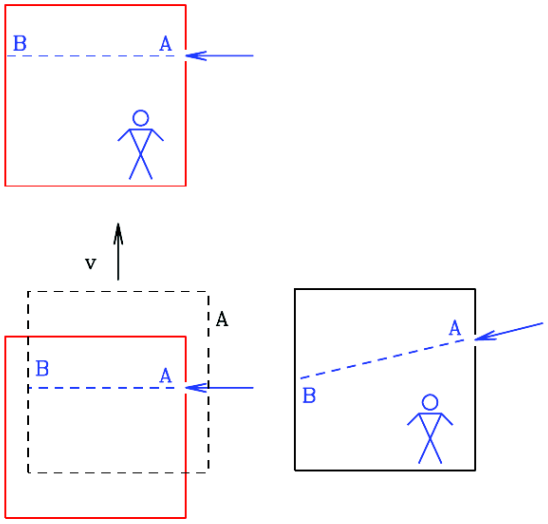

Figure 2-3: The relativistic lift, to explain relativistic aberration of light. Assume first a stationary lift (shown on top in red solid lines), with a hole on the right wall. A light ray, coming perpendicularly to the right wall, enters through the wall at A and ends its travel at B. If the lift is moving up with a constant velocity v, it changes its position (shown at the bottom left in black dashed lines; the horizontal shift is only to separate the stationary and moved lift and does not represent any motion in horizontal direction) when the photon arrives at the left wall. For the observer inside the lift, it appears that the light path is tilted as shown at the bottom right in solid dashed lines, since the point B where the photon smashes into the left wall is vertically below the point A (Ghisellini, 2013).

moving forward, the rain falling on your window will appear to be at an angle with respect to the vertical direction; the higher the speed of the train, the larger is the angle observed. This apparent change in the direction of the incoming raindrops is aberration.

To illustrate the aberration effect, we take the example of a lift moving up with constant relativistic velocity v as shown in Fig. 2-3. If the lift were still, the light ray perpendicular to the right wall will enter from hole at A and end at B as in the lift illustrated in the top panel of the figure; the path followed by the light ray in the stationary lift will be the blue dashed AB line. However, if we consider the lift to be moving, as shown in bottom panel, by the time the light ray reaches the left wall, the lift has moved up and hence, the observer inside the lift sees it as a tilted path. If the lift was accelerating instead of moving with a constant velocity, the oblique path as seen by an observer inside the lift would be curved. This illustrates why the angle of propagation as observed by two inertial frames is not same. If we consider θ as the angle between the direction of the velocity vector of a source and the direction of the

emitted photon, we get,

$$\sin\theta = \frac{1}{\gamma}\frac{\sin\theta'}{1+(v/c)\cos\theta'} \tag{2.21}$$

$$\cos\theta = \frac{\cos\theta' + (v/c)}{1+(v/c)\cos\theta'} \tag{2.22}$$

Both the propagation effects for a relativistic particle described above are utilized in the following chapters.

2.3 Two pole caustic model

Now we have all the basic knowledge about the radiation processes and relativistic propagation effects needed to understand the radiation model we used. The emission model is referred to as the two pole caustic model. This model was described by Dyks & Rudak (2003) who proposed this new picture of the origin of high energy radiation within the pulsar magnetosphere based on the slot gap model. The slot gap model is a geometrical model for the vacuum gaps, and is not directly related to the emission process. We use two pole caustic model because it relies on the slot gap model which is better than the outer gap and the polar cap model, in the sense that the latter two cannot explain the observed light curves. The vacuum gap region, where particle acceleration takes place and radiation originates, suggested by them is confined to the surface of the last open magnetic field lines and light cylinder. The illustration of how the slot gap and the outer gap regions vary is shown in Fig. 2-4.

In this model, the light curves are dominated by strong peaks (either double or single) of caustic origin (Dyks et al., 2004). The caustics are a result of the special relativistic effects, aberration of photon emission directions and time of flight delays due to the finite speed of light. It causes photons emitted at different altitudes within some regions of the magnetosphere to pile up at the same phase of a pulse (Morini, 1983; Romani & Yadigaroglu, 1995). Unlike in other pulsar models with caustic effects, the double peaks arise due to crossing two caustics, each of which is

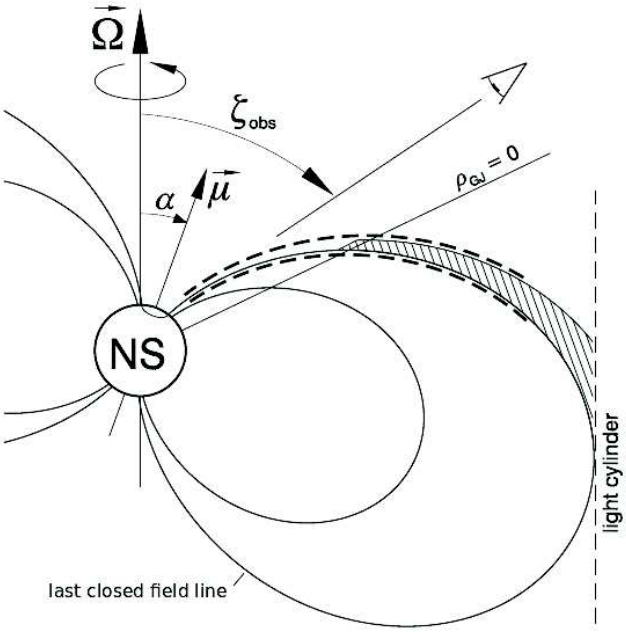

Figure 2-4: Illustration of the two-pole caustic model. The radiating region (within the dashed lines) is confined to the surface of the last closed field lines, and it extends from the polar cap to the light cylinder. For comparison, the conventional outer gap region is shown (shaded area), extending from the surface of the null space charge (where $\Omega \cdot B = 0$, or $\rho_{GJ} = 0$ where ρ_{GJ} is the GJ charge density) to the light cylinder (Dyks & Rudak, 2003).

associated with a different magnetic pole.

However, the aberration formula used by Dyks & Rudak (2003) was justified to be only as a reasonable approximation by Bai & Spitkovsky (2010). We will be presenting both of them here to understand the differences. The former used the following aberration formula to transform photon propagation direction from the co-rotating frame $\hat{\boldsymbol{\eta}}'$ to the inertial frame $\hat{\boldsymbol{\eta}}$ of a distant observer.

$$\hat{\boldsymbol{\eta}} = \frac{\hat{\boldsymbol{\eta}}' + (\gamma + (\gamma - 1)(\boldsymbol{\beta_c} \cdot \hat{\boldsymbol{\eta}}')/\boldsymbol{\beta_c^2})\boldsymbol{\beta_c}}{\gamma(1 + \boldsymbol{\beta_c} \cdot \hat{\boldsymbol{\eta}}')} \tag{2.23}$$

where $\gamma = 1/\sqrt{(1 - \boldsymbol{\beta_c^2})}$ and $\boldsymbol{\beta_c} = (\boldsymbol{\omega} \times \mathbf{r})/c$ with $\boldsymbol{\omega}$ being the angular velocity of the pulsar and $\mathbf{r}$ being the radial position of the emission point. The revised version given by the latter taking photon propagation direction in the co-rotating frame as $\boldsymbol{\beta_c}$ and in the lab frame as $\boldsymbol{\beta_0}$, was given by;

$$\boldsymbol{\beta_0} = f\mathbf{B} + \boldsymbol{\beta_c} \tag{2.24}$$

where f is a coefficient which is determined by implementing the $|\boldsymbol{\beta_0}| \to 1$ condition for the emitted particle. Also, in this limit, $\boldsymbol{\beta_0} \to \hat{\boldsymbol{\eta}}$. The equation gives two solutions; one corresponds to the particle emitted in the direction of the magnetic field line while the other corresponds to the opposite direction. The former solution i.e. the forward moving particle is to be considered.

Also, to consider the photon travel delays, the phase ϕ is taken to be

$$\phi = -\phi_{em} - \mathbf{r} \cdot \hat{\boldsymbol{\eta}}/R_L \tag{2.25}$$

where ϕ_{em} is the azimuth for the direction $\hat{\boldsymbol{\eta}}$ and R_L is the radius of the light cylinder.

For the high energy and radio emission study in Chapter 3 we use both the aberration effects to compare high energy emission for our off centred approach with the standard centred assumption; however, for the radio emission and light curves, we use the revised model given by Bai & Spitkovsky (2010).

However, for the frequency resolved study of the high energy and radio emission in Chapter 4, we use the Dyks & Rudak (2003) approach. Since, for this model, the calculation of frequency gives frequency in the co rotating frame (as opposed to the observer's frame in the Bai & Spitkovsky (2010) approach), we need to include the relativistic Doppler effect and make a transformation of the frequency from this frame to the observer's frame, which gives us the frequency in the observer's frame ν (using Eqn. 2.19, 2.20) as,

$$\nu = \frac{\nu_{CF}}{\gamma_D(1 - \beta_n)} \tag{2.26}$$

where $\gamma_D = 1/\sqrt{(1 - \boldsymbol{\beta_c^2})}$, $\beta_n = \boldsymbol{\beta_c} \cdot \mathbf{T}$ and $\boldsymbol{\beta_c} = (\boldsymbol{\omega} \times \mathbf{r})/c$ where $\mathbf{T}$ is the unit tangent vector, $\boldsymbol{\omega}$ being the angular velocity of the pulsar and $\mathbf{r}$ being the radial position of the emission point (see Eqn. 2.23).

2.4 Simulation techniques

After laying out the radiation theory including other significant effects, we now describe the numerical techniques used to calculate the following features which are then analyzed and discussed in the thesis.

2.4.1 Magnetic field line structure

Calculating magnetic field lines was the foremost step for all the calculations. To calculate the structure of the magnetic field lines, the following steps have been used :

- *Transformation from magnetic axis frame to rotations axis frame*

  The reason to consider the initial point with respect to the magnetic axis frame, as also mentioned in Appendix A.1.1, is to be sure that the entire magnetospheric region is examined and no points are missed during the transformation between the magnetic axis and the rotation axis frame. We take initial points for the magnetic axis frame and use the method shown in Appendix A.1.1 to get to the rotation frame. And equations from Appendix A.1.2 are used to transform between Cartesian and spherical coordinate systems throughout.

- *Magnetic field component for each coordinate point*

  Using the magnetic field equations from Section 3.2 of Petri (2016), we find the spherical component of the magnetic field for each point of our system. And then, using the transformation described in Appendix A.2, we finally have the magnetic field components in Cartesian coordinate system.

- *Calculating the tangent vector to the magnetic field line*

  Our next step is to find the next coordinate of the magnetic field line so as to have a full geometry of the field lines. To get to the next point, we need to calculate the direction of the magnetic field at the current point i.e. the tangent

at the point under consideration. To achieve that, the equation relating the tangent vector of the field line $\mathbf{T}$ to the field $\mathbf{B}$ is used

$$\mathbf{T} = \frac{\mathbf{B}}{|\mathbf{B}|} \tag{2.27}$$

- *Calculating next point using the tangent vector*

The final step is to use an integration method to calculate the following point using the tangent. We use *JST* scheme (Jameson, 1981, 2017) to solve the equations which is a modified form of the standard fourth order *Runge Kutta* method and is faster than the latter. The JST algorithm, in form of equations, goes like this,

$$\begin{aligned}
\mathbf{x_1} &= \mathbf{x_o} + \frac{ds\mathbf{T}(\mathbf{x_o})}{4} \\
\mathbf{x_2} &= \mathbf{x_o} + \frac{ds\mathbf{T}(\mathbf{x_1})}{3} \\
\mathbf{x_3} &= \mathbf{x_o} + \frac{ds\mathbf{T}(\mathbf{x_2})}{2} \\
\mathbf{x_4} &= \mathbf{x_o} + \frac{ds\mathbf{T}(\mathbf{x_3})}{1}
\end{aligned} \tag{2.28}$$

where $\mathbf{x_o}$ is the initial point and $\mathbf{x_4}$ is the final point $\mathbf{x}$ we need and the two points are separated by an arc length ds. The tangents $\mathbf{T}(\mathbf{x_i})$ are calculated k number of times. The order of the loop k is 4, hence four equations changing the value of k in denominator from 4 to 1. The value of k is considered to be 4 since it is accurate enough for our calculations and going to a higher order increases computation time without giving any significant change in accuracy. This gives us the next point for the field line and continuing these steps for all field lines, we get the complete structure of the field lines.

2.4.2 Polar cap geometry

The basic idea to calculate the polar cap geometry is to find the polar angle θ for the last closed field line i.e. the field line grazing the light cylinder. The procedure used for the calculations is described here in brief.

For a given azimuthal angle ϕ, a bracket for θ i.e. a range within which the θ corresponding to the last closed field line lies, is searched for. To find the last closed field line, for every field line corresponding to a θ lying between 0° and 90°, a check is made if the radial distance of a field point from the centre of the star is less than the radius of the star (implying it is making a closed loop and touches the surface of the star again) or not. If it doesn't, we move on to the next θ and repeat the check. When the check returns a value, another one close to it is checked for and is saved, so as to have two values to form a proper bracket and look within this range to find a more precise value. Now, when we have a range within which our desired value surely exists, using the standard bisection method (Press, 2007), we find the best iterated solution for θ, precise up to an accuracy of up to 10 decimal digits. These roots in θ corresponding to each ϕ are the points defining the polar cap boundary.

2.4.3 Emission diagrams

The technique applied to calculate emission diagrams, also referred to as sky maps or phase plots, is described below.

A grid of line of sight angle ζ and phase ϕ is considered surrounding the pulsar. Each *unit* element of the grid is considered to span 1° for both, ζ and ϕ; therefore, the dimensions of the grid are $[180^\circ \times 360^\circ]$.

We place a photon at each point on the field line after every length element ds and apply the two pole caustic model (refer Section 2.3) to consider its propagation. Next, we check the final coordinates of the photon to calculate which unit of the grid it belongs to. This process is repeated over the entire magnetosphere which gives the photon count for every unit in the grid at the end. We refer to it as intensity or photon count in emission diagrams in Chapter 3.

However, if instead of only counting just the number of photons, if the power radiated by each photon is considered and is used to assign a weight to it, we can find the power radiated for every unit. To do that - the number of photons for each unit in this grid is calculated and each individual photon is assigned a weight which is equal to the power radiated P_{crv} by it (refer Eqn. 2.14, derived by using curvature radiation mechanism). Adding all photons within a unit, after individually multiplied by the power radiated by each single photon, gives us the total power emitted from all the photons from that particular unit. The unit emitting the highest amount of power is considered the reference for normalization while plotting frequency resolved emission diagrams in Chapter 4 and this maximum power is referred to as P_{max} throughout the text.

The difference between the calculations lies in the fact that for the latter case, curvature frequency of every particle being emitted is calculated, which gives the power emitted by each particle depending on its location in the magnetosphere, or better, on the radius of curvature at the point on the field line under consideration.

Chapter 3

Pulsed emission from a rotating off-centred magnetic dipole in a vacuum

Major portions taken from our published paper: (Kundu & Petri, 2017)

3.1 Abstract

The topology of the electromagnetic field around neutron stars severely impacts pulsar physics. While most of the works assume a standard centred dipolar magnetic field model, recently some effort has been made to explain how inclusion of higher multipolar components could change our understanding of these objects. Also, for simplicity, it has always been assumed that the magnetic moment coincides with the geometrical centre of the star. However, lately, a more general picture has been put forward in which the magnetic dipole moment is shifted from the centre of the star. It has been demonstrated that the rotating off-centred dipole can be expanded into multipolar components. We study the effects of an off-centred rotating dipole on various characteristic emission features of pulsars in a vacuum. The reliability of the off-centred case and its consequences on the magnetic field line structure, shape of the polar caps, high energy and radio emission phase plots and corresponding light

curves along with a comparison with the standard centred case are discussed. It has been seen that an off-centred dipole breaks the north-south symmetry and allows for more flexibility in radio and high-energy light-curve fitting and phase lags.

3.2 Introduction

The neutron stars for which the direction of pulsed emission is directed towards the Earth, enabling their observation, are termed as pulsars (Gold, 1968). They have strong magnetic fields typically up to an order of 10^8 T and rotation period lying between 1.4 ms (Hessels et al., 2006) and 6.67 hr (Borghese et al., 2018). Since their discovery (Hewish et al., 1968), many attempts have been made to understand these mysterious objects. The magnetic field strength and topology of pulsars seems to play a central role in pulsar physics. They, indeed, provide insight into the physical processes like particle acceleration, radiation and emission mechanisms.

The electromagnetic field equations for a rotating dipole in vacuum were first presented by Deutsch (1955) considering that the field is symmetrical about the magnetic axis which is inclined at an angle to the rotation axis of the star. One of the first pulsar models describing the magnetic poles and the magnetic field line structure was put forward by Radhakrishnan & Cooke (1969) who compared the polarisation properties of a pulsar for different frequencies and proposed that the origin of the emission must lie in the proximity of the poles. Goldreich & Julian (1969) further discussed the electrodynamics of neutron stars for the simplest case which assumes that the magnetic dipole moment is aligned with the rotation axis and assessed various properties of the region surrounding the star. Later, the inclined cases were considered and it was highlighted by Michel & Goldwire (1970) and Davis & Goldstein (1970) that the radiation torque aligns the magnetic axis with the rotation axis. However, they assumed the star to be a perfectly conducting sphere. It was Goldreich (1970) who investigated the alignment of a rotating magnetic dipole in a conducting, rigid, but non spherical body. Pacini (1967) considered the oblique rotator model and discussed the energy emission from a neutron star and also presented the equations for the com-

ponents of an external electromagnetic field in vacuum (Pacini, 1968). Davis (1947) had discussed a possibility that the ion distribution in space modifies the electric and magnetic fields and hence, have a bearing on the electromagnetic field equations. He also suggested that both the fields extend far into space and that the magnetic field cannot be purely dipolar.

Most of the literature which followed focused on these standard assumptions where a centred dipolar field was considered with its magnetic axis inclined at some angle to the rotation axis.

However, with the discovery of PSR J2144-3933 which has a period of 8.51 s, the longest of any known radio pulsar at the time of its discovery, the existing models were challenged and it was realised that this simple assumption needs revision (Young et al., 1999). It was argued by Gil & Mitra (2001) that to explain this extreme observation of the rotation period, a complicated magnetic field with multipolar components has to be considered. Soon, Gil et al. (2002) modelled the surface magnetic field of neutron stars which required strong and non-dipolar surface magnetic field near the pulsar polar cap. The electromagnetic field was considered to be a superposition of the global dipole field and a small scale magnetic anomaly. Petri (2015) included multipolar components to the electromagnetic field in a self-consistent way and demonstrated that working with only a dipole field can, indeed, be very misleading in understanding of the emission characteristics of the pulsars.

It is also assumed, by default, that the centre of the magnetic dipole coincides with the centre of the rotation axis i.e. with the centre of the pulsar. However, it has been shown by Stift (1974) and Komesaroff (1976) that a deviation from this centred assumption i.e. an off-centred geometry is possible for stars and planets respectively.

The offset idea was first applied to neutron stars by Harding & Muslimov (2011) to investigate the effects of offset polar caps on pair cascades near the surface. Recently, Petri (2016) studied the effect of an offset dipole anchored in the neutron star interior and calculated exact analytic solutions for the electromagnetic field in a vacuum outside the star. We will be using these equations to study the consequences of the off-centred approach.

Some recent works have shown positive inclinations towards the multipolar field and the off-centred approach. Archibald et al. (2016) reported the observation of a pulsar with a high braking index. If it is not just a glitch and proven to be stable in the future, one possible explanation for such a high braking index would be the presence of higher order multipoles and could highlight the significance of considering higher components while studying pulsar spin down. Barnard et al. (2016) modelled the pulsar light curves with an offset dipole prescription to fit them with the observations of the Vela pulsar using different emission geometries. It was concluded that for small shifts($\lesssim 20\%$ of the radius of the pulsar) from the centre and constant emissivity, the offset polar cap dipole magnetic field is a good candidate and also favoured, but only to an extent, for larger shifts considering variable emissivity.

The aim of this paper is to study how an off-centred rotating dipole affects the emission features of pulsars in a vacuum by outlining the comparison with the centred dipole and to discuss the major differences for an understanding of the emission processes. The outline of the sections in the paper is as follows. We present an overview of the off-centred geometry and a description of the inclination angles and other parameters in Section 3.3. Section 3.4 shows the structure of the magnetic field lines for an orthogonal case. In Section 3.5, we discuss the results obtained for the shape of the polar caps (Section 3.5.1), make an analysis of the error associated with our approach in Section 3.5.2, the radio and high energy emission phase plots (Section 3.5.4) pursuing a goal similar to that of Bai & Spitkovsky (2010) i.e. to study emission mechanism in vacuum. The phase plots are followed by the corresponding light curves in Section 3.5.5 and we conclude our results in Section 3.6.

3.3 Off-centred geometry

In this section, we summarize the description of the characteristic parameters for an off-centred dipolar magnetic field and present its geometry.

The underlying assumption for an off-centred geometry is to consider the magnetic moment to be shifted away with respect to the geometric centre of the star. While

dealing with the oblique case (in which the rotation axis and the magnetic moment axis are not aligned) for a centred geometry we need only one parameter denoted by χ which defines the obliquity of the star, but for an off-centred star we need to define three additional parameters for a complete geometric description of the magnetic topology. The four characteristic parameters are defined as follows:

- α represents the obliquity of the magnetic moment with respect to the rotation axis.

- β is a measure of the projection of the magnetic moment out of the meridional plane defined by the plane xOz where (O,x,y,z) represents the Cartesian coordinate system.

- δ is the angle between the rotation axis and the line joining the centre of star to the centre of the magnetic moment.

- D is the distance between the stellar centre and the magnetic moment whose vector representation is $\mathbf{d} = D(\sin\delta, 0, \cos\delta)$.

Two important parameters but not directly related to the pulsar are the inclination ζ of the line of sight with respect to the rotation axis and the emission height h taking the stellar surface as a reference meaning zero altitude, $h = 0$. The angle ζ determines the light-curve profiles and whether radio and/or high energy photons are detected.

Fig. 3-1 (adopted from Petri (2017b)) depicts the geometry of an off-centred dipole for a star of radius R. Because the electromagnetic field equations under consideration are with respect to the rotation axis of the pulsar, we need to make our calculations in the same frame. However, all our information about the magnetic moment and inclination is in the magnetic axis frame. Therefore, we always begin from the latter frame and make a transformation to the former to proceed with the calculations. Hence, two reference frames are considered which are described as follows.

First is the unprimed reference frame xyz whose centre coincides with the geometrical centre O of the star, which means it is also the frame attached to the rotation

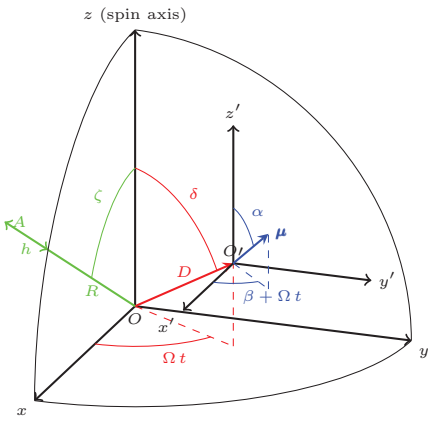

Figure 3-1: Geometry of the off-centred dipole showing the three important angles $\{\alpha, \beta, \delta\}$ and the distance D. Two additional parameters related to observations are the line of sight inclination ζ and the emission height h. The plot corresponds to time t assuming that $\boldsymbol{\mu}$ lies in the (xOz) plane at $t = 0$. The figure is adopted from Petri (2017b).

(spin) axis of star. The position vector for any point located inside the sphere of radius R in this centred frame is defined as $\mathbf{r} = r\mathbf{n}$ with $\mathbf{n} = (\sin\theta\cos\phi, \sin\theta\sin\phi, \cos\theta)$ where r is the spherical radius and θ and ϕ are the polar and azimuth angles respectively.

Second is the primed reference frame $x'y'z'$ whose centre coincides with the magnetic moment of the star which is located at O'. The coordinate axis x, y and z remain parallel to the coordinate axis x', y' and z' respectively. This primed reference frame $x'y'z'$ will be referred to as an off-centred frame from now onwards. The magnetic moment $\boldsymbol{\mu} = \mu\mathbf{m}$ ($\mathbf{m}$ is a unit vector) is shown in blue with polar angle and azimuth angle as α and β respectively as seen from the off-centred frame. It is located at $\mathbf{d}$ and directed along the unit vector $\mathbf{m} = (\sin\alpha\cos\beta, \sin\alpha\sin\beta, \cos\alpha)$. Our calculations correspond to time $t = 0$ and hence, instead of $\beta + \Omega\, t$, where Ω is the angular velocity, we always use β for phase.

The distance between the origins of two frames, D and other characteristic parameters are also shown in the figure. An important condition used throughout is $D < R$ as the magnetic moment must remain within the star. We define a normalised quantity $\epsilon = D/R$ to keep this in consideration and hence, we have, $\epsilon \in [0, 1[$. We do not include the point $\epsilon = 1$ because in that case, at the surface, the magnetic field strength would diverge.

The lowest order correction to the dipole corresponds to a quadrupolar moment

which is combined with the centred dipole in order to get an accurate analytical description of the electromagnetic field outside the star when $D \ll R$. In our work, we neglect higher order multipolar perturbations but in principle they can be added if higher precision is required, especially when $D \lesssim R$. The exact analytical expressions for dipolar and quadrupolar electromagnetic fields recently published in Appendix C of Petri (2016) are used for all the calculations. We have implemented these exact analytical expressions using the spherical Hankel functions $h_\ell^{(1)}(x)$. Thus, our code can handle pulsars with any period from millisecond to second, our solution generalising the Deutsch field without restriction on the ratio $R/R_{\rm L}$ ($R_{\rm L}$ is the radius of the light cylinder defined by last closed magnetic field lines and equals c/Ω, where c is the speed of light).

The angles α, β and δ are shuffled to get different orientations for the off-centred geometry. As the parameter space defined by the off-centred dipole is at least five dimensional, it is impractical to explore the full range of inclination angles and distances. We restrict our study to a sample of judiciously chosen configurations to emphasise the discrepancies between centred and off-centred geometry. Throughout the paper, the pulsar period is set to $R/R_{\rm L} = 0.1$ for every topology, corresponding approximately to a 2 ms pulsar, and $\epsilon = 0.2$ is considered for the off-centred calculations. The former is chosen because the lower the ratio $R/R_{\rm L}$, the higher the resolution (which depends on the radius of the star) which increases the simulation time significantly. The latter is chosen to have a large shift from the centre but not too large as the error scales with increase in ϵ as ϵ^2 (see Table 3.2).

3.4 Magnetic field lines structure

Our work investigates the implication of the magnetic topology on several important characteristics of the multi-wavelength pulsed emission. A good intuitive picture of the magnetic field lines will help to interpret the results discussed in subsequent sections. So, in this section we focus on the structure of the magnetic field lines. We also show the structure of the individual components of the magnetic field to visualize

their independent contributions to the total electromagnetic field.

As specified in Section 3.2 of Petri (2016), the expressions for the magnetic and the electric field have been decomposed into the dipolar and the quadrupolar components both normalised separately and independently with some well-defined chosen weights for each component. Note that this normalisation is arbitrary but must remain consistent with the coefficients of the expansions presented below. The expression for the field is as shown below:

$$\begin{aligned}\mathbf{F}^{\rm off} = \mathbf{F}^{\rm dip}(\psi \to \psi - \beta) + \epsilon[(2\cos\alpha\cos\delta - \sin\alpha\sin\delta\cos\beta)\mathbf{F}^{\rm quad}_{m=0}(\psi) \\ + \cos\alpha\sin\delta\mathbf{F}^{\rm quad}_{m=1}(\psi) + \sin\alpha\cos\delta\mathbf{F}^{\rm quad}_{m=1}(\psi \to \psi - \beta) \\ + \sin\alpha\sin\delta\mathbf{F}^{\rm quad}_{m=2}(2\psi \to 2\psi - \beta)].\end{aligned} \tag{3.1}$$

$\mathbf{F}$ represents the field (electric displacement $\mathbf{D}$ or magnetic field $\mathbf{B}$) and $\mathbf{F}^{\rm dip}$ and $\mathbf{F}^{\rm quad}$ represents the dipolar and the quadrupolar components of the field respectively. α, β and δ are the angles used to determine the geometry of the system as described in the previous section. The subscript m represents the azimuthal modes, where $m = 1$ for dipole, $m = 2$ for quadrupole, $m = 4$ for octopole, and so on. The term $\psi = \phi - \Omega\, t$ represents the actual phase (at time t). The change $(\psi \to \psi - \beta)$ corresponds to a simple shift in the azimuthal direction as expected from the orientation of the magnetic moment with respect to the xOz plane.

We use the technique laid out in Section 2.4 to calculate the structure of the magnetic field lines. Displaying the full 3D geometry of magnetic field line is difficult to lay in 2D. Thus, to simplify things for visualisation purposes, we present only the equatorial magnetic field lines structure. Indeed for special topologies, some magnetic field lines reside fully in the equatorial plane from the stellar surface to large distances. This can be achieved by setting the angles to appropriate values. We show the orthogonal geometry for two cases; $(\alpha, \beta, \delta) = (90^\circ, 0^\circ, 90^\circ), (90^\circ, 90^\circ, 90^\circ)$. An example of individual contributions of both the dipolar and the quadrupolar components for an orthogonal off-centred case where $\beta = 90^\circ$ and $\epsilon = 0.2$ is shown in

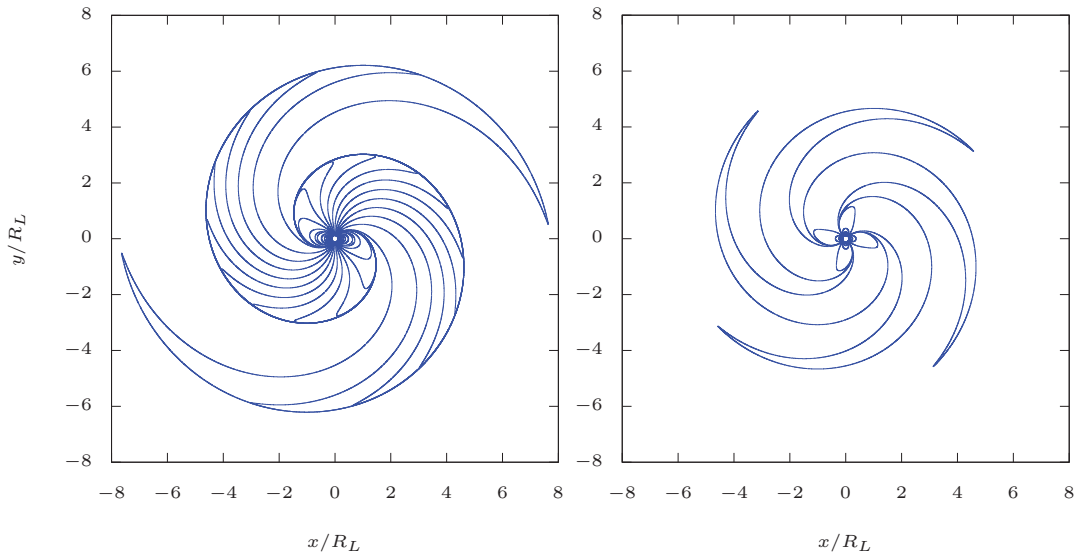

Figure 3-2: The individual contribution of the dipolar (left) and the quadrupolar (right) components to the magnetic field line structure for an orthogonal off-centred case with $(\alpha, \beta, \delta) = (90°, 90°, 90°)$ and $\epsilon = 0.2$.

Fig. 3-2. We distinguish the basic property of a two-armed and a four-armed spiral pattern with quantum numbers respectively $(\ell, m) = (1, 1)$ and $(\ell, m) = (2, 2)$.

When both components, dipolar and quadrupolar, are added with appropriate weights according to Eqn. (3.1), we get a faithful representation of a radiating off-centred dipole as long as the shift remains small $\epsilon \ll 1$. The resulting structure of the magnetic field lines for the equatorial case where $\beta = 90°$ are compared for the two cases $\epsilon = 0$ and $\epsilon = 0.2$ as shown in Fig. 3-3 in red and blue respectively. Comparing the field pattern for the two cases, it is found that the spiral arms corresponding to both the poles are symmetric for the centred case, while they show an asymmetry for the other one. Also, a comparable shift in the entire field line geometry for both cases is prominent. To highlight this difference, we zoom in to a small section of the first quadrant shown on the left where the shift between the two cases is more clearly visible.

The same is checked for another orthogonal configuration with $\beta = 0°$ in Fig. 3-

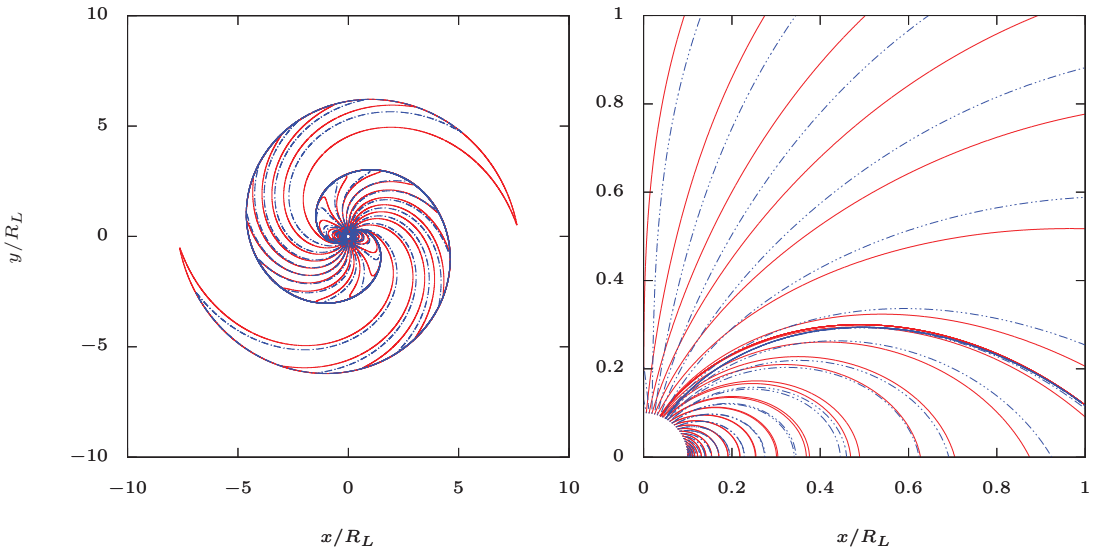

Figure 3-3: Magnetic field line structure in the equatorial plane for the orthogonal ($(\alpha, \beta, \delta) = (90°, 90°, 90°)$) centred case ($\epsilon = 0$, in red) and off-centred case ($\epsilon = 0.2$, in blue).

4. We realise that the spiral symmetry which was present in the centred case but missing in the off-centred case for $\beta = 90°$, follows the same criteria here. Although, the asymmetry for the off-centred case (shown in blue) is much more pronounced than that in the previous case. We also see the shift mentioned for $\beta = 90°$ persisting here at large distances. As already stated in Petri (2016), this asymmetry would reflect even in the region outside the light cylinder through the striped wind originating from inside. The right side, again, zooms in to a better resolution to visualize the shift.

3.5 Results and discussions

Studying magnetic field lines is only glancing at the tip of the iceberg. Major observational consequences of our modified topology are thoroughly investigated in this section. The shape of the polar caps, considered to be the locus of the base of the last closed field lines, is central to the problem of the pulsed emission. Pulsed emission

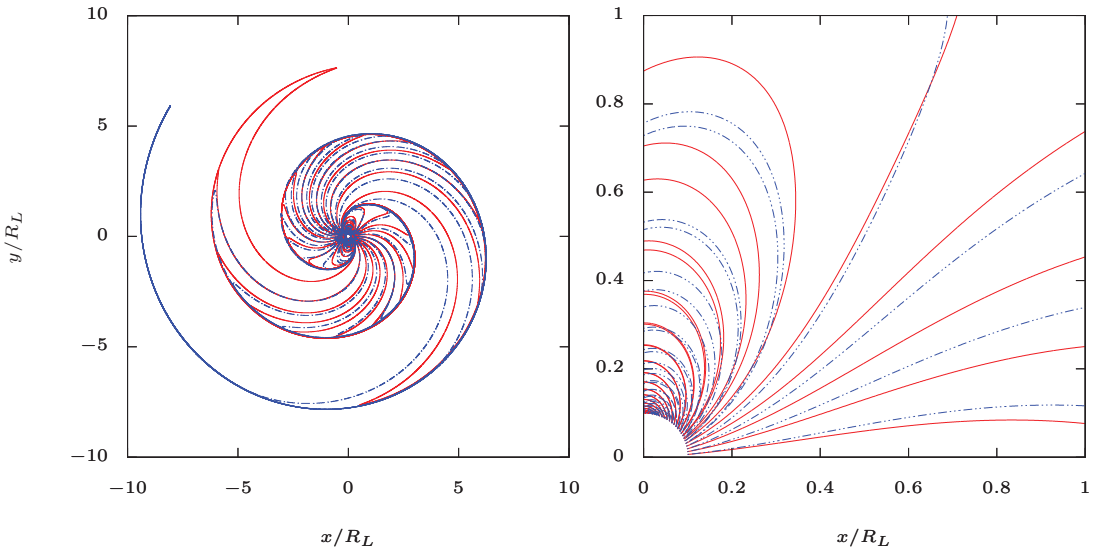

Figure 3-4:]
Magnetic field line structure in the equatorial plane for the orthogonal ($(\alpha, \beta, \delta) = (90°, 0°, 90°)$) centred case ($\epsilon = 0$, in red) and the off-centred ($\epsilon = 0.2$, in blue).

is expected from sites of efficient particle acceleration where the electric field component parallel to the magnetic field is significant. These regions are suspected to be closely related to the locus of last closed field lines (Ruderman & Sutherland, 1975; Ginzburg & Zhelezniakov, 1975; Kazbegi et al., 1991). Several attempts to localize these sites have been made since the discovery of the first pulsar in 1967. The question of emission close to the surface and/or close to the light-cylinder was debated until the launch of the Fermi telescope in June 2008. Spectral analysis showed that high-energy emission must be located closer to the light-cylinder (Abdo et al., 2013) in order to observe a sub-exponential cut-off. Moreover, the misaligned radio and gamma-ray pulses gives hints about separated emission sites. Thus, radio photons are probably produced closer to the surface than gamma-ray photons (Michel, 1978; Arons, 1981; Michel, 1982). Indeed, the polar cap model (Sturrock, 1971) suggests that the radio emission emanates mostly from the field lines on the stellar surface enclosing the polar caps with possible core and conal emission (Backer, 1976; Rankin,

1993). The slot gap models have been designed (Arons, 1983) to explain the high energy emission, photons are assumed to be produced in the vicinity of the last closed field lines from the surface up to the light cylinder. Some other variants also exist like an extended volume depicted by the outer gaps (Cheng et al., 1986a) and the annular gaps (Qiao et al., 2004). We do not consider them further in this paper. The differences between radio and high-energy light-curves are described with several predictions based on phase plots, light-curves and the phase lag between radio and high-energy peaks.

3.5.1 Polar cap location and geometry

The first step in understanding the polar cap geometry requires the knowledge of the location of the magnetic poles i.e. points of the intersection of the magnetic axis with the surface of the pulsar. To determine the coordinates of the poles, we employ the following method. The distance from the centre of the magnetic moment to the centre of the pulsar is D, as shown in Fig. 3-1. It is represented by the vector

$$\mathbf{d} = D(\sin\delta, 0, \cos\delta). \tag{3.2}$$

The direction of the magnetic moment axis is

$$\mathbf{m} = (\sin\alpha\cos\beta, \sin\alpha\sin\beta, \cos\alpha). \tag{3.3}$$

Using Eqn. (3.2) and Eqn. (3.3) and the general equation for a straight line, we can write the equation for the magnetic axis as

$$\mathbf{r} = \mathbf{d} + \lambda\mathbf{m} \tag{3.4}$$

where λ is a parameter defined to find the position coordinates. Considering Cartesian coordinates with $\hat{\mathbf{i}}$, $\hat{\mathbf{j}}$, $\hat{\mathbf{k}}$ being the unit vectors for the x, y and z directions respectively, the position vector is written as $\mathbf{r} = x\hat{\mathbf{i}} + y\hat{\mathbf{j}} + z\hat{\mathbf{k}}$. Comparing this with Eqn. (3.4),

we get

$$x = D\sin\delta + \lambda\sin\alpha\cos\beta y = \lambda\sin\alpha\sin\beta z = D\cos\delta + \lambda\cos\alpha. \tag{3.5}$$

To find the intersection of the magnetic axis and pulsar we substitute the above coordinates representing all the points lying on a magnetic axis in the equation of a sphere of radius R i.e. in $x^2 + y^2 + z^2 - R^2 = 0$;

$$\Rightarrow (D\sin\delta + \lambda\sin\alpha\cos\beta)^2 + (\lambda\sin\alpha\sin\beta)^2 + (D\cos\delta + \lambda\cos\alpha)^2 - R^2 = 0$$
$$\Rightarrow \lambda^2 + 2D(\cos\alpha\cos\delta + \sin\alpha\sin\delta\cos\beta)\lambda + (D^2 - R^2) = 0.$$

The equation above represents a quadratic equation in λ of form $a\lambda^2 + b\lambda + c = 0$. We will consider only the real roots i.e. roots satisfying $b^2 - 4ac \geq 0$ which is equivalent to the condition $D < R$, we get:

$$\lambda = -D\Bigg[\cos\alpha\cos\delta + \sin\alpha\sin\delta\cos\beta \mp \sqrt{\cos\alpha^2\cos\delta^2 + \sin\alpha^2\sin\delta^2\cos\beta^2 + 2\cos\alpha\cos\delta\sin\delta\sin\beta\cos\beta - \left(1 - \frac{R^2}{D^2}\right)}\Bigg]. \tag{3.6}$$

Using Eqn. (3.6) in Eqn. (3.5), we get coordinates for the two poles.

Following this procedure, we calculate the location of the poles and present them in the Table 3.1 for three particular cases for both; the centred and the off-centred geometries. It is interesting to note that the difference in azimuth of the two poles for $(\alpha, \beta, \delta) = (90°, 90°, 90°)$ gives a phase difference of exactly 180° for the centred case ($\epsilon = 0$) while it is higher than that for the off-centred case ($\epsilon = 0.2$). This difference is affiliated to the geometry. We make an attempt in Fig. 3-5 to geometrically visualise these locations.

In the figure, we show three cases with $(\alpha, \beta, \delta) = (0°, 0°, 0°)$ in (a), $(30°, 0°, 0°)$ in (b) and $(90°, 90°, 90°)$ in (c). The xyz and the $x'y'z'$ set of coordinate axis represent the centred and the off-centred frame with their centres being O and O' respectively.

$(\boldsymbol{\alpha, \beta, \delta})$	**Pole 1**		**Pole 2**		$\triangle\boldsymbol{\phi}$
	$\boldsymbol{\theta_1}$	$\boldsymbol{\phi_1}$	$\boldsymbol{\theta_2}$	$\boldsymbol{\phi_2}$	$\boldsymbol{\phi_2 - \phi_1}$
	$\boldsymbol{\epsilon = 0}$				
$(0°, 0°, 0°)$	$0°$	$0°$	$180°$	$0°$	$0°$
$(30°, 0°, 0°)$	$30°$	$0°$	$150°$	$180°$	$180°$
$(90°, 90°, 90°)$	$90°$	$90°$	$90°$	$270°$	$180°$
	$\boldsymbol{\epsilon = 0.2}$				
$(0°, 0°, 0°)$	$0°$	$0°$	$180°$	$0°$	$0°$
$(30°, 0°, 0°)$	$24°$	$0°$	$144°$	$180°$	$180°$
$(90°, 90°, 90°)$	$90°$	$78°$	$90°$	$282°$	$203°$

Table 3.1: Location of poles in terms of polar angle θ and azimuth angle ϕ (both rounded off), for various configurations defined by (α, β, δ).

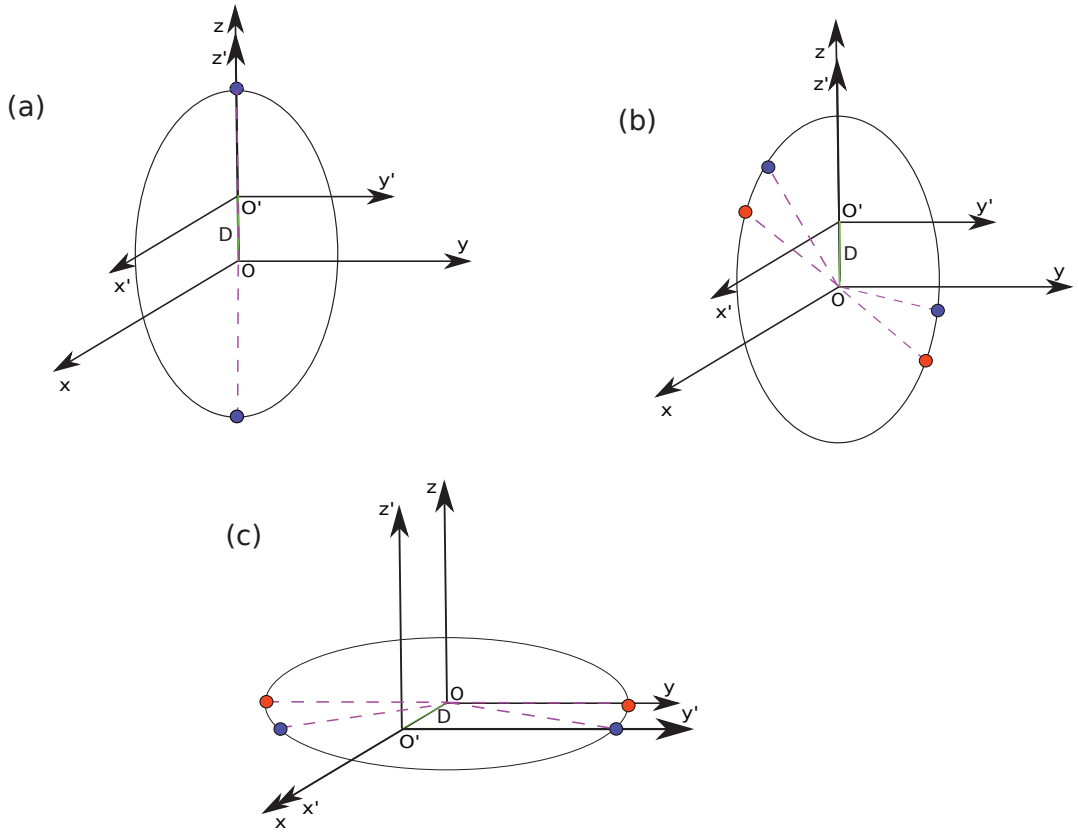

Figure 3-5: A geometrical description for the location of the poles for various geometries; $(\alpha, \beta, \delta) = (0°, 0°, 0°)$ in (a), $(30°, 0°, 0°)$ in (b) and $(90°, 90°, 90°)$ in (c). The xyz and the $x'y'z'$ set of coordinate axis represent the centred and the off-centred frame with their centres being O and O' respectively. The green solid line shows the shift D between the two geometries. The black ring is a section of the surface of the pulsar in the xz plane for (a) and (b) while in the xy plane for (c). The solid-filled dots are the pole positions for the centred (in red) and the off-centred cases (in blue). Dashed magenta lines highlight the angles for the poles with respect to the rotation axis frame. Figures not to scale and provide only a rough depiction.

Shift D between two frames is shown in green. The black ring is a section of the surface of the pulsar in xz plane for (a) and (b) while in xy plane for (c) chosen based on location of the poles. The colour scheme is the same as used throughout the paper with red representing the centred case while blue representing the off-centred case. The solid-filled dots are the location of the poles. The magenta dashed lines highlight the angles for the poles with respect to the unprimed i.e. the rotation axis frame and are plotted based on the values given in the Table 3.1. The representation is not to scale and represents only a crude approximation of the geometry of the poles.

In part (a) of the figure, which is an aligned case, we see that both the poles perfectly overlap for the centred and off-centred case while they are at appreciable angles in the other two geometries as shown in (b) and (c). As the polar caps are linked to the location of poles, we get an estimate of the relative shift in the position of the polar cap for the centred and the off-centred geometry.

In (b) it is interesting to notice that θ for the poles i.e. the angle with respect to the z-axis, is smaller for both the poles in the off-centred case (blue) than in the centred case (red) which implies a shift in θ and might also be responsible for a small polar cap. In (c) when we look at ϕ i.e. the angle with respect to the x-axis, we witness that it is smaller in the off-centred case than in the centred case for one pole but the opposite in the other, implying a sort of phase shift (discussed in Table 3.1) in the location of poles which must be evident in the polar cap shapes too, which we discuss in the following paragraph.

The polar cap is the region mapped out by the base of the magnetic field lines grazing the light cylinder. Considering studies, for instance, by Rankin (1993), we believe that the pulsar radio emission is centred on the magnetic axis i.e. centred at the polar caps and hence, studying polar caps is crucial to understand the coherent radio emission. Polar caps strongly impact on the high-energy counterpart too, because slot gaps and the underlying two-pole caustic model of Dyks & Rudak (2003) as well as outer gaps (Cheng et al., 1986b) also rely on the last closed field lines thus on the polar cap shape. We present a comparison of the polar cap geometry for the centred and the off-centred approach. To study the polar cap geometry we need to

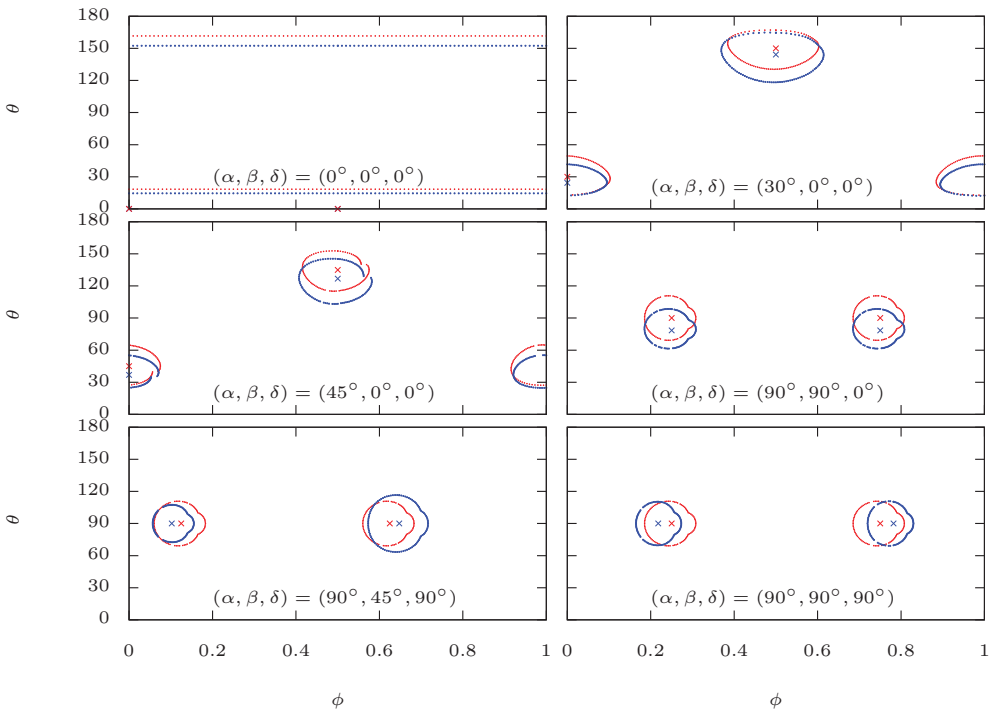

Figure 3-6: Polar cap geometry comparison for the centred case with $\epsilon = 0$ (in red) and the off-centred case with $\epsilon = 0.2$ (in blue) for various cases. The x-axis and the y-axis represent the azimuth ϕ and the polar angle θ respectively. Crosses are the location of the poles as calculated using Eqn. (3.4).

find the polar angle θ for the last closed field line i.e. the field line grazing the light cylinder for each *phi*. This approach serves as a fine estimation for the calculations associated with the polar caps. The procedure used for the calculations is described in Section 2.4

The shapes of the polar caps for the off-centred dipole are shown in Fig. 3-6 for various inclination angles. The x-axis and the y-axis represent the azimuth angle ϕ and the polar angle θ respectively. The centred case (in red), shown for comparison, has been calculated by considering $\epsilon = 0$ and for the off-centred case (in blue), ϵ is taken to be 0.2. The crosses represent the location of the poles with the colour scheme being the same as stated before.

We see that the polar caps are asymmetric and distorted as expected from a rotating dipole (Arendt & Eilek, 1998). A broad view distinction depicts that the shape is not affected due to the shift of the centre of the dipole from the geometrical centre but size and locations are, indeed, affected. The contrast in size is prominent

for all the inclination geometries.

The size of the polar cap is one of the determining factors for the pulse profile width of pulsar. The larger or smaller polar caps as evident especially for $(\alpha, \beta, \delta) = (30^\circ, 0^\circ, 0^\circ)$ and $(90^\circ, 45^\circ, 90^\circ)$ could be used to justify observations with pulse widths showing discrepancy with respect to what is expected. For instance, as seen in the pulse width versus the rotation period plots in Weltevrede & Johnston (2008), there are many pulsars which lie away from the pulse width in the power law fit region. We know from such plots (also mentioned by Kramer et al. (1998), Pilia et al. (2016), Malov & Malofeev (2010)) that there is a wide range of pulse widths corresponding to almost all rotation periods possible and that the extremes of the widths could be explained by this approach.

We refer to the geometries in which $\delta = 0^\circ$ representing that the centred and the off-centred frames have their z-axis aligned with each other and the ones with $\delta = 90^\circ$ representing that the two frames are perpendicular to each other as aligned and orthogonal cases respectively.

We show four aligned cases i.e. $(\alpha, \beta, \delta) = (0^\circ, 0^\circ, 0^\circ)$, $(30^\circ, 0^\circ, 0^\circ)$, $(45^\circ, 0^\circ, 0^\circ)$, $(90^\circ, 90^\circ, 0^\circ)$ in Fig. 3-6 in which we clearly see the shift for the location of poles in ζ. The same variation is prominent in Fig. 3-5(a) and (b) as discussed.

In contrast to the aligned case, the orthogonal geometries show a shift in ϕ. The shift for each pole location is in opposite directions as seen in $(\alpha, \beta, \delta) = (90^\circ, 45^\circ, 90^\circ)$ and $(90^\circ, 90^\circ, 90^\circ)$. This variation in ϕ is also noticeable in Fig. 3-5(c).

Correspondingly, we see the shift for the polar caps in ζ for the aligned cases and in ϕ for the orthogonal cases. It has been noted by Abdo et al. (2013) in the second Fermi-LAT catalogue of gamma ray pulsars that pulsars indicate a phase lag between their radio and the high energy peak. The shift in ϕ (representing phase delay) for the orthogonal cases in our approach could be compared with observational phase delays in pulse profiles which could add to our understanding and hopefully, might serve as one of the factors, among many others like emission height, varying the delay time by adjusting the emission altitude, aberration, magnetic field distortion, which are not yet fully known, to explain such observations.

3.5.2 Error analysis

Expanding only up to the first order correction ϵ in the electromagnetic field can be justified a posteriori by checking the error made by neglecting higher order terms. We expect errors of the order ϵ^2 because higher order corrections require higher order multipoles. It was, indeed, shown by Petri (2016) that an error of order ϵ^ℓ is associated with neglecting multipoles starting at order $\ell+1$. In the present work, we consider up to $\ell = 2$, the first correction. This discrepancy scaling like ϵ^2 is tested in the following paragraph analysing the error made by computing the polar cap shape. To make such an analysis we compare the analytical solutions with the solutions we obtain from our numerical method. For simplicity, we consider only an aligned case with $(\alpha, \beta, \delta) = (0°, 0°, 0°)$.

To generate the analytical results for the aligned off-centred case, we shift the entire coordinate system under consideration for several values of the shift parameter ϵ. In this shifted system the surface of the pulsar (with a shift D along the z-axis) is represented by the equation

$$x'^2 + y'^2 + (z' + D)^2 = R^2 \tag{3.7}$$

where using the Cartesian to Spherical Coordinate System transformation we get,

$$r'^2 + 2D\cos\theta' r' + (D^2 - R^2) = 0. \tag{3.8}$$

To find the analytical value of the root, we find the polar angle at which the field lines from this shifted pulsar intersects the light cylinder. For this, we need the equation of field lines grazing the light cylinder, $r' = R_{\rm L}\sin^2\theta'$ where $R_{\rm L}$ is the radius of the light cylinder. Substituting this condition in Eqn. (3.8), we have:

$$R_{\rm L}^2\,\sin^4\theta' + 2\,D\,R_{\rm L}\,\sin^2\theta'\,\cos\theta' + D^2 - R^2 = 0. \tag{3.9}$$

To calculate θ' from this equation, we consider an unknown $X = \cos\theta'$ and replace

Shift ϵ	**Analytical value of** θ **(in deg)**	**Numerical value of** θ **(in deg)**	**Error (in deg)**	**Relative Error** $R.E.$	$\boldsymbol{R.E./\epsilon^2}$
		Pole 1			
0	18.4349	18.4349	0.0000	0.0000	–
0.01	18.4349	18.1686	0.0048	0.0002	2.674
0.02	17.8937	17.9128	0.0191	0.0011	2.674
0.05	17.0906	17.2026	0.1121	0.0066	2.623
0.1	15.7762	16.1794	0.4032	0.0256	2.555
0.2	13.2434	14.5719	1.3285	0.1003	2.508
		Pole 2			
0	161.5650	161.5651	0.0000	0.0000	–
0.01	161.2927	161.2876	0.0051	0.0000	0.316
0.02	161.0192	160.9982	0.0210	0.0001	0.327
0.05	160.1920	160.0499	0.1421	0.0009	0.355
0.1	158.7916	158.1424	0.6491	0.0041	0.409
0.2	155.9127	152.4586	3.4540	0.0222	0.554

Table 3.2: Error analysis for both poles with several shifts for aligned case $(\alpha, \beta, \delta) = (0^\circ, 0^\circ, 0^\circ)$ with $R = 0.1R_{\rm L}$.

$\sin^2\theta'$ by $1 - \cos^2\theta'$, and we get a quartic equation in X:

$$X^4 - 2\,\epsilon\,a\,X^3 - 2\,X^2 + 2\,\epsilon\,a\,X + (\epsilon^2 - 1)\,a^2 + 1 = 0 \tag{3.10}$$

where we introduced $a = R/R_{\rm L}$. Solving this equation, we have θ' i.e. our required root but in off-centred frame.

To be compared with numerical results, we need a value of θ with respect to the rotation axis frame, therefore, a transformation is required. As it is an aligned case with the shift along the z-axis, the Cartesian transformation can be carried out simply using $z = z' + D$. Using this and making the transformation between the Cartesian and the spherical coordinate system using Appendix A.1.2, we get the analytical value of the roots i.e. θ.

We compare the error between the roots obtained from the analytical method explained above and our numerical approach in Table 3.2. The radius of pulsar R is taken to be $0.1R_L$.

The upper and lower section of the table shows the results for each of the poles. The left most column shows the shift parameter ϵ taken for a few values in between the centred case and going up to a shift of 20% of R. It is clearly visible from the following two columns that for very small shifts the results are accurate up to the second decimal place. However, we start to see the appreciable difference as we move towards larger shifts from the centre. These differences are highlighted in the next columns where we compute absolute error and the relative error.

It is significant to note that the order of the error confirms with what we expect by neglecting the higher order terms in the off-centred electromagnetic field equations. The equations have been considered to be precise up to an order of ϵ^2 and we see the same order of accuracy while comparing the results from the analytical and the numerical approach. This, indeed, establishes that considering only a quadrupolar correction in the electromagnetic field equations is justified as long as ϵ remains small. If we go towards the higher shifts, error becomes larger scaling as ϵ^2. If we accept truncation errors up to several percent, let us fix the limit to 5%, then adding only the quadrupolar corrections to the dipole is justified because the first neglected term, the hexapolar component $\ell = 3$, is of the order $\epsilon^2 = 0.04$ (4%). Going to $\epsilon \gtrsim 0.25$ would lead to too high truncation errors impacting on the precision of the pulse profile unacceptable with the high quality of observations from radio to gamma-rays. Adding higher order multipoles is the only way to study satisfactorily larger off-centred dipoles.

We can write the magnetic field equation in simple terms up to the second order in ϵ as $B = B_{dip} + \epsilon B_{quad} + \epsilon^2 B_{hex}$ or, for more convenience, as $B - B_{dip} - \epsilon B_{quad} = \epsilon^2 B_{hex}$. B is the total magnetic field while B_{dip}, B_{quad} and B_{hex} are its dipolar, quadrupolar and hexapolar components. As the left hand side of this equation is giving us an estimate of the error between the total magnetic field and the magnetic field represented as a sum of its components, we expect that the ratio of the relative error to ϵ^2 will give us a good estimate of the component B_{hex}. As we would expect that this value should be a constant, we see in the last column of Table 3.2 that they are quite close for all the cases; at least up to the first decimal place. This provides

an even stronger claim for the point that the equations are accurate up to the second order in ϵ.

3.5.3 A study of pulse widths of radio emission

The idea is to calculate pulse widths of the radio emission for different heights of emission for the off-centred case (Petri, 2016) and to compare it with the empirical result for pulse widths (Rankin, 1990) along with the standard centred case. The method is similar to what has been explained in Section 2.4 with an additional step after calculating the polar caps - the 'rim' of the emission at different heights is utilized to find the pulse widths for corresponding heights of emission.

Parameters

- Two orthogonal orientations are considered $(\alpha, \beta, \delta) = (90°, 90°, 90°)$ and $(90°, 0°, 90°)$.
- The analytical pulse width is taken to be the core component width (Rankin, 1990)

  $$W_{core} = 2°.45\eta^{1/2}P^{-1/2} \tag{3.11}$$

  P is the period of the pulsar and $\eta = H/R$ where R is the radius of the pulsar (considered to be 10 km) and H is the height of emission (considered to be between $H_l = R$ and $H_u = 5R$
- For calculations for the centred and off-centred case, the parameter $\epsilon = D/R$ is taken to be 0.0 and 0.2 respectively where D is the scalar off shift.
- Three pulsar periods are considered with periods being 2 ms, 20 ms and 200 ms which implies the radius of light cylinder to be 10^2 km, 10^3 km and 10^4 km respectively.
- A grid of 500×500 in θ and ϕ is used for calculations with resolution of $1°$ for each.

Comments

- The results for $(\alpha, \beta, \delta) = (90°, 90°, 90°)$ are summarized in Table 3.3 and plotted in Fig 3-7. The same is done for $(\alpha, \beta, \delta) = (90°, 0°, 90°)$ in Table 3.4 and Fig 3-8.

- The values vary from the analytical case for all the periods which is affiliated to the scaling factor 2.45°. Making a reverse scaling from the calculated values gives a factor of 3°. They vary appreciably for the $(90°, 0°, 90°)$ case than the $(90°, 90°, 90°)$ case.

- The pulse widths for smaller period like 2 ms show a difference between the centred and the off-centred case lying anywhere between 1° to 4° but for higher periods like 20 ms and 200 ms there seem to be no appreciable differences at all.

3.5.4 Radio and high energy phase plots

Observing light curves in the radio and high energy bands offers a means to diagnose the magnetic topology inside the magnetosphere; close to the surface for radio pulse profiles and close to the light-cylinder for high-energy light curves. Accurate fits of broad band observations gives us some hints about the possible deviation from a perfect centred dipole. The technique to calculate phase plots, also referred to as sky maps, is shown in Section 2.4. In this section, we present detailed phase plots for radio and high energy emission. The two-pole caustic model (Dyks & Rudak, 2003) for calculating high energy emission light curves as explained in Section 2.3 is used. However, the aberration formula used by them was justified as only a reasonable approximation by Bai & Spitkovsky (2010). We show both of them here to show the differences among them for our off-centred approach.

We show the high energy emission for $\epsilon = 0.2$ for several cases using both formulae - Fig. 3-9 uses Eqn. (2.23) and Fig. 3-10 uses the revised Eqn. (2.24). In both figures, the x-axis spans the phase ϕ while the y-axis represents the angle of the line of sight ζ.

η	**Analytical**	**Calculated**			
H/R	$2.45\sqrt{\eta}/\sqrt{P}$	$\epsilon = 0$		$\epsilon = 0.2$	
		$P = 2$ ms			
		Pole 1	**Pole 2**	**Pole 1**	**Pole 2**
1	54.8	67	67	66	68
2	77.5	95	95	94	98
3	94.9	116	116	115	119
4	109.6	133	133	131	135
5	122.5	146	146	145	149
		$P = 20$ ms			
		Pole 1	**Pole 2**	**Pole 1**	**Pole 2**
1	17.3	20	20	20	21
2	24.5	29	29	29	30
3	30.0	36	36	36	36
4	34.6	42	42	42	42
5	38.7	46	46	46	46
		$P = 200$ ms			
		Pole 1	**Pole 2**	**Pole 1**	**Pole 2**
1	5.5	6	6	6	6
2	7.7	9	9	9	9
3	9.5	11	11	11	11
4	10.9	13	13	13	13
5	12.2	15	15	15	15

Table 3.3: Pulse widths (in degrees) for different heights (η) for analytical, centred (both poles) and off centred (both poles) cases for $(\alpha, \beta, \delta) = (90°, 90°, 90°)$.

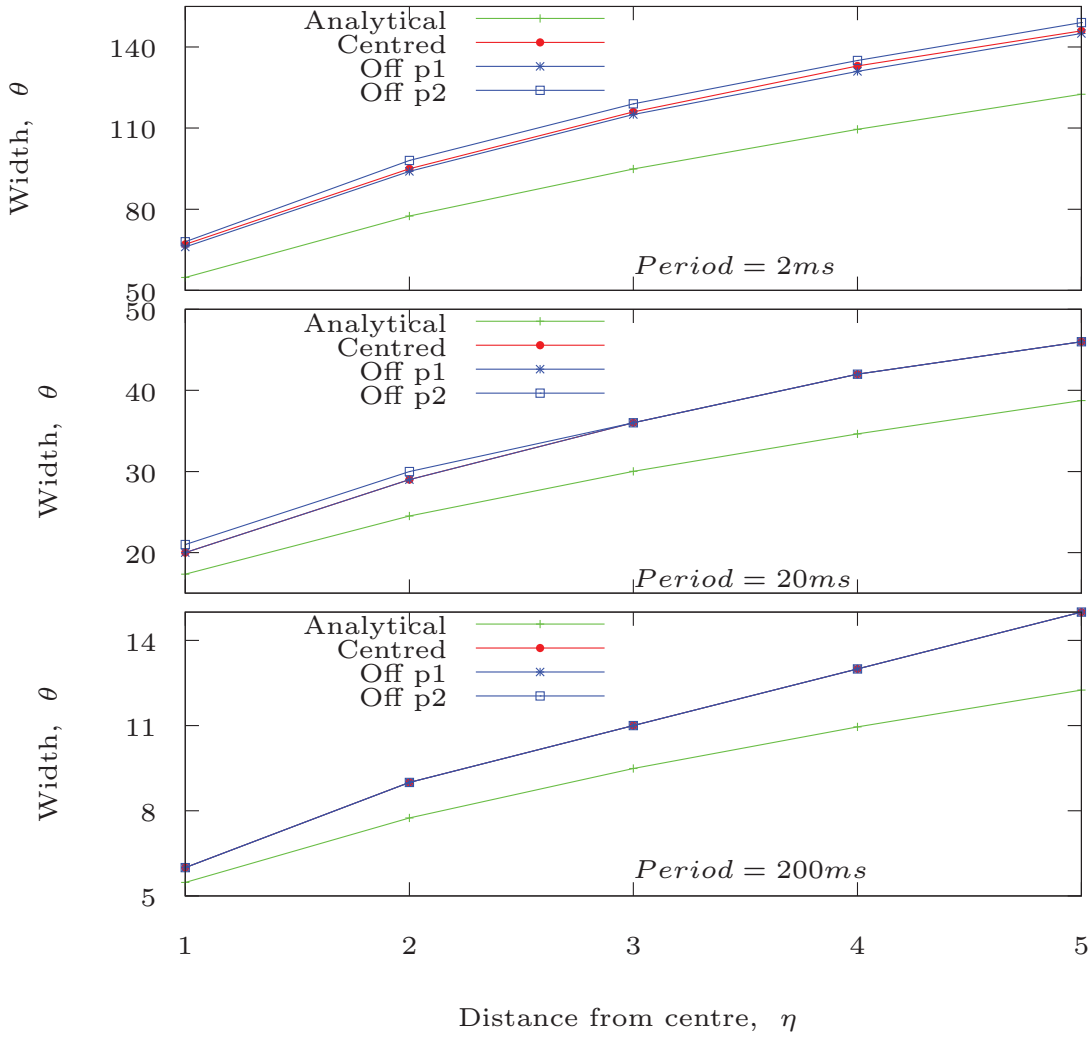

Figure 3-7: Pulse widths (in degrees) for different heights for analytical, centred and off centred (both poles) cases with $(\alpha, \beta, \delta) = (90°, 90°, 90°)$. Please note that $y - axis$ have different scaling for all plots.

η	**Analytical**	**Calculated**			
H/R	$2.45\sqrt{\eta}/\sqrt{P}$	$\epsilon = 0$		$\epsilon = 0.2$	
		$P = 2$ ms			
		Pole 1	**Pole 2**	**Pole 1**	**Pole 2**
1	54.8	67	67	58	68
2	77.5	95	95	89	99
3	94.9	116	116	111	121
4	109.6	133	133	127	138
5	122.5	146	146	141	152
		$P = 20$ ms			
		Pole 1	**Pole 2**	**Pole 1**	**Pole 2**
1	17.3	20	20	18	17
2	24.5	29	29	28	30
3	30.0	36	36	34	36
4	34.6	42	42	40	42
5	38.7	46	46	46	47
		$P = 200$ ms			
		Pole 1	**Pole 2**	**Pole 1**	**Pole 2**
1	5.5	6	6	5	5
2	7.7	9	9	9	9
3	9.5	11	11	11	11
4	10.9	13	13	13	13
5	12.2	15	15	14	15

Table 3.4: Pulse widths (in degrees) for different heights (η) for analytical, centred (both poles) and off centred (both poles) cases for $(\alpha, \beta, \delta) = (90^\circ, 0^\circ, 90^\circ)$.

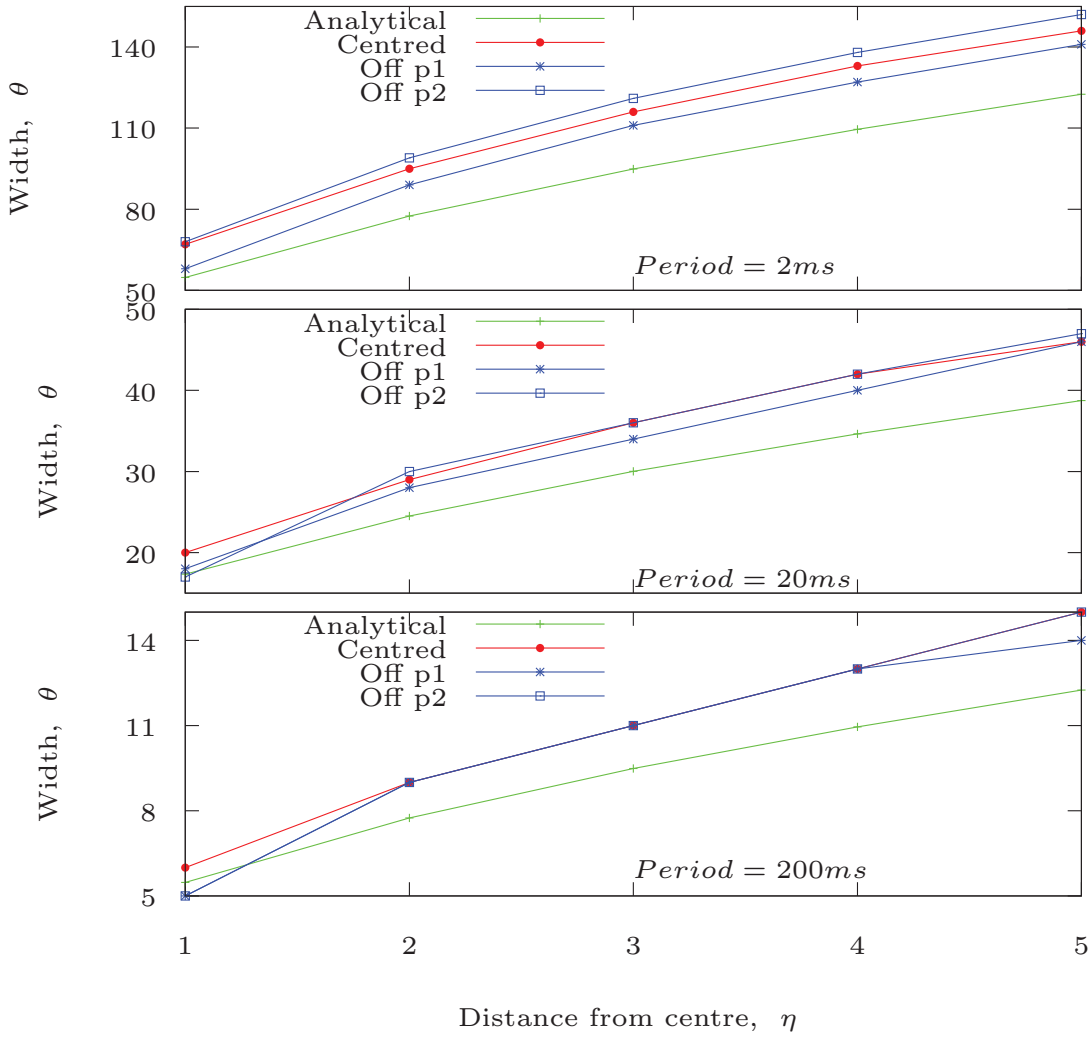

Figure 3-8: Pulse widths (in degrees) for different heights for analytical, centred and off centred (both poles) cases with $(\alpha, \beta, \delta) = (90°, 0°, 90°)$. Please note that $y - axis$ have different scaling for all plots.

The white region corresponds to 'no emission' region and moving towards blue-black via yellow-orange signifies an increase in the photon count.

Due to caustic effects (explained in Section 2.3), in the two-pole caustic model, significant emission emanates from regions close to the light-cylinder. We see these high energy emission regions in blue-black in all the cases. The white regions specify no emission observed when the line of sight crosses the polar caps which are free of high energy photons. Also, the asymmetry in the size of the polar cap for the two poles as seen in Fig. 3-6 for $(\alpha, \beta, \delta) = (90^\circ, 45^\circ, 90^\circ)$ is reflected in the emission too. It is important to note that there is a small 'bump' disturbing the symmetry of the polar cap shape in Fig. 3-6 which is also visible in Fig. 3-9 and Fig. 3-10 but the direction stands reversed. This is because these two plots describe totally different scenarios. The former is merely a geometric description of the polar cap while the latter two are representing the photon emission at respective points, and hence, the reflected asymmetry is not something surprising.

It was pointed out by Bai & Spitkovsky (2010) for the centred case that the corrected aberration leads to wider caustics. We notice the same trend to be followed in the off-centred case as the corrected aberration in Fig. 3-10 displays a different caustic structure than the older version in Fig. 3-9. We will use the corrected formulae for the radio emission later without showing it separately for both cases because aberration effects are not significant in that region.

Our calculations for the high energy emission phase diagrams for the centred case ($\epsilon = 0$) given by Eqn. (2.23) and those given by Eqn. (2.24) match well with Petri (2015) and Bai & Spitkovsky (2010) respectively. The small differences are only because the boundary conditions used by us are different from earlier works; we terminate our calculations of the photon count at a distance going as far as $0.95R_{\rm L}$ (other works used $0.75 - 0.80R_{\rm L}$). Also, in orthogonal cases with $\alpha = 90^\circ$, we notice sharp peak points close to both the poles. This is because our boundary is further away (implying large distance away from the pole) which caused the emission from pole 1, calculated separately, extending up to the regions corresponding to pole 2 and hence, adding to the emission of pole 2. This behaviour is highlighted in Fig. 3-11

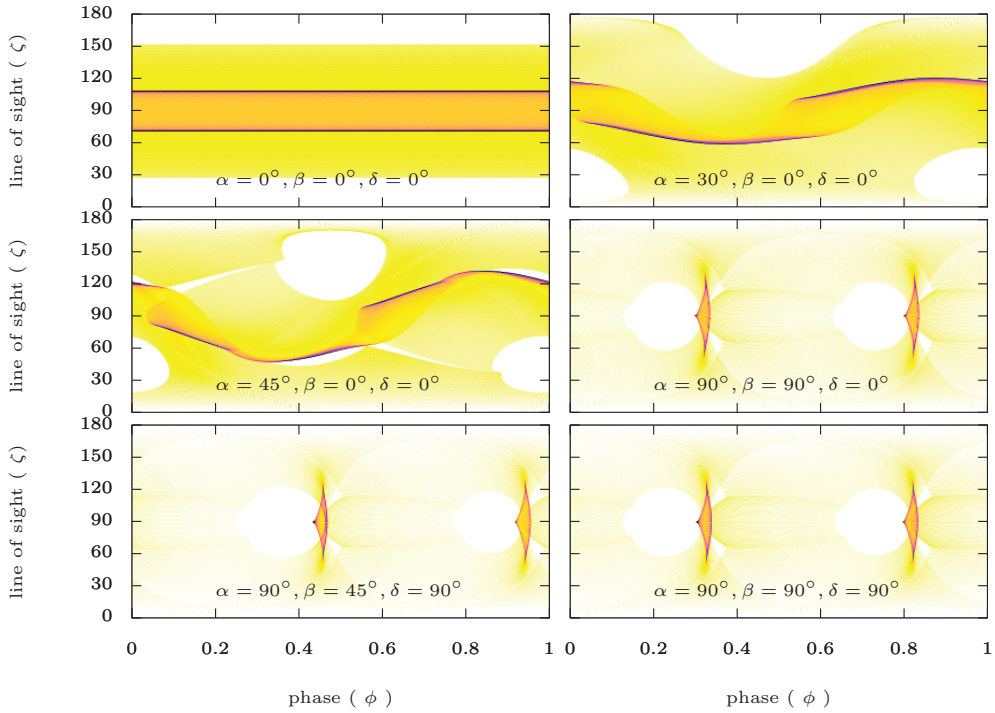

Figure 3-9: High energy emission phase diagrams for the off-centred case with $\epsilon = 0.2$ for various cases for the aberration formula as given by Dyks & Rudak (2003). The white region corresponds to region with no emission and moving towards blue-black via yellow-orange signifies an increase in the photon count.

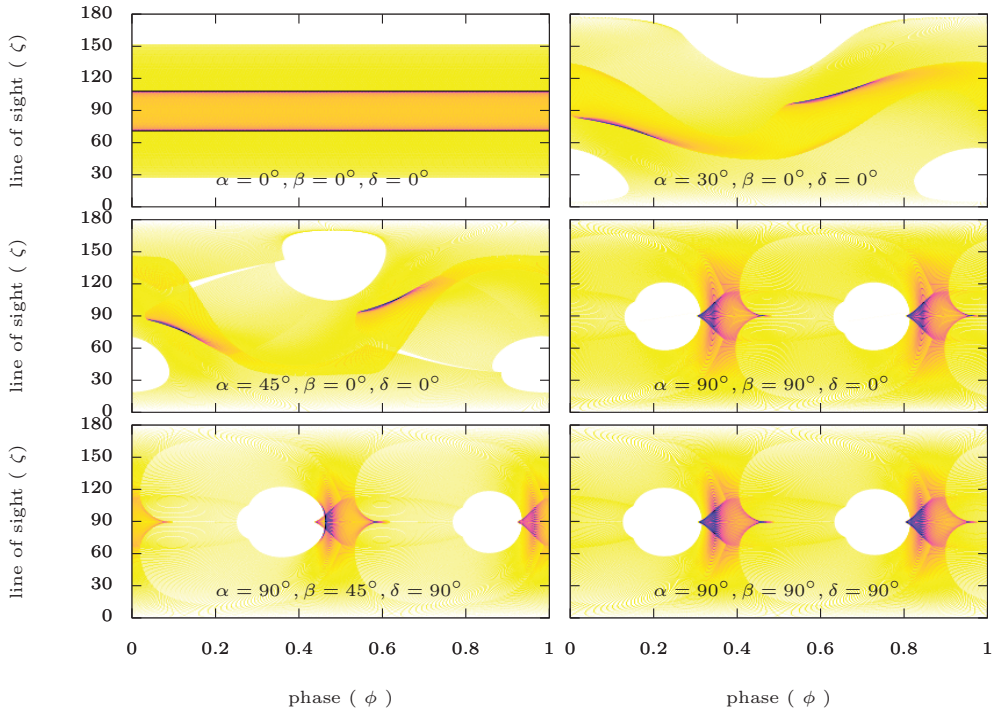

Figure 3-10: High energy emission phase diagrams for the off-centred case with $\epsilon = 0.2$ for various cases for the aberration formula corrected by Bai & Spitkovsky (2010). The white region corresponds to region with no emission and moving towards blue-black via yellow-orange signifies an increase in the photon count.

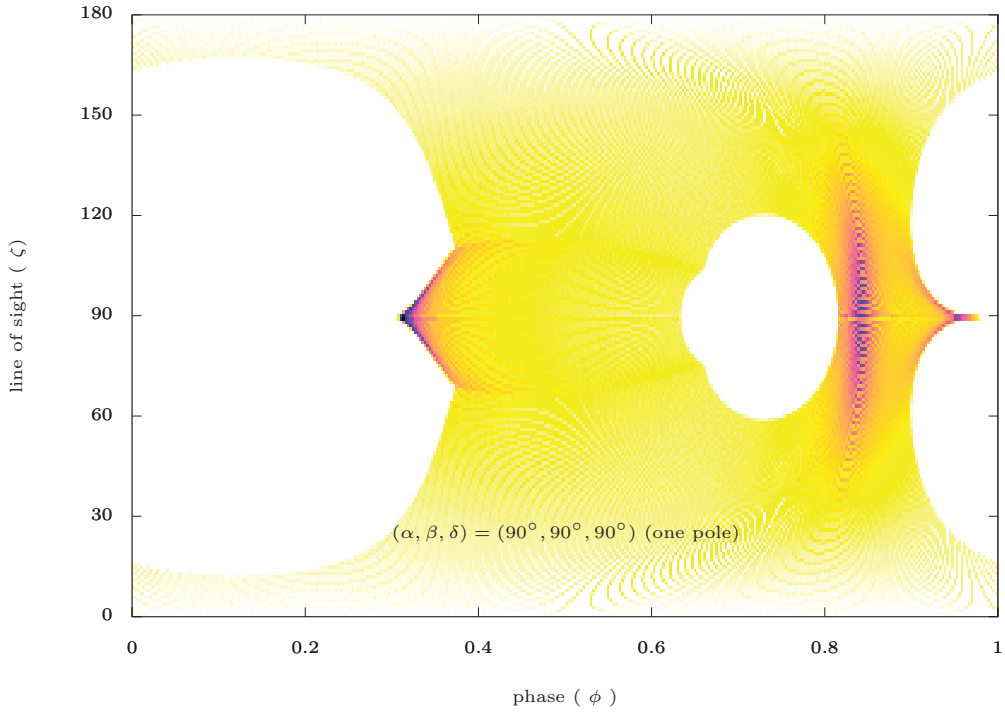

Figure 3-11: High energy emission phase diagram for an off-centred ($\epsilon = 0.2$) case of $(\alpha, \beta, \delta) = (90°, 90°, 90°)$ for one pole. The white region corresponds to region with no emission and moving towards blue-black via yellow-orange signifies an increase in the photon count.

where the result for one pole (on the right; say pole 1) is shown. Calculation of photon count only from pole 1 shows it extending up to the phase of pole 2. Similar behaviour is observed from individual calculations for pole 2. This justifies the sharp peak points noticed in the orthogonal cases.

It is difficult to precisely conclude anything related to the off-centred approach from these phase diagrams because the differences between the two approaches are small. Thus, in the next section we pick out some special geometric configurations to point out the major discrepancies between centred and off-centred dipole but before showing these pulse profiles and light-curves, let's have a look at the phase diagrams for the radio emission.

Current wisdom assumes that radio emission is produced mostly in the vicinity of the polar caps up to altitude of several hundreds of kilometres. These conclusions are drawn from polarization angle studies conducted by several authors; for instance Mitra & Li (2004), Gangadhara & Gupta (2001) and Johnston et al. (2007), where the

shift in the inflexion point of polarization is used to localize the emission site. This statement is generally not true for millisecond pulsars or for the Crab which possess extended collocated radio and high-energy emission and some phase-aligned emission from radio through optical, X-ray up to gamma-ray pulses (Moffett & Hankins, 1996). We focus on this radio emission region by specifying a minimum altitude H_l and a maximum altitude H_u where emission is produced. These distances are measured in spherical coordinates such that the volume of emission is comprised between the radii $r = H_l$ and $r = H_u$.

Before analysing the radio emission phase diagrams for different cases, we show how the emission varies with respect to the height from the surface for a single case of $(\alpha, \beta, \delta) = (90°, 90°, 90°)$ for $\epsilon = 0.2$ in Fig. 3-12. We consider four distinct emission volumes, each of height one stellar radius R, going from the surface up to an altitude which is four times R and look at the emission from those regions. More explicitly, the intervals chosen are $[R, 2\,R]$, $[2\,R, 3\,R]$, $[3\,R, 4\,R]$ and $[4\,R, 5\,R]$. To highlight the boundary of the emission region, we show the rim of each region as a surrounding perimeter in blue. The white region corresponds to region with no emission and moving towards blue-black via yellow-pink signifies an increase in the photon count.

Clearly, the radio emission is in the vicinity of the polar caps and is strongest when considered close to the centre, as assumed in the model we use. The emission decreases in intensity with an increase in altitude. This is because the higher the altitude, more sparse the magnetic field lines and lesser is the photon density as they are spread out over a larger solid angle. For a better understanding, we compare this off-centred case with a simple case of a static dipole and also with the Deutsch field solutions in Fig. 3-13 where we plot the rims of the radio emission region at several heights for all three cases. The red rims are for the static centred dipole case, green rims for the Deutsch solutions without accounting for retardation and aberration while blue rims represent the boundary of emission region for an off-centred case with time delay and aberration effects included. Starting from $H_l = R$ and going until $H_u = 5R$, we notice an increase in size of the rims. Also, for static dipole the rims are symmetric but as soon as we include rotation (Deutsch solutions), an asymmetry

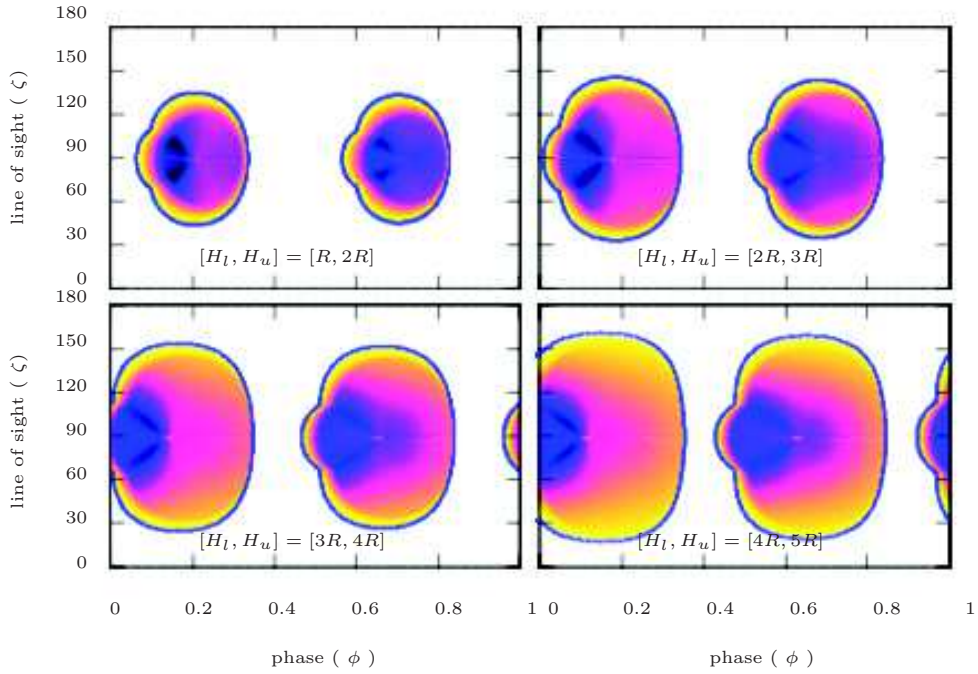

Figure 3-12: Radio emission phase diagrams for several sections of heights between $[H_l, H_u] = [R, 5R]$ for $(\alpha, \beta, \delta) = (90°, 90°, 90°)$ for an off-centred case with $\epsilon = 0.2$. The blue boundary depicts the outer rim of the emission region. The white region corresponds to region with no emission and moving towards blue-black via yellow-pink signifies an increase in the photon count.

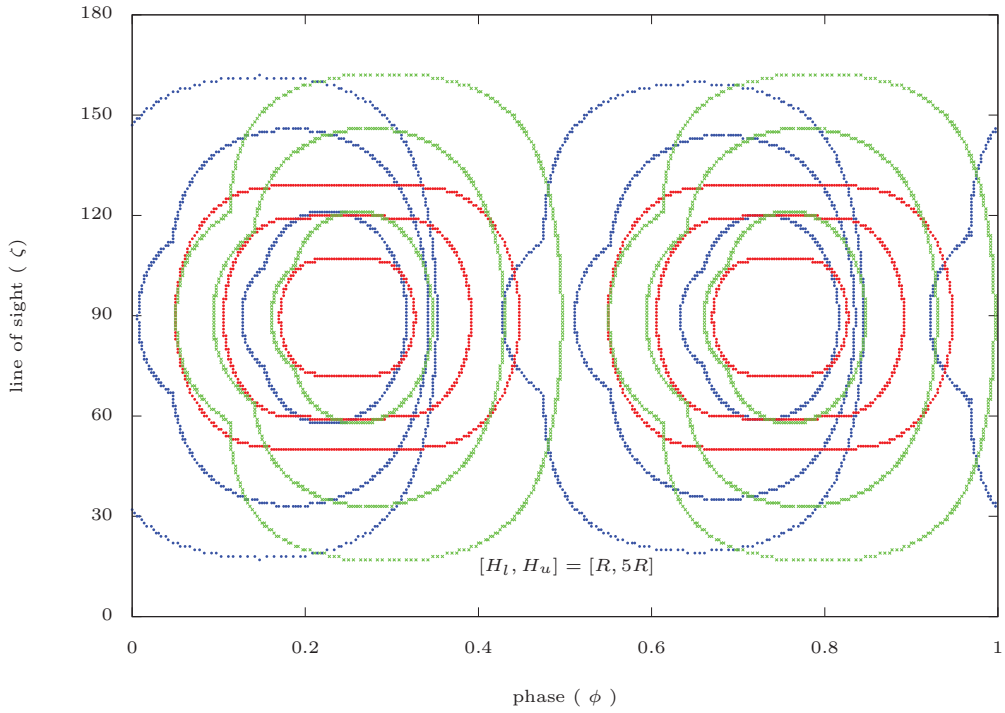

Figure 3-13: Outer rims of the radio emission region for heights $R, 3R, 5R$ (radial distance from centre) for $(\alpha, \beta, \delta) = (90°, 90°, 90°)$. The blue rims are for an off-centred case ($\epsilon = 0.2$) with retardation and aberration effects included, green rims for Deutsch solutions without accounting for retardation and aberration while the red rims correspond to a static centred dipole. The smallest rim correspond to $H_l = R$ and the largest one to $H_u = 5R$. The intermediate rims have been removed for a clear visualisation.

is introduced which is further intensified on inclusion of retardation effects in the off-centred case.

As is clear from the figure, the width of the rim, which is basically an indication of the width of the pulse, increases with an increase in height. This relation between the altitude of emission and pulse width can be easily calculated for a simple orthogonal static centred dipole using following method.

To simplify our discussion, let us assume that photons are emitted in the equatorial plane. As this plane is a symmetry plane, photons are restricted to move in this plane. We set up a polar coordinate system (r, ϕ). The last closed field line is then represented by $r = R_{\rm L} \sin^2\phi = R \sin^2\phi / \sin^2\phi_{\rm pc}$. Photons are emitted in a direction tangent locally to field lines. This tangent vector is defined by

$$\mathbf{t} = \frac{d\mathbf{r}}{ds} \tag{3.12}$$

where $ds^2 = R_{\rm L}^2 \sin^2 \phi\,(3\cos^2\phi + 1)\,d\phi^2$ is the infinitesimal curvilinear abscissa along the last closed field line. Expressing the tangent vector in Cartesian coordinates, the angle of the photon direction with respect to the x-axis becomes

$$\tan\alpha = \frac{t_y}{t_x} = \frac{3\,\cos\phi\,\sin\phi}{3\,\cos^2\phi - 1}. \tag{3.13}$$

The altitude of emission $H = \eta\,R$ is related to the angle ϕ by $H = R_{\rm L}\,\sin^2\phi$ and thus the photon created at a height H is pointing into a direction

$$\tan\alpha_H = \frac{\sqrt{\frac{H}{R_{\rm L}}\,\left(1 - \frac{H}{R_{\rm L}}\right)}}{\frac{2}{3} - \frac{H}{R_{\rm L}}} = \frac{\sqrt{\eta\,a\,(1 - \eta\,a)}}{\frac{2}{3} - \eta\,a} \tag{3.14}$$

where $a = \frac{R}{R_L}$.

A good estimate for the pulse width at an altitude H is therefore $w = 2\,\alpha_H$ or in fraction of the total period α_H/π. If the magnetic moment axis points towards the observer at time $t = 0$ then the radio pulse will be seen starting from time $t = -\alpha_H/\Omega$ up to time $t = \alpha_H/\Omega$.

We make an estimate of the widths using this formula for several values of η and compare it with the numerical values in Table 3.5. All the numerical calculations for the phase plots have been made considering a resolution of 1° which limits the calculation of pulse widths to the same degree of accuracy. The analytical values are in excellent agreement with the numerical values for a static centred dipole. We also show the corresponding values for the Deutsch solutions and for an off-centred case with $\epsilon = 0.2$. The width remains the same for both the poles except in the off-centred case as shown in separate columns where time delay and aberration effects are considered.

There is another important point to be noticed in Fig. 3-12. We notice a shift in the entire emission region which moves towards lower ϕ as we move towards higher heights. For instance, the phase for the interval $[4\,R, 5\,R]$ is shifted to the left (lower ϕ) as compared to that in $[R, 2\,R]$. This shift is also prominent in Fig. 3-13 but only for the retarded off-centred case. For the static dipole case without any delay, the

η	**Static dipole (Analytical)**	**Static dipole (Numerical)**	**Deutsch (Numerical)**	**Off-centred (Numerical)** ($\epsilon = 0.2$)	
				Pole 1	**Pole 2**
1	55.8°	57°	67°	66°	68°
2	81.2°	81°	97°	95°	99°
3	102.7°	103°	121°	117°	121°
4	122.9°	123°	142°	134°	139°
5	143.1°	143°	161°	150°	155°

Table 3.5: Pulse widths for various values of $\eta = H/R$ for an orthogonal static centred dipole (analytical and numerical both), for Deutsch fields (numerical) and for both poles an off-centred case with $\epsilon = 0.2$ (numerical). The width is same for both the poles in the former two cases and hence, not mentioned separately. The retardation and aberration effects are considered only in the latter case.

geometrical centre of the rim is observed to remain fixed for all heights. This indicates that this shift in phase with heights is affiliated to time delay effects because of the term $-\mathbf{r} \cdot \hat{\boldsymbol{\eta}}/R_L$ discussed in Eqn. (2.25).

This behaviour is explained geometrically in Fig. 3-14 (Dyks & Rudak, 2002). The figure is not to scale and is only used for a rough approximation. In the figure, a 2D representation of the equatorial plane is shown with the z-axis pointing in the plane of paper. O is the geometrical centre of the pulsar, a part of whose surface is shown with a black solid line. The curved black arrow represents the anti clockwise direction of the rotation of the pulsar. The blue vector is the direction of the magnetic moment axis (not necessarily perpendicular to the surface as shown) and the blue solid curved lines are two magnetic field lines under consideration. The magnetic field line which is labelled as 1 is responsible for the leading peak of emission while 2 is the corresponding trailing emission peak.

Now, we study the path of the photon propagation along these two field lines. We consider photons at three different points a, b and c on the field lines in increasing order of heights (radial distance from the geometric centre of the pulsar). Without aberration, the red dashed line is the direction of the photon propagation which is nothing but the tangent at the point of consideration. Now, as the pulsar rotates, the aberration effects influence the direction of photon travel as observed by an observer.

Considering the observer is looking in the x direction (shown with small black solid arrows), the photon propagation in an observer's frame is shown as red solid arrows. The observer tends to observe the photon a bit earlier than it would have been observed if the pulsar were not rotating.

The angle ϕ represents the phase of the photon with the first subscript indicating the field point considered for the emission of a particle and the second subscript mentioning the field line considered. For instance, for the leading peak, the photon at point a has phase ϕ_{a1}. As evident from the figure geometry, $\phi_{a1} > \phi_{b1} > \phi_{c1}$ which implies that as we move higher, the phase ϕ decreases which justifies the shift observed towards lower ϕ with increasing height in Fig. 3-12 and also in Fig. 3-13 for the leading peak. And, for the trailing peak, we notice the opposite i.e. $\phi_{a2} < \phi_{b2} < \phi_{c2}$, which is apparent in Fig. 3-13 where the trailing edge of emission has higher ϕ for higher heights.

Next we consider the full emission volume starting from $H_l = R$ up to $H_u = 5R$ for calculating the radio emission phase diagrams.

Fig. 3-15 presents the phase diagram for the radio emission for the same parameters used as for the high energy emission in Fig. 3-10. There are some discontinuities which are quite apparent in some cases like a strange line in the equatorial region for the orthogonal case. It persists for several different samplings considered to calculate the emission. However, we intend to apply more uniform sampling in the future to improve the results even further.

We see the emission regions clearly complement the high energy emission regions that is emission is almost only within the polar caps contrary to high energy. We have considered emission starting from the surface of the pulsar going to a height which is five times its radius. The emission slowly decreases in intensity as we move away from the centre of the polar cap because photons are spread in wider directions when moving away from the polar cap centre. It is interesting to notice that the emission is not identical for the two poles which is affiliated to the retardation effects. However, aberration can usually be neglected for photons produced in the vicinity of the neutron star surface.

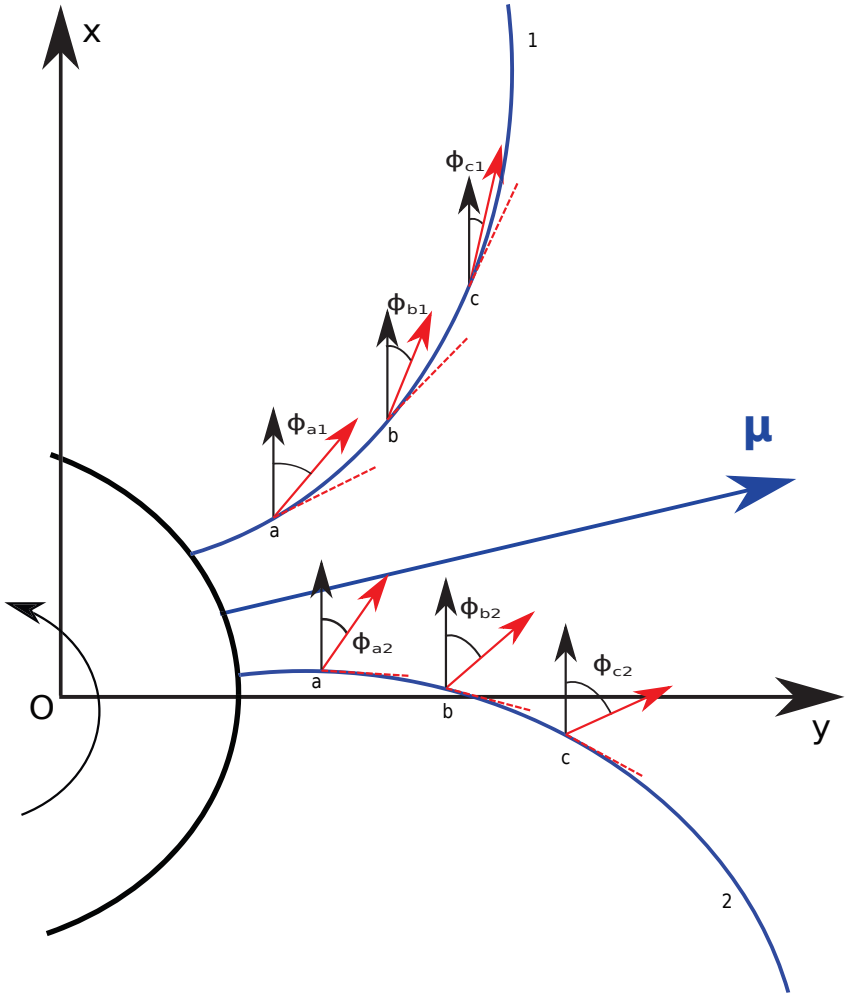

Figure 3-14: 2D representation of the equatorial plane for the off-centred geometry with $(\alpha, \beta, \delta) = (90°, 90°, 90°)$ to show the phase of the photon propagation direction. z-axis is pointing in the plane of paper. O is the geometrical centre of the pulsar, a part of whose surface is shown as black solid line. The curved black arrow represents the anti clockwise direction of the rotation of the pulsar. The blue vector is the magnetic moment axis and the blue solid curved lines are magnetic field lines; the one labelled as 1 is the field line corresponding to leading peak while 2 is the same for the trailing peak. a, b and c are the three points on the field lines in increasing order of heights (radial distance from the geometric centre). The red dashed line represents the direction of the photon propagation at any instant without time delay or aberration effects while the red solid arrow represents the direction of the path followed by photon as seen by an observer when these effects are included. ϕ is an indication of the phase for the photon propagation with subscripts describing the point and the field line. Figure not to scale and provide only a rough depiction.

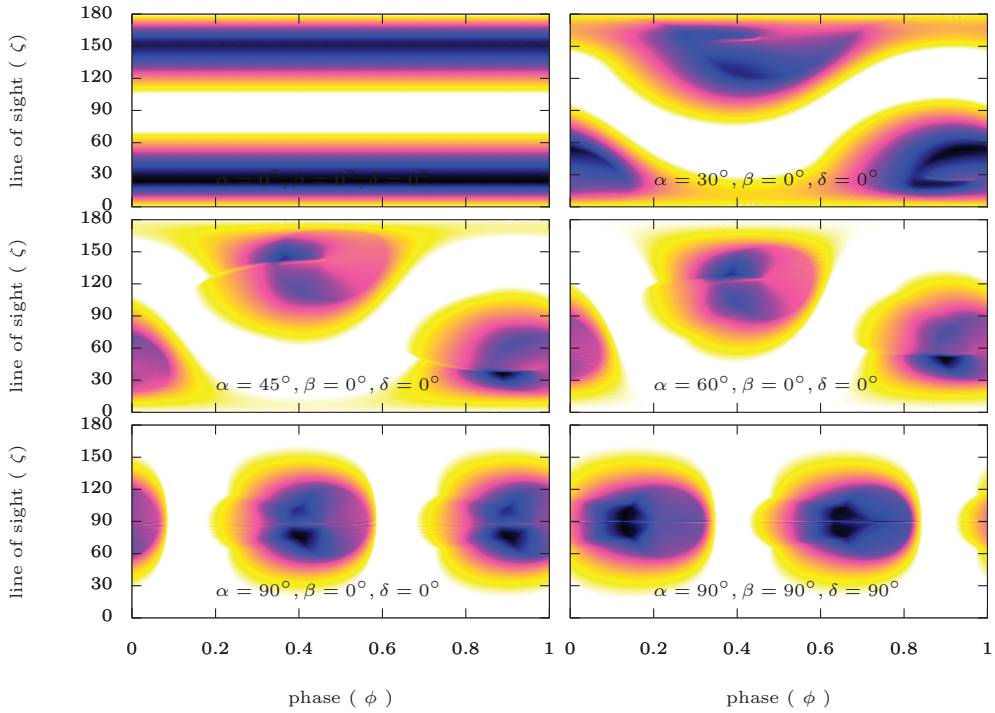

Figure 3-15: Radio emission phase diagrams for the off-centred case with $\epsilon = 0.2$ for various cases. The white region corresponds to region with no emission and moving towards blue-black via yellow-orange signifies an increase in the photon count.

3.5.5 Radio and high energy emission light curves

Two dimensional phase plots give full information about the emission patterns but they render the direct comparison between the centred and the off-centred cases difficult. In order to better assert the phase shift between both geometries, we extract specific light-curves and radio pulse profiles overlapping both topologies on a same graph.

To be able to do so, we need to choose a particular line of sight to see how the photon intensity varies over the whole range of ϕ with it. The intensities have been normalized to unity for an easy comparison.

The light curves for high energy and radio regimes for $(\alpha, \beta, \delta) = (30°, 0°, 0°)$ with $\epsilon = 0$ (in red) and $\epsilon = 0.2$ (in blue) for various lines of sight (ζ) are shown in Fig. 3-16. The angles of the line of sight ζ are chosen in a range between 20° and 50° in (a) and between 130° and 160° in (b) in steps of 10° each. We also show another case with $(\alpha, \beta, \delta) = (90°, 90°, 90°)$ in Fig. 3-17 with ζ ranging between 80° to 110°. The high energy emission curves are represented in solid lines and the radio emission curves in dashed lines. All the curves are normalized in terms of intensity. The normalization factor chosen for the radio and high energy emission is the maximum photon count corresponding to each of those cases separately.

A quick look at Fig. 3-16 reveals that the radio emission and the high energy emission complement each other. The former peaks in the vicinity of the polar regions which is in accord with the current models based on the assumption that radio emission is produced exclusively near the polar caps while the latter peaks where radio emission is at its lowest.

For $\zeta = 20°$, the radio emission peak for the off-centred case is higher in intensity than that for the centred case. As we move towards higher ζ in Fig. 3-16(a) we notice there is a switch between them. The fact that the radio emission peaks at a lower ζ for the off-centred case while at a higher value for the centred case actually denotes a shift in the polar cap as the emission region for the radio regime lies in the proximity of the polar caps. This highlights the shift associated with the difference in

two geometries as discussed in Section 3.5.1. A similar shift in the polar cap geometry is seen for the other pole centred at about $\zeta = 160°$ in Fig. 3-16(b).

Apart from the expected shift in phase for both the emission regimes between the centred and off-centred case, we notice that the pulse width is also varying. These pulse widths give us an estimate of the size of the polar cap. For instance, in Fig. 3-16(a), the width of the 'dip' in the high energy curves decreases as we move from $\zeta = 20°$ to $\zeta = 50°$. Based on our current understanding of high energy emission, we know that the emission is concentrated in regions closer to the light cylinder (inside or outside) than to the surface of the star because of the spectral sub-exponential cut-off in the GeV range as reported by the Fermi/LAT collaboration (Abdo et al., 2013). Opacity in a strong magnetic field as the one present in the polar cap model of Ruderman & Sutherland (1975) would lead to a super-exponential cut-off not seen in gamma-rays. Moreover, recent pulsed TeV photons detection from the Crab pulsar (Ansoldi et al., 2016) suggests even another mechanism of radiation, for instance inverse Compton or synchrotron self-Compton from outer parts of the magnetosphere (Hirotani, 2007) or even from the wind (Mochol & Petri, 2015). High-energy emission is minimum at poles which means, that this dip can give us, at least a rough estimate of the differences in the size of the polar caps between the centred and the off-centred case. In part (b) of the same figure we notice the polar cap getting widened (i.e. the high energy emission dip increasing) as we move from $\zeta = 130°$ to $\zeta = 160°$ for both, the centred and the off-centred case with the width increasing more for the latter as compared to the former. These differences in the widths of the dips of the high energy emission signifies the difference in the size of the polar caps between the two geometries which we highlighted in Section 3.5.1.

We also plot the orthogonal case in Fig. 3-17 for $\zeta = 80°$ to $\zeta = 110°$ where $\zeta = 90°$ is for the equatorial plane containing both the poles for this inclination. Looking at ζ's in vicinity of the equatorial plane enables us to look at the emission from both the poles considering one line of sight and hence, we see two peaks of radio emission, one from each pole, with a phase difference of around 180° between them. Similarly, two high energy emission peaks from two opposite sides of the light cylinder lying

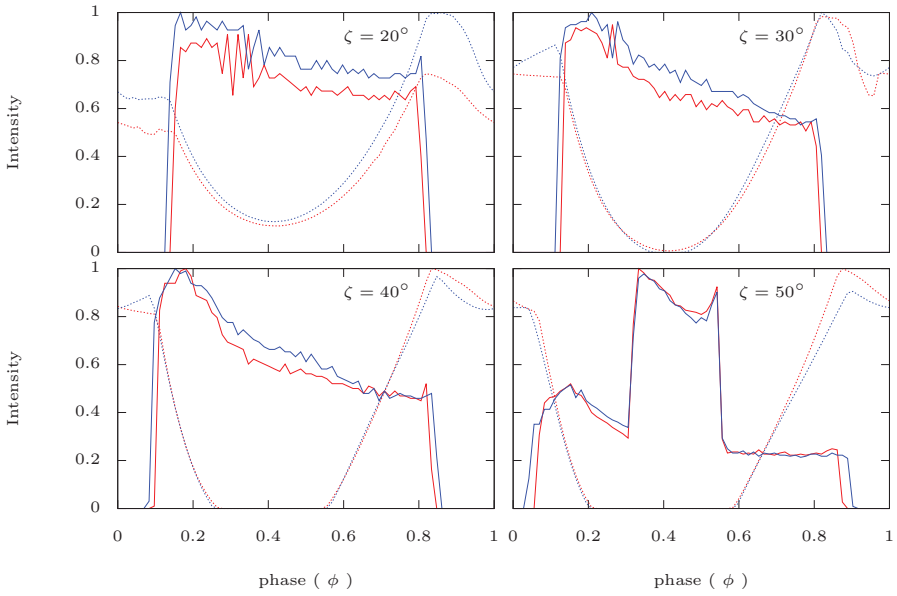

(a) $\zeta = 20^\circ\ , 30^\circ\ , 40^\circ\ , 50^\circ$

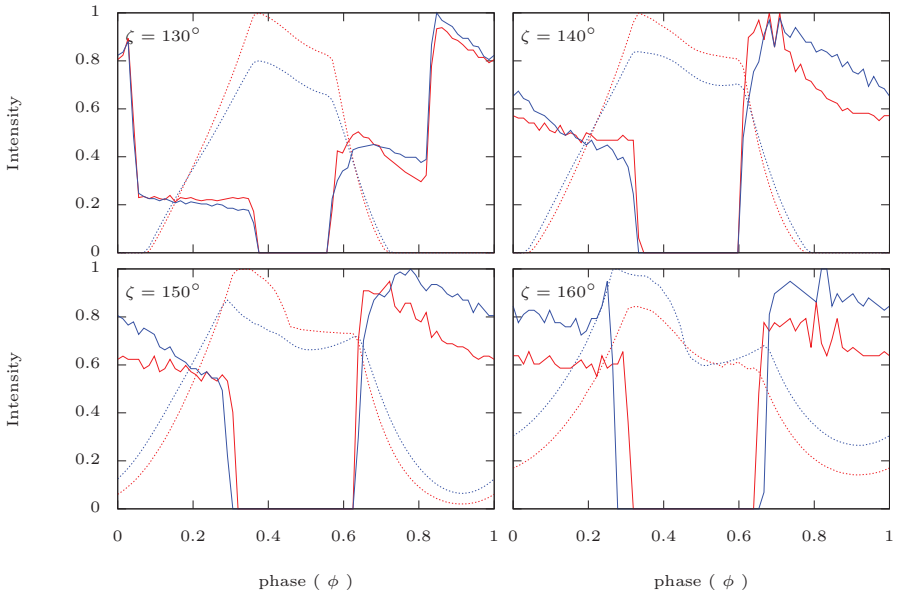

(b) $\zeta = 130^\circ\ , 140^\circ\ , 150^\circ\ , 160^\circ$

Figure 3-16: High energy and radio emission light curves for $(\alpha, \beta, \delta) = (30^\circ, 0^\circ, 0^\circ)$ for the centred case ($\epsilon = 0$, in red) and the off-centred case ($\epsilon = 0.2$, in blue) for various line of sights (ζ). In (a) we have ζ ranging from 20° to 50° and (b) has ζ from 130° to 160° in steps of 10° each. The high energy emission curves are represented in solid lines and the radio emission curves in dashed lines.

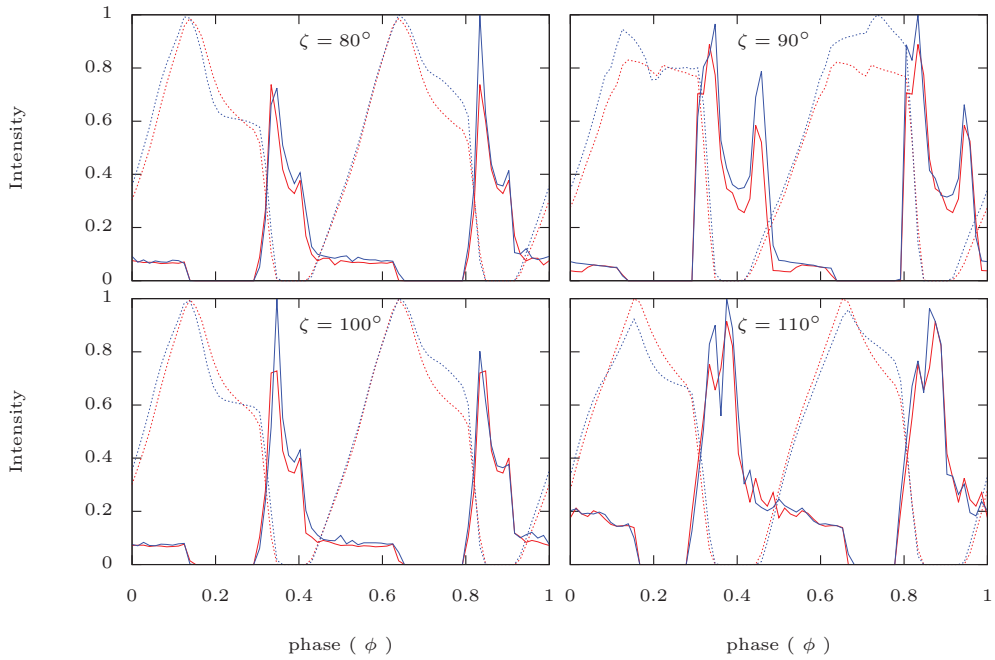

Figure 3-17: High energy and radio emission light curves for $(\alpha, \beta, \delta) = (90°, 90°, 90°)$ for the centred case ($\epsilon = 0$, in red) and the off-centred case ($\epsilon = 0.2$, in blue) for various line of sights ($\zeta = 80°$, $90°$, $100°$, $110°$). The high energy emission curves are represented in solid lines and the radio emission curves in dashed lines.

orthogonal to the location of the poles are prominent.

From an observers point of view, the light curves hold significance when the emission peak is considered to be the point corresponding to zero phase. It would be convenient to compare the results with observational data if we consider plotting the phase zero light curves. With light curves already available, it is not too difficult to generate phase zero light curves. To make it so, the phase corresponding to each radio emission peak i.e. the location of the maximum intensity of the emission, is put as a reference phase zero and the rest of the curve is shifted accordingly. For the same inclination geometries discussed above, the corresponding phase zero light curves are plotted in Fig. 3-18 and Fig. 3-19 with the colour scheme and other parameters being the same as for above light curves.

In Fig. 3-18 we see the phase lag between the radio emission peak and high energy emission peak varies for both the centred and the off-centred cases as we move to higher ζ's. It might be of interest to note that in (a) part of the figure, the phase

difference between the radio and high energy emission peak decreases with increase in angle of line of sight for both the geometries but comparing them closely reveals that it is faster for the centred case, implying the lag between the radio and high energy emission peaks stays for a longer range of ζ in the off-centred geometry. While in part (b) of the same figure, the phase difference increases with the angle of line of sight with a faster increase with respect to ζ in the off-centred geometry.

The phase zero light curves for the orthogonal geometry are shown in Fig. 3-19 which contrast the difference between the centred and off-centred cases clearer than the light curves for the same geometry discussed earlier. We hope to extract more conclusions by comparing the results with observational data at some later stage.

3.6 Conclusions

We extend the radio and high-energy pulsed emission properties of the rotating dipole to an off-centred rotating dipole. The off-centred topology is a reliable approach trying to better fit the broadband spectrum of pulsar radiation and the associated phase-resolved polarisation.

Comparing the polar caps shapes from our approach with the prevalent standard one shows a shift highlighting the difference in size of the polar caps between the two cases and also a phase difference establishing the presence of a time lag between the radio and high energy emission photons. This could explain observational signatures of time lags.

Study of the emission mechanisms with the phase diagrams for the radio and the high energy emission gives strong hints about the site of production of pulsed radiation which could give a better insight in our understanding of the emission mechanism. Also, a comparison of the emission light curves shows phase contrasts between the radio and high-energy profiles for the two geometries. We expect to extract more understanding from the results in the future while making a comparison with observational data.

Also, even more constraints could be gained for the emission mechanisms by in-

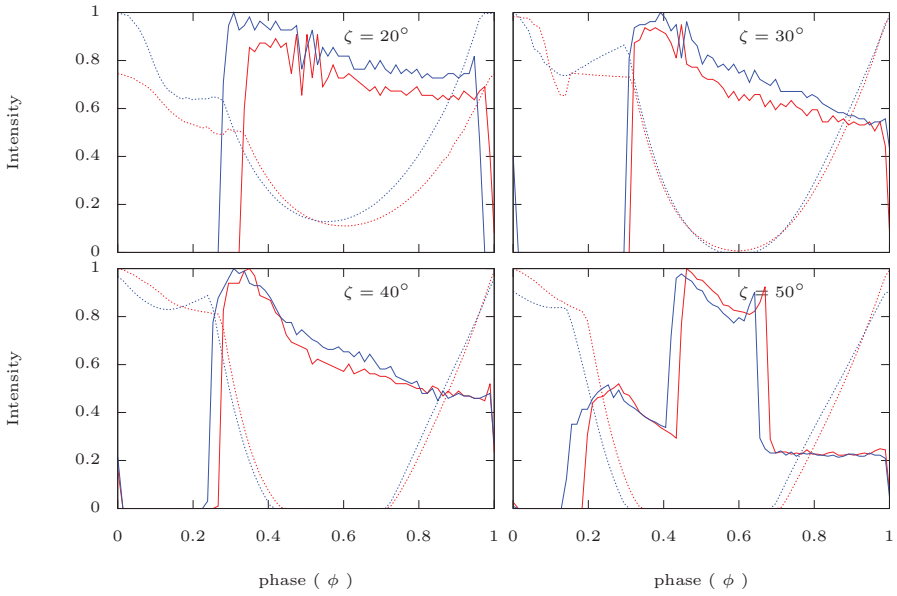

(a) $\zeta = 20^\circ\ , 30^\circ\ , 40^\circ\ , 50^\circ$

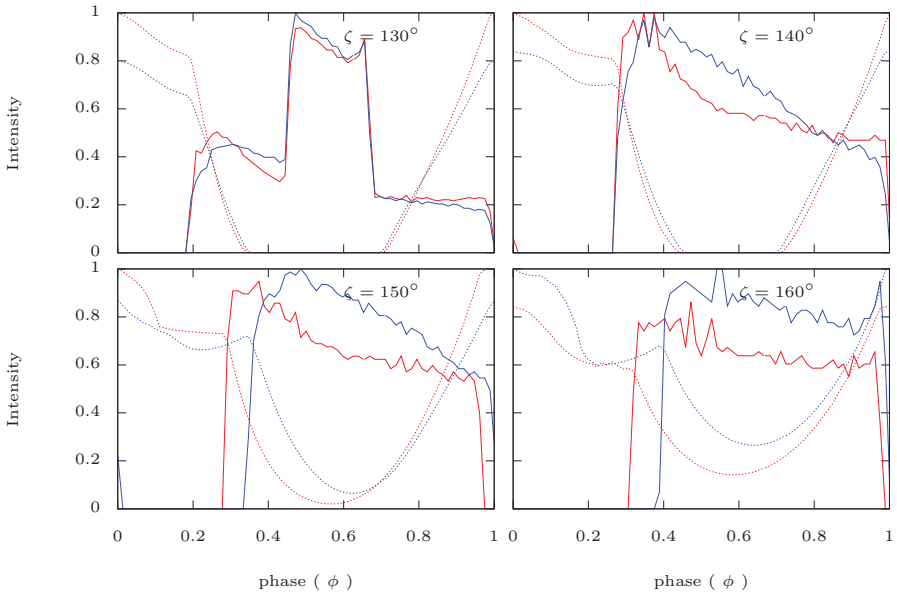

(b) $\zeta = 130^\circ\ , 140^\circ\ , 150^\circ\ , 160^\circ$

Figure 3-18: High energy and radio emission light curves with zero phase considered to be the phase of the peak of radio emission for $(\alpha, \beta, \delta) = (30^\circ, 0^\circ, 0^\circ)$ for centred case ($\epsilon = 0$, in red) and off-centred case ($\epsilon = 0.2$, in blue) for various line of sights (ζ). In (a) we have ζ ranging from 20° to 50° and (b) has ζ from 130° to 160° in steps of 10° each. The high energy emission curves are represented in solid lines and the radio emission curves in dashed lines.

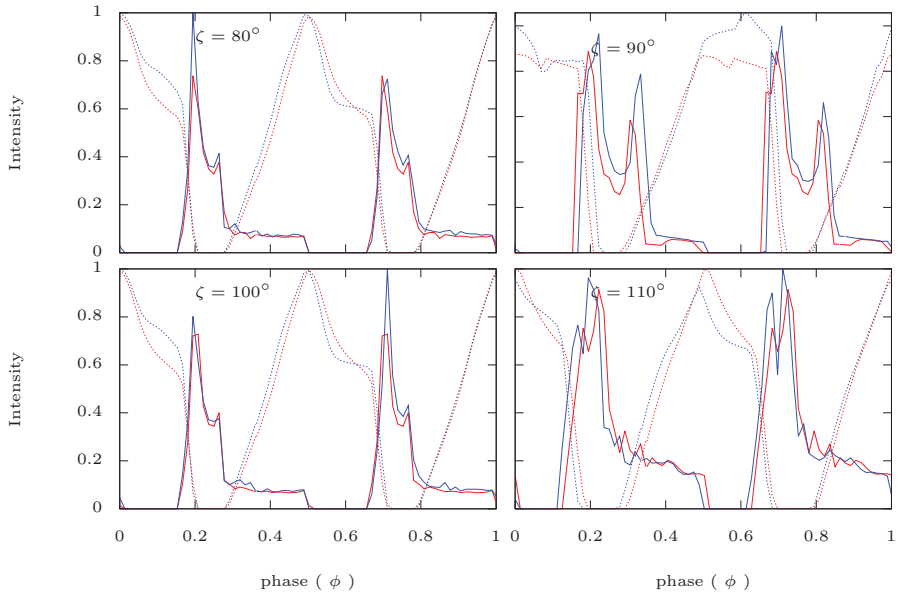

Figure 3-19: High energy and radio emission light curves with zero phase considered to be the phase of the peak of radio emission for $(\alpha, \beta, \delta) = (90°, 90°, 90°)$ for the centred case ($\epsilon = 0$, in red) and the off-centred case ($\epsilon = 0.2$, in blue) for various line of sights ($\zeta = 80°$, $90°$, $100°$, $110°$). The high energy emission curves are represented in solid lines and the radio emission curves in dashed lines.

spection of the polarization features of an off-centred dipole (Petri, 2017b). Our next goal would be a detailed and accurate analysis of phase-resolved polarization using this approach in a vacuum. We plan also to extend our study to a pulsar force-free magnetosphere.

Chapter 4

Emission by curvature radiation

4.1 Introduction

Pulsars emit in a broad wavelength domain. Any change in frequency, and hence energy, is echoed by the emission in the corresponding wavelength. This behaviour is apparent in the shape of the light curves which are consequently modified. A study of the light curves over a range of frequencies could reveal significant information regarding the distribution of particles in physical space, as well as, in energy space. The former is handy in uncovering the geometrical features of the field lines while the latter provides valuable insights on the particle behaviour in the magnetosphere. Up until now, not many studies have focused on self consistent resolution of light curves based on their frequency dependence. Recently, Venter et al. (2017) presented a brief discussion on example light curves due to curvature emission, as a first approach and predicting that it could help in ensuring the responsible emission mechanism for different emission wavelengths.

In Chapter 3, we studied radio and high energy emission without resolving the curves based on the frequency of emission of the particles. They are usually referred to as 'frequency integrated' profiles. However, since the multi wavelength observations are well available resolved in frequencies and energy, it is a good idea to resolve the light curves from the models and see how they compare with the observations. In this chapter, we will be using curvature radiation as the emission mechanism to find

out the frequency and the corresponding power emitted by each particle under consideration. Once the information on frequency and power is known, the propagation of the particle within the magnetosphere is followed.

It is worth mentioning that a substantial time of the thesis work under this chapter was devoted to the calculation of the curvature using the Bai & Spitkovsky (2010) aberration method. We succeeded to do it for the one used by Dyks & Rudak (2003) but considering the amount of time available, we decided to stop using calculations of the curvature using the latter study. This made us aware that the calculation of the curvature using the first approach is tricky. And hence, this chapter is still a work in progress where we still need to look into the subtle approach to calculate the frequency resolved emission (ultimately) for the other approach. Because our estimation of time needed to calculate the curvature was not as short as we guessed, this chapter can be seen as the initiation of a study which is yet to be completed. However, we still discuss everything needed to make the calculations and present the results we already have of the portion we have finished in proper detail.

We start by defining curvature and the necessary reference frame used to make the calculations to find curvature in Section. 4.2. In Section. 4.3, the emission by curvature radiation has been discussed with derivations of the involved formulae and finally, in Section. 4.4 the frequency resolved high energy and radio emission have been studied thoroughly in their corresponding subsections. For sake of brevity inside the chapter, various results have been put in Appendix B to complete a proper atlas of our study.

4.2 Curvature

To understand the curvature radiation process, there is an important quantity called curvature which needs to be discussed first. In simple terms, curvature is a measure of the extent by which a curve deviates from a straight line or a curved surface deviates from a flat plane. There are a number of ways to precisely define the curvature.

Considering a purely geometrical point of view. The curvature of a straight line

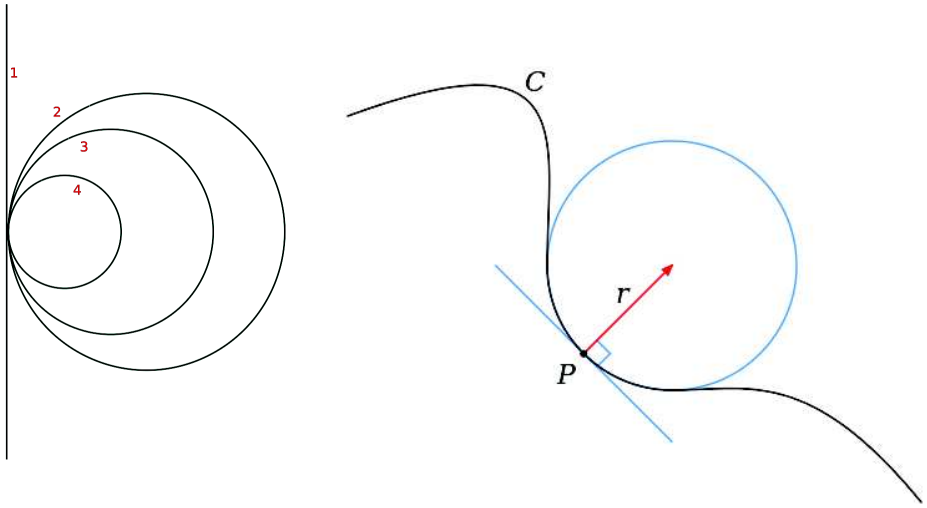

(a) (b)

Figure 4-1: (a) The straight line marked as 1 has zero curvature. Moving from larger to smaller circle, i.e. from 2 to 3 to 4, the curvature increases. This intuitively implies that curvature of a circle is inversely proportional to its radius. (b) Osculating circle (in blue) for a curve C at point P (Cepheus, 2006)

is naturally zero. Also, the larger the deviation of a curve from being a straight line, the larger is the curvature. For instance, in Fig. 4-1 (a), the straight line is marked as 1 and has zero curvature. The circle marked as 2 deviates from 1 (curved away from 1) by a lesser extent than circle marked as 4. Since, the radius of circle 2 is larger than that of 3 and 4, we can safely imply that the curvature of a circle, in general, is inversely proportional to its size, or its radius. Thus, the curvature κ of a circle is defined to be the reciprocal of its radius R. Another way to look at it is to see a straight line as a circle of infinite radius, and hence the inverse relation gives zero curvature.

$$\kappa = \frac{1}{R} \tag{4.1}$$

Now, for a curve of any shape, say curve C in Fig. 4-1 (b), curvature at point P could be found by constructing a unique circle or line which most closely approximates the curve near P, the osculating circle at P (in blue in the figure). The curvature of this curve at point P is then the curvature of this circle, hence $1/r$ as per the figure where r is the radius of the osculating circle, also called *radius of curvature*. However,

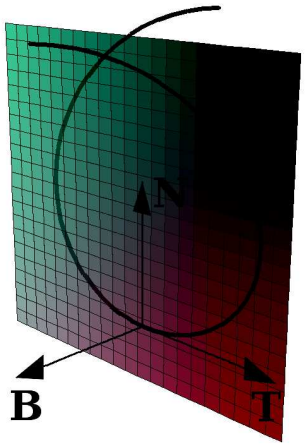

Figure 4-2: The tangent vector **T**, normal vector **N** spanning the osculating plane (coloured grid plane) for the curve shown. **B** is the binormal vector perpendicular to the osculating plane. (Alba, 2007).

it is only valid for a $2D$ geometry. For a $3D$ perspective, we need to consider a couple of physical quantities associated with the trajectory of the particle. This is explained below.

From a physical point of view, the curvature can be defined in a more general way and hence, expressions to derive curvature for any given curve could be calculated. The approach begins with considering a physical particle moving along the curve. Mathematically, there is a frame called *Frenet-Serret frame* which is generally used to describe the kinematic properties of a particle moving along a curve in Euclidean space; we explain it here to simplify the understanding.

Let $\mathbf{r}(t)$ be a curve, also representing the position vector of the particle moving along it as a function of time t. The velocity vector and the acceleration vector for the particle are, thus, represented as $\mathbf{r}'(t)$ and $\mathbf{r}''(t)$ respectively. For simplification, the curve is parametrized in terms of its arc length $s(t)$ which represents the length of the curve, or arc, which the particle has covered while moving along the curve in time t with respect to an assumed reference point on the curve, or trajectory of the particle. Here t is a function of s and hence, we can easily write $\mathbf{r}(s) = \mathbf{r}(t(s))$. Now, with all the ingredients available to define the Frenet-Serret frame, its construction is described below :

- $\mathbf{T}$ is the unit vector tangent to the curve, pointing in the direction of motion

$$\mathbf{T} = \frac{d\mathbf{r}}{ds} \tag{4.2}$$

- $\mathbf{N}$ is the normal unit vector, the derivative of $\mathbf{T}$ with respect to the arc length parameter of the curve s, divided by its length

$$\mathbf{N} = \frac{d\mathbf{T}}{ds} \tag{4.3}$$

- $\mathbf{B}$ is the binormal unit vector, perpendicular to both $\mathbf{T}$ and $\mathbf{N}$ which are always perpendicular to each other (by definition), hence $\mathbf{B}$ is always normalized,

$$\mathbf{B} = \mathbf{T} \times \mathbf{N} \tag{4.4}$$

All the above quantities are illustrated in Fig. 4-2 where the coloured grid plane is the osculating plane described as the linear span of the tangent and normal vectors where $\mathbf{T}$, $\mathbf{N}$ and $\mathbf{B}$ form an orthonormal basis. The Frenet-Serret formulae are:

$$\frac{d\mathbf{T}}{ds} = \kappa\mathbf{N} \tag{4.5}$$

$$\frac{d\mathbf{N}}{ds} = -\kappa\mathbf{T} + \tau\mathbf{B} \tag{4.6}$$

$$\frac{d\mathbf{B}}{ds} = -\tau\mathbf{N} \tag{4.7}$$

where $\kappa = \|ds/d\mathbf{T}\|$ is the curvature, and τ is the torsion of the curve. Intuitively, curvature measures the failure of a curve to be a straight line, while torsion measures the failure of a curve to be planar. Using the above equations, curvature is calculated as

$$\kappa(t) = \frac{\|\hat{\mathbf{T}}'(t)\|}{\|\mathbf{r}''(t)\|} \tag{4.8}$$

where $\hat{\mathbf{T}}'(t)$ is the derivative of the unit tangent vector $\mathbf{T}$ which is defined in

Eqn. 4.2, the difference being that here t is used instead of the parametrized arc length s. Using the above equations, the explicit expression for curvature, finally, is

$$\kappa = \frac{\|\mathbf{r}'(t) \times \mathbf{r}''(t)\|}{\|\mathbf{r}'(t)\|^3} \tag{4.9}$$

The above scheme is true for any $3D$ curve. Now, switching to planar curves : For a curve which is parametrized in *Cartesian coordinates* as $r(t) = (x(t), y(t))$, the curvature, using Eqn. 4.9, is

$$\kappa = \frac{|x'y'' - y'x''|}{(x'^2 + y'^2)^{3/2}} \tag{4.10}$$

where primes refer to derivatives d/dt.

Similarly, for a curve in *polar coordinates* as $r(\theta)$, the curvature is,

$$\kappa(\theta) = \frac{|r^2 + 2r'^2 - rr''|}{(r^2 + r'^2)^{3/2}} \tag{4.11}$$

Calculating curvature for static dipole solutions : As a good exercise, and to confirm our approach to calculate the curvature, we checked the curvature for the simple case of the solution of a static dipole in vacuum. To calculate the curvature for the static dipole solutions numerically, the central difference derivative technique is used. In this technique, to calculate the second derivative at a particular point, say i; we consider two points $i-1$ and $i+1$ at similar distance from i and calculate the tangent at these points which assists us in calculating the second derivative at i. The distance between i and other two points is the arc length ds of the magnetic field line. We use Eqn. 2.27 (Section 2.4) to find the tangent vector at points $i-1$ and $i+1$ to be $\mathbf{T}_{i-1}$ and $\mathbf{T}_{i+1}$ respectively. To calculate the second derivative at point i, $\mathbf{T}'_i$ (derivative of the unit tangent vector $\mathbf{T}$), we use the central finite difference technique, which is

$$\mathbf{T}'_i = \frac{\mathbf{T}_{i+1} - \mathbf{T}_{i-1}}{2ds} \tag{4.12}$$

Substituting Eqn. 4.12 in Eqn 4.8, we have the curvature for the field line.

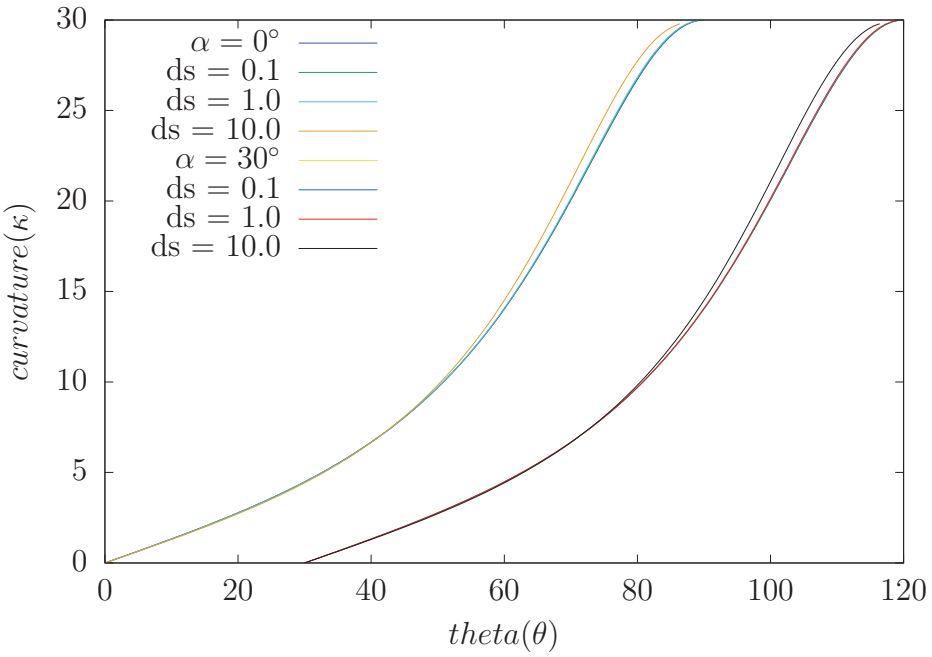

Figure 4-3: Curvature for static dipole vacuum solutions for the radius of star $R = 0.1R_L$ where $R_L = 1.0$. The $x - axis$ and $y - axis$ represent polar angle (θ) and curvature κ of the magnetic field line. Two orientations are considered, $\alpha = 0°$ and $\alpha = 30°$. In the legend, key $\alpha = 0$ represent analytical case for $\alpha = 0°$ and the three keys following it with different values of arc length (ds in terms of percentage of R) are the numerical results. Same four keys are for $\alpha = 30°$.

The analytical curvature for a static dipole is easy to calculate. The equation for the magnetic field line for an aligned dipole can be represented analytically by considering a sphere of radius R_* as

$$r(\theta) = \lambda \sin^2\theta = R_* \frac{\sin^2\theta}{\sin^2\theta_*} \tag{4.13}$$

Using Eqn. 4.13, $r' = 2\lambda \sin\theta\cos\theta$ and $r'' = 2\lambda(2\cos^2\theta - 1)$ in Eqn. 4.11, the curvature is

$$\kappa = \frac{3\sin\theta(1+\cos^2\theta)}{r(1+3\cos^2\theta)^{3/2}} \tag{4.14}$$

The numerically calculated curvature (Eqn. 4.12, Eqn 4.8) and the analytically calculated curvature (Eqn. 4.14) for the static dipole has been compared in Fig. 4-3 for the radius of star; $R = 0.1R_L$. Two orientations are considered, $\alpha = 0°$ and $\alpha = 30°$, where α is the angle between the rotation and the magnetic dipole axis. In

the legend, key $\alpha = 0$ represents the analytical case for $\alpha = 0°$ and the three keys following it with different values of arc length (ds in terms of percentage of R) are the numerical results. Same four keys are for $\alpha = 30°$. We see that the curvature for $\theta = 0$ is 0 which is expected as the lines originating at this angle tend to move straight up; and as we move towards higher θ, the curvature keeps increasing as magnetic field line becomes more and more curved. Also, we notice that for smaller arc lengths, the analytical and numerical plots coincide to a great accuracy. The only case where $ds = 0.1R$ is the one where the analytical results deviate from the numerical case, which is expected, since greater the arc length considered for integration of magnetic field lines, lower is the resolution and higher becomes the error. We also checked the same characteristics for the radius $R = 0.01R_L$ and found exactly the same inferences in the plots. This concludes that as long as the value of arc length for integration is considered within reasonable limits, our approach gives accurate results for any radii.

4.3 Curvature radiation

For strong curved magnetic field lines, the relativistic particle moving along the field line, would be accelerated transversely to emit curvature radiation. It was briefly discussed in Section 2.1.3. Now, we present a detailed mathematical study of the curvature radiation (reviewed by Longair (2011)).

Consider a particle moving with a relativistic velocity v and emitting radiation as it moves along the curved field line. The path of the particle is represented in Fig. 4-4 as AB where A is the initial position. Let the distance between point A and observer be R, which means that the radiation emitted from A reaches the observer at time R/c. Now, the distance between point A and B is L, so the time taken by the particle in reaching B from its initial position is L/v. The radiation from B needs to travel a distance $R - L$ to reach the observer, which, therefore, it does in time $(R - L)/c$. Hence, the observer receives the radiation from B at time $L/v + (R - L)/c$. The

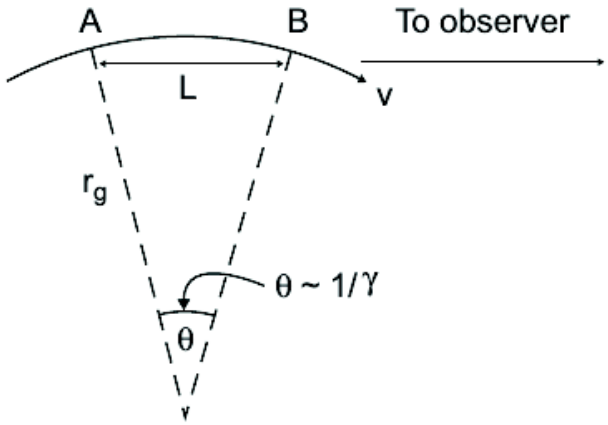

Figure 4-4: The geometry of the path of a particle moving from A to B with velocity v during the time when the beamed radiation is observed by the distant observer (Longair, 2011).

observed duration of the pulse is, therefore,

$$\triangle t = \left[\frac{L}{v} + \frac{(R-L)}{c}\right] - \frac{R}{c} = \frac{L}{v}\left(1 - \frac{v}{c}\right) \tag{4.15}$$

Since $v \sim c$, the observed duration of pulse is much less than the distance L/v between the two points of emission, implying that the relativistic particle *almost* catches up with the radiation emitted at A. Also, we know the relativistic aberration formula for the angle transformation between the two frames from Eqn. 2.21, to be,

$$\sin\theta = \frac{1}{\gamma}\frac{\sin\theta'}{1 + (v/c)\cos\theta'} \tag{4.16}$$

where θ' and θ are the beaming angles in the rest frame of the particle and the observer's frame. Considering the angles $\theta' = \pm\pi/4$ to be the ones where the intensity falls to half its maximum value i.e. $\theta' = \pi/2$ in the instantaneous rest frame of the particle, and plugging in this value in Eqn. 4.16, we get

$$\sin\theta \approx \theta \approx \pm 1/\gamma \tag{4.17}$$

From the geometry of the path in Fig. 4-4, we can write $L = r_g\theta$. Using this and

Eqn. 4.17,

$$\frac{L}{v} = \frac{r_g \theta}{v} \approx \frac{1}{\gamma \omega_r} = \frac{1}{\omega_g} \tag{4.18}$$

where $\omega_r = v/r_g$ and $\omega_g = \omega_r \gamma$ are the relativistic and non relativistic gyrofrequencies respectively. Also, rewriting $1 - v/c$ as,

$$\left(1 - \frac{v}{c}\right) = \frac{\left[1 - (v/c)\right]\left[1 + (v/c)\right]}{\left[1 + (v/c)\right]} = \frac{(1 - v^2/c^2))}{1 + (v/c)} \approx \frac{1}{2\gamma^2} \tag{4.19}$$

where approximation using the binomial theorem is made in the numerator and the $v \approx c$ is used in the denominator. Substituting Eqn. 4.18 and Eqn. 4.19 in Eqn. 4.15, we have a simple expression for the duration of the pulse,

$$\triangle t \approx \frac{1}{2\gamma^2 \omega_g} \tag{4.20}$$

The spectrum of the radiation received by the observer is the Fourier transform of this pulse. Decomposing the pulse into its Fourier components, gives the maximum component corresponding to a frequency $\nu \sim \triangle t^{-1}$, hence,

$$\nu \sim \triangle t^{-1} \sim \gamma^2 \nu_g \tag{4.21}$$

where ν_g is the non relativistic gyrofrequency. Let ν_r be the relativistic gyrofrequency and r_g the radius of the particle's orbit (as shown in Fig. 4-4), the observed frequency can be rewritten as,

$$\nu \approx \gamma^2 \nu_g = \gamma^3 \nu_r = \frac{\gamma^3 v}{2\pi r_g} \tag{4.22}$$

The radius r_g is interpreted as the *instantaneous radius of curvature* of the particle's orbit and ν/r_g as the associated angular frequency. The expression for the observed frequency in Eqn. 4.22 is used to calculate the frequency of emission (at which most of radiation is emitted) provided the radius of curvature is known. The

most commonly used form of Eqn. 4.22 is given as,

$$\nu_{CF} = \frac{3c}{4\pi\rho}\gamma^3 \tag{4.23}$$

4.4 Results and Discussions

In this section, the phase plots illustrating the power radiated by photons over the entire range of phase ϕ and line of sight ζ are shown with their corresponding light curves. The method to calculate the phase plots is discussed in Section 2.4.

Using this approach, we calculate the frequency of every particle. The maximum frequency is used as an upper limit to define the range of our frequency and the lower limit is considered to be zero. Basically, we show the evolution of emission for different frequency ranges. The upper limit of frequency is termed as f_u and lower limit f_l is zero. We choose to divide the whole frequency range (f_l, f_u) into six equal intervals with each interval being $f_o = (f_u - f_l)/6$. In the results below, however, not all six intervals will be shown because lower ranges have either zero or negligible total radiated power to be of any value for the results, so they are removed from the plots for better visualization. Also, the corresponding values of this range for high energy and radio emission are given in their respective sections below. The maximum frequency and the interval for every orientation shown is summarized in form of tables in each corresponding section.

The following subsections discuss the phase plots for high energy and radio emission. Each phase plot is normalized with respect to the power of the unit radiating maximum power (P_{max}) for each plot to one. To make sure that no information about the values of the power being emitted is lost in this process, we also show the P_{max} for each frequency interval corresponding to every orientation in subsequent plots. And finally, to better visualize the phase plots, we plot the light curves for different line of sights ζ for all the cases. We choose three orientations $(\alpha, \beta, \delta) = (30°, 0°, 0°), (60°, 0°, 0°), (90°, 90°, 90°)$ to discuss in this section. Various other orientations are shown in Appendix B to complete a proper atlas of our study.

(α, β, δ)	**Maximum energy**	**Energy interval**
	$\epsilon = 0$	
$(30°, 0°, 0°)$	8.3	1.4
$(60°, 0°, 0°)$	11.0	1.8
$(90°, 90°, 90°)$	16.0	2.6
	$\epsilon = 0.2$	
$(30°, 0°, 0°)$	11.0	1.8
$(60°, 0°, 0°)$	11.0	1.9
$(90°, 90°, 90°)$	16.0	2.7

Table 4.1: Calculated values of maximum energy and intervals taken for different orientations for centred $\epsilon = 0$ and off centred case $\epsilon = 0.2$ considering high energy emission. All energy values are in GeV. Refer to Fig. 3-1 for the angles α, β, δ.

4.4.1 Frequency resolved high energy emission

For the high energy emission, γ is taken to be 10^7 which corresponds to an energy of about 10 GeV. Then, Eqn. 2.26 and Eqn. 2.14 are used to find the frequency and power emitted by every particle respectively. The calculated values of maximum energy corresponding to maximum frequency f_u and energy interval corresponding to frequency interval f_o taken for different orientations for centred $\epsilon = 0$ and off centred case $\epsilon = 0.2$ are summarized in Table 4.1.

The emission phase plots for high energy emission for $(\alpha, \beta, \delta) = (30°, 0°, 0°)$, $(60°, 0°, 0°)$ and $(90°, 90°, 90°)$ are shown in the top panels of Fig. 4-5, Fig. 4-7 and Fig. 4-9 respectively. The $x - axis$ and $y - axis$ represent phase (ϕ) and line of sight angle (ζ) respectively with the former being normalized to one. The panels on the left and the right are for the centred case $\epsilon = 0$ and for the off centred case $\epsilon = 0.2$ respectively. The lowest plot is for the frequency range $(f_l, f_u) = (f_o, 2f_o)$ and top most is for $(5f_o, 6f_o)$; each increasing in steps of f_o (corresponding energy values in Table. 4.1). The white region corresponds to region with no emission and moving towards blue-black via yellow-orange signifies an increase in the radiated power. The bottom panels of the corresponding plots show the power radiated corresponding to the unit with highest power, P_{max}, vs the lowest frequency. The $x - axis$ and $y - axis$

represent the lower frequency f_l of the frequency range increasing in steps of f_o and the P_{max} which is chosen to normalize the power in phase plots in top panels.

The high energy emission light curves for $(\alpha, \beta, \delta) = (30°, 0°, 0°)$, $(60°, 0°, 0°)$ and $(90°, 90°, 90°)$ are shown in Fig. 4-6, Fig. 4-8 and Fig. 4-10 respectively for various line of sights (ζ varying between 30° and 150°) shown on top of each column. The $x-axis$ and $y-axis$ represent phase (ϕ) and emitted power (P) respectively with the latter being normalized with respect to the power emitted by the unit with maximum power for each corresponding ζ. The centred case $\epsilon = 0$ and the off-centred case $\epsilon = 0.2$ are shown in red and blue respectively. Each row corresponds to one frequency range (f_l, f_u); lowest row for $(f_o, 2f_o)$ and top most is for $(5f_o, 6f_o)$; each increasing in steps of f_o (corresponding energy values in Table. 4.1) similar to phase plots mentioned above.

In Fig. 4-5, showing high energy emission for $(\alpha, \beta, \delta) = (30°, 0°, 0°)$, we need to look at the top and bottom panel to read the whole information about the emission. Considering the lowest frequency interval $(f_o, 2f_o)$, we see that the span of the emission i.e. its extent in the magnetosphere, is low as compared to the higher frequency ranges. In fact, most of the emission is at the higher frequencies, the majority of it lying in $(5f_o, 6f_o)$. In the latter case, the emission is almost all over the entire magnetosphere with varying power. It also shows clearly the standard caustic effect (explained in Section 2.3) prominent in red-blue-black dark colours which is apparent in all the ranges; however, it is less intense for the lower frequency ranges as their corresponding P_{max} is lower (see the bottom panel). Now, considering the bottom panels alone, we see that moving towards higher frequencies increases the maximum power radiated and considering the top panels alone, we see the increase in the area of emission spanned in the plots which implies that the chance to observe the high energy emission increases for any angle or phase as we move from lower towards higher frequency ranges.

The centred and off centred phase plots do not show much difference, which we expect considering the value of ϵ we use for our numerical methods; apparently $\epsilon = 0.2$ is a small shift to show any significant differences and increasing the shift to higher

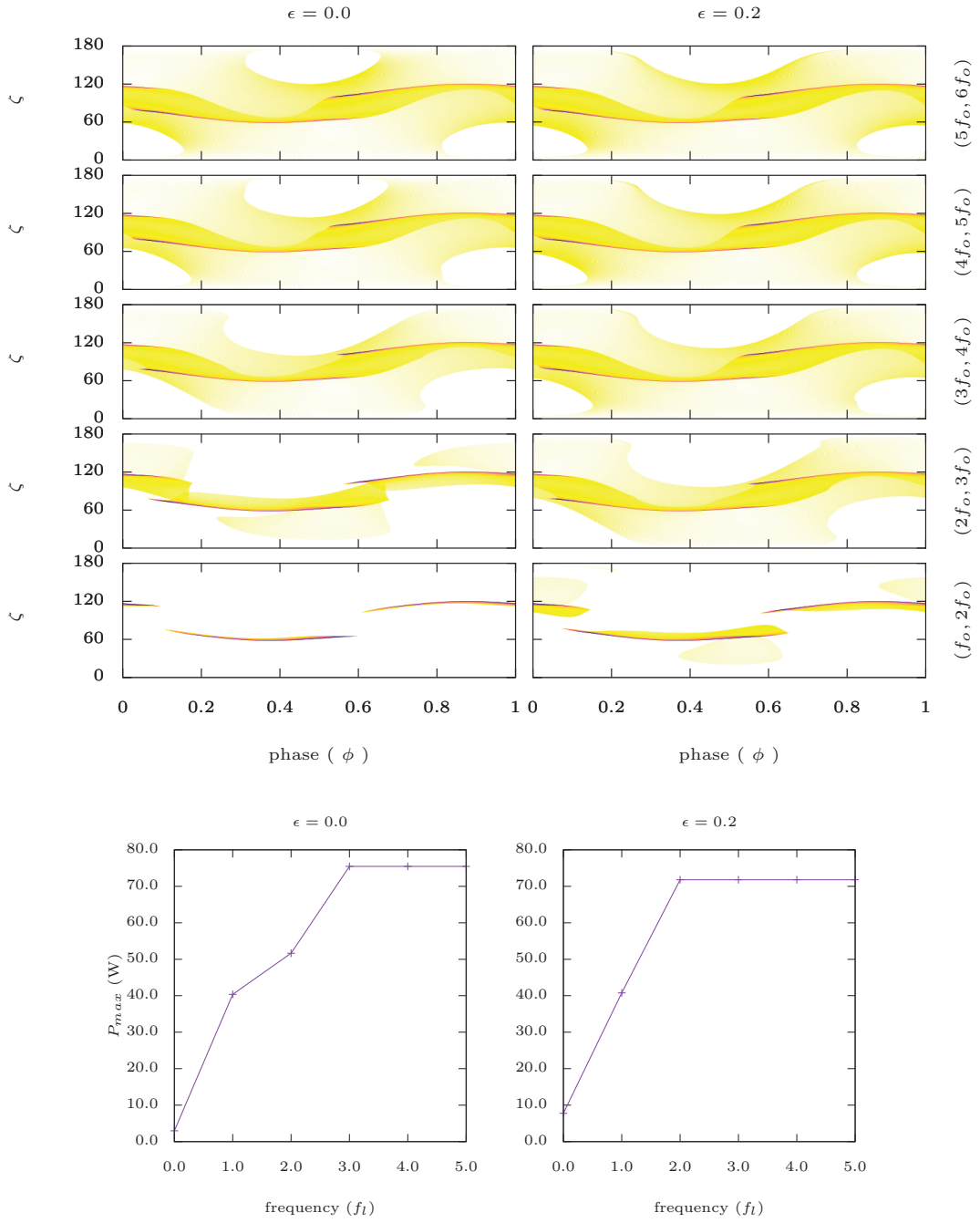

Figure 4-5: **Top :** Frequency resolved high energy emission for $(\alpha, \beta, \delta) = (30°, 0°, 0°)$. The $x - axis$ and $y - axis$ represent phase (ϕ) and line of sight angle (ζ) respectively with the former being normalized to one. The panels on left and right are for the centred case $\epsilon = 0$ and for the off centred case $\epsilon = 0.2$ respectively. The lowest plot is for frequency range $(f_l, f_u) = (f_o, 2f_o)$ and top most is for $(5f_o, 6f_o)$; each increasing in steps of f_o (corresponding energy values in Table. 4.1). The white region corresponds to region with no emission and moving towards blue-black via yellow-orange signifies an increase in the power emitted. **Bottom :** The $x - axis$ represent the lower frequency f_l of the frequency range increasing in steps of f_o and the $y - axis$ shows the power radiated corresponding to the unit with highest power, P_{max} (in W), which is chosen to normalize the power emitted in phase plots in top panels.

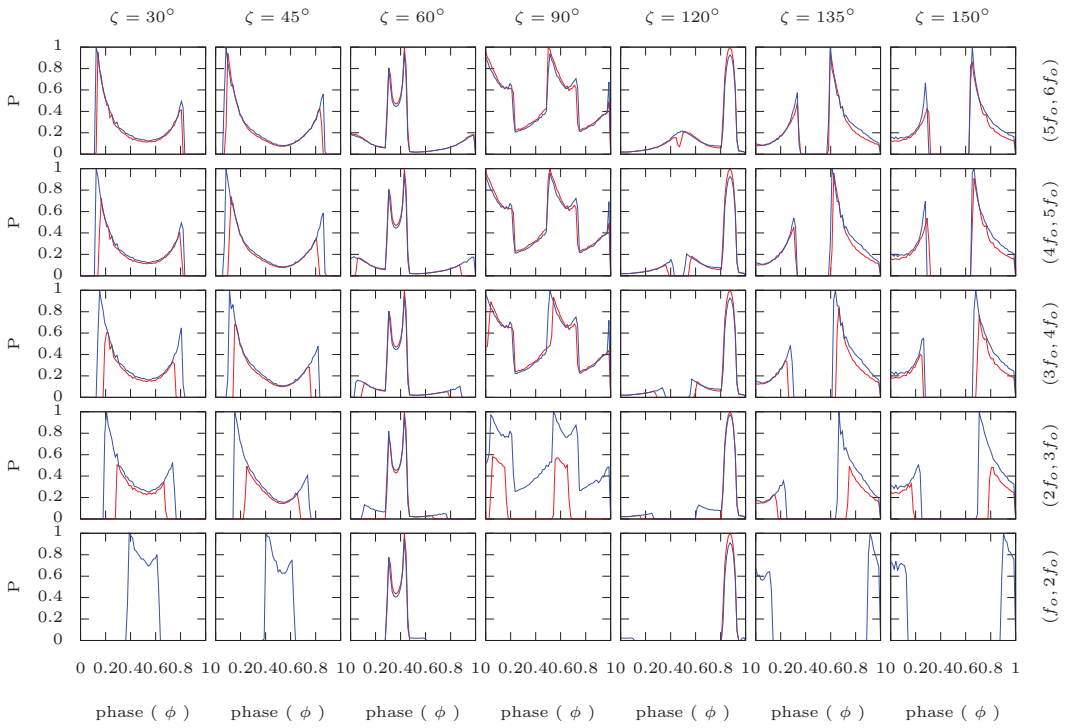

Figure 4-6: Frequency resolved high energy light curves for $(\alpha, \beta, \delta) = (30°, 0°, 0°)$ for centred case ($\epsilon = 0$, in red) and off-centred case ($\epsilon = 0.2$, in blue) for various line of sights (ζ) shown on top of each column. The $x - axis$ represent phase (ϕ) being normalized to one. The $y - axis$ shows emitted power (P) which is being normalized with respect to the power emitted by the unit with maximum power for each corresponding ζ. Each row corresponds to one frequency range (f_l, f_u); lowest row for $(f_o, 2f_o)$ and top most is for $(5f_o, 6f_o)$; each increasing in steps of f_o (corresponding energy values in Table. 4.1).

values decreases the accuracy, so this value is a compromise to maintain accuracy of our approach. We move towards a finer detailed study of each plots, by plotting their light curves which show emission corresponding to particular lines of sight angles (ζ). Fig. 4-6 represents the evolution of the light curves over a range of frequencies for different lines of sight. The caustic peak is evident for 60° and 120° over the entire frequency range although the power radiated is much smaller for the lower range as shown in the bottom panel of Fig. 4-6 and increases only when we move towards a higher range. Also, for the uppermost frequency range $(5f_o, 6f_o)$ the emission is prominent for all line of sights, but since the caustics exist around 60° and 120°, in those two cases, we see peaks in power with rest of the region having low power emitted which is resultant of the normalization with respect to the power emitted by the unit with maximum power for each corresponding plot.

The high energy emission for $(\alpha, \beta, \delta) = (60°, 0°, 0°)$ in Fig. 4-7 shows the same behaviour as discussed above for $(30°, 0°, 0°)$ orientation with the emission span increasing slowly as frequency increases. The caustics are apparent even for lower frequencies and as we move towards higher frequency range, the emission is spread out over the whole region, except for near to the poles, and the caustics become more and more vivid and intense. The Fig. 4-8 shows the light curve evolution for this orientation. The peaks represent strong emission due to caustic effects which has stronger power emitted than the rest of the radiation and hence, peaks become extremely prominent as compared to the rest of the emission, since it is normalized with respect to the power emitted by the unit with maximum power for each corresponding plot. This leads to the rest of the emitted power relatively being lowered, and for the peaks to become much clearer.

The Fig. 4-9 gives the high energy emission information for $(\alpha, \beta, \delta) = (90°, 90°, 90°)$. Considering polar regions as two reference points, it is noticed that the emission is similar around both reference points for $\epsilon = 0$ in all the cases but for $\epsilon = 0.2$ we see a little asymmetrical behaviour which is an expected behaviour of the off centred geometry. It is interesting to note that the P_{max} is similar for all the frequency ranges (see bottom panels) implying that the power radiated is similar in value irrespective

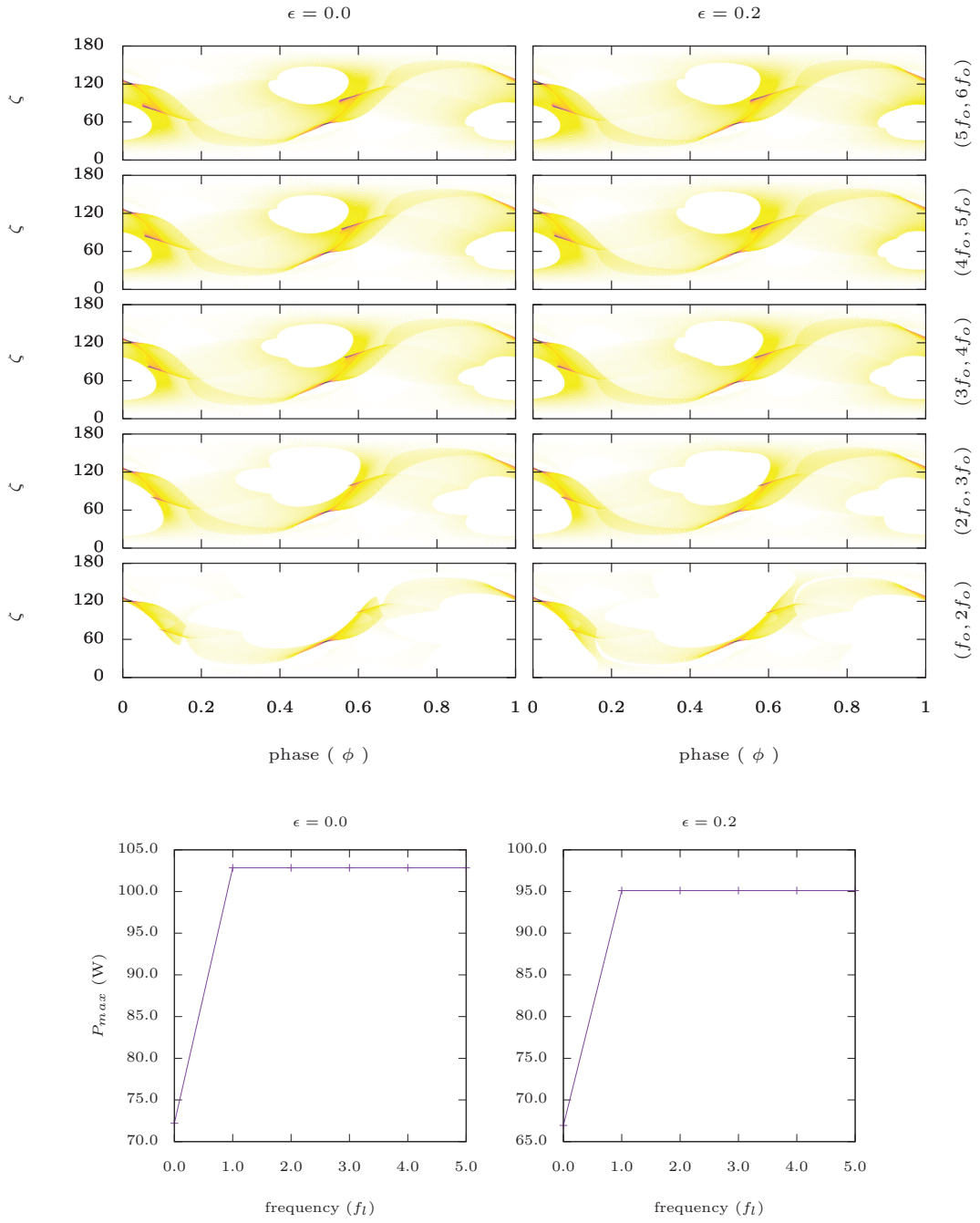

Figure 4-7: **Top :** Frequency resolved high energy emission for $(\alpha, \beta, \delta) = (60°, 0°, 0°)$. The $x - axis$ and $y - axis$ represent phase (ϕ) and line of sight angle (ζ) respectively with the former being normalized to one. The panels on left and right are for the centred case $\epsilon = 0$ and for the off centred case $\epsilon = 0.2$ respectively. The lowest plot is for frequency range $(f_l, f_u) = (f_o, 2f_o)$ and top most is for $(5f_o, 6f_o)$; each increasing in steps of f_o (corresponding energy values in Table. 4.1). The white region corresponds to region with no emission and moving towards blue-black via yellow-orange signifies an increase in the power emitted. **Bottom :** The $x - axis$ represent the lower frequency f_l of the frequency range increasing in steps of f_o and the $y - axis$ shows the power radiated corresponding to the unit with highest power, P_{max} (in W), which is chosen to normalize the power emitted in phase plots in top panels.

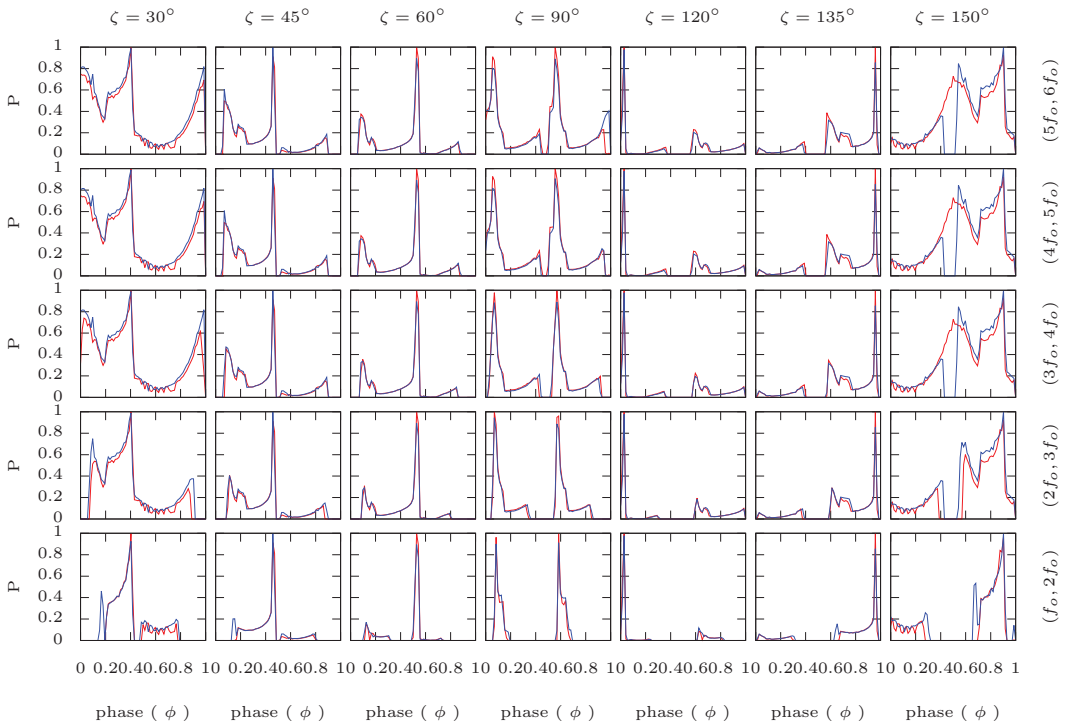

Figure 4-8: Frequency resolved high energy light curves for $(\alpha, \beta, \delta) = (60°, 0°, 0°)$ for centred case ($\epsilon = 0$, in red) and off-centred case ($\epsilon = 0.2$, in blue) for various line of sights (ζ) shown on top of each column. The $x - axis$ represent phase (ϕ) being normalized to one. The $y - axis$ shows emitted power (P) which is being normalized with respect to the power emitted by the unit with maximum power for each corresponding ζ. Each row corresponds to one frequency range (f_l, f_u); lowest row for $(f_o, 2f_o)$ and top most is for $(5f_o, 6f_o)$; each increasing in steps of f_o (corresponding energy values in Table. 4.1).

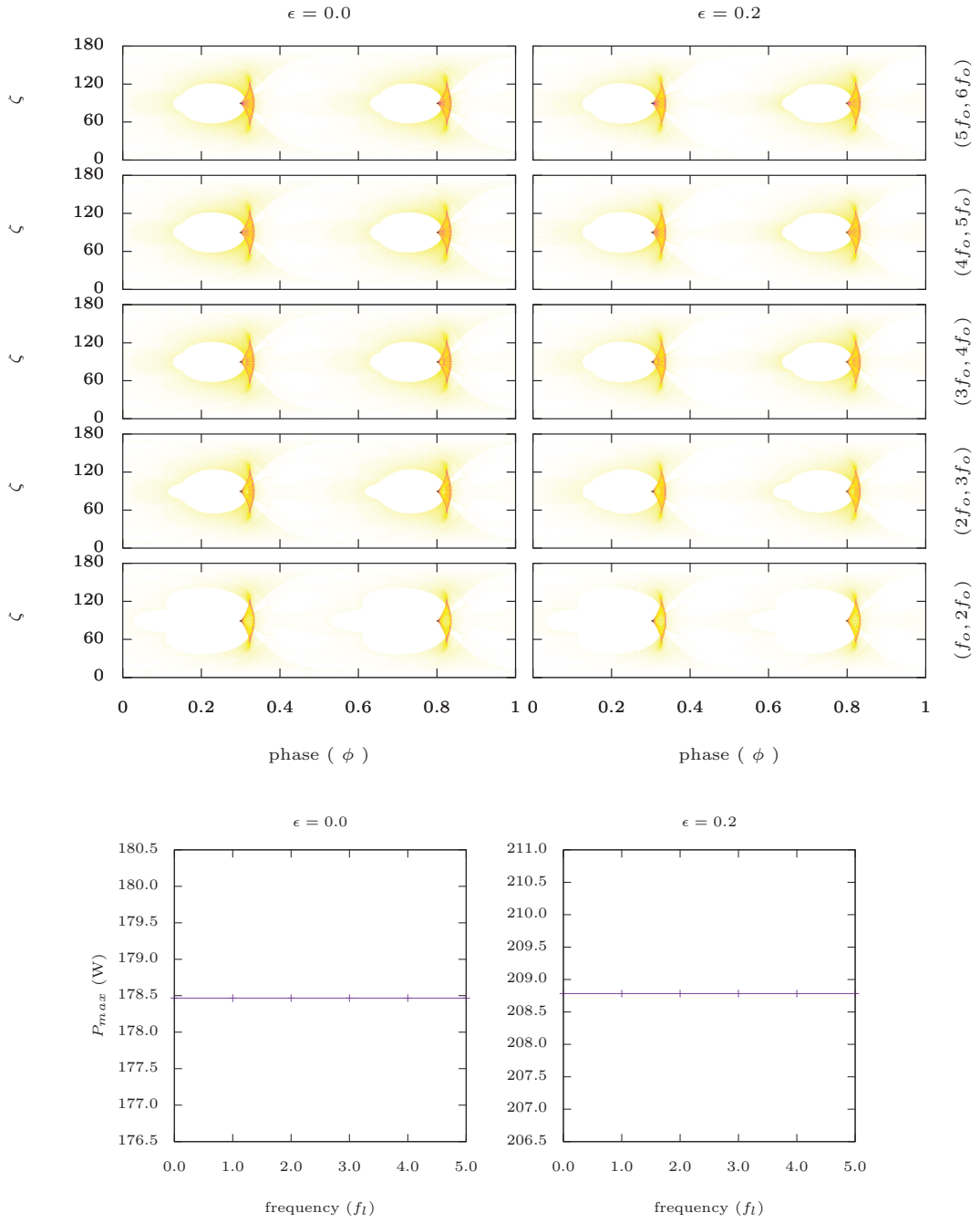

Figure 4-9: **Top :** Frequency resolved high energy emission for $(\alpha, \beta, \delta) = (90°, 90°, 90°)$. The $x - axis$ and $y - axis$ represent phase (ϕ) and line of sight angle (ζ) respectively with the former being normalized to one. The panels on left and right are for the centred case $\epsilon = 0$ and for the off centred case $\epsilon = 0.2$ respectively. The lowest plot is for frequency range $(f_l, f_u) = (f_o, 2f_o)$ and top most is for $(5f_o, 6f_o)$; each increasing in steps of f_o (corresponding energy values in Table. 4.1). The white region corresponds to region with no emission and moving towards blue-black via yellow-orange signifies an increase in the power emitted. **Bottom :** The $x - axis$ represent the lower frequency f_l of the frequency range increasing in steps of f_o and the $y - axis$ shows the power radiated corresponding to the unit with highest power, P_{max} (in W), which is chosen to normalize the power emitted in phase plots in top panels.

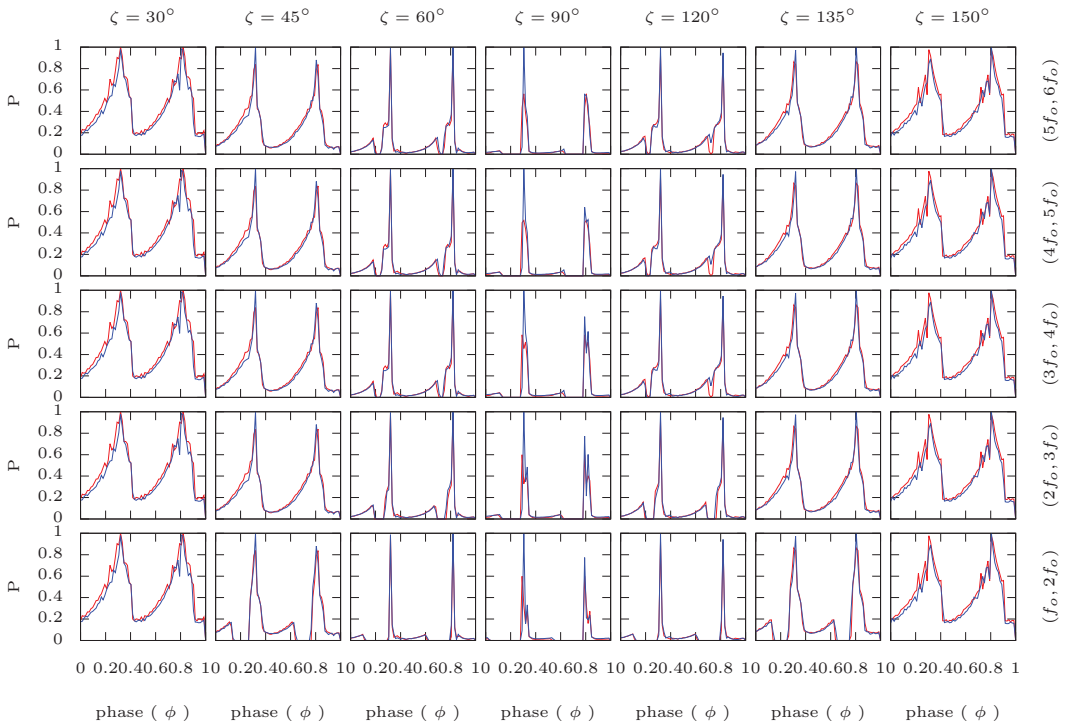

Figure 4-10: Frequency resolved high energy light curves for $(\alpha, \beta, \delta) = (90°, 90°, 90°)$ for centred case ($\epsilon = 0$, in red) and off-centred case ($\epsilon = 0.2$, in blue) for various line of sights (ζ) shown on top of each column. The $x - axis$ represent phase (ϕ) being normalized to one. The $y - axis$ shows emitted power (P) which is being normalized with respect to the power emitted by the unit with maximum power for each corresponding ζ. Each row corresponds to one frequency range (f_l, f_u); lowest row for $(f_o, 2f_o)$ and top most is for $(5f_o, 6f_o)$; each increasing in steps of f_o (corresponding energy values in Table. 4.1).

(α, β, δ)	**Maximum frequency** f_u	**Frequency interval** $f_o = f_u/6$
	$\epsilon = 0$	
$(30°, 0°, 0°)$	1.99	0.33
$(60°, 0°, 0°)$	2.17	0.36
$(90°, 90°, 90°)$	2.24	0.37
	$\epsilon = 0.2$	
$(30°, 0°, 0°)$	2.33	0.39
$(60°, 0°, 0°)$	2.67	0.44
$(90°, 90°, 90°)$	2.54	0.42

Table 4.2: Calculated values of maximum frequency and intervals taken for different orientations for centred $\epsilon = 0$ and off centred case $\epsilon = 0.2$ considering radio emission. All frequency values are in GHz. Refer to Fig. 3-1 for the angles α, β, δ.

of the frequency range. The only difference between the lower and higher frequency emission lies in the area span of the emission; for higher frequencies it is spread out larger in area than that for the lower frequencies. The light curves for this case are shown in Fig. 4-10. The two-peak behaviour is clearly present which is a standard signature of $\alpha = 90°$ orientation i.e. where the magnetic dipole axis is perpendicular to the rotation axis of the pulsar. The emission peak is consistent for $\zeta = 90°$ over the entire frequency range while for the rest of the cases, it increases as we move towards higher frequencies.

4.4.2 Frequency resolved radio emission

For the radio emission, γ is taken to be 100 which corresponds to frequency of about 1 GHz. The method to calculate curvature and frequency is same as discussed for high energy emission. The f_o for radio emission taken for different orientations for centred $\epsilon = 0$ and off centred case $\epsilon = 0.2$ are summarized in Table 4.2.

The radio emission phase plots for $(\alpha, \beta, \delta) = (30°, 0°, 0°)$, $(60°, 0°, 0°)$ and $(90°, 90°, 90°)$ are shown in top panels of Fig. 4-11, Fig. 4-13 and Fig. 4-15 respectively. The description of colours and other quantities is same as mentioned for high energy emission.

The lowest plot is for frequency range $(f_l, f_u) = (f_o, 2f_o)$ and top most is for $(5f_o, 6f_o)$; each increasing in steps of f_o (value in Table. 4.2). The number of frequency ranges being shown for radio emission is lower than that shown in high energy emission. The lower frequency ranges, as pointed earlier, have zero or negligible contribution and hence, have been removed for better visualization. This is because the radio emission is considered to be generating from the polar caps, the region surrounding the poles from where the open field lines are emanating. These field lines have a smaller radius of curvature since they are less curved than those lying within the light cylinder (those considered responsible for high energy emission). Also, the frequency is inversely proportional to the radius of curvature (see Eqn. 2.13), therefore emission is significant only in the higher frequency range for such low radii of curvature.

The radio emission light curves for $(\alpha, \beta, \delta) = (30°, 0°, 0°)$, $(60°, 0°, 0°)$ and $(90°, 90°, 90°)$ are shown in Fig. 4-12, Fig. 4-14 and Fig. 4-16 respectively for various line of sights (ζ varying between 30° and 150°) shown on top of each column. The colour scheme and other quantities is the same as mentioned for high energy emission.

The radio emission for $(\alpha, \beta, \delta) = (30°, 0°, 0°)$ is shown in Fig. 4-11 where, again, the top and the bottom panels both will be read together to not risk missing significant information about the power emission. The first thing to notice is that the colour intensity is higher in radio emission plots than their corresponding high energy emission counterparts. This does not imply that the power radiated by photons in radio emission is higher than high energy emission because both plots have been calculated and normalized separately. Also, the number of points considered for calculations is the same for both cases but because radio emission is only limited to the polar cap region while the high energy emission spans all over the magnetosphere from the polar cap boundary to the light cylinder, the density of field lines for radio emission is much higher than that in high energy emission, hence, resulting in stronger colour intensity in radio emission plots.

The bottom panels showing maximum power radiated P_{max} for each frequency range shows the P_{max} on $y - axis$ which is extremely low compared to that in the high energy case. This is because the frequency for radio emission is only of order of

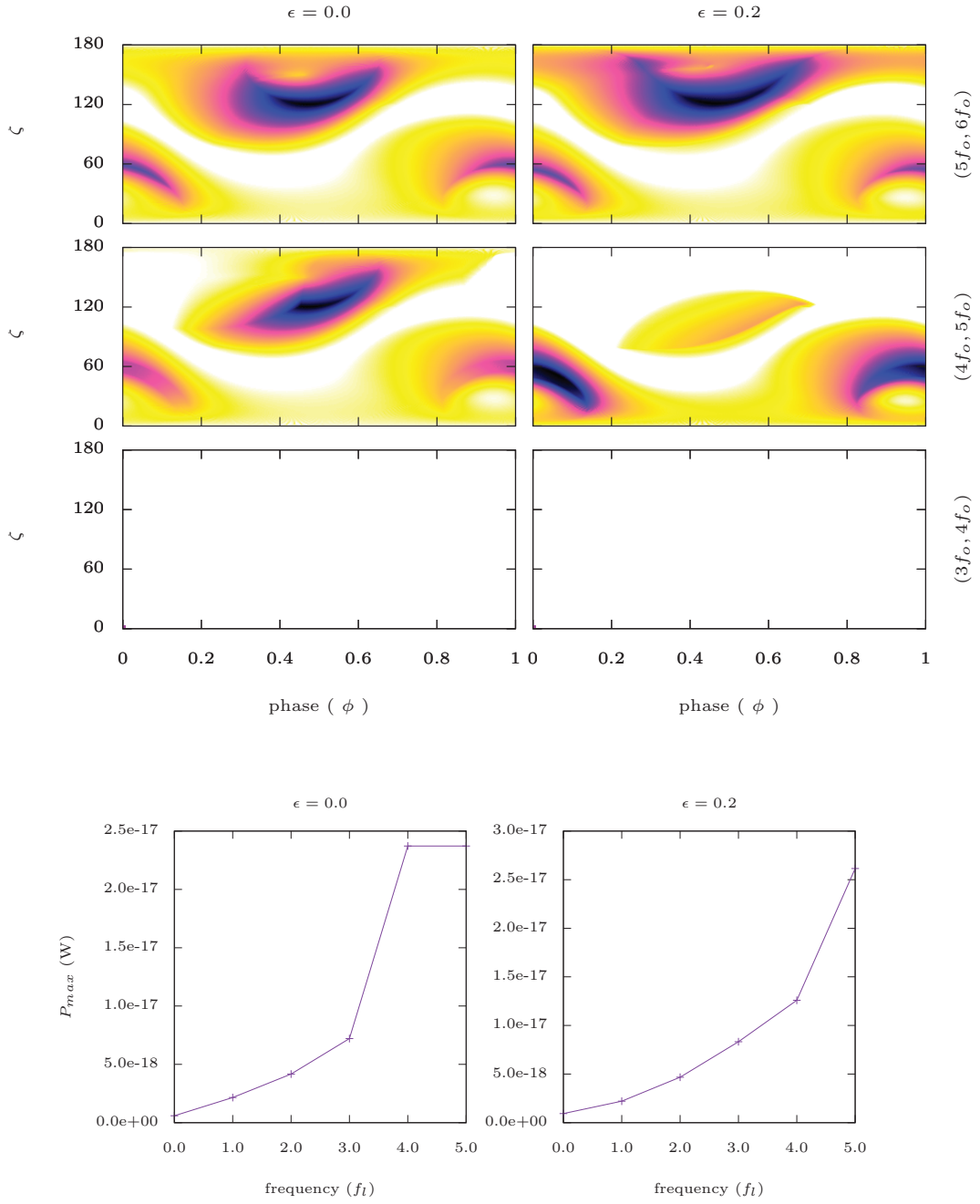

Figure 4-11: **Top :** Frequency resolved radio emission for $(\alpha, \beta, \delta) = (30°, 0°, 0°)$. The $x-axis$ and $y-axis$ represent phase (ϕ) and line of sight angle (ζ) respectively with the former being normalized to one. The panels on left and right are for the centred case $\epsilon = 0$ and for the off centred case $\epsilon = 0.2$ respectively. The lowest plot is for frequency range $(f_l, f_u) = (3f_o, 4f_o)$ and top most is for $(5f_o, 6f_o)$; each increasing in steps of f_o (value in Table. 4.2). The white region corresponds to region with no emission and moving towards blue-black via yellow-orange signifies an increase in the power emitted. **Bottom :** The $x-axis$ represent the lower frequency f_l of the frequency range increasing in steps of f_o and the $y-axis$ shows the power radiated corresponding to the unit with highest power, P_{max} (in W), which is chosen to normalize the power emitted in phase plots in top panels.

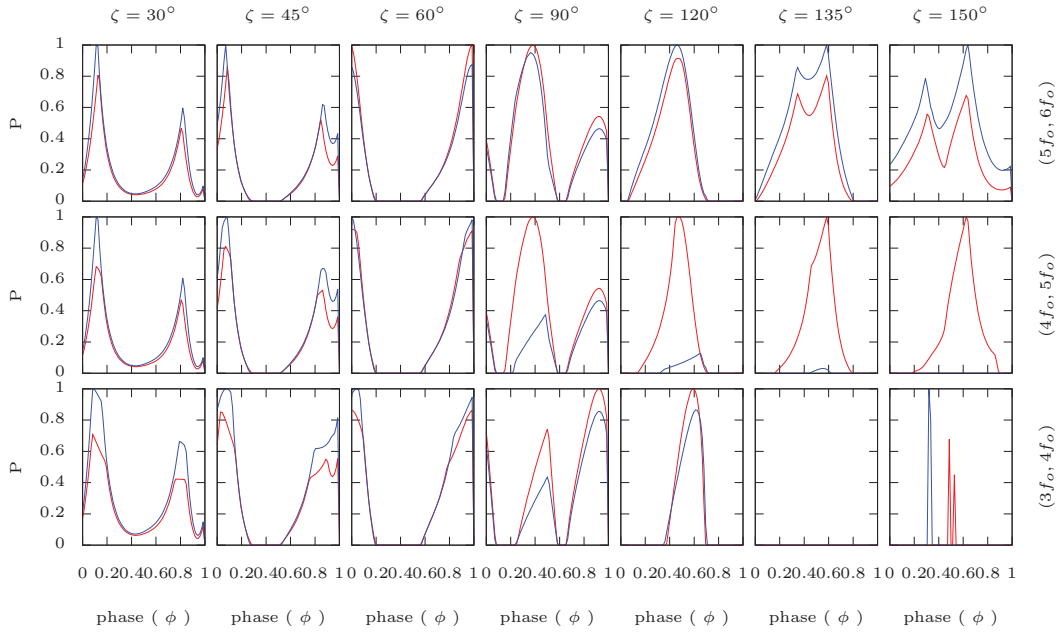

Figure 4-12: Frequency resolved radio emission light curves for $(\alpha, \beta, \delta) = (30°, 0°, 0°)$ for centred case ($\epsilon = 0$, in red) and off-centred case ($\epsilon = 0.2$, in blue) for various line of sights (ζ) shown on top of each column. The $x - axis$ represent phase (ϕ) being normalized to one. The $y - axis$ shows emitted power (P) which is being normalized with respect to the power emitted by the unit with maximum power for each corresponding ζ. Each row corresponds to one frequency range (f_l, f_u); lowest row for $(3f_o, 4f_o)$ and top most is for $(5f_o, 6f_o)$; each increasing in steps of f_o (value in Table. 4.2).

1 GHz as compared to that of the high energy emission of order of 10^{15} GHz. Since the power radiated is directly proportional to the frequency of the particle being emitted (see Eqn. 2.14), the P_{max} values are significantly lower by a large order of magnitude for radio emission than that for the high energy emission.

Again, the centred and off centred phase plots do not show much difference, owing to the lower resolution we use for our numerical methods as a compromise to save computation time, as mentioned earlier. The emission is limited only around the polar regions which is a result of the model we consider in which radio emission is limited to the field lines lying within the polar cap. For the lower range of frequency, the emission spans smaller area than that in higher frequency range; it increases as the frequency gets higher.

Fig. 4-12 represents the evolution of light curves over a range of frequencies for different lines of sight for the same orientation. For the uppermost frequency range $(5f_o, 6f_o)$ the emission is prominent over all line of sights. In some cases, the peak of the power emitted by the centred case and the off centred can be seen to be varying significantly; for instance, for $\zeta = 90°, 120°$, which is an important information in terms of power emission observed. Depending on which model we consider for the geometry of the pulsar, it makes a difference in its emission despite of considering the same mechanism for generation of emission.

Fig. 4-13 shows the same behaviour with radio emission increasing slowly as frequency gets higher for the orientation $(\alpha, \beta, \delta) = (60°, 0°, 0°)$. The emission is largely concentrated close to the polar cap region and emitted power decreases as we move away from the 'centre' of the polar region to that of its boundary. This is because the radius of curvature of the field lines increases as we move away from the field line emanating from the centre of the polar cap which will have zero radius of curvature, since they extend like a straight line up to infinity. Fig. 4-14 gives the information on the light curve evolution and the two peaks of emission, one from each pole which are apparent in almost every plot.

The last orientation $(\alpha, \beta, \delta) = (90°, 90°, 90°)$ in this chapter is shown in Fig. 4-15. This emission from the two poles is similar for $\epsilon = 0$ in all the cases but for $\epsilon = 0.2$

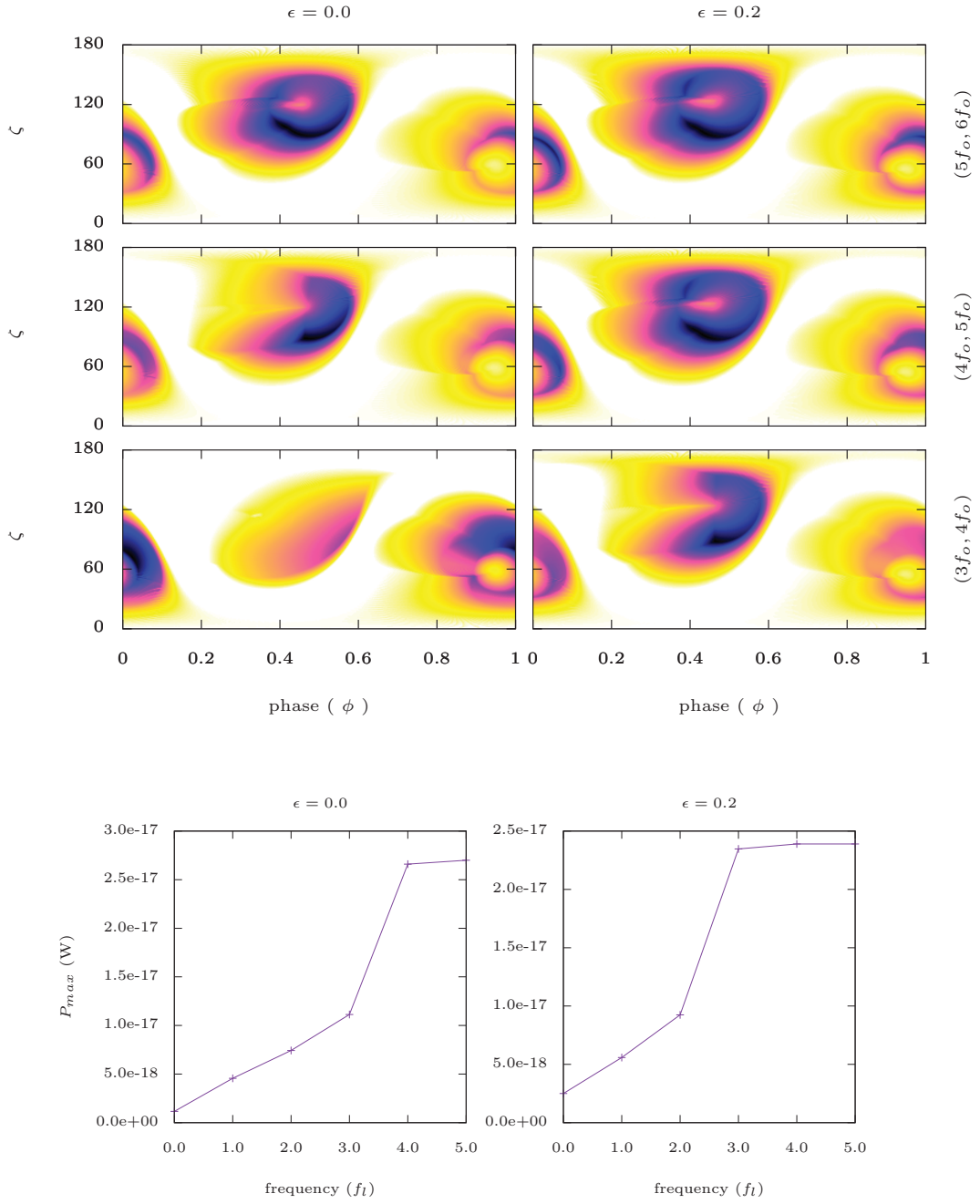

Figure 4-13: **Top :** Frequency resolved radio emission for $(\alpha, \beta, \delta) = (60°, 0°, 0°)$. The $x-axis$ and $y-axis$ represent phase (ϕ) and line of sight angle (ζ) respectively with the former being normalized to one. The panels on left and right are for the centred case $\epsilon = 0$ and for the off centred case $\epsilon = 0.2$ respectively. The lowest plot is for frequency range $(f_l, f_u) = (3f_o, 4f_o)$ and top most is for $(5f_o, 6f_o)$; each increasing in steps of f_o (value in Table. 4.2). The white region corresponds to region with no emission and moving towards blue-black via yellow-orange signifies an increase in the power emitted. **Bottom :** The $x-axis$ represent the lower frequency f_l of the frequency range increasing in steps of f_o and the $y-axis$ shows the power radiated corresponding to the unit with highest power, P_{max} (in W), which is chosen to normalize the power emitted in phase plots in top panels.

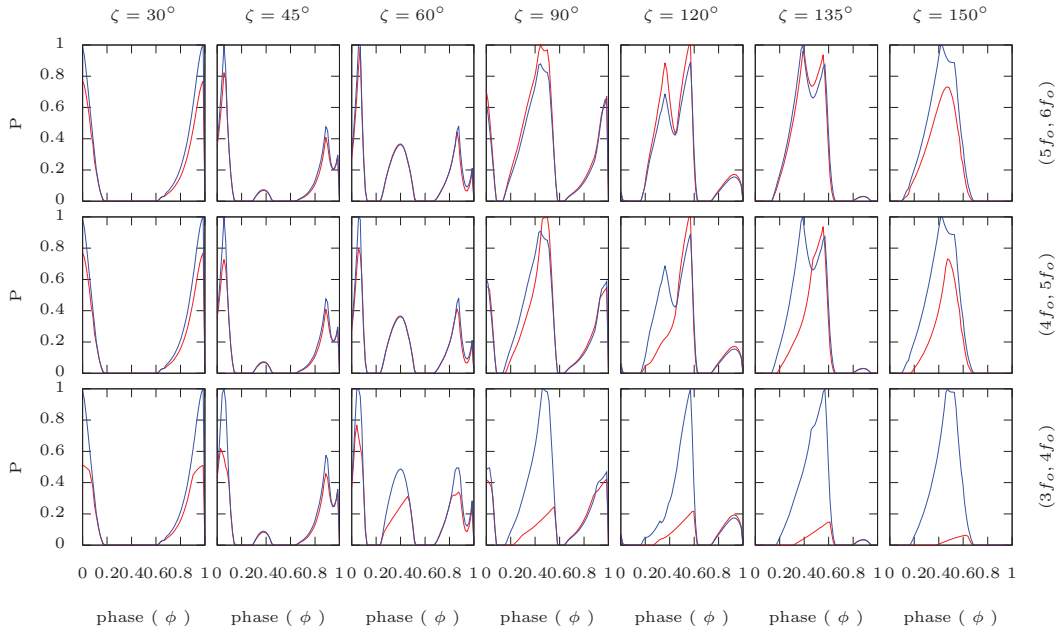

Figure 4-14: Frequency resolved radio emission light curves for $(\alpha, \beta, \delta) = (60°, 0°, 0°)$ for centred case ($\epsilon = 0$, in red) and off-centred case ($\epsilon = 0.2$, in blue) for various line of sights (ζ) shown on top of each column. The $x - axis$ represent phase (ϕ) being normalized to one. The $y - axis$ shows emitted power (P) which is being normalized with respect to the power emitted by the unit with maximum power for each corresponding ζ. Each row corresponds to one frequency range (f_l, f_u); lowest row for $(3f_o, 4f_o)$ and top most is for $(5f_o, 6f_o)$; each increasing in steps of f_o (value in Table. 4.2).

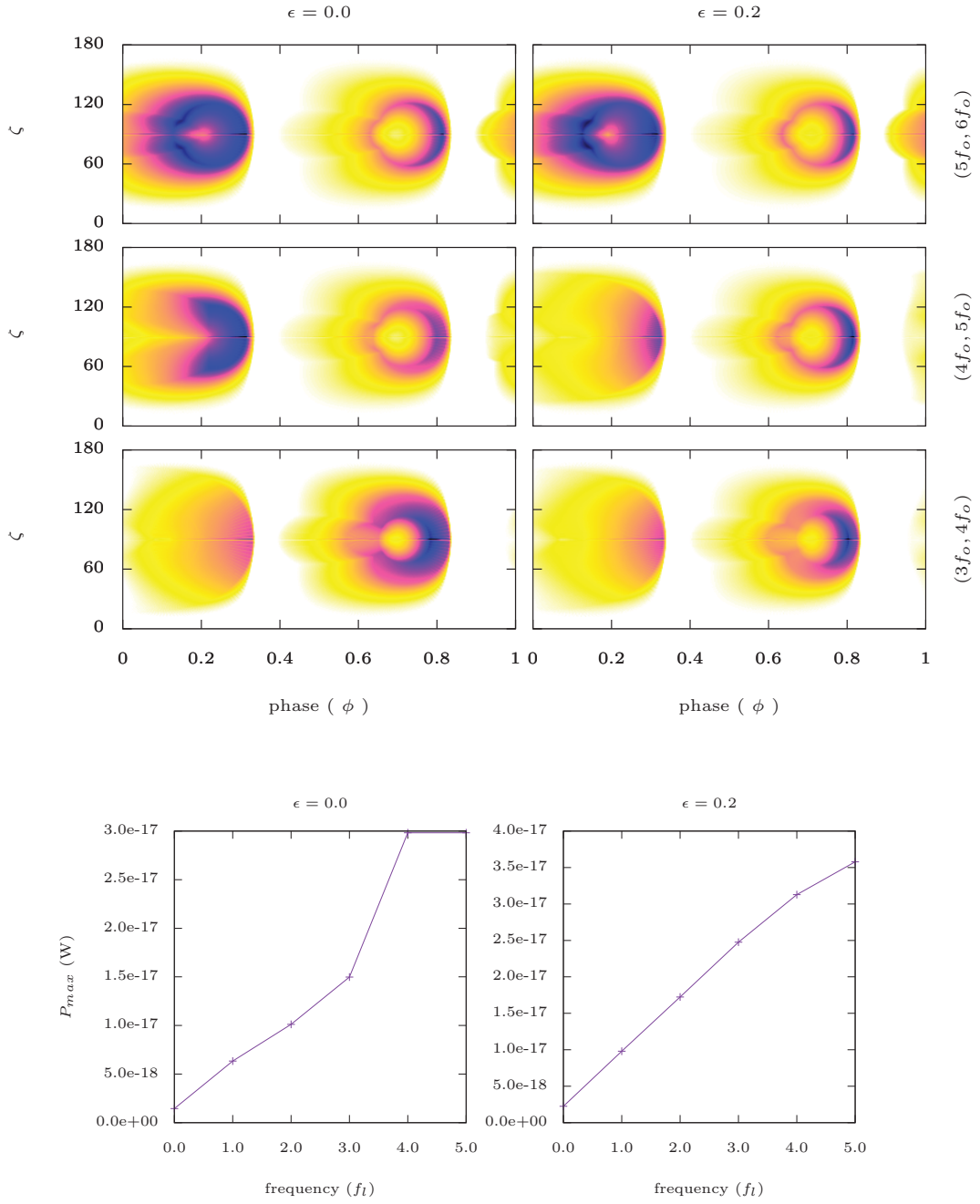

Figure 4-15: **Top :** Frequency resolved radio emission for $(\alpha, \beta, \delta) = (90°, 90°, 90°)$. The $x - axis$ and $y - axis$ represent phase (ϕ) and line of sight angle (ζ) respectively with the former being normalized to one. The panels on left and right are for the centred case $\epsilon = 0$ and for the off centred case $\epsilon = 0.2$ respectively. The lowest plot is for frequency range $(f_l, f_u) = (3f_o, 4f_o)$ and top most is for $(5f_o, 6f_o)$; each increasing in steps of f_o (value in Table. 4.2). The white region corresponds to region with no emission and moving towards blue-black via yellow-orange signifies an increase in the power emitted. **Bottom :** The $x - axis$ represent the lower frequency f_l of the frequency range increasing in steps of f_o and the $y - axis$ shows the power radiated corresponding to the unit with highest power, P_{max} (in W), which is chosen to normalize the power emitted in phase plots in top panels.

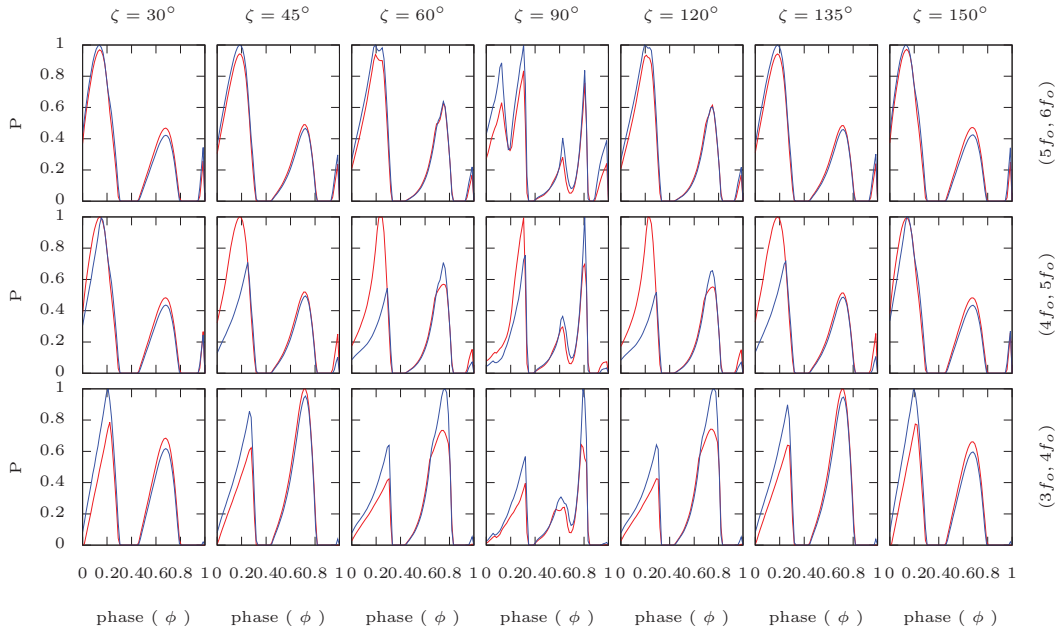

Figure 4-16: Frequency resolved radio emission light curves for $(\alpha, \beta, \delta) = (90°, 90°, 90°)$ for centred case ($\epsilon = 0$, in red) and off-centred case ($\epsilon = 0.2$, in blue) for various line of sights (ζ) shown on top of each column. The $x - axis$ represent phase (ϕ) being normalized to one. The $y - axis$ shows emitted power (P) which is being normalized with respect to the power emitted by the unit with maximum power for each corresponding ζ. Each row corresponds to one frequency range (f_l, f_u); lowest row for $(3f_o, 4f_o)$ and top most is for $(5f_o, 6f_o)$; each increasing in steps of f_o (value in Table. 4.2).

we notice a difference in radiated power between the two poles, most prominent in the top most frequency range. This asymmetric behaviour is similar to that in high energy emission cases and attributed to the off centred geometry which disturbs the symmetry of the size of two poles and also the curvature radius owing to the field line asymmetry. The two poles, have completely separate regions of emission which gives rise to two pulses standard to the perpendicular orientation cases where magnetic dipole axis is perpendicular to the rotation axis of the pulsar i.e. $\alpha = 90°$. Fig. 4-16 highlights the two peak behaviour in form of the light curve evolution for the same case.

4.4.3 Spectra for power law distribution

In above sections, we considered one value of γ each for the high energy and the radio emission. This is the reason we see the sharp cut in frequency in bottom panels of Fig. 4-5, Fig. 4-7, Fig. 4-9 for the high energy emission and in Fig. 4-11, Fig. 4-13, Fig. 4-15 for radio emission. This is not a limitation of the simulation technique, instead, this is what we expect while considering a monoenergetic distribution (single γ value).

Next step, to overcome this, is to consider a power law distribution, which is a more realistic case. We use the range of γ to be $10^5 - 10^7$ for high energy emission and $10 - 10^3$ for the radio emission. This implies that at each point of the field line, we consider a distribution of particles with different frequency values. Although the distribution is same for all the points, but the different curvature at every point makes the frequency (which is dependent on curvature radius) and hence, the power emitted, different for all the points.

The phase plots for high energy emission for $\gamma = 10^5 - 10^7$ is shown in Fig. 4-17 for $(\alpha, \beta, \delta) = (30°, 0°, 0°)$. The $x - axis$ and $y - axis$ represent phase (ϕ) and line of sight angle (ζ) respectively with the former being normalized to one. The panels on left and right are for the centred case $\epsilon = 0$ and for the off centred case $\epsilon = 0.2$ respectively. The lowest plot is for frequency range $(f_l, f_u) = (f_o, 2f_o)$ and top most is for $(5f_o, 6f_o)$ each divided in equal intervals f_o. The white region corresponds to

region with no emission and moving towards blue-black via yellow-orange signifies an increase in the power emitted. Also, each phase plot is normalized with respect to the power of the unit radiating maximum power for each plot to one. In the bottom panel, the $x-axis$ represent the lower frequency f_l of the frequency range increasing in steps of f_o and the $y-axis$ shows the total power emitted summed up for each individual emission diagram in the top panel, P_{total} (in W).

The light curves for the corresponding cases for different line of sights ζ (varying between 30° and 150°, shown on top of each column) are plotted in the top panel of Fig. 4-18. Both, the centred case ($\epsilon = 0$, in red) and the off-centred case ($\epsilon = 0.2$, in blue) are shown. The $x-axis$ represent phase (ϕ) being normalized to one. The $y-axis$ shows emitted power (P) which is being normalized with respect to the power emitted for the unit with maximum power for each corresponding ζ. Each row corresponds to one frequency range (f_l, f_u); lowest row for $(f_o, 2f_o)$ and top most is for $(5f_o, 6f_o)$ each divided in equal intervals. In the bottom panel, the $x-axis$ represent the lower frequency f_l of the frequency range increasing in equal steps and the $y-axis$ shows the total power emitted summed up for each corresponding ζ, P_{total} (in W).

Similarly, the phase plots and the corresponding light curves, for radio emission, for $\gamma = 10 - 10^3$ are shown in Fig. 4-19 and Fig. 4-20 respectively.

The Fig. 4-17 shows the similar trend as displayed by Fig. 4-5 and in the bottom panel, we again see the sharp cut in frequency. The light curves in the top panel of Fig. 4-18 are different from that in the Fig. 4-6 which should be expected as now, every point on the field line is considered to have a distribution of particles rather than a single particle. The power distribution for particular line of sights in the bottom panel of Fig. 4-18 also shows the similar cut off as in the total power distribution in the bottom panel of Fig. 4-17. Similar scenario exists for the radio emission as shown in Fig. 4-19 and Fig. 4-20.

In the power distribution over the frequency range, we expected a power law distribution but instead, we see a sharp cut off at particular frequencies. We believe that this behaviour could be accountable to two factors - One, the calculations of

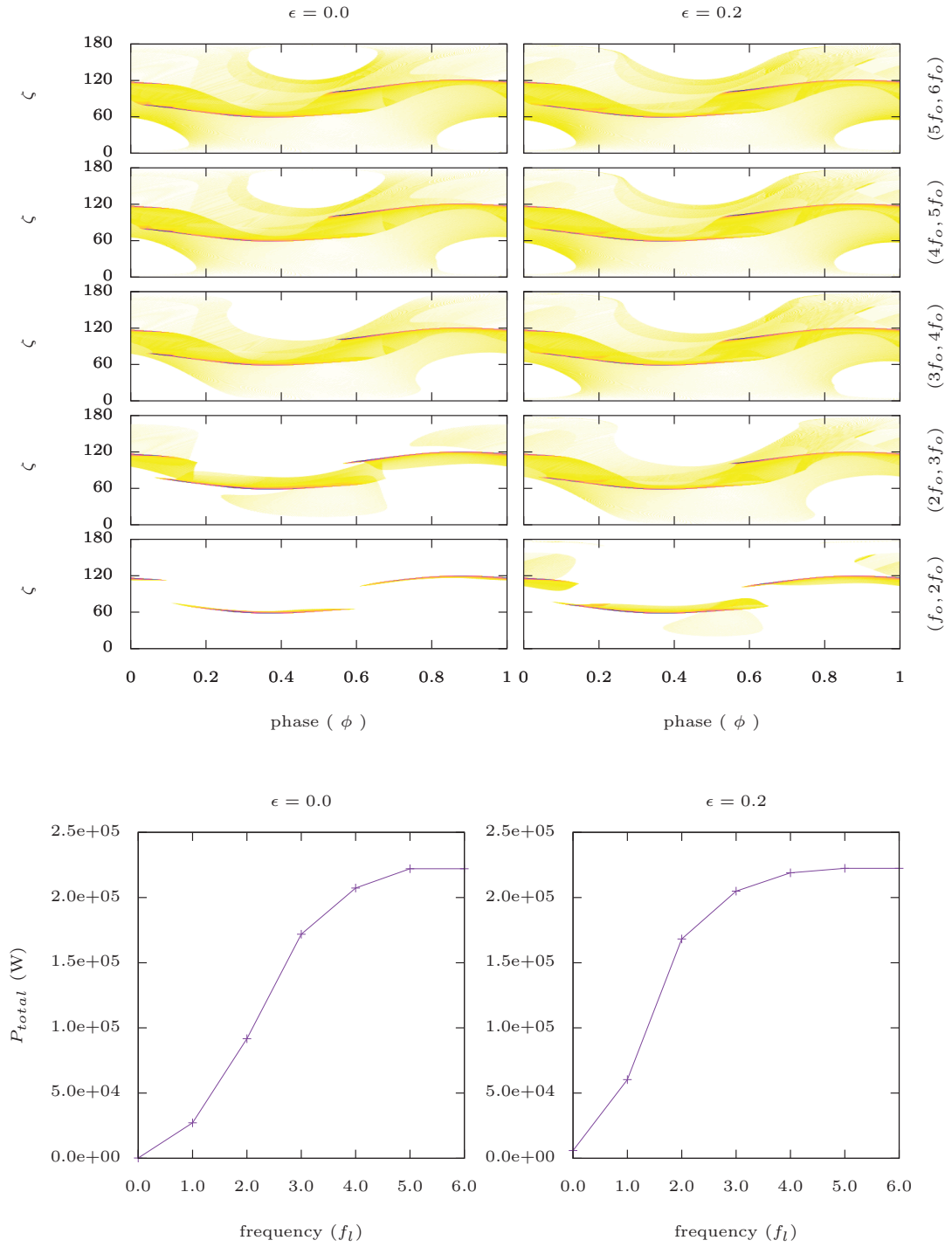

Figure 4-17: **Top** :Frequency resolved radio emission for $(\alpha, \beta, \delta) = (30°, 0°, 0°)$ for $\gamma = 10^5 - 10^7$. The $x - axis$ and $y - axis$ represent phase (ϕ) and line of sight angle (ζ) respectively with the former being normalized to one. The panels on left and right are for the centred case $\epsilon = 0$ and for the off centred case $\epsilon = 0.2$ respectively. The lowest plot is for frequency range $(f_l, f_u) = (f_o, 2f_o)$ and top most is for $(5f_o, 6f_o)$ each divided in equal intervals f_o. The white region corresponds to region with no emission and moving towards blue-black via yellow-orange signifies an increase in the power emitted. **Bottom :** The $x - axis$ represent the lower frequency f_l of the frequency range increasing in steps of f_o and the $y - axis$ shows the total power emitted summed up for each individual emission diagram in the top panel, P_{total} (in W).

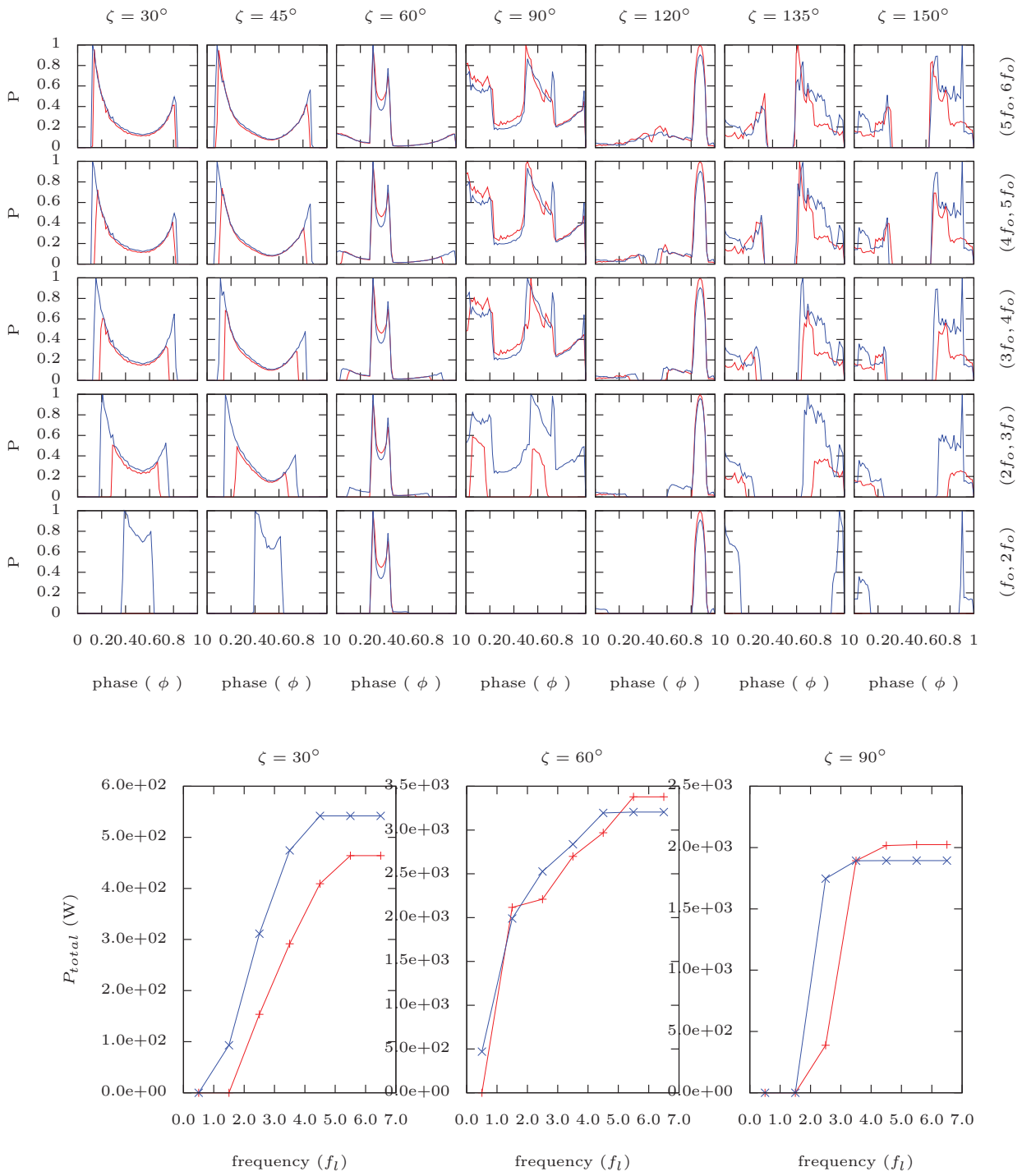

Figure 4-18: **Top :** Frequency resolved radio emission light curves for $(\alpha, \beta, \delta) = (30°, 0°, 0°)$ for $\gamma = 10^5 - 10^7$ for the centred case ($\epsilon = 0$, in red) and the off-centred case ($\epsilon = 0.2$, in blue) for various line of sights (ζ) shown on top of each column. The $x - axis$ represent phase (ϕ) being normalized to one. The $y - axis$ shows emitted power (P) which is being normalized with respect to the power emitted for the unit with maximum power for each corresponding ζ. Each row corresponds to one frequency range (f_l, f_u); lowest row for $(f_o, 2f_o)$ and top most is for $(5f_o, 6f_o)$ each divided in equal intervals. **Bottom :** The $x - axis$ represent the lower frequency f_l of the frequency range increasing in equal steps and the $y - axis$ shows the total power emitted summed up for each corresponding ζ, P_{total} (in W).

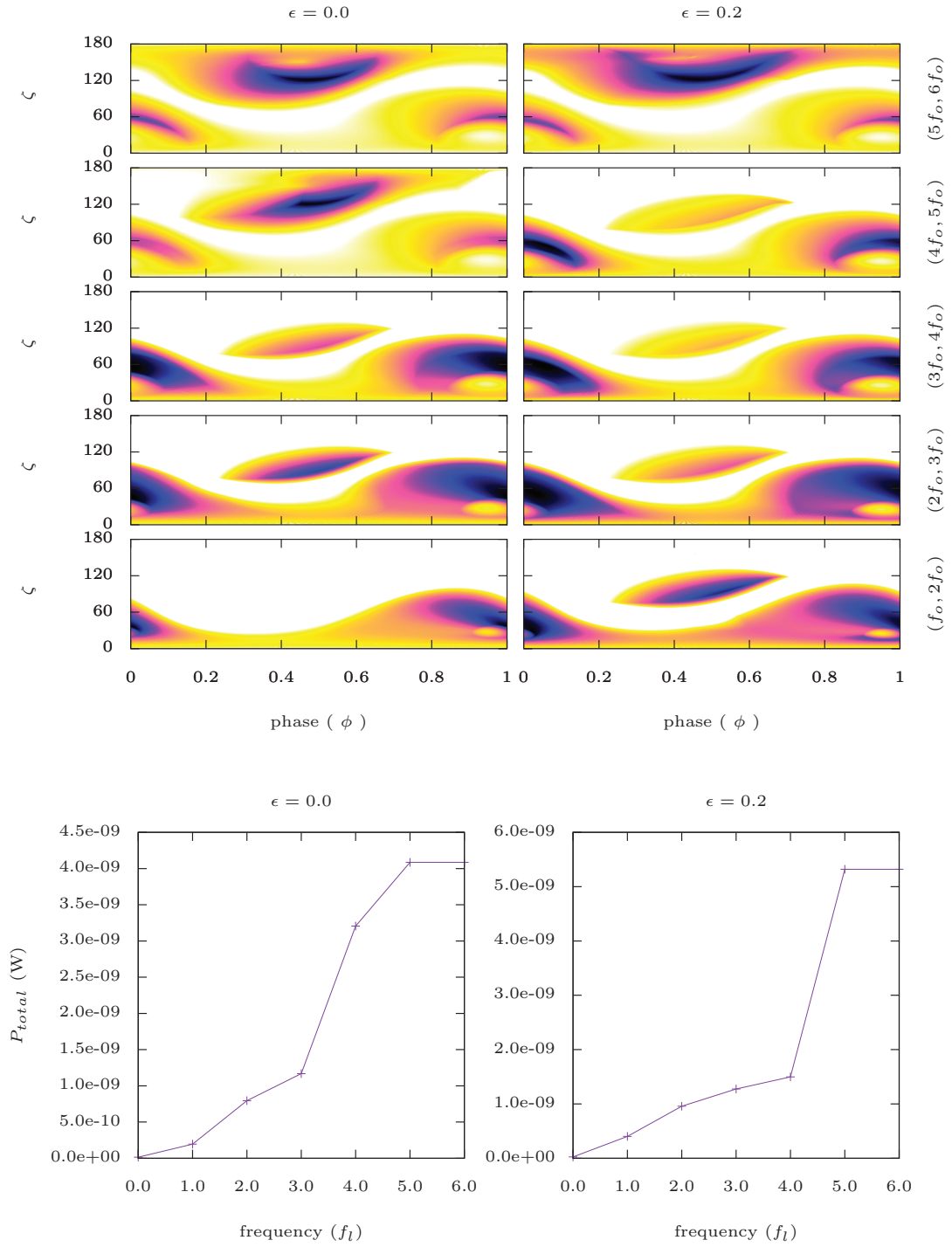

Figure 4-19: **Top** :Frequency resolved radio emission for $(\alpha, \beta, \delta) = (30°, 0°, 0°)$ for $\gamma = 10 - 10^3$. The $x - axis$ and $y - axis$ represent phase (ϕ) and line of sight angle (ζ) respectively with the former being normalized to one. The panels on left and right are for the centred case $\epsilon = 0$ and for the off centred case $\epsilon = 0.2$ respectively. The lowest plot is for frequency range $(f_l, f_u) = (f_o, 2f_o)$ and top most is for $(5f_o, 6f_o)$ each divided in equal intervals f_o. The white region corresponds to region with no emission and moving towards blue-black via yellow-orange signifies an increase in the power emitted. **Bottom :** The $x - axis$ represent the lower frequency f_l of the frequency range increasing in steps of f_o and the $y - axis$ shows the total power emitted summed up for each individual emission diagram in the top panel, P_{total} (in W).

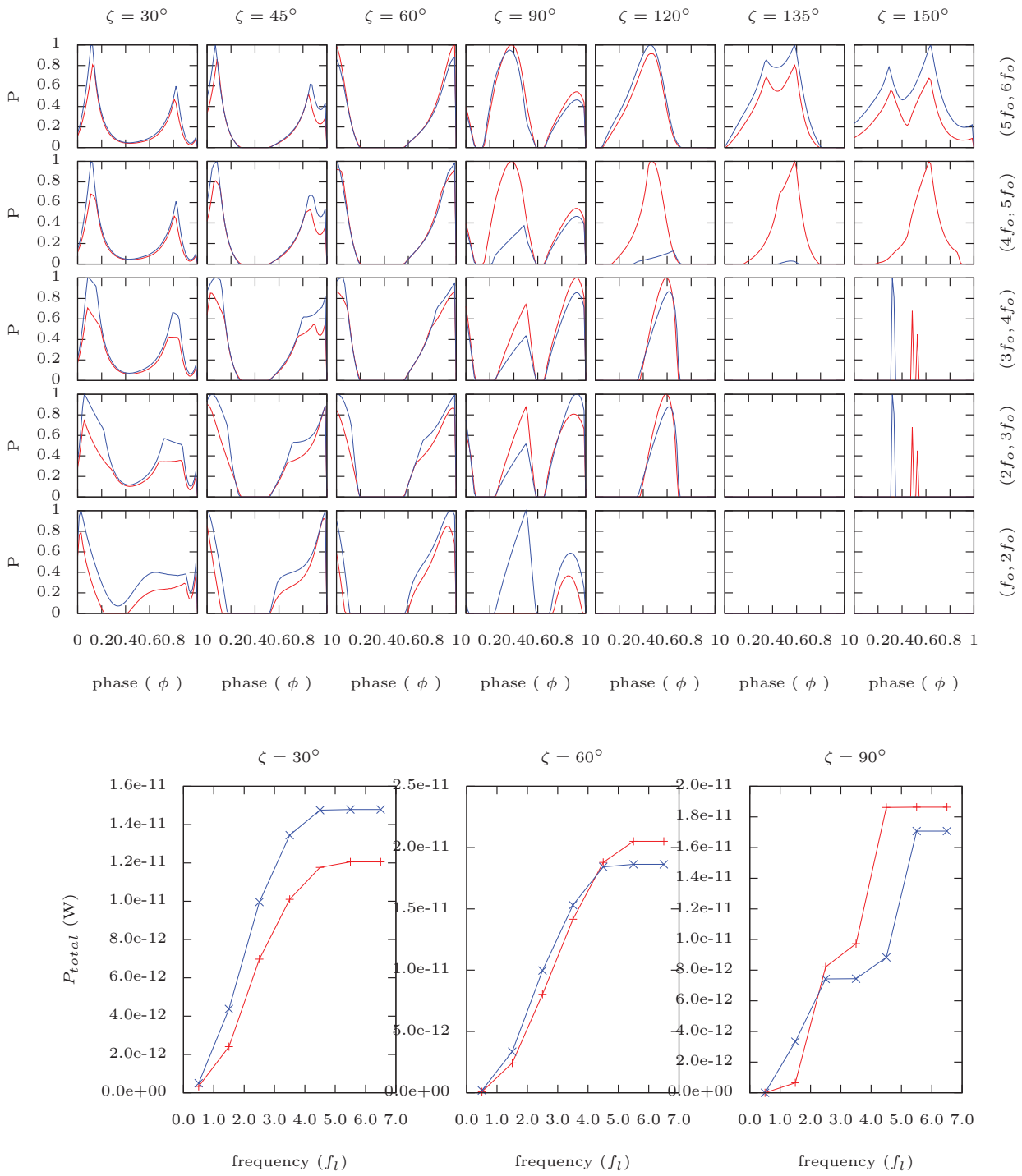

Figure 4-20: **Top :** Frequency resolved radio emission light curves for $(\alpha, \beta, \delta) = (30°, 0°, 0°)$ for $\gamma = 10 - 10^3$ for the centred case ($\epsilon = 0$, in red) and the off-centred case ($\epsilon = 0.2$, in blue) for various line of sights (ζ) shown on top of each column. The $x - axis$ represent phase (ϕ) being normalized to one. The $y - axis$ shows emitted power (P) which is being normalized with respect to the power emitted for the unit with maximum power for each corresponding ζ. Each row corresponds to one frequency range (f_l, f_u); lowest row for $(f_o, 2f_o)$ and top most is for $(5f_o, 6f_o)$ each divided in equal intervals. **Bottom :** The $x - axis$ represent the lower frequency f_l of the frequency range increasing in equal steps and the $y - axis$ shows the total power emitted summed up for each corresponding ζ, P_{total} (in W).

frequency are approximate solutions as we manually input the value of γ from the literature. A more accurate solution would be to use γ calculated from the analytical solutions of electric field. Two, the power distribution is highly sensitive to the value of γ, so considering a wider range, could help converge the results to a better precision and help in finding the point where the power peaks which would be the approximate central point for the distribution.

Chapter 5

Discussions

In this chapter, we discuss the conclusions of the entire work presented in this thesis while also talking about how the techniques and methods we have used could be improved further. We end by discussing the possible projects which could follow this work and/or could add more to it as an extensive study.

5.1 Conclusions

We have based our study on the fact that electromagnetic field strength and topology of pulsars plays a central role in the investigation of understanding these mysterious objects. Almost all the physical processes in the magnetosphere of pulsars, rely on the field topology, in one way or another. Most importantly, the processes like the acceleration of the relativistic particles, the radiation emitted by them and the entire emission mechanism, in general, need a proper and the best possible description of the field we can formulate. Our ultimate aim has been to look beyond the prevalent conventional ideas used through out in literature without being based on valid reasons apart from mere simplification of models.

The first and the major part of the thesis questions the standard assumptions of the electromagnetic field topology prevalent in the field. The usual consideration of centred dipolar magnetic field is a simplification of the field to a great extent. We make an effort to highlight the significance of the off centred magnetic field model,

which is a more realistic and more general approximation towards a more accurate description of the electromagnetic field. The analytical field equations and the basic modelling theory of the off centred approach (Petri, 2016) has been used to study its consequences on pulsar physics (Kundu & Petri, 2017). Studying the magnetospheric structure using this approach has been the very first step to visualize the field line topology spread out in the magnetosphere. Comparing it with the standard centred model helped us investigate the inferences solely based on magnetic field structure and also emphasize on the implications of those inferences. The structure of the field line is shown to be asymmetric for the off centred approach as compared to the standard centred case. This led us to confirm the argument given by Petri (2016) claiming that this asymmetry would reflect even in the region outside the light cylinder through the striped wind originating from inside.

After field line structure, we focused on the polar cap geometry because of their significance in defining the different form of field lines. The field lines emanating from the polar cap are considered to be the open field lines, which gives us a boundary for the closed magnetosphere. Various orientations of the pulsar's magnetic dipole axis with respect to the rotation axis and also the shift of the centre of the former's axis from the latter's are considered. A comparison of standard and off centred approach for the polar cap geometry is made for all these cases and geometry based conclusions are drawn. A clear contrast in size of the polar cap for different approaches led to an inference that the pulse beam width would be different, too. It leads to a proposition that the pulse width discrepancies in observations deviating from the standard models could be justified by considering the off centred approach. Another significant difference is noticed for some cases like the orthogonal cases, where the rotation axis is perpendicular to the magnetic dipole axis. These cases showed the 'width' of the polar cap in terms of azimuth angle ϕ to be varying for both the approaches. This could imply a delay in phase and time lag for different wavelengths shown in various observations. However, this implication was not concluding since this was a pure geometrical study of the polar cap.

The sky maps for radio and high energy emission were then studied, making a

comparison for both approaches. However, owing to the low shift ϵ from the centred frame, the differences are not very prominent. Hence, light curves are calculated which consider one particular line of sight from a sky map and show the intensity of the emission in finer detail for comparison. The light curves for radio and high energy emission showed complementing behaviour, meaning, the high energy emission peaked for phases where radio emission is at its minimum. This is in agreement with the models considered for our calculations in which radio emission is considered to be close to the polar caps and high energy emission in the rest of the magnetosphere. The size difference in polar cap geometry was inflicted in emission diagrams, too. The phase difference between the radio and the high energy emission in light curves is analyzed for different line of sights, which is explained to be showing the time lag between the two peaks. This time delay between the radio and high energy emission regime has been one of the observational results presented in the second Fermi gamma ray telescope catalogue. We propose that our analysis of light curves showing similar time lag could be one of the contributing factors to explain such observational lags.

In a nutshell, this part of the thesis extended the radio and high-energy pulsed emission properties of the rotating dipole to an off-centred rotating dipole and provided reasonable arguments in favour of the off-centred topology in being a reliable approach attempting to better fit the pulsar emission features.

The latter part of the thesis is devoted to investigating the broadband spectrum of pulsar radiation. The objective is to explore the evolution of emission features in terms of energy by calculating frequency resolved emission. The pulsar observations are well resolved in terms of frequencies attributed to the availability of the classified instruments for separate wavelength regimes and the simple methods available to isolate one wavelength from another. However, there has been no focus on inspecting the pulsar emission in terms of energy range in the models and theories in the literature. The idea is to create a map of the radio and the high energy emission regimes distributed in different frequency ranges. Again, both the centred and the off-centred approaches are examined to make a full analysis but the prime focus is to review the evolution of the pulse profile with varying frequency. The curvature radiation is

utilized as the process responsible for radiation. The maps are provided for various orientations and inclination angles.

Unlike most of the literature and investigations on emission processes, here, the power emitted by every photon is considered which depends on its frequency. This interesting feature connected to each photon, presents this work as a multi wavelength project to visualize the emission evolving from lower to higher frequencies. It contributes in envisioning which magnetospheric locations are dominated by higher frequency photons and which are influenced by lower frequency radiation. This picture is useful to comprehend the sites of emission in a finer fashion and the distribution of the radiation of different wavelengths in the magnetosphere. This is a major step forward towards connecting the theoretical models and observations and ultimately, to gain more insight in the behaviour of the physical processes in pulsars.

5.2 Possible improvements

Computational techniques have been utilized to calculate the consequences of the rotating off-centred dipolar magnetic field on pulsars using the analytical expressions for the fields. Throughout the thesis, the pulsar period has been set to $R/R_{\rm L} = 0.1$ for all cases, corresponding approximately to a 2 ms pulsar. This is chosen because lower the ratio $R/R_{\rm L}$, higher is the resolution (which depends on the radius of the star), which is proportional to the simulation time. Considerations of higher time period pulsars is theoretically possible to be inspected in this approach; so with faster computing facilities, even utilizing parallel computation techniques, it could be expanded to pulsars with larger time periods.

Similarly, because of computational and time restraints, the length element ds used to integrate magnetic field lines is chosen to be 0.01 times the radius of the pulsar. However, taking even smaller value could reveal the finer details of the structure of the field lines and the emission.

Also, for the calculations concerning the emission, the resolution factor of 1° has been used throughout to save simulation time. Replacing the current resolution to a

finer one would probably result in refined emission maps and light curves and hence, more detailed characteristics could be inferred from them.

5.3 Perspectives

The thesis marks an important initial milestone to uncover how significant and reliable the off centred approach could be. As a follow up of the consequences of the approach on the polarization features have already been published by Petri (2017b). This already provides another strong reason to pursue the continuation of this approach. Until now, we have considered the vacuum magnetosphere, the next step could be to consider the force-free magnetosphere. The solutions for this scheme are currently a work in progress. Also, one project is also to move beyond just the special relativistic effects and to include the general relativistic effects on particle motion and photon propagation. Researching the consequences for such sophisticated magnetosphere would make the approach much closer to the realistic environment. The analysis following it could refine the already significant results to a great extent. Another important prospect, the most significant of others, is to compare the radio and high-energy observational data with this model for a more profound analysis assisting in making more robust predictions regarding the nature of the emission.

Also, the investigation of the broadband spectrum of pulsar radiation is the first study ever made to consider emission resolved by frequency range. The prospects are enormous and comparing the standard model and our model while exploring it, is already a huge step to initiate it. The ultimate project could be to work on producing much more sophisticated maps and to put them on a test by making a comparison with the observational data. Upcoming future missions like the Imaging X-ray Polarimetry Explorer (IXPE) (Weisskopf et al., 2016; Houston et al., 2018) aimed on expanding understanding of high energy astrophysical processes and sources like neutron stars by measuring the polarization could be highly useful in enhance our understanding of the origin and the physical processes producing X ray emission. Making more efforts towards multi wavelength observations of the same object simultaneously could help

us in exploring the missing puzzles in the understanding of the big picture of pulsars.

Appendix A

Coordinate frame transformation

A.1 Transformation of coordinates

A.1.1 From magnetic axis frame to rotation axis frame :

To ensure that no points are lost attributed to the complexity of the off-centred geometry, we begin all our calculations considering the initial coordinates with respect to the magnetic axis frame and then, make a transformation to the rotation axis frame for further simulations. The transformation between the two frames requires two steps of rotation; first along the y-axis and then second one along the z-axis. Rotation matrix for such transformations (Arfken et al., 2013), respectively, are:

$$\mathbf{R}(y) = \begin{bmatrix} \cos\theta & 0 & \sin\theta \\ 0 & 1 & 0 \\ -\sin\theta & 0 & \cos\theta \end{bmatrix}$$

and

$$\mathbf{R}(z) = \begin{bmatrix} \cos\phi & -\sin\phi & 0 \\ \sin\phi & \cos\phi & 0 \\ 0 & 0 & 1 \end{bmatrix}$$

where θ and ϕ are the polar and the azimuth angles for poles with respect to the rotation axis. We get the coordinates in rotation axis frame ($\mathbf{x}$) using above transformation matrices and the coordinates in the magnetic axis frame ($\mathbf{x}'$) using

$\mathbf{x} = \mathbf{R}(z)\mathbf{R}(y)\mathbf{x}'$.

A.1.2 Between Cartesian coordinate system and spherical coordinate system :

To transform the Cartesian coordinates (x, y, z) to spherical coordinate system (r, θ, ϕ), we use the standard transformation (Griffiths, 2013):

$r = \sqrt{x^2 + y^2 + z^2}$

$\theta = \cos^{-1} \frac{z}{r}$

$\phi = \tan^{-1} \frac{y}{x}$

and the following for the inverse transformation :

$x = r \sin\theta \cos\phi$

$y = r \sin\theta \sin\phi$

$z = r \cos\theta$

with $\theta \in [0, \pi]$, $\phi \in [0, 2\pi)$ and $r \in [0, \infty)$.

A.2 Transformation of magnetic field from spherical coordinate system to Cartesian coordinate system

To transform the magnetic field from the spherical coordinates (B_r, B_θ, B_ϕ) to Cartesian coordinates (B_x, B_y, B_z), following transformation scheme was used :
Writing the total magnetic field $\mathbf{B}$ in terms of spherical coordinates using spherical unit basis vector $(\hat{\mathbf{r}}, \hat{\boldsymbol{\theta}}, \hat{\boldsymbol{\phi}})$,

$$\mathbf{B}(r, \theta, \phi) = B_r(r, \theta, \phi)\hat{\mathbf{r}} + B_\theta(r, \theta, \phi)\hat{\boldsymbol{\theta}} + B_\phi(r, \theta, \phi)\hat{\boldsymbol{\phi}}. \tag{A.1}$$

Now, to convert the spherical unit basis vector to Cartesian unit basis vector, the transformation equations (Griffiths, 2013) are :

$\hat{\mathbf{r}} = \sin\theta \cos\phi \hat{\mathbf{x}} + \sin\theta \sin\phi \hat{\mathbf{y}} + \cos\theta \hat{\mathbf{z}}$

$\hat{\boldsymbol{\theta}} = \cos\theta\cos\phi\hat{\mathbf{x}} + \cos\theta\sin\phi\hat{\mathbf{y}} - \sin\theta\hat{\mathbf{z}}$

$\hat{\boldsymbol{\phi}} = -\sin\phi\hat{\mathbf{x}} + \cos\phi\hat{\mathbf{y}}.$

Using above transformation equations in Eqn. (A.1) and then, comparing all individual components of the magnetic field with,

$$\mathbf{B}(r,\theta,\phi) = B_x(r,\theta,\phi)\hat{\mathbf{x}} + B_y(r,\theta,\phi)\hat{\mathbf{y}} + B_z(r,\theta,\phi)\hat{\mathbf{z}}$$

we get, the individual components of the magnetic field in Cartesian coordinate system as, $B' = T\,B$ where $B' = (B_x, B_y, B_z)$ and $B = (B_r, B_\theta, B_\phi)$ are magnetic fields in Cartesian and spherical coordinates respectively, and T is the transformation matrix written as :

$$\begin{bmatrix} \sin\theta\cos\phi & \cos\theta\cos\phi & -\sin\phi \\ \sin\theta\sin\phi & \cos\theta\sin\phi & \cos\phi \\ \cos\theta & -\sin\theta & 0 \end{bmatrix}$$

Appendix B

An atlas for emission by curvature radiation

For details on the approach and the numerical technique used, refer Chapter 4.

B.0.1 Frequency resolved high energy emission

B.0.2 Frequency resolved radio emission

(α, β, δ)	**Maximum energy**	**Energy interval**
	$\epsilon = 0$	
$(45°, 0°, 0°)$	8.75	1.46
$(90°, 90°, 0°)$	15.65	2.61
$(90°, 45°, 90°)$	15.65	2.61
$(90°, 0°, 90°)$	15.65	2.61
$(90°, 0°, 0°)$	15.65	2.61
	$\epsilon = 0.2$	
$(45°, 0°, 0°)$	10.33	1.72
$(90°, 90°, 0°)$	15.71	2.62
$(90°, 45°, 90°)$	15.84	2.64
$(90°, 0°, 90°)$	15.74	2.62
$(90°, 0°, 0°)$	15.71	2.62

Table B.1: Calculated values of maximum energy and intervals taken for different orientations for centred $\epsilon = 0$ and off centred case $\epsilon = 0.2$ considering high energy emission. All energy values are in GeV. Refer to Fig. 3-1 for the angles α, β, δ.

(α, β, δ)	**Maximum frequency** f_u	**Frequency interval** $f_o = f_u/6$
	$\epsilon = 0$	
$(45°, 0°, 0°)$	2.09	0.35
$(90°, 90°, 0°)$	2.24	037
$(90°, 45°, 90°)$	2.24	0.37
$(90°, 0°, 90°)$	2.24	0.37
$(90°, 0°, 0°)$	2.24	0.37
	$\epsilon = 0.2$	
$(45°, 0°, 0°)$	2.50	0.42
$(90°, 90°, 0°)$	2.56	0.43
$(90°, 45°, 90°)$	2.51	0.42
$(90°, 0°, 90°)$	3.39	0.56
$(90°, 0°, 0°)$	2.56	0.43

Table B.2: Calculated values of maximum frequency and intervals taken for different orientations for centred $\epsilon = 0$ and off centred case $\epsilon = 0.2$ considering radio emission. All frequency values are in GHz. Refer to Fig. 3-1 for the angles α, β, δ.

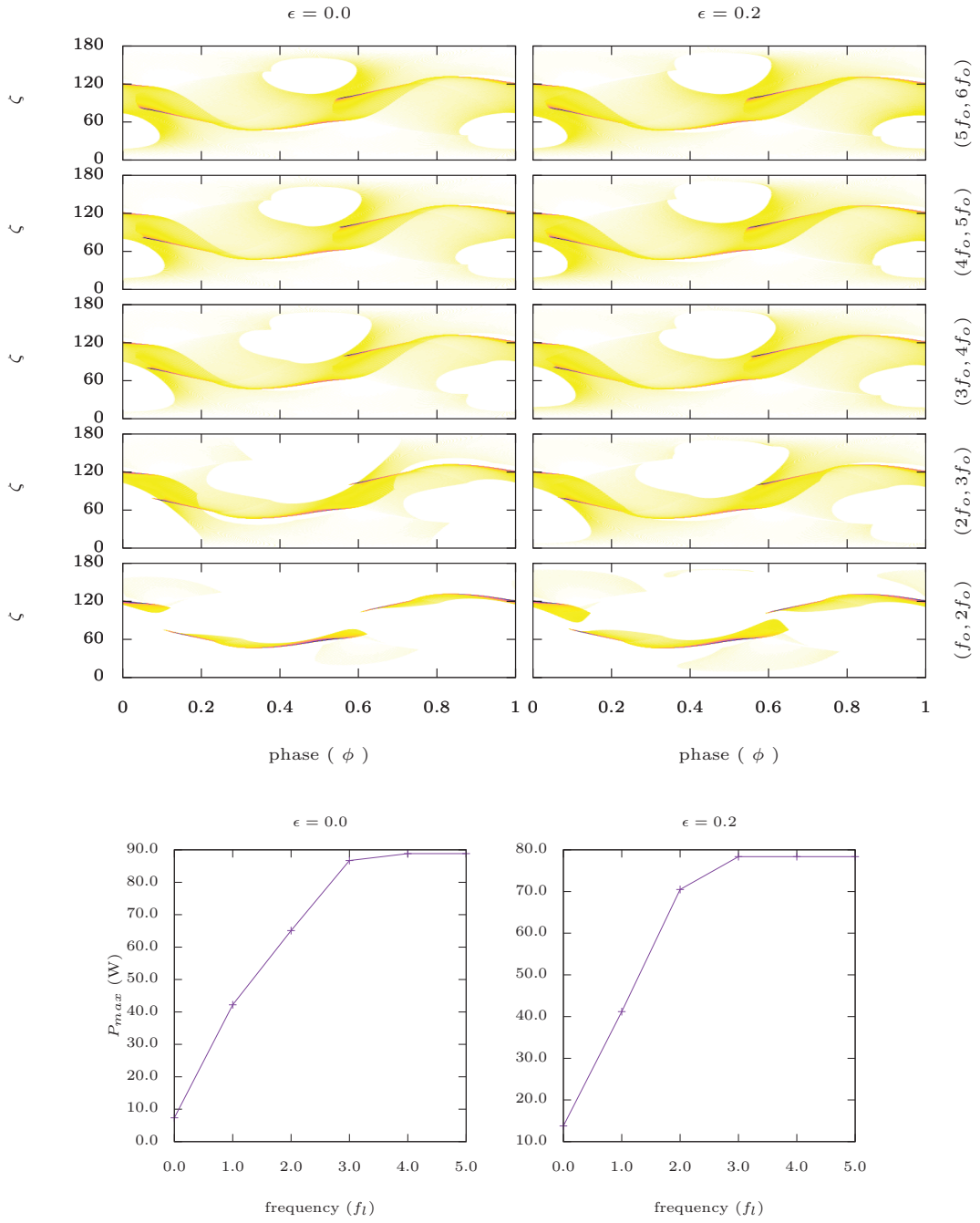

Figure B-1: **Top :** Frequency resolved high energy emission for $(\alpha, \beta, \delta) = (45°, 0°, 0°)$. The $x - axis$ and $y - axis$ represent phase (ϕ) and line of sight angle (ζ) respectively with the former being normalized to one. The panels on left and right are for the centred case $\epsilon = 0$ and for the off centred case $\epsilon = 0.2$ respectively. The lowest plot is for frequency range $(f_l, f_u) = (f_o, 2f_o)$ and top most is for $(5f_o, 6f_o)$; each increasing in steps of f_o (corresponding energy values in Table. B.1). The white region corresponds to region with no emission and moving towards blue-black via yellow-orange signifies an increase in the power emitted. **Bottom :** The $x - axis$ represent the lower frequency f_l of the frequency range increasing in steps of f_o and the $y - axis$ shows the power radiated corresponding to the unit with highest power, P_{max} (in W), which is chosen to normalize the power emitted in phase plots in top panels.

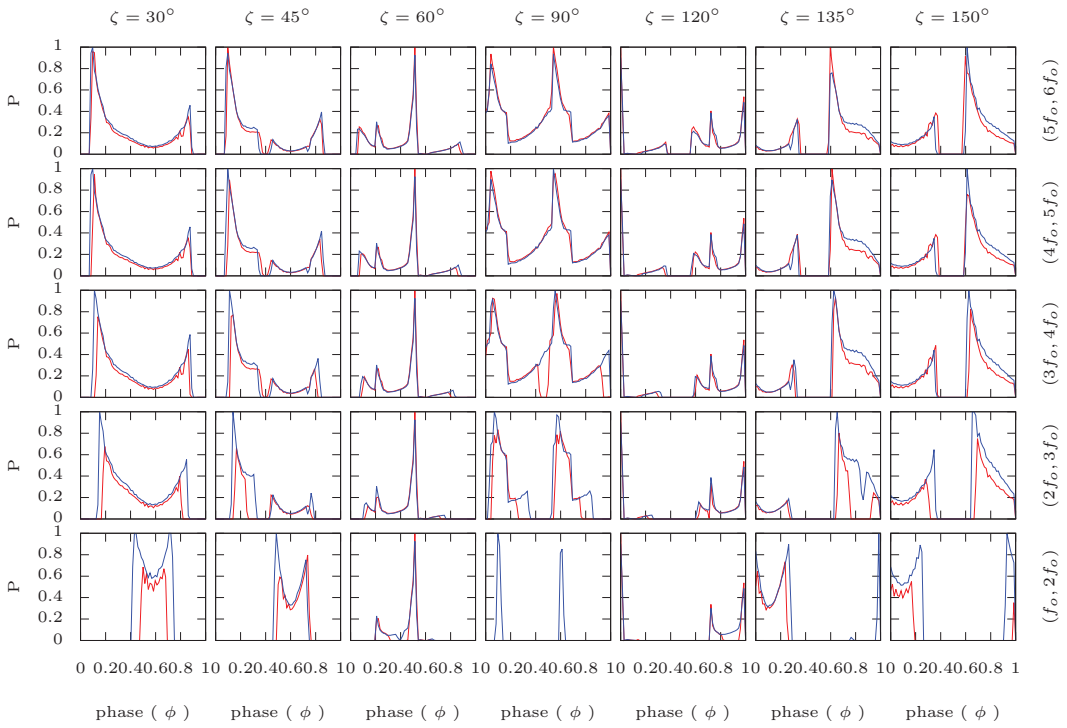

Figure B-2: Frequency resolved high energy light curves for $(\alpha, \beta, \delta) = (45°, 0°, 0°)$ for centred case ($\epsilon = 0$, in red) and off-centred case ($\epsilon = 0.2$, in blue) for various line of sights (ζ) shown on top of each column. The $x - axis$ represent phase (ϕ) being normalized to one. The $y - axis$ shows emitted power (P) which is being normalized with respect to the power emitted by the unit with maximum power for each corresponding ζ. Each row corresponds to one frequency range (f_l, f_u); lowest row for $(f_o, 2f_o)$ and top most is for $(5f_o, 6f_o)$; each increasing in steps of f_o (corresponding energy values in Table. B.1).

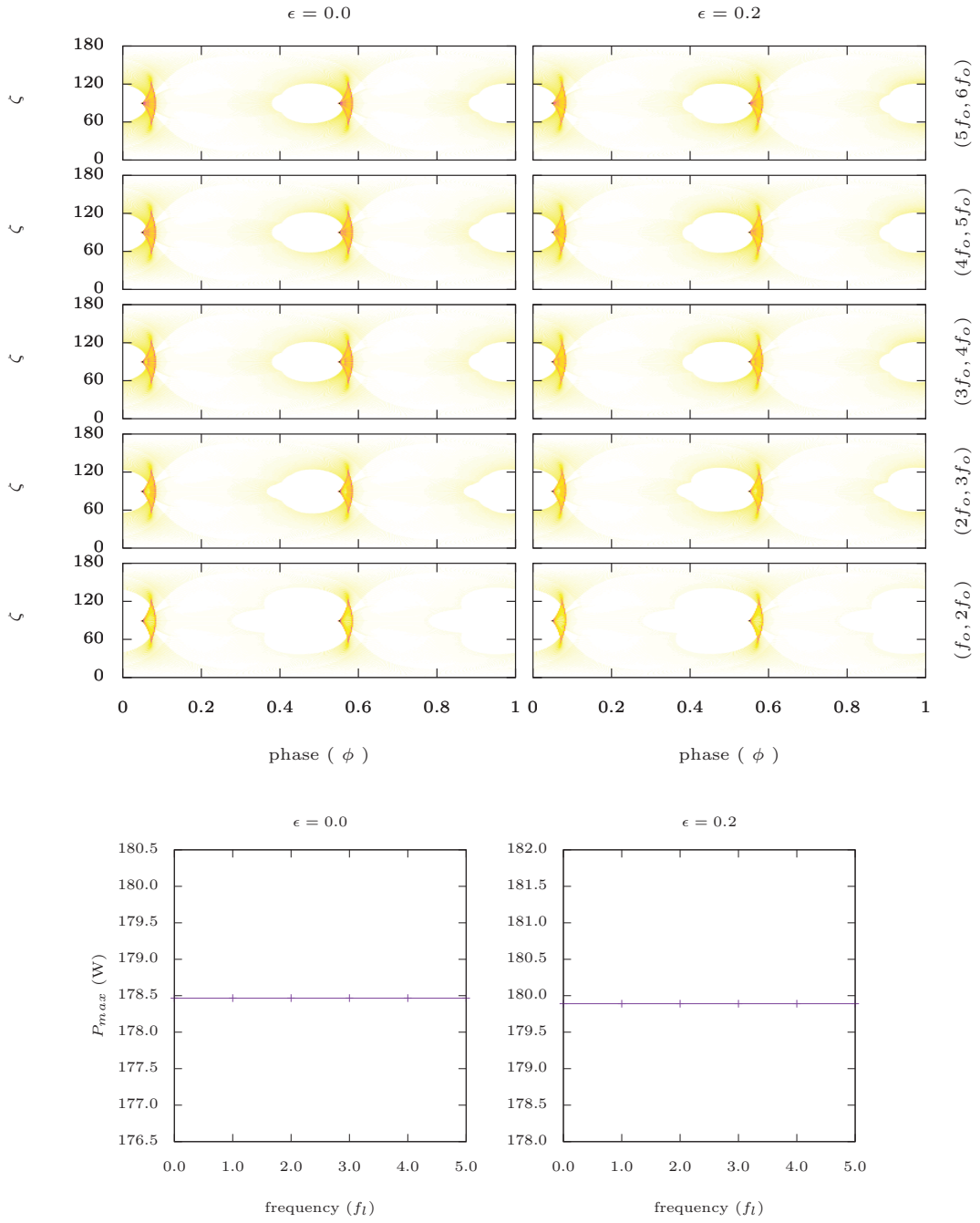

Figure B-3: **Top :** Frequency resolved high energy emission for $(\alpha, \beta, \delta) = (90°, 0°, 0°)$. The $x - axis$ and $y - axis$ represent phase (ϕ) and line of sight angle (ζ) respectively with the former being normalized to one. The panels on left and right are for the centred case $\epsilon = 0$ and for the off centred case $\epsilon = 0.2$ respectively. The lowest plot is for frequency range $(f_l, f_u) = (f_o, 2f_o)$ and top most is for $(5f_o, 6f_o)$; each increasing in steps of f_o (corresponding energy values in Table. B.1). The white region corresponds to region with no emission and moving towards blue-black via yellow-orange signifies an increase in the power emitted. **Bottom :** The $x - axis$ represent the lower frequency f_l of the frequency range increasing in steps of f_o and the $y - axis$ shows the power radiated corresponding to the unit with highest power, P_{max} (in W), which is chosen to normalize the power emitted in phase plots in top panels.

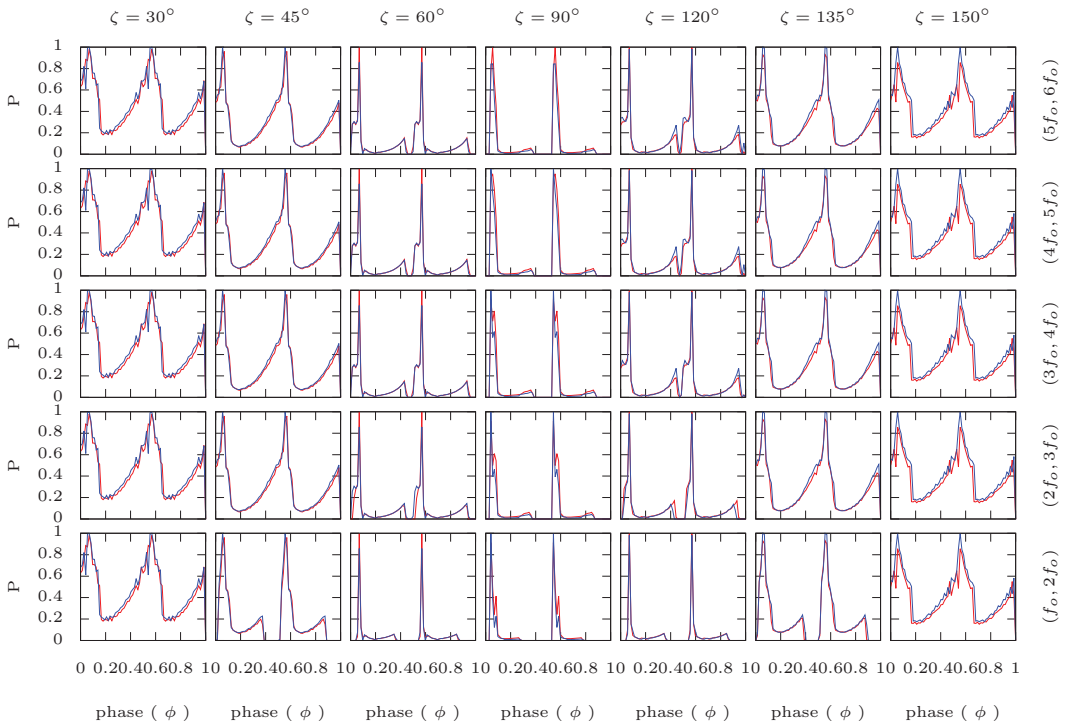

Figure B-4: Frequency resolved high energy light curves for $(\alpha, \beta, \delta) = (90°, 0°, 0°)$ for centred case ($\epsilon = 0$, in red) and off-centred case ($\epsilon = 0.2$, in blue) for various line of sights (ζ) shown on top of each column. The $x - axis$ represent phase (ϕ) being normalized to one. The $y - axis$ shows emitted power (P) which is being normalized with respect to the power emitted by the unit with maximum power for each corresponding ζ. Each row corresponds to one frequency range (f_l, f_u); lowest row for $(f_o, 2f_o)$ and top most is for $(5f_o, 6f_o)$; each increasing in steps of f_o (corresponding energy values in Table. B.1).

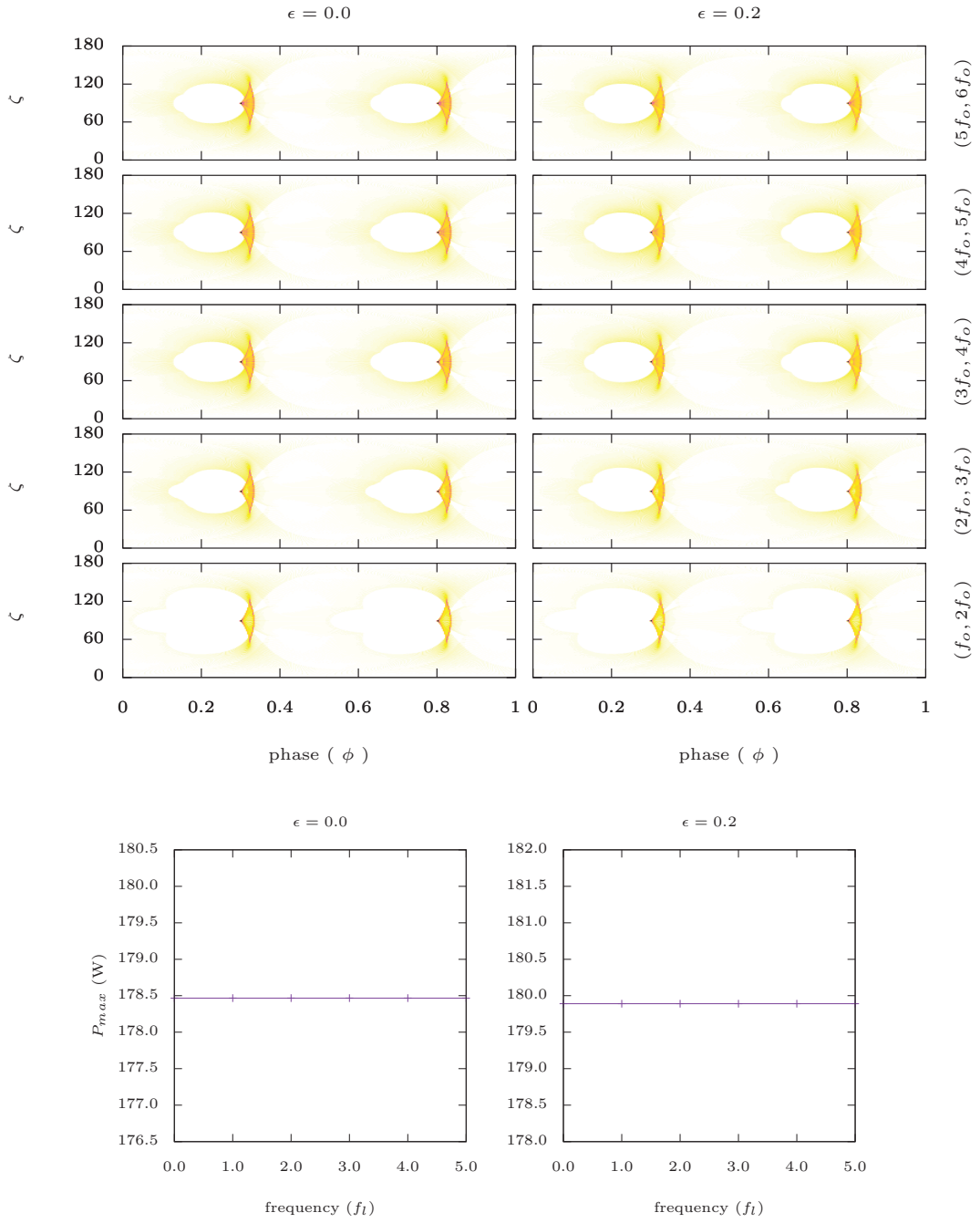

Figure B-5: **Top :** Frequency resolved high energy emission for $(\alpha, \beta, \delta) = (90°, 90°, 0°)$. The $x - axis$ and $y - axis$ represent phase (ϕ) and line of sight angle (ζ) respectively with the former being normalized to one. The panels on left and right are for the centred case $\epsilon = 0$ and for the off centred case $\epsilon = 0.2$ respectively. The lowest plot is for frequency range $(f_l, f_u) = (f_o, 2f_o)$ and top most is for $(5f_o, 6f_o)$; each increasing in steps of f_o (corresponding energy values in Table. B.1). The white region corresponds to region with no emission and moving towards blue-black via yellow-orange signifies an increase in the power emitted. **Bottom :** The $x - axis$ represent the lower frequency f_l of the frequency range increasing in steps of f_o and the $y - axis$ shows the power radiated corresponding to the unit with highest power, P_{max} (in W), which is chosen to normalize the power emitted in phase plots in top panels.

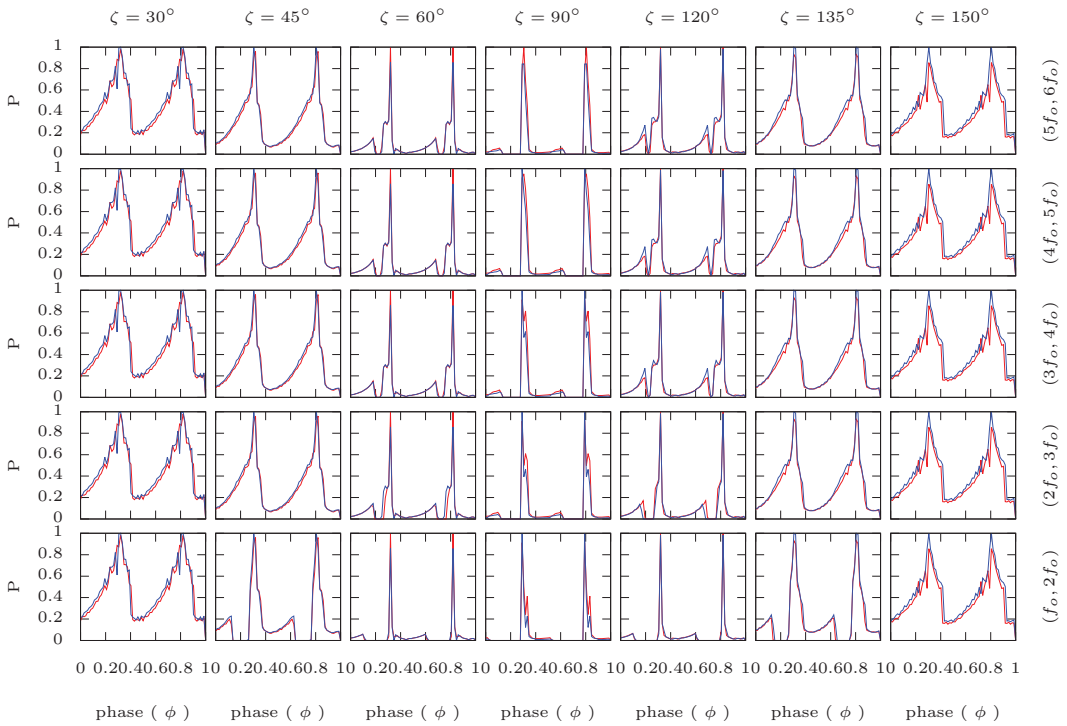

Figure B-6: Frequency resolved high energy light curves for $(\alpha, \beta, \delta) = (90°, 90°, 0°)$ for centred case ($\epsilon = 0$, in red) and off-centred case ($\epsilon = 0.2$, in blue) for various line of sights (ζ) shown on top of each column. The $x - axis$ represent phase (ϕ) being normalized to one. The $y - axis$ shows emitted power (P) which is being normalized with respect to the power emitted by the unit with maximum power for each corresponding ζ. Each row corresponds to one frequency range (f_l, f_u); lowest row for $(f_o, 2f_o)$ and top most is for $(5f_o, 6f_o)$; each increasing in steps of f_o (corresponding energy values in Table. B.1).

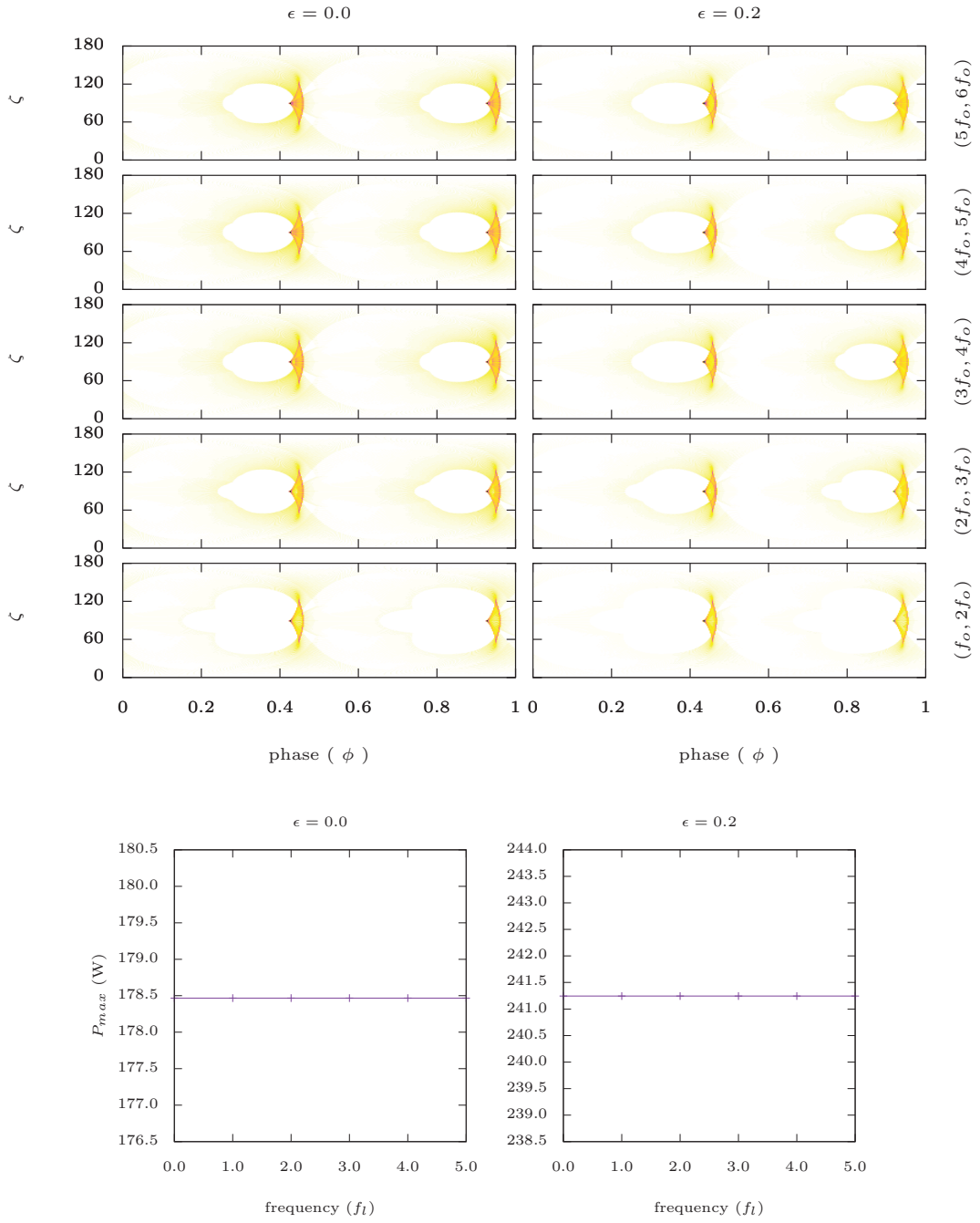

Figure B-7: **Top :** Frequency resolved high energy emission for $(\alpha, \beta, \delta) = (90°, 45°, 90°)$. The $x-axis$ and $y-axis$ represent phase (ϕ) and line of sight angle (ζ) respectively with the former being normalized to one. The panels on left and right are for the centred case $\epsilon = 0$ and for the off centred case $\epsilon = 0.2$ respectively. The lowest plot is for frequency range $(f_l, f_u) = (f_o, 2f_o)$ and top most is for $(5f_o, 6f_o)$; each increasing in steps of f_o (corresponding energy values in Table. B.1). The white region corresponds to region with no emission and moving towards blue-black via yellow-orange signifies an increase in the power emitted. **Bottom :** The $x-axis$ represent the lower frequency f_l of the frequency range increasing in steps of f_o and the $y-axis$ shows the power radiated corresponding to the unit with highest power, P_{max} (in W), which is chosen to normalize the power emitted in phase plots in top panels.

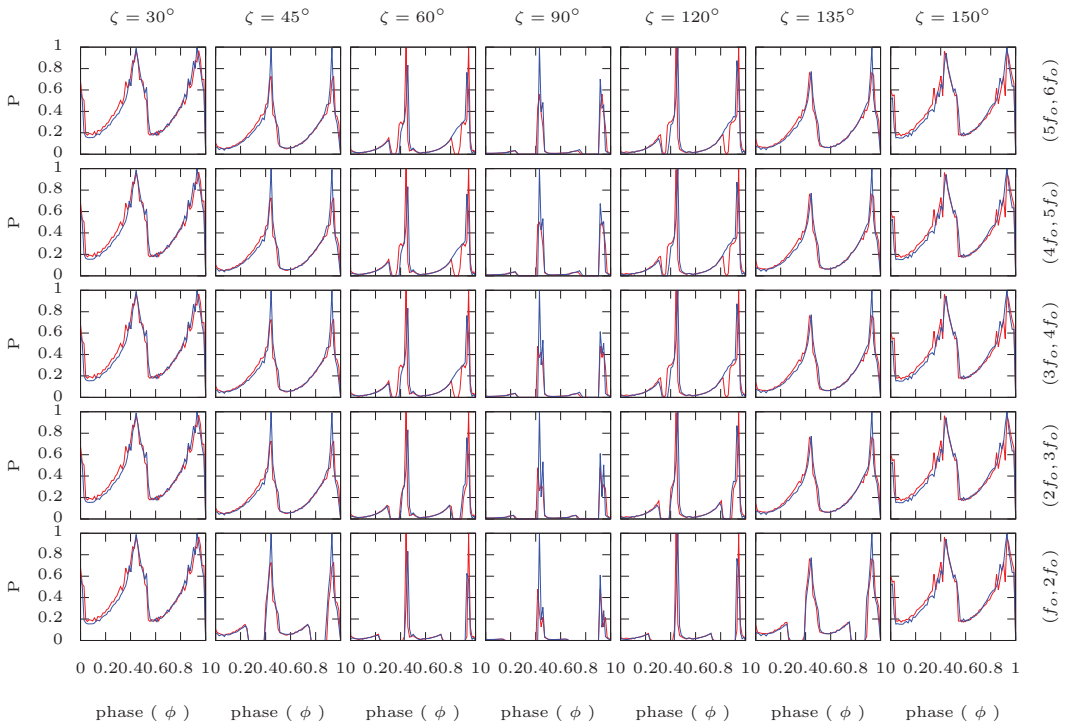

Figure B-8: Frequency resolved high energy light curves for $(\alpha, \beta, \delta) = (90°, 45°, 90°)$ for centred case ($\epsilon = 0$, in red) and off-centred case ($\epsilon = 0.2$, in blue) for various line of sights (ζ) shown on top of each column. The $x - axis$ represent phase (ϕ) being normalized to one. The $y - axis$ shows emitted power (P) which is being normalized with respect to the power emitted by the unit with maximum power for each corresponding ζ. Each row corresponds to one frequency range (f_l, f_u); lowest row for $(f_o, 2f_o)$ and top most is for $(5f_o, 6f_o)$; each increasing in steps of f_o (corresponding energy values in Table. B.1).

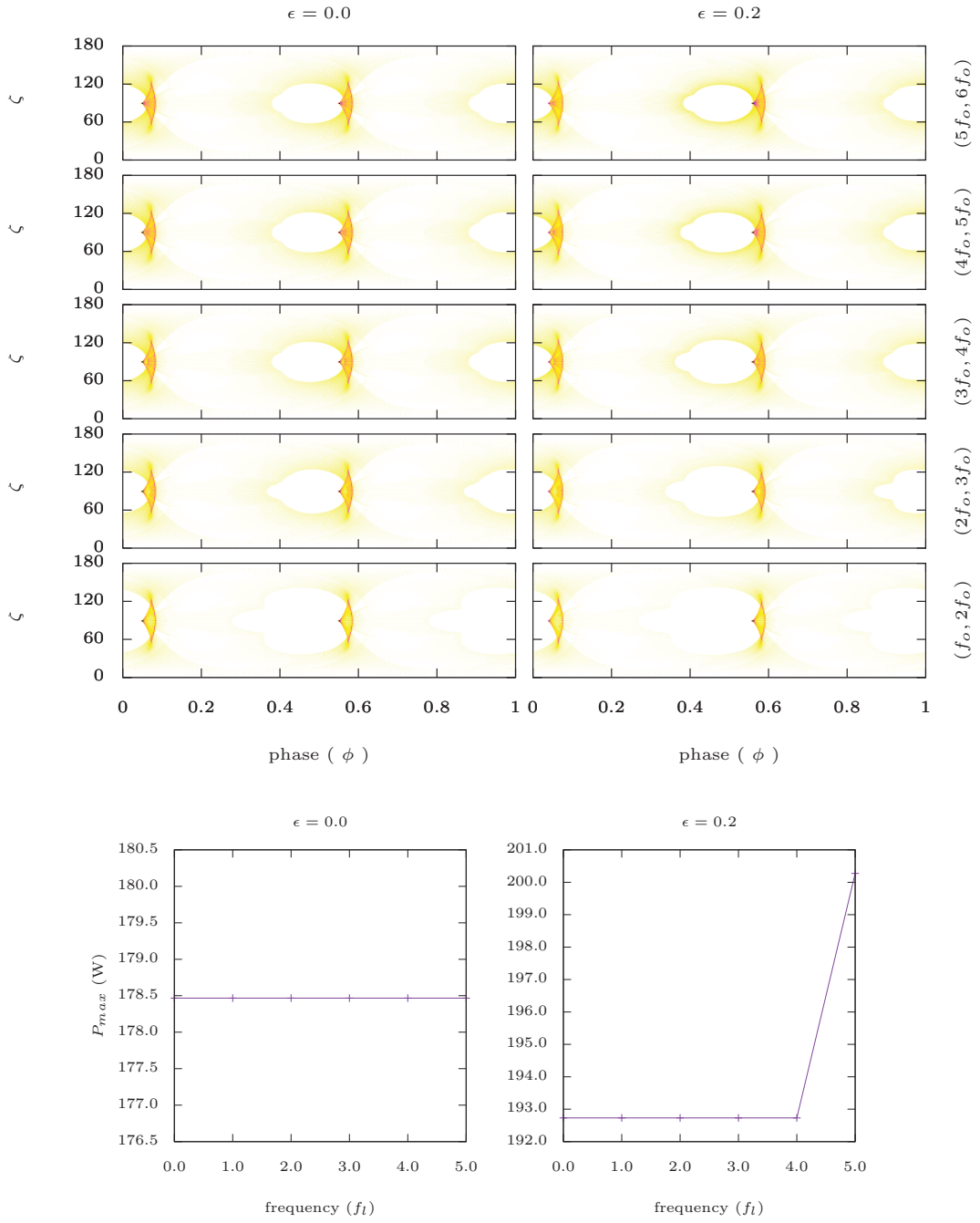

Figure B-9: **Top :** Frequency resolved high energy emission for $(\alpha, \beta, \delta) = (90°, 0°, 90°)$. The $x - axis$ and $y - axis$ represent phase (ϕ) and line of sight angle (ζ) respectively with the former being normalized to one. The panels on left and right are for the centred case $\epsilon = 0$ and for the off centred case $\epsilon = 0.2$ respectively. The lowest plot is for frequency range $(f_l, f_u) = (f_o, 2f_o)$ and top most is for $(5f_o, 6f_o)$; each increasing in steps of f_o (corresponding energy values in Table. B.1). The white region corresponds to region with no emission and moving towards blue-black via yellow-orange signifies an increase in the power emitted. **Bottom :** The $x - axis$ represent the lower frequency f_l of the frequency range increasing in steps of f_o and the $y - axis$ shows the power radiated corresponding to the unit with highest power, P_{max} (in W), which is chosen to normalize the power emitted in phase plots in top panels.

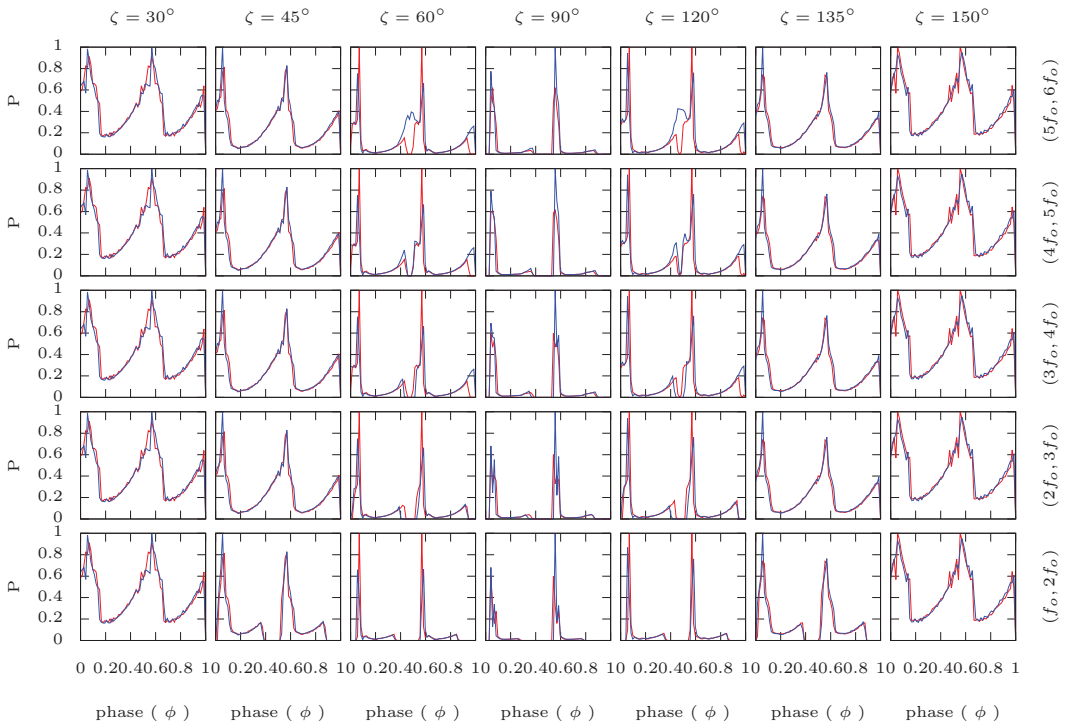

Figure B-10: Frequency resolved high energy light curves for $(\alpha, \beta, \delta) = (90°, 0°, 90°)$ for centred case ($\epsilon = 0$, in red) and off-centred case ($\epsilon = 0.2$, in blue) for various line of sights (ζ) shown on top of each column. The $x - axis$ represent phase (ϕ) being normalized to one. The $y - axis$ shows emitted power (P) which is being normalized with respect to the power emitted by the unit with maximum power for each corresponding ζ. Each row corresponds to one frequency range (f_l, f_u); lowest row for $(f_o, 2f_o)$ and top most is for $(5f_o, 6f_o)$; each increasing in steps of f_o (corresponding energy values in Table. B.1).

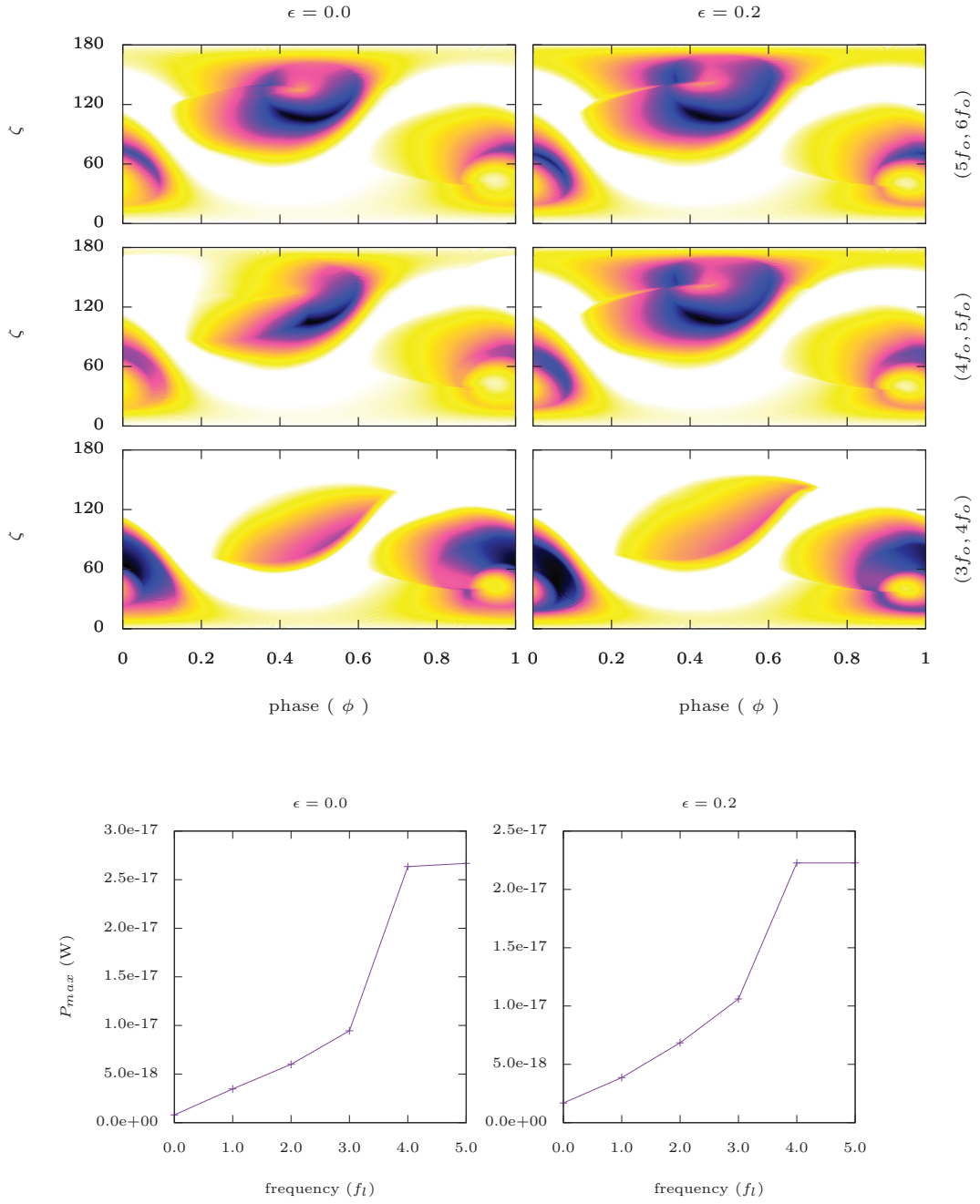

Figure B-11: **Top :** Frequency resolved radio emission for $(\alpha, \beta, \delta) = (45°, 0°, 0°)$. The $x-axis$ and $y-axis$ represent phase (ϕ) and line of sight angle (ζ) respectively with the former being normalized to one. The panels on left and right are for the centred case $\epsilon = 0$ and for the off centred case $\epsilon = 0.2$ respectively. The lowest plot is for frequency range $(f_l, f_u) = (3f_o, 4f_o)$ and top most is for $(5f_o, 6f_o)$; each increasing in steps of f_o (value in Table. B.2). The white region corresponds to region with no emission and moving towards blue-black via yellow-orange signifies an increase in the power emitted. **Bottom :** The $x-axis$ represent the lower frequency f_l of the frequency range increasing in steps of f_o and the $y-axis$ shows the power radiated corresponding to the unit with highest power, P_{max} (in W), which is chosen to normalize the power emitted in phase plots in top panels.

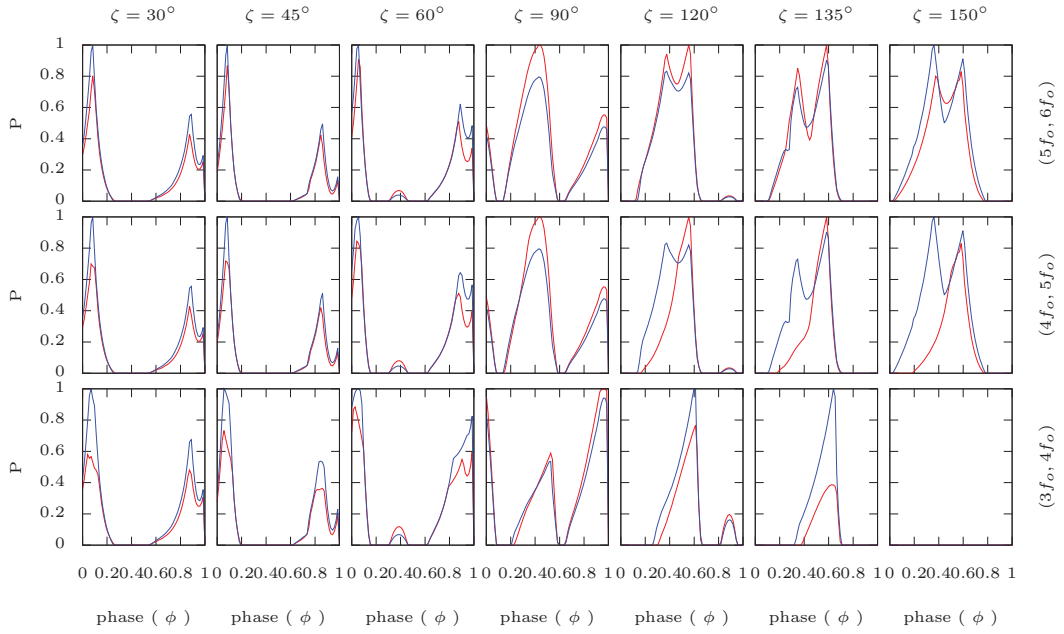

Figure B-12: Frequency resolved radio emission light curves for $(\alpha, \beta, \delta) = (45°, 0°, 0°)$ for centred case ($\epsilon = 0$, in red) and off-centred case ($\epsilon = 0.2$, in blue) for various line of sights (ζ) shown on top of each column. The $x - axis$ represent phase (ϕ) being normalized to one. The $y - axis$ shows emitted power (P) which is being normalized with respect to the power emitted by the unit with maximum power for each corresponding ζ. Each row corresponds to one frequency range (f_l, f_u); lowest row for $(3f_o, 4f_o)$ and top most is for $(5f_o, 6f_o)$; each increasing in steps of f_o (value in Table. B.2).

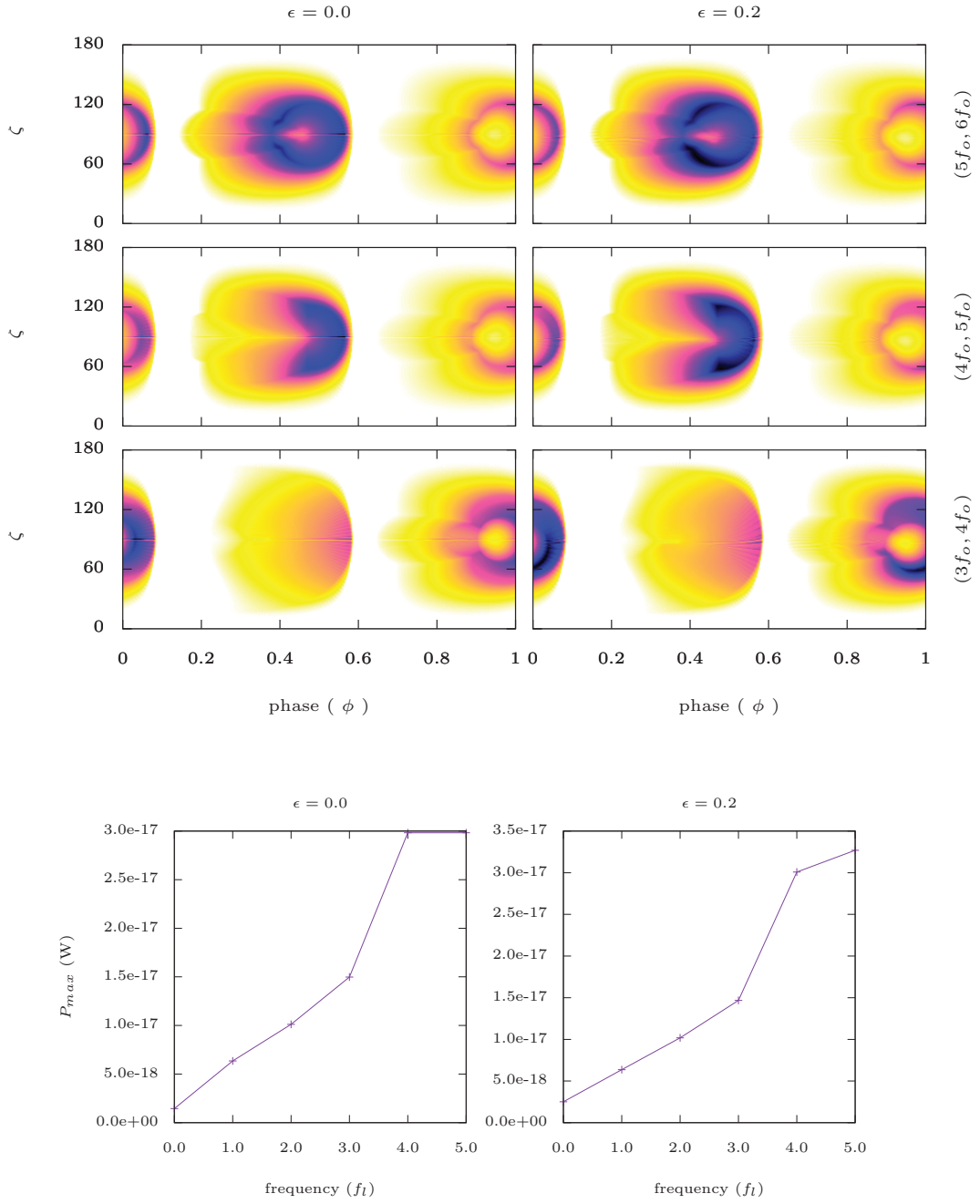

Figure B-13: **Top :** Frequency resolved radio emission for $(\alpha, \beta, \delta) = (90°, 0°, 0°)$. The $x-axis$ and $y-axis$ represent phase (ϕ) and line of sight angle (ζ) respectively with the former being normalized to one. The panels on left and right are for the centred case $\epsilon = 0$ and for the off centred case $\epsilon = 0.2$ respectively. The lowest plot is for frequency range $(f_l, f_u) = (3f_o, 4f_o)$ and top most is for $(5f_o, 6f_o)$; each increasing in steps of f_o (value in Table. B.2). The white region corresponds to region with no emission and moving towards blue-black via yellow-orange signifies an increase in the power emitted. **Bottom :** The $x-axis$ represent the lower frequency f_l of the frequency range increasing in steps of f_o and the $y-axis$ shows the power radiated corresponding to the unit with highest power, P_{max} (in W), which is chosen to normalize the power emitted in phase plots in top panels.

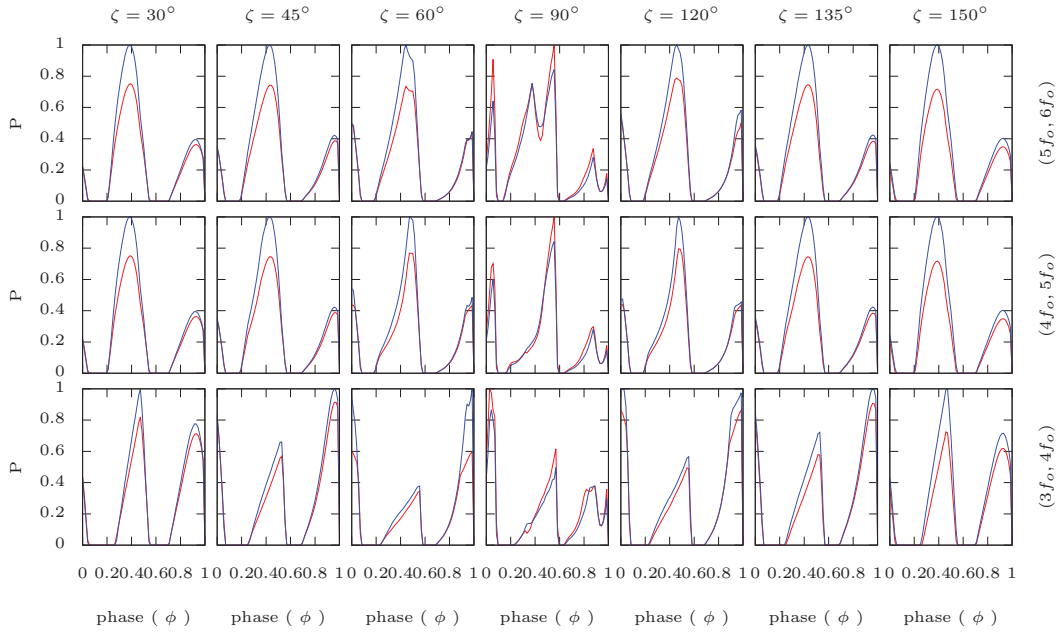

Figure B-14: Frequency resolved radio emission light curves for $(\alpha, \beta, \delta) = (90°, 0°, 0°)$ for centred case ($\epsilon = 0$, in red) and off-centred case ($\epsilon = 0.2$, in blue) for various line of sights (ζ) shown on top of each column. The $x - axis$ represent phase (ϕ) being normalized to one. The $y - axis$ shows emitted power (P) which is being normalized with respect to the power emitted by the unit with maximum power for each corresponding ζ. Each row corresponds to one frequency range (f_l, f_u); lowest row for $(3f_o, 4f_o)$ and top most is for $(5f_o, 6f_o)$; each increasing in steps of f_o (value in Table. B.2).

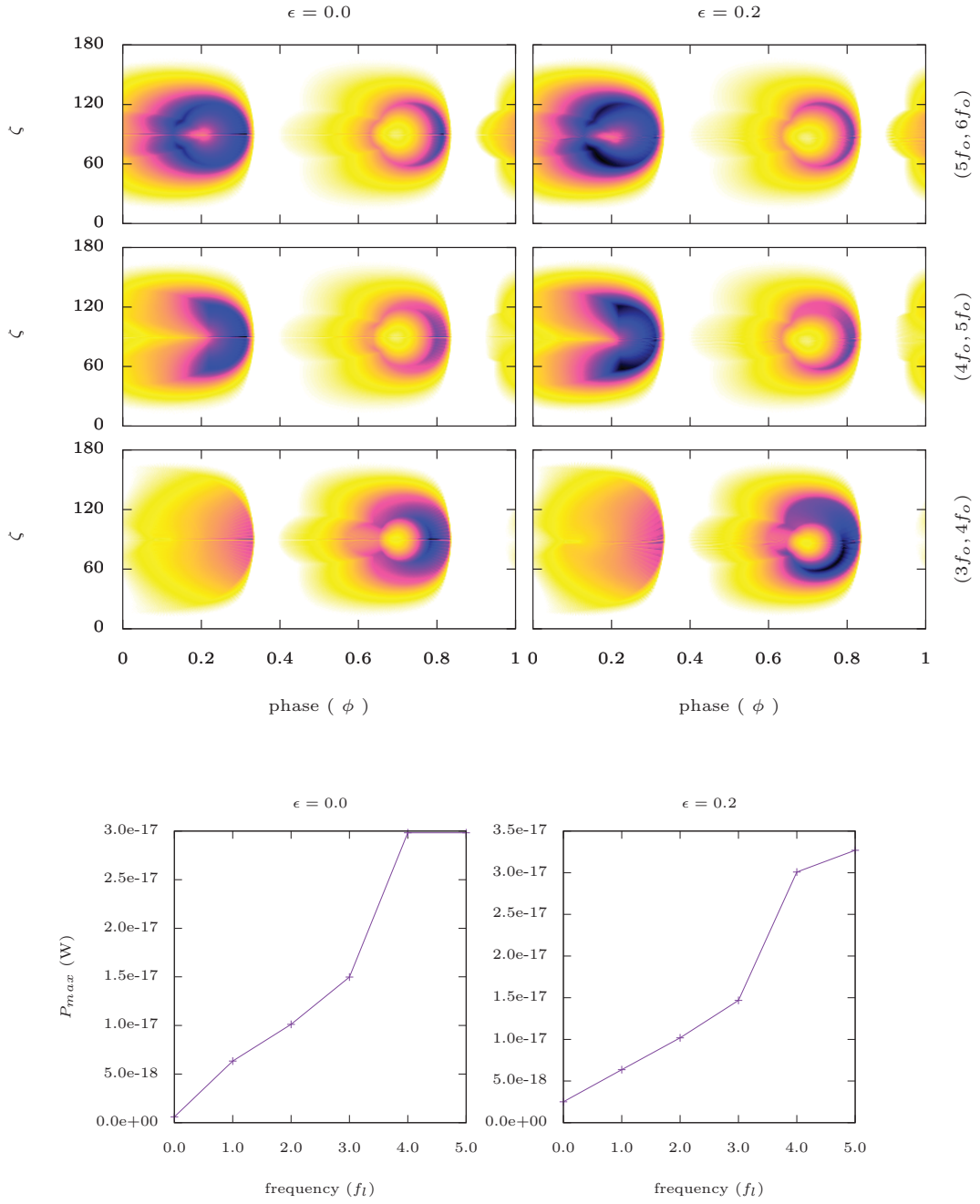

Figure B-15: **Top :** Frequency resolved radio emission for $(\alpha, \beta, \delta) = (90°, 90°, 0°)$. The $x - axis$ and $y - axis$ represent phase (ϕ) and line of sight angle (ζ) respectively with the former being normalized to one. The panels on left and right are for the centred case $\epsilon = 0$ and for the off centred case $\epsilon = 0.2$ respectively. The lowest plot is for frequency range $(f_l, f_u) = (3f_o, 4f_o)$ and top most is for $(5f_o, 6f_o)$; each increasing in steps of f_o (value in Table. B.2). The white region corresponds to region with no emission and moving towards blue-black via yellow-orange signifies an increase in the power emitted. **Bottom :** The $x - axis$ represent the lower frequency f_l of the frequency range increasing in steps of f_o and the $y - axis$ shows the power radiated corresponding to the unit with highest power, P_{max} (in W), which is chosen to normalize the power emitted in phase plots in top panels.

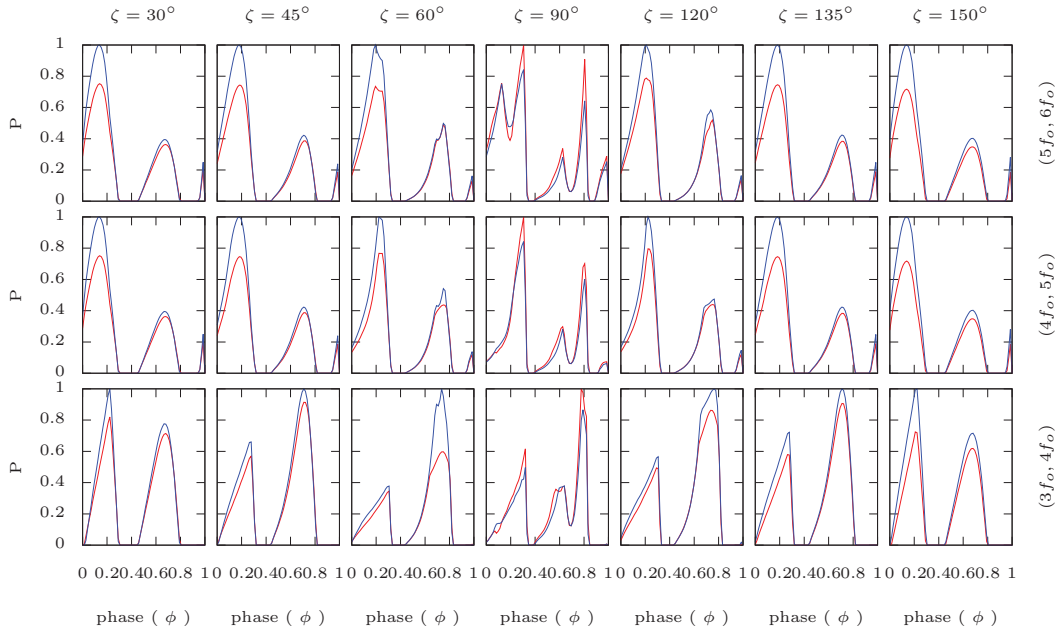

Figure B-16: Frequency resolved radio emission light curves for $(\alpha, \beta, \delta) = (90°, 90°, 0°)$ for centred case ($\epsilon = 0$, in red) and off-centred case ($\epsilon = 0.2$, in blue) for various line of sights (ζ) shown on top of each column. The $x - axis$ represent phase (ϕ) being normalized to one. The $y - axis$ shows emitted power (P) which is being normalized with respect to the power emitted by the unit with maximum power for each corresponding ζ. Each row corresponds to one frequency range (f_l, f_u); lowest row for $(3f_o, 4f_o)$ and top most is for $(5f_o, 6f_o)$; each increasing in steps of f_o (value in Table. B.2).

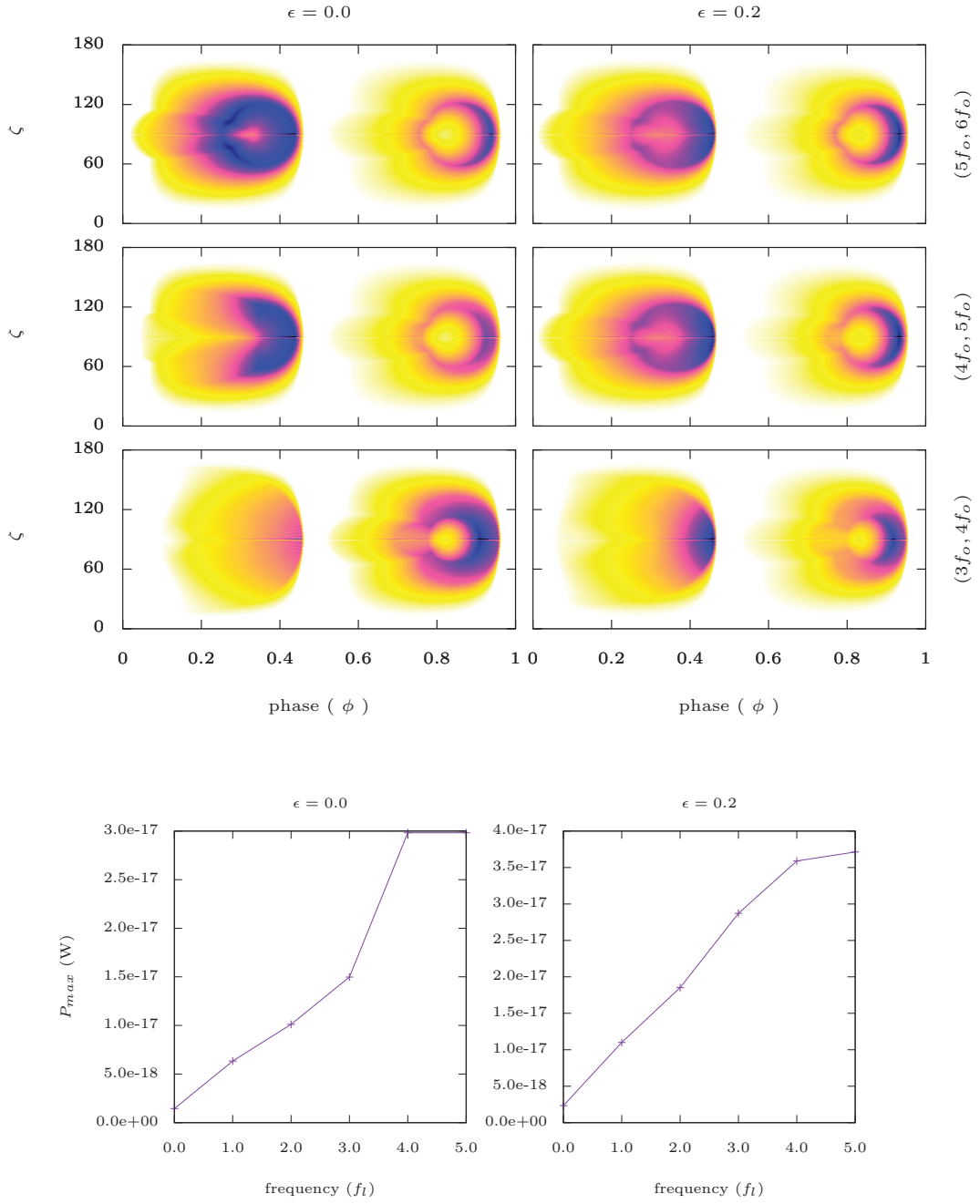

Figure B-17: **Top :** Frequency resolved radio emission for $(\alpha, \beta, \delta) = (90°, 45°, 90°)$. The $x - axis$ and $y - axis$ represent phase (ϕ) and line of sight angle (ζ) respectively with the former being normalized to one. The panels on left and right are for the centred case $\epsilon = 0$ and for the off centred case $\epsilon = 0.2$ respectively. The lowest plot is for frequency range $(f_l, f_u) = (3f_o, 4f_o)$ and top most is for $(5f_o, 6f_o)$; each increasing in steps of f_o (value in Table. B.2). The white region corresponds to region with no emission and moving towards blue-black via yellow-orange signifies an increase in the power emitted. **Bottom :** The $x - axis$ represent the lower frequency f_l of the frequency range increasing in steps of f_o and the $y - axis$ shows the power radiated corresponding to the unit with highest power, P_{max} (in W), which is chosen to normalize the power emitted in phase plots in top panels.

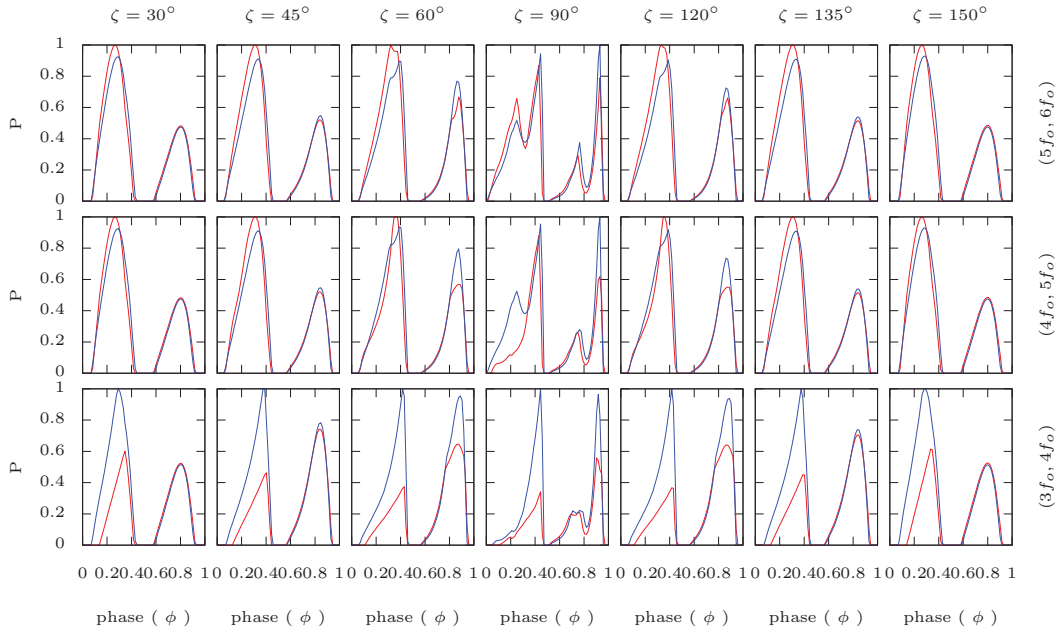

Figure B-18: Frequency resolved radio emission light curves for $(\alpha, \beta, \delta) = (90°, 45°, 90°)$ for centred case ($\epsilon = 0$, in red) and off-centred case ($\epsilon = 0.2$, in blue) for various line of sights (ζ) shown on top of each column. The $x - axis$ represent phase (ϕ) being normalized to one. The $y - axis$ shows emitted power (P) which is being normalized with respect to the power emitted by the unit with maximum power for each corresponding ζ. Each row corresponds to one frequency range (f_l, f_u); lowest row for $(3f_o, 4f_o)$ and top most is for $(5f_o, 6f_o)$; each increasing in steps of f_o (value in Table. B.2).

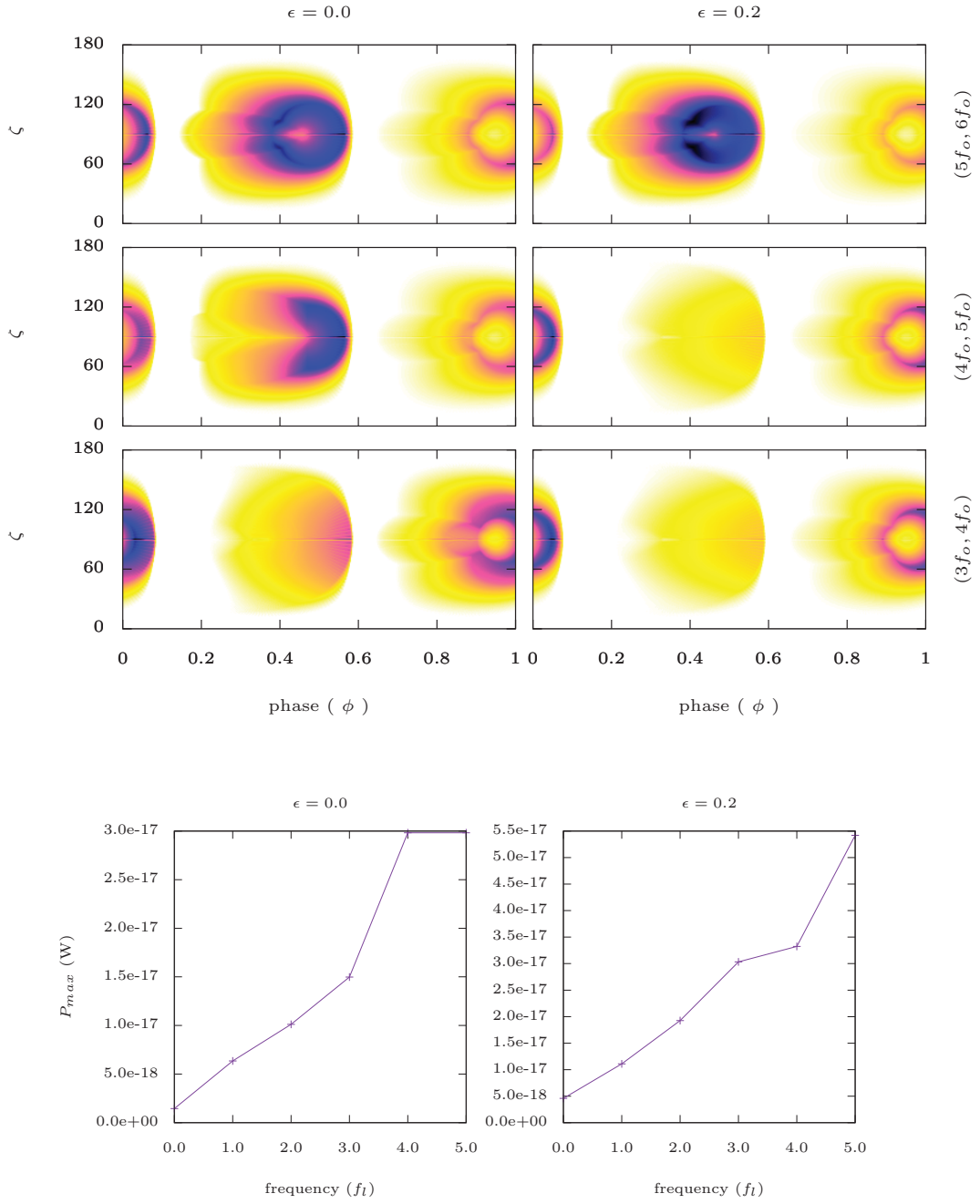

Figure B-19: **Top :** Frequency resolved radio emission for $(\alpha, \beta, \delta) = (90°, 0°, 90°)$. The $x - axis$ and $y - axis$ represent phase (ϕ) and line of sight angle (ζ) respectively with the former being normalized to one. The panels on left and right are for the centred case $\epsilon = 0$ and for the off centred case $\epsilon = 0.2$ respectively. The lowest plot is for frequency range $(f_l, f_u) = (3f_o, 4f_o)$ and top most is for $(5f_o, 6f_o)$; each increasing in steps of f_o (value in Table. B.2). The white region corresponds to region with no emission and moving towards blue-black via yellow-orange signifies an increase in the power emitted. **Bottom :** The $x - axis$ represent the lower frequency f_l of the frequency range increasing in steps of f_o and the $y - axis$ shows the power radiated corresponding to the unit with highest power, P_{max} (in W), which is chosen to normalize the power emitted in phase plots in top panels.

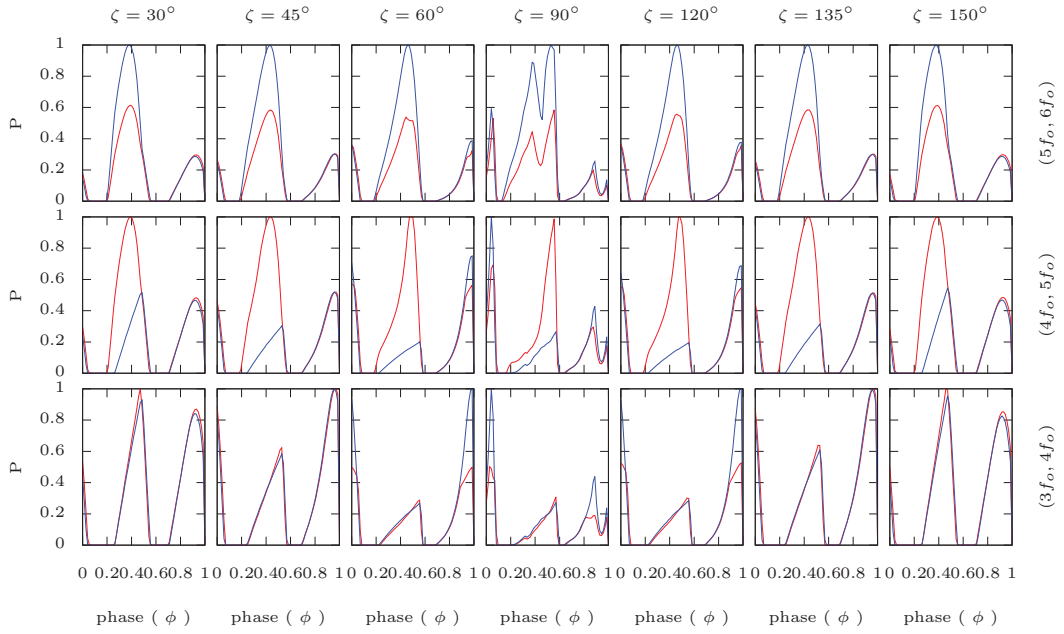

Figure B-20: Frequency resolved radio emission light curves for $(\alpha, \beta, \delta) = (90°, 0°, 90°)$ for centred case ($\epsilon = 0$, in red) and off-centred case ($\epsilon = 0.2$, in blue) for various line of sights (ζ) shown on top of each column. The $x - axis$ represent phase (ϕ) being normalized to one. The $y - axis$ shows emitted power (P) which is being normalized with respect to the power emitted by the unit with maximum power for each corresponding ζ. Each row corresponds to one frequency range (f_l, f_u); lowest row for $(3f_o, 4f_o)$ and top most is for $(5f_o, 6f_o)$; each increasing in steps of f_o (value in Table. B.2).

Appendix C

Abstract (in French)

Un astre de masse intermédiaire (masse supérieure à 8 $M_{\odot}$) termine sa vie d'étoile de la séquence principale en une gigantesque explosion appelée supernova. Au cœur de l'explosion, la matière peut se comprimer suffisamment pour donner naissance à un résidu d'étoile appelé "étoile à neutrons". Les pulsars sont une classe particulière d'étoiles à neutrons ayant des champs magnétiques puissants pouvant aller jusqu'à 10^{12} G et une période de rotation comprise entre 1,4 milliseconde et 6,67 heures. Depuis leur découverte, plusieurs tentatives ont été faites pour comprendre ces objets mystérieux. L'intensité du champ électromagnétique et sa topologie jouent un rôle central dans l'étude des pulsars. En effet, la nature du champ magnétique donne un aperçu des processus physiques tels que l'accélération des particules, le rayonnement et les mécanismes d'émission et, par conséquent, une vaste littérature existe à ce sujet.

La plupart des théories développées pour les pulsars ont été basées sur des hypothèses standards considérant que le champ magnétique est centré sur l'étoile et dipolaire. Cependant, de nouvelles découvertes ont montrées de nombreuses incohérences des modèles existants. De plus, aucun de ces modèles n'a été en mesure d'expliquer pleinement le comportement des pulsars. A la lumière de ce qui précède, des efforts ont été faits récemment pour modifier les hypothèses standards de champ centré et dipolaire afin de se concentrer sur des scénarios plus réalistes. Petri (2015), en particulier, a étudié la composante dipolaire du champ magnétique ainsi que les composantes multipolaires. Il a démontré qu'il est préférable d'inclure des composants

multipolaires dans le champ électromagnétique de manière auto-cohérente plutôt que de travailler uniquement avec un champ dipôlaire, ce qui, en effet, pourrait amener á des incohérences physiques. Ce travail a abouti á des résultats aux conséquences potentiellement drastiques dans notre compréhension du comportement de ces pulsars. En outre, une approche plus générale a été proposée dans laquelle le moment magnétique est décalé par rapport au centre géométrique de l'étoile (Petri, 2016), contrairement à l'hypothèse par défaut dans laquelle le dipôle magnétique coincide avec le centre de l'étoile. Des travaux récents ont également montré des résultats plus cohérents en utilisant les hypothèses de champ multipolaire et l'approche décentrée évoquée ci-dessus.

Cette thèse de doctorat est consacrée à l'étude des différentes caractéristiques des pulsars en utilisant une approche décentrée. Le modèle développé par Petri (2016), qui a calculé les solutions analytiques exactes du champ électromagnétique dans le vide à l'extérieur de l'étoile pour un dipôle décentré, est utilisé pour étudier les conséquences d'une telle approche sur les caractéristiques des pulsars. Notre objectif principal est d'étudier l'émission pulsée de ce dipôle magnétique excentré tournant dans le vide, dont les résultats sont publiés dans Kundu & Petri (2017) et sont résumés ci-dessous.

Nous avons calculé les effets du déplacement du centre du dipôle magnétique par rapport au centre géométrique du pulsar (c'est-à-dire excentré) sur le champ électromagnétique et sur les propriétés d'émission. Des méthodes numériques sont utilisées pour analyser le champ magnétique dipolaire excentré des pulsars à l'aide des expressions analytiques des champs mentionnés ci-dessus. Les conséquences de l'approche susmentionnée sur la structure des lignes de champ magnétique, la géométrie de la calotte polaire, les courbes de lumière et les propriétés d'émission sont examinées. La comparaison de notre approche avec le dipôle centré est détaillée afin de discuter des différences majeures dans le but de mieux comprendre le processus d'émission.

La géométrie de la calotte polaire des pulsars est calculée pour plusieurs angles d'inclinaison pour les deux cas, centré et excentré. Les deux géométries présentent un net contraste en termes de taille de la colatte. Comme la taille de cette calotte

polaire est directement liée à la largeur des pulses émis, ces différences centré/excentré sont proposées pour justifier les écarts notés dans les observations de la largeur des pulses. De plus, la comparaison d'un couple de cas spéciaux, comme le cas orthogonal où l'axe de rotation et perpendiculaire au vecteur dipôle magnétique, a montré une différence dans la position du pic des pulses indiqué par l'azimut ϕ et qui pourrait être liée aux observations de retard et de décalage de phase, comme cela a été conclu à partir des tracés de l'émission pulsée discutés plus loin.

Les courbes de lumière issues de l'émission radio et haute énergie sont ensuite comparées entre elles. Le comportement complémentaire des deux régimes de longueur d'onde est clairement visible, c'est-à-dire que l'on note un pic d'émission d'énergie élevé lorsque l'émission radio est à son minimum, ce qui est en accord avec la façon dont nous comprenons le processus d'émission. De plus, les régions où l'émission d'énergie élevée est nulle correspond à la taille de la calotte polaire car cette émission n'est pas attendue à proximité des pôles ; nous avons remarqué cette différence de taille ici aussi, du point de vue des propriétés de l'émission, contrairement à un point de vue géométrique tel que vu de la comparaison de la géométrie des calottes polaires. Pour faciliter l'observation, nous avons utilisé des courbes de lumière pour lesquelles la phase zéro correspond au pic de l'émission radio. Ainsi, en regardant la phase correspondante à l'émission haute énergie, nous obtenons la différence de phase entre les deux régimes d'émission. La différence de phase varie selon la ligne de visée. Ce retard de phase montre en fait le décalage temporel entre les deux pics qui a été observé dans certains pulsars répertoriés dans le deuxième catalogue du télescope gamma *Fermi*. Nous avons proposé que cela pourrait être l'un des facteurs qui contribuent à expliquer ces retards.

Dans cette étude, nous avons essentiellement étendu les propriétés de l'émission pulsée radio et à haute énergie du dipôle tournant à un dipôle tournant excentré et avons donné de solides arguments en faveur de la topologie excentrée comme approche fiable essayant de mieux s'adapter aux caractéristiques d'émission des pulsars. Nous avons également discuté de la façon dont on pourrait obtenir encore plus de contraintes pour les mécanismes d'émission en inspectant les caractéristiques de polarisation d'un

dipôle décentré qui ont été publiées par Petri (2017b). Cette étude des propriétés de polarisation dans le présent document a fourni une base solide pour poursuivre cette approche. Les perspectives d'avenir de cette approche résident dans les tentatives de comparaison des données d'observation radio et des données d'observation à hautes énergies et on s'attend à ce que l'analyse nous aide à faire des prédictions solides concernant la nature de l'émission pulsée des pulsars.

Une partie importante du temps de cette thèse a été consacrée à l'étude du spectre à large bande du rayonnement d'un pulsar. L'idée est de créer une carte des différentes régions d'émission des pulsars, divisées en différentes gammes de fréquences. Les cartes d'émission correspondants à différentes régions, les fréquences et les angles d'inclinaison sont discutées dans cette thèse dont le but principal est de rechercher l'évolution du profil des pulses avec la fréquence.

Cette thèse présente tous les résultats explicités ci-dessus, en s'accompagnant de discussions sur les perspectives d'avenir de l'approche employée. Par exemple, l'un des travaux potentiels qui pourraient prolonger cette étude serait d'étendre nôtre étude à une magnétosphère remplie de plasmas et déformant la structure des lignes de champ, ce qui donnerait l'occasion d'examiner un modéle plus réaliste et, par conséquent, d'affiner encore plus des résultats déjà hautement significatifs.

Appendix D

Resumé (in French)

Publications

Nombre total de publications = 2 (publiés = 1, en préparation = 1)

- Publiés
  - *Pulsed emission from a rotating off-centred magnetic dipole in vacuum*, 2017
    Kundu A., Pétri J., published in *MNRAS* (ADS entry)
- En préparation
  - *Studying the broadband spectrum of pulsar radiation*
    Kundu A., Pétri J., *in prep*

Oraux et posters

Nombre total de : Oraux = 8, Revues de conférence = 2, Posters = 3

Scientific conferences

- Oraux
  - **International Conference Physics of Neutron Stars (PNS)** à St Petersburg, Russie, du 10 au 14 juillet 2017.
    Un **oral** de 20 minutes a été présenté sur le sujet "*Pulsed emission from a*

rotating off-centred magnetic dipole in vacuum"

Un **article de revue de conférence** a été soumis (IOP entry)

– **Workshop Neutron stars and their environments (MODE-SNR-PWN)** à Caen, France, du 9 au 11 mai 2017.

Un **oral** de 25 minutes a été présenté sur le sujet "*Pulsed emission from a rotating off-centred magnetic dipole in vacuum*".

– **Semaine de l'Astrophysique Française (SF2A)** à Lyon, France, du 14 au 17 juin 2016.

Un **oral** de 15 minutes a été présenté sur le sujet "*Consequences of Off-Centred Dipolar Electromagnetic Field around Pulsars*"

Un **article de revue de conférence** a été soumis (ADS entry)

– **Le Congrés de l'Ecole Doctorale 182** à Strasbourg, France, 17 novembre 2017.

Un **oral** de 15 minutes a été présenté sur le sujet "*The mysterious dead stars : Pulsars*"

- Posters

– **European Week of Astronomy and Space Science (EWASS)** à Liverpool, Royaume-Uni, du 3 au 6 avril 2018.

Un **poster** a été présenté sur le sujet "*Understanding pulsar emission considering a rotating off-centred dipole*"

Schools/meetings

- Oraux

– **Astro lunch meeting at Observatoire Astronomique de Strasbourg** à Strasbourg, France le 24 avril 2018.

Un **oral** de 25 minutes a été présenté sur le sujet "*Understanding pulsar emission considering a rotating off-centred dipole*".

- **Journée L'Agence nationale de la recherche (ANR)** à Paris, France, le 15 novembre 2017.
  Un **oral** de 25 minutes a été présenté sur le sujet "*Électrodynamique de la magnétosphère des pulsars : équilibre, reconnexion, émission*".
- **Journal Club meeting at Observatoire Astronomique de Strasbourg** à Strasbourg, France le 10 avril 2017.
  Un **oral** de 25 minutes a été présenté sur le sujet "*Pulsed emission from a rotating off-centred dipole in vacuum*".
- **ASTERICS Virtual Observatory (VO) School** à Strasbourg, France, du 15 au 17 novembre 2016.
  Un **oral** de 10 minutes a été présenté sur le sujet "*Pulsar population distribution using ATNF and FERMI-LAT catalogue*".

- Posters

  - **1st Institute of Space Sciences Summer School : Neutron Stars and their Environments** à Barcelona, Espagne, du 3 au 7 juillet 2017.
    En association avec l'école de formation, un **poster** a été présenté et s'intitule "*Pulsed emission from a rotating off-centred magnetic dipole in vacuum*".
  - **International School of Computational Astrophysics** aux Houches, France, du 16 au 27 mai 2016.
    En association avec l'école de formation, un **poster** a été présenté et s'intitule "*Consequences of Off-Centred Dipolar Electromagnetic Field around Pulsars*".

Bibliography

Abbott B. P., et al., 2017, The Astrophysical Journal Letters, 848, L12

Abdo A. A., et al., 2013, The Astrophysical Journal Supplement Series, 208, 17

Alba S., 2007, Illustration of the frenet frame., https://commons.wikimedia.org/wiki/File:Frenet.png

Ansoldi S., et al., 2016, Astronomy and Astrophysics, 585, A133

Antoniadis J., et al., 2013, Science, 340, 448

Archibald R. F., et al., 2016, The Astrophysical Journal, 819, L16

Arendt J., Eilek J. A., 1998, arXiv:astro-ph/9801257

Arfken G. B., Weber H.-J., Harris F. E., 2013, Mathematical methods for physicists: a comprehensive guide, 7th ed edn. Elsevier, Amsterdam ; Boston

Arons J., 1981, Pulsars: 13 Years of Research on Neutron Stars, 95, 69

Arons J., 1983, The Astrophysical Journal, 266, 215

Arons J., 1993, The Astrophysical Journal, 408, 160

Arons J., Scharlemann E. T., 1979, The Astrophysical Journal, 231, 854

Arponen J., 1972, Nuclear Physics A, 191, 257

Asseo E., Khechinashvili D., 2002, Monthly Notices of the Royal Astronomical Society, 334, 743

Astronomy 2018, Content Library - OpenStax CNX, https://cnx.org/contents/LnN76Opl@14.4:_45u6IpQ@4/Introduction

Atwood W. B., et al., 2009, ApJ, 697, 1071

Baade W., Zwicky F., 1934, PNAS, 20, 254

Backer D. C., 1976, The Astrophysical Journal, 209, 895

Bai X.-N., Spitkovsky A., 2010, The Astrophysical Journal, 715, 1270

Barnard M., Venter C., Harding A. K., 2016, The Astrophysical Journal, 832, 107

Barsukov D. P., Tsygan A. I., 2010, Monthly Notices of the Royal Astronomical Society, 409, 1077

Baym G., Pethick C., Sutherland P., 1971a, The Astrophysical Journal, 170, 299

Baym G., Bethe H. A., Pethick C. J., 1971b, Nuclear Physics A, 175, 225

Bhattacharya D., van den Heuvel E. P. J., 1991, Physics Reports, 203, 1

Blandford R. D., Romani R. W., 1988, Monthly Notices of the Royal Astronomical Society, 234, 57P

Blaskiewicz M., Cordes J. M., Wasserman I., 1991, The Astrophysical Journal, 370, 643

Bombaci I., 1996, Astronomy and Astrophysics, 305, 871

Bonazzola S., Mottez F., Heyvaerts J., 2015, Astronomy and Astrophysics, 573, A51

Bordovitsyn V. A., 1999, SYNCHROTRON RADIATION THEORY AND ITS DEVELOPMENT

Borghese A., Rea N., Zelati F. C., Esposito P., 2018, Pulsar Astrophysics the Next Fifty Years, 337, 104

Cameron A. G. W., 1965, Nature, 205, 787

Cameron A. G. W., 1966, The Astronomical Journal, 71, 379

Cepheus 2006, English: Osculating circle for curvature, `https://commons.wikimedia.org/wiki/File:Osculating_circle.svg`

Chandrasekhar S., 1931, The Astrophysical Journal, 74, 81

Chen A. Y., Beloborodov A. M., 2014, The Astrophysical Journal Letters, 795, L22

Cheng K. S., Ho C., Ruderman M., 1986a, The Astrophysical Journal, 300, 500

Cheng K. S., Ho C., Ruderman M., 1986b, The Astrophysical Journal, 300, 522

Chiang J., Romani R. W., 1994, The Astrophysical Journal, 436, 754

Contopoulos I., Kazanas D., Fendt C., 1999, The Astrophysical Journal, 511, 351

Das C. B., Das Gupta S., Gale C., Li B.-A., 2003, Physical Review C, 67, 034611

Daugherty J. K., Harding A. K., 1982, The Astrophysical Journal, 252, 337

Daugherty J. K., Harding A. K., 1983, The Astrophysical Journal, 273, 761

Davis L., 1947, Phys. Rev., 72, 632

Davis L., Goldstein M., 1970, The Astrophysical Journal Letters, 159

Demorest P. B., Pennucci T., Ransom S. M., Roberts M. S. E., Hessels J. W. T., 2010, Nature, 467, 1081

Deutsch A. J., 1955, Annales d'Astrophysique, 18, 1

Dodson R., Golap K., 2002, Monthly Notices of the Royal Astronomical Society, 334, L1

Douchin F., Haensel P., 2001, Astronomy and Astrophysics, 380, 151

Du Y. J., Qiao G. J., Han J. L., Lee K. J., Xu R. X., 2010, Monthly Notices of the Royal Astronomical Society, 406, 2671

Dwarkadas V., Ball L., Caswell J., Green A., Johnston S., Schmidt B., Wardle M., 2000, Publications of the Astronomical Society of Australia, 17, 83

Dyks J., Rudak B., 2002, Astronomy and Astrophysics, 393, 511

Dyks J., Rudak B., 2003, The Astrophysical Journal, 598, 1201

Dyks J., Harding A. K., Rudak B., 2004, The Astrophysical Journal, 606, 1125

ESA-AOESMedialab 2012, Life cycle of stars, http://sci.esa.int/education/50385-life-cycle-of-stars/

Esposito-Farese G., 1996, arXiv:gr-qc/9612039

Gangadhara R. T., Gupta Y., 2001, The Astrophysical Journal, 555, 31

Gendreau K. C., Arzoumanian Z., Okajima T., 2012, in Space Telescopes and Instrumentation 2012: Ultraviolet to Gamma Ray. International Society for Optics and Photonics, p. 844313, doi:10.1117/12.926396, https://www.spiedigitallibrary.org/conference-proceedings-of-spie/8443/844313/The-Neutron-star-Interior-Composition-ExploreR-NICER--an-Explorer/10.1117/12.926396.short

Ghisellini G., 2013, arXiv:1202.5949 [astro-ph 10.1007/978-3-319-00612-3, 873

Gil J., Mitra D., 2001, The Astrophysical Journal, 550, 383

Gil J. A., Melikidze G. I., Mitra D., 2002, Astronomy and Astrophysics, 388, 235

Ginzburg V. L., Zhelezniakov V. V., 1975, Annual Review of Astronomy and Astrophysics, 13, 511

Gold T., 1968, Nature, 218, 731

Goldreich P., 1970, The Astrophysical Journal Letters, 160, L11

Goldreich P., Julian W. H., 1969, The Astrophysical Journal, 157, 869

Good M. L., Ng K. K., 1985, The Astrophysical Journal, 299, 706

Gordon K. J., 1987, in Kleczek J., ed., , Exercises in Astronomy: Revised and Extended Edition of "Practical Work in Elementary Astronomy" by M.G.J. Minnaert. Springer Netherlands, Dordrecht, pp 237–246, doi:10.1007/978-94-009-3769-7˙56, https://doi.org/10.1007/978-94-009-3769-7_56

Griffiths D. J., 2013, Introduction to electrodynamics, fourth edition edn. Pearson, Boston

Haensel P., Zdunik J. L., Douchin F., 2002, A&A, 385, 301

Haensel P., Potekhin A. Y., Yakovlev D. G., 2007. p. Haensel, http://adsabs.harvard.edu/abs/2007ASSL..326.....H

Han J. L., Manchester R. N., Xu R. X., Qiao G. J., 1998, Monthly Notices of the Royal Astronomical Society, 300, 373

Harding A. K., 1981, . ., 245, 7

Harding A. K., 2005, arXiv:astro-ph/0503300

Harding A. K., 2013, arXiv:1302.0869 [astro-ph]

Harding A. K., Muslimov A. G., 2011, The Astrophysical Journal, 743, 181

Harding A. K., Tademaru E., Esposito L. W., 1978, The Astrophysical Journal, 225, 226

Harrison E. R., Tademaru E., 1975, The Astrophysical Journal, 201, 447

Hessels J. W. T., Ransom S. M., Stairs I. H., Freire P. C. C., Kaspi V. M., Camilo F., 2006, Science, 311, 1901

Hester J. J., 2008, Annual Review of Astronomy and Astrophysics, 46, 127

Hewish A., Okoye S. E., 1965, Nature, 207, 59

Hewish A., Bell S. J., Pilkington J. D. H., Scott P. F., Collins R. A., 1968, Nature, 217, 709

Hibschman J. A., Arons J., 2001, The Astrophysical Journal, 546, 382

Hirotani K., 2007, The Astrophysical Journal, 662, 1173

Houston J., Deininger W., Del Monte E., Erickson J., Kalinowski W., 2018, in 2018 IEEE Aerospace Conference. IEEE, Big Sky, MT, pp 1–8, doi:10.1109/AERO.2018.8396516, https://ieeexplore.ieee.org/document/8396516/

Hoyle F., Narlikar J., 1968, Nature, 218, 123

Hoyle F., Fowler W. A., Burbidge G. R., Burbidge E. M., 1964, The Astrophysical Journal, 139, 909

Jackson J. D., 1962, Classical electrodynamics. Wiley, New York

Jameson A. S., 1981, Numerical solution of the Euler equations by finite volume methods using Runge Kutta time stepping schemes, https://ntrs.nasa.gov/search.jsp?R=19920044075

Jameson A., 2017, AIAA Journal, 55, 1487

Jessner A., Slowikowska A., Klein B., Lesch H., Jaroschek C. H., Kanbach G., Hankins T. H., 2004,] 10.1016/j.asr.2005.01.091

Jiang L., Zhang C.-M., Tanni A., Zhao H.-H., 2013, International Journal of Modern Physics: Conference Series, 23, 95

Johnston S., Kramer M., Karastergiou A., Hobbs G., Ord S., Wallman J., 2007, Monthly Notices of the Royal Astronomical Society, 381, 1625

Kalapotharakos C., Kazanas D., Harding A., Contopoulos I., 2012, The Astrophysical Journal, 749, 2

Kalapotharakos C., Harding A. K., Kazanas D., 2014, The Astrophysical Journal, 793, 97

Kanbach G., et al., 1994, Astronomy and Astrophysics, 289, 855

Kazbegi A. Z., Machabeli G. Z., Melikidze G. I., 1991, Monthly Notices of the Royal Astronomical Society, 253, 377

Kelner S. R., Prosekin A. Y., Aharonian F. A., 2015, The Astronomical Journal, 149, 33

Kijak J., Gil J., 1997, Monthly Notices of the Royal Astronomical Society, 288, 631

Kobulnicky H. A., Skillman E. D., 1997, The Astrophysical Journal, 489, 636

Koester D., Reimers D., 1996, Astronomy and Astrophysics, 313, 810

Komesaroff M. M., 1970, Nature, 225, 612

Komesaroff M. M., 1976, Proceedings of the Astronomical Society of Australia, 3, 51

Komesaroff M. M., Morris D., Cooke D. J., 1970, Astrophysical Letters, 5, 37

Komissarov S. S., 2007, Monthly Notices of the Royal Astronomical Society, 382, 995

Kramer M., Xilouris K. M., Lorimer D. R., Doroshenko O., Jessner A., Wielebinski R., Wolszczan A., Camilo F., 1998, The Astrophysical Journal, 501, 270

Kramer M., Backer D. C., Cordes J. M., Lazio T. J. W., Stappers B. W., Johnston S., 2004, New Astronomy Reviews, 48, 993

Kramer M., Lyne A. G., O'Brien J. T., Jordan C. A., Lorimer D. R., 2006, Science, 312, 549

Krolik J. H., 1991, The Astrophysical Journal Letters, 373, L69

Kundu A., Petri J., 2017, Monthly Notices of the Royal Astronomical Society, 471, 3359

Kurkela A., Vuorinen A., 2016, Phys. Rev. Lett., 117, 042501

Lamers H. J., Levesque E. M., 2017, Understanding Stellar Evolution. IOP Publishing, doi:10.1088/978-0-7503-1278-3, http://iopscience.iop.org/book/978-0-7503-1278-3

Lattimer J. M., Prakash M., 2001, The Astrophysical Journal, 550, 426

Lattimer J. M., Prakash M., 2004, Science, 304, 536

Lattimer J. M., Prakash M., 2007, Physics Reports, 442, 109

Li B.-A., Steiner A. W., 2006, Physics Letters B, 642, 436

Li B.-A., Das C. B., Das Gupta S., Gale C., 2004a, Physical Review C, 69, 011603

Li B.-A., Das C. B., Das Gupta S., Gale C., 2004b, Nuclear Physics A, 735, 563

Li J., Spitkovsky A., Tchekhovskoy A., 2012, The Astrophysical Journal, 746, 60

Linares M., Shahbaz T., Casares J., 2018, ApJ, 859, 54

Longair M. S., 2011, High energy astrophysics, 3rd ed edn. Cambridge University Press, Cambridge ; New York

Lorimer D. R., 2012, Proceedings of the International Astronomical Union, 8, 237

Lyne A. G., Graham-Smith F., 1990, Pulsar astronomy. http://adsabs.harvard.edu/abs/1990puas.book.....L

Lyne A. G., Smith F. G., 1968, Nature, 218, 124

Lyne A., Jordan C., Graham-Smith F., Espinoza C., Stappers B., Weltrvrede P., 2015, Monthly Notices of the Royal Astronomical Society, 446, 857

Maeder A., 1992, Astronomy and Astrophysics, 264, 105

Malov O. I., Malofeev V. M., 2010, Astronomy Reports, 54, 210

Manchester R. N., Taylor J. H., 1977, Pulsars. http://adsabs.harvard.edu/abs/1977puls.book.....M

Manchester R. N., Durdin J. M., Newton L. M., 1985, Nature, 313, 374

Margalit B., Metzger B., 2017, The Astrophysical Journal, 850, L19

Melatos A., 1997, Monthly Notices of the Royal Astronomical Society, 288, 1049

Michel F. C., 1978, The Astrophysical Journal, 220, 1101

Michel F. C., 1982, Reviews of Modern Physics, 54, 1

Michel F. C., Goldwire Jr. H. C., 1970, Astrophysical Letters, 5, 21

Mitchell J. W. H., 2015. Kissimmee, Fl, United States, https://ntrs.nasa.gov/search.jsp?R=20150001327

Mitra D., Li X. H., 2004, Astronomy and Astrophysics, 421, 215

Mitra D., Rankin J. M., 2002, The Astrophysical Journal, 577, 322

Mochol I., Petri J., 2015, Monthly Notices of the Royal Astronomical Society: Letters, 449, L51

Moffett D. A., Hankins T. H., 1996, The Astrophysical Journal, 468, 779

Morini M., 1983, Monthly Notices of the Royal Astronomical Society, 202, 495

Morsink S. M., Stergioulas N., Blattnig S. R., 1999, The Astrophysical Journal, 510, 854

Muslimov A., Harding A. K., 1997, ApJ, 485, 735

Muslimov A. G., Harding A. K., 2003, The Astrophysical Journal, 588, 430

Muslimov A. G., Harding A. K., 2004, The Astrophysical Journal, 606, 1143

Nicastro L., Johnston S., Koribalski B., 1996, Astronomy and Astrophysics, 306, L49

Olausen S. A., Kaspi V. M., 2014, The Astrophysical Journal Supplement Series, 212, 6

Oppenheimer J. R., Volkoff G. M., 1939, Phys. Rev., 55, 374

Ozel F., Freire P., 2016, Annual Review of Astronomy and Astrophysics, 54, 401

Pacini F., 1967, Nature, 216, 567

Pacini F., 1968, Nature, 219, 145

Pandharipande V. R., Ravenhall D. G., 1989, NATO Advanced Science Institutes (ASI) Series B, 205, 103

Petri J., 2015, Monthly Notices of the Royal Astronomical Society, 450, 714

Petri J., 2016, Monthly Notices of the Royal Astronomical Society, 463, 1240

Petri J., 2017a, A Brief Incursion into the Realm of Pulsars , Horizons in World Physics. Volume 290, https://www.novapublishers.com/catalog/product_info.php?products_id=60803&osCsid=7a0c013b116f3f3d0069aca17edcd472

Petri J., 2017b, Monthly Notices of the Royal Astronomical Society, 466, L73

Philippov A. A., Spitkovsky A., 2014, The Astrophysical Journal Letters, 785, L33

Pilia M., et al., 2016, Astronomy and Astrophysics, 586, A92

Press W. H., ed. 2007, Numerical recipes: the art of scientific computing, 3rd ed edn. Cambridge University Press, Cambridge, UK ; New York

Qiao G. J., Lee K. J., Wang H. G., Xu R. X., Han J. L., 2004, The Astrophysical Journal Letters, 606, L49

Radhakrishnan V., Cooke D. J., 1969, Astrophysical Letters, 3, 225

Rankin J. M., 1990, The Astrophysical Journal, 352, 247

Rankin J. M., 1993, The Astrophysical Journal, 405, 285

Ray P., 2018, Public List of LAT-Detected Gamma-Ray Pulsars - GLAST LAT Multiwavelength Coordinating Group - SLAC Confluence, https://confluence.slac.stanford.edu/display/GLAMCOG/Public+List+of+LAT-Detected+Gamma-Ray+Pulsars

Rea N., Borghese A., Esposito P., Coti Zelati F., Bachetti M., Israel G. L., De Luca A., 2016, The Astrophysical Journal, 828, L13

Rezzolla L., Most E. R., Weih L. R., 2018, The Astrophysical Journal, 852, L25

Rhoades C. E., Ruffini R., 1974, Phys. Rev. Lett., 32, 324

Roberts W. J., 1979, The Astrophysical Journal Supplement Series, 41, 75

Romani R. W., 1996, The Astrophysical Journal, 470, 469

Romani R. W., Yadigaroglu I.-A., 1995, The Astrophysical Journal, 438, 314

Ruderman M. A., Sutherland P. G., 1975, The Astrophysical Journal, 196, 51

Ruiz M., Shapiro S. L., Tsokaros A., 2018, Physical Review D, 97

Ryle M., Bailey J. A., 1968, Nature, 217, 907

SKA Science Website S. K. A., 2011, Square Kilometre Array, https://astronomers.skatelescope.org/

Saslaw W. C., 1968, Nature, 217, 1222

Schulze R., 2010, English: Vector compound of en:File:Neutron_star_structure.JPG and en:File:Neutron_star_cross_section.jpg, data from Paweł Haensel, Alexander Y. Potekhin (Aleksandr Ûrevič Potekhin), Dmitry G. Yakovlev (2007). Neutron Stars, p. 12. Springer., https://commons.wikimedia.org/wiki/File:Neutron_star_cross_section.svg

Science A. A. f. t. A. o., 2003, Science, 301, 1285

Shibata M., Fujibayashi S., Hotokezaka K., Kiuchi K., Kyutoku K., Sekiguchi Y., Tanaka M., 2017, Physical Review D, 96

Smith D. A., Guillemot L., Kerr M., Ng C., Barr E., 2017, arXiv:1706.03592 [astro-ph]

Spitkovsky A., 2006, The Astrophysical Journal, 648, L51

Stairs I. H., et al., 2011, arXiv:1012.3507 [astro-ph 10.1063/1.3615151, pp 335–340

Stift M. J., 1974, Monthly Notices of the Royal Astronomical Society, 169, 471

Sturrock P. A., 1971, The Astrophysical Journal, 164, 529

Tan C. M., et al., 2018, arXiv:1809.00965 [astro-ph]

Tchekhovskoy A., Spitkovsky A., Li J. G., 2013, Monthly Notices of the Royal Astronomical Society: Letters, 435, L1

Thorsett S. E., Chakrabarty D., 1999, The Astrophysical Journal, 512, 288

Venter C., 2017, arXiv:1702.00732 [astro-ph]

Venter C., Harding A. K., Guillemot L., 2009, The Astrophysical Journal, 707, 800

Venter C., Barnard M., Harding A. K., Kalapotharakos C., 2017, arXiv:1710.08677 [astro-ph]

Venter C., Harding A. K., Grenier I., 2018, arXiv:1802.00204 [astro-ph]

Vigano D., Torres D. F., 2015, Monthly Notices of the Royal Astronomical Society, 449, 3755

Vigano D., Torres D. F., Hirotani K., Pessah M. E., 2015a, Monthly Notices of the Royal Astronomical Society, 447, 1164

Vigano D., Torres D. F., Hirotani K., Pessah M. E., 2015b, Monthly Notices of the Royal Astronomical Society, 447, 2631

Vigano D., Torres D. F., Hirotani K., Pessah M. E., 2015c, Monthly Notices of the Royal Astronomical Society, 447, 2649

Weisberg J. M., Taylor J. H., 2003. eprint: arXiv:astro-ph/0211217, p. 93, http://adsabs.harvard.edu/abs/2003ASPC..302...93W

Weisskopf M. C., et al., 2016, Results in Physics, 6, 1179

Weltevrede P., Johnston S., 2008, Monthly Notices of the Royal Astronomical Society, 391, 1210

Wex N., Liu K., Eatough R. P., Kramer M., Cordes J. M., Lazio T. J. W., 2012, Proceedings of the International Astronomical Union, 8, 171

Woltjer L., 1971. p. 389, http://adsabs.harvard.edu/abs/1971IAUS...46..389W

Wu X., Manchester R. N., Lyne A. G., Qiao G., 1993, Monthly Notices of the Royal Astronomical Society, 261, 630

Yadigaroglu I.-A., Romani R. W., 1995, The Astrophysical Journal, 449, 211

Yan W., et al., 2011, Monthly Notices of the Royal Astronomical Society, 414, 2087

Young M. D., Manchester R. N., Johnston S., 1999, Nature, 400, 848

Zwicky F., 1938a, Publications of the Astronomical Society of the Pacific, 50, 215

Zwicky F., 1938b, The Astrophysical Journal, 88, 522

Université de Strasbourg

Anu KUNDU

Observatoire astronomique de Strasbourg | ObAS

Contribution of multipolar electromagnetic fields to the radio and high energy emission of pulsars

Résumé

L'étude du champ électromagnétique autour des étoiles à neutrons est l'une des méthodes vitales pour comprendre la physique des pulsars. Alors que la plupart des publications utilisent l'hypothèse d'un champ électromagnétique dipolaire centré standard, des études récentes se sont concentrées sur l'inclusion de composantes de champ multipolaire plus élevées et ont présenté une image plus générale pour les pulsars dans lesquels le moment du dipôle magnétique est décalé du centre de l'étoile. Ce travail discute des conséquences d'un dipôle magnétique rotatif excentré dans le vide en montrant diverses caractéristiques des lignes de champ magnétique et de l'émission de pulsar. Une étude à large bande du spectre du rayonnement pulsar est également présentée par la création de cartes des différentes régions d'émission des pulsars distinguées sur la base de leur fréquence dans le but principal de rechercher l'évolution du profil d'impulsion avec la fréquence. La thèse présente tous les résultats ci-dessus accompagnés des discussions nécessaires pour comprendre les modèles théoriques utilisés et les détails des méthodes numériques appliquées.

Mots-clés : étoile à neutrons, champ magnétique, excentré, pulsar, émission, émission.

Résumé en anglais

Studying the electromagnetic field around neutron stars is one of the vital methods to understand the physics of the pulsars. While major literature uses assumption of a standard centred dipolar electromagnetic field, recent studies have focused on including higher multipolar field components and have presented a more generalized picture for pulsars in which the magnetic dipole moment is shifted off from the centre of the star. This work discusses the consequences of an off centred rotating magnetic dipole in vacuum by showing various characteristic features of magnetic field lines and pulsar emission. A broadband spectrum study of pulsar radiation is also laid out by creating maps of different emission regions of pulsars distinguished on the basis of their frequency with the main aim of looking for the evolution of the pulse profile with frequency. The thesis presents all the above results accompanied by the necessary discussions to understand the theoretical models used and the details of the numerical methods applied.

Keywords : neutron star, magnetic field, off centred, pulsar, emission